Improving Estimates of Ice Sheet Elevation Change Derived from AltiKa and CryoSat-2 Satellite Radar Altimetry

Inès Natsuki Otosaka

The University of Leeds

School Earth and Environment

Submitted in accordance with the requirements for the degree of

Doctor of Philosophy

July, 2021

Intellectual Property Statement

The candidate confirms that the work submitted is their own, except where work which has formed part of jointly authored publications has been included. The contribution of the candidate and the other authors to this work has been explicitly indicated below. The candidate confirms that appropriate credit has been given within the thesis where reference has been made to the work of others.

Chapter 3

The research described in Chapter 3 has been published as: Otosaka, I. N., Shepherd, A. and McMillan, M.: Ice Sheet Elevation Change in West Antarctica From Ka-Band Satellite Altimetry, *Geophysical Research Letters*, 46, 13135 - 13143. doi:10.1029/2019GL084271, 2019.

Author contributions: I. N. Otosaka led the study, processed and analysed the data and wrote the manuscript supervised by A. Shepherd. M. McMillan helped with implementation of the slope correction. All authors commented on the manuscript.

Chapter 4

The research described in Chapter 4 has been published as: Otosaka, I. N., Shepherd, Casal, T. G. D., Coccia, A., Davidson, M., Di Bella, A., Fettweis, X., Forsberg, R., Helm, V., Hogg, A. E., Hvidegaard, S. M., Lemos, A., Macedo, K., Kuipers Munneke, P., Parrinello, T., Simonsen, S. B., Skourup, H. and Sørensen, L. S.: Surface Melting Drives Fluctuations in Airborne

Radar Penetration in West Central Greenland, *Geophysical Research Letters*, 47, doi:10.1029/2020GL088293, 2020.

Author contributions: I. N. Otosaka led the study, processed and analysed the data and wrote the manuscript supervised by A. Shepherd. S. Simonsen helped with the analysis of the radar profiles. T. G. D. Casal, A. Coccia, M. Davidson, A. Di Bella, R. Forsberg, V. Helm, A. E. Hogg, S. M. Hvidegaard, A. Lemos, K. Macedo, T. Parrinello, S. Simonsen, H. Skourup and L. S. Sørensen collected the data and/or supported the ESA CryoVEx campaigns. X. Fettweis provided firn modelling outputs. P. Kuipers Munneke provided firn modelling outputs. All authors commented on the manuscript.

Chapter 5

The research described in Chapter 5 is prepared as a manuscript to be submitted as: Otosaka, I. N., Shepherd, A., Groh, A.: Changes in Northwest Greenland Ice Sheet Elevation and Mass.

Author contributions: I. N. Otosaka led the study, processed and analysed the data and wrote the manuscript supervised by A. Shepherd. A. Groh provided the gravimetry data and the solid Earth corrections. A. Shepherd commented on the manuscript.

Acknowledgements

Enfin, merci à ma famille et tout particulièrement à mon exceptionnelle soeur jumelle Diane, sans laquelle cette aventure n'aurait pas été la même. Merci pour tes encouragements, les longues nuits passées ensemble à écrire nos thèses et tous les heureux moments partagés. Merci Diane !

Abstract

While satellite Ku-band (13.5 GHz) radar altimetry has been used since the 1990s to track changes in the Greenland and Antarctic ice sheets' shape, the launch of AltiKa in 2013 provided the first opportunity to use data from higher frequency Ka-band (36 GHz) and compare it to contemporaneous Ku-band CryoSat-2 data. In this thesis, I develop novel methods and datasets, based on the processing of Ku-band CryoSat-2 and Ka-band AltiKa data, to improve our ability to detect and interpret trends in elevation change from satellite radar altimetry.

First, I produced an assessment of higher-frequency Ka-band AltiKa data in West Antarctica. By developing a new slope correction algorithm and applying a least-square model fit to AltiKa surface elevation measurements, I demonstrated that AltiKa detects trends in surface elevation in good agreement with coincident Ku-band CryoSat-2 and airborne laser data within 0.6 ± 2.4 cm yr^{-1} and 0.1 ± 0.1 cm yr^{-1}, respectively, showing that trends in penetration are minor in this region. Using this new dataset, I showed that surface lowering at Pine Island Glacier has fallen by 9 % since the 2000s, while at Thwaites Glacier it has risen by 43 %.

Next, I examined the impact of surface melting on firn stratigraphy and radar penetration in West Central Greenland by using a combination of airborne radar data, in-situ firn density measurements, and firn densification models. I showed that surface melt strongly affects the degree of radar penetration into the firn, with the largest fluctuations recorded after the extreme melt event of 2012, which caused a 6.2 ± 2.4 m reduction in Ku-band radar penetration. I further assessed different methods to mitigate the effect of fluctuations in radar penetration on surface heights and showed that using threshold retracking algorithms results in surface heights to within 14 cm from coincident airborne laser data. In addition, I showed that over this transect, Ka-band radar penetration is half that of coincident Ku-band data.

Finally, I used a decade of CryoSat-2 data to study the imbalance of the Northwest sector of the Greenland Ice Sheet and showed that the margins of this region are rapidly thinning at an average rate of 42.7 ± 0.9 cm yr^{-1}. I derived mass balance within 73 individual glacier drainage basins of this region, showing that the Northwest sector lost a total of 386.0 ± 3.7 Gt of ice between July 2010 and July 2019 with all glacier basins losing mass. I compared this new altimetry-based mass balance estimate to independent estimates from the gravimetry and mass budget techniques and found that, while the altimetry estimate is the least negative, differences between techniques vary regionally, with the mass budget and gravimetry exhibiting higher and lower ice losses, respectively.

Contents

CONTENTS

List of Figures

List of Tables

Abbreviations

ALS	Airborne Laser Scanner
ASIRAS	Airborne SAR/Interferometric Radar Altimeter System
ATM	Airborne Topographic Mapper
DEM	Digital Elevation Model
CryoVEx	CryoSat Validation Experiment
EGIG	Expéditions Glaciologiques Internationales au Groenland
ESA	European Space Agency
GIA	Glacial Isostatic Adjustment
IMAU-FDM	Insitute for Marine and Atmospheric Research Utrecht Firn Densification Model
KAREN	MetaSensing Ka-band altimeter
LRM	Low Resolution Mode
MAR	Modèle Atmosphérique Régional
NASA	National Aeronautics and Space Administration
OCOG	Offset Centre of Gravity
OIB	Operation IceBridge
POCA	Point of Closest Approach
PIG	Pine Island Glacier
PRF	Pulse Repetition Frequency
RACMO	Regional Atmospheric Climate Model
RMS	Root Mean Square
SAR	Synthetic Aperture Radar

SARAL	Satellite with Argos and Altika
SARIn	Synthetic Aperture Radar Interferometric
SIRAL	Synthetic Aperture Interferometric Radar Altimeter
SMB	Surface Mass Balance
TCOG	Threshold Offset Center of Gravity
TFMRA	Threshold First-Maximum Retracker
THW	Thwaites Glacier

This page intentionally left blank.

CHAPTER 1

Introduction

In this introductory chapter, I describe the state of the polar ice sheets and review the recent ice sheet changes including changes in ice sheet flow, surface elevation, grounding line location, calving front location, supraglacial and subglacial lakes observed from satellite data during the past three decades. I then summarise the different processes that lead to a change in the surface elevation of the ice sheets. Finally, I introduce the aim, objectives and structure of this thesis.

1.1 The Polar Ice Sheets in the Climate System

The Greenland and Antarctic Ice Sheets are today's last remaining ice sheets since the Last Ice Age (Pleistocene). Thus, they store crucial information about the past climate and play an essential role in the current climate system. In this section, I introduce the polar ice sheets, review their recent mass loss during the 'satellite era' and its impact on sea level rise and ocean circulation patterns, before looking at future projections of ice sheet mass loss.

1.1.1 The Greenland and Antarctic Ice Sheets

Global mean surface temperature is currently rising at a rate of 0.2°C per decade compared to pre-industrial time due to the anthropogenic increase in greenhouse gas concentrations in the atmosphere. It is estimated that human-induced warming of 1°C above pre-industrial levels was reached around 2017 (Masson-Delmotte et al., 2018). However, the level of warming is not uniform across the global and some regions, in particular the Arctic, which has experienced a more pronounced level of warming than the rest of the world, with air temperatures increasing at a rate more than two-fold that of the global average (Meredith et al., 2019). In the Southern hemisphere, rapid regional warming has been observed at the Antarctic Peninsula with air temperatures increasing at a rate of 0.6°C per decade during the 20th century (Vaughan et al., 2003) and water from the Bellingshausen and Amundsen seas, intruding the continental shelf, has warmed at a rate of 0.1 to 0.3°C per decade since the 1990s (Schmidtko et al., 2014). The response of the ice sheets to this changing climate is expected to have wide impacts on sea level, ocean circulation, and ecosystems.

The polar ice sheets covering most of Greenland and Antarctica (Figure 1.1) are part of the cryosphere – which encompasses all areas made of frozen water, including ice sheets, ice shelves, glaciers, sea ice, lake and river ice, permafrost and snow. Among the different elements of the cryosphere, ice sheets and glaciers directly influence global mean sea level by raising sea levels when they lose ice. While mountain glaciers contain less than 1 % of the global ice volume (Farinotti et al., 2019), the polar ice sheets cover vast areas and store about 68 % of the Earth's freshwater resources. The Greenland Ice Sheet (GrIS) covers an area of 1.7 million km^2 and stores a volume of 3.0 million km^3 of ice (Morlighem et al., 2017), while the Antarctic Ice Sheet (AIS) covers an area 4 times larger (12.3 million km^2, excluding the ice shelves) and stores 26.5 million km^3 of frozen water (Fretwell et al., 2013). Combined, the two ice sheets hold enough frozen water to raise global mean sea level by 65.3 m, with the Greenland Ice Sheet holding a potential sea level rise of 7.42 m (Morlighem et al., 2017) and the Antarctic Ice Sheet an equivalent sea level rise of 57.9 m (Morlighem et al., 2020).
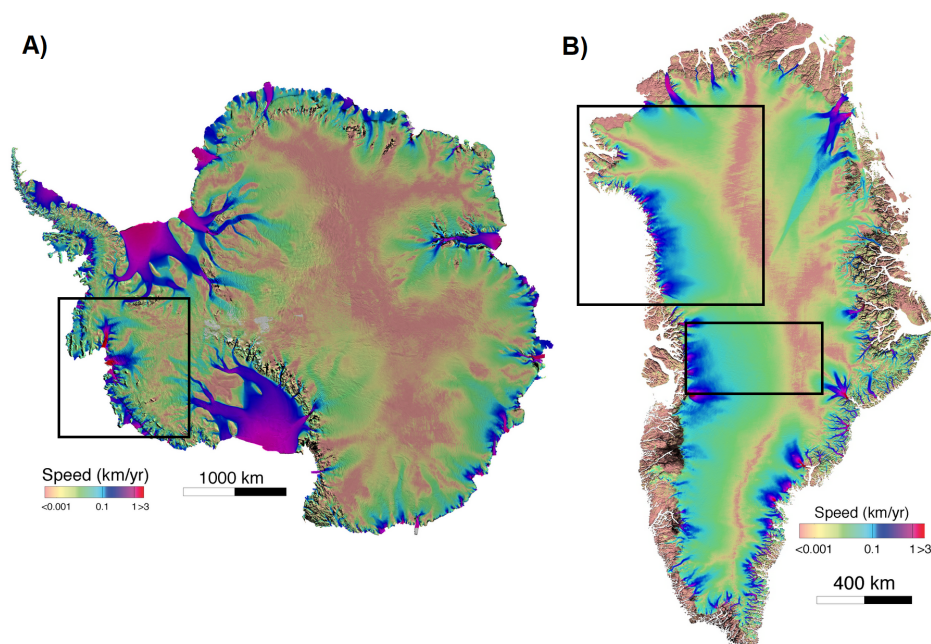
Figure 1.1: a) Antarctic Ice Sheet and b) Greenland Ice Sheet velocity maps between 1992 and 2016. Reproduced from Mouginot et al. (2017). The regions studied in this thesis are outlined in black.

The Antarctic Ice Sheet is centred around the South Pole and is surrounded by the Southern Ocean. It is divided into the West and East Antarctic Ice Sheets by the Transantarctic Mountains. West Antarctica is the most vulnerable region of the continent as its bedrock is grounded well below sea level and is therefore at greater risk than other parts of the ice sheet. Indeed, the ice sheet bed in West Antarctica is deeper at its centre than at the grounding line, suggesting that West Antarctica is prone to marine ice sheet instability (Mercer, 1978; Schoof, 2007). The instability hypothesis has been formulated for parts of the ice sheets where the grounding line – the boundary between the grounded ice and floating ice shelf – is located on a retrograde slope. In that configuration, a retreat of the grounding line leads to an increase in ice discharge as the ice thickness increases inland and in turn, entails a further retreat of the grounding line in a hysteretic behaviour. This unstable retreat goes on until a region with a downward sloping bed or

a new pinning point is reached (Figure 1.2). West Antarctica counts some of the world's fastest glaciers, with the prominent examples of Pine Island and Thwaites Glaciers located in the Amundsen Sea Embayment (Rignot, 2008). This region of the Antarctic Ice Sheet is further explored in Chapter 3 of this thesis.
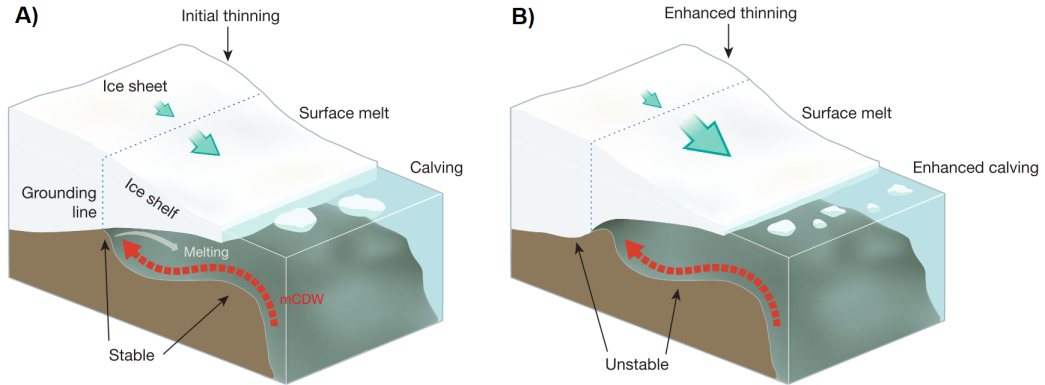
Figure 1.2: Illustration of a marine ice sheet cross section and ocean melting at the grounding line. a) The ice sheet starts thinning at the grounding line due to melting from warm Circumpolar Deep Water (CDW), leading to ice shelf thinning and grounding line retreat. b) The ice sheet now retreats on an upward sloping bed, leading to unstable retreat. The ice thickness increases further inland and thus the ice discharge at the grounding line increases, causing further thinning and grounding line retreat. Reproduced from Hanna et al. (2013)

The Antarctic Peninsula is the northernmost region of Antarctica and is often distinguished from the rest of the West Antarctic Ice Sheet due to its milder climate. The Antarctic Peninsula is a mountainous region extending over more than 1300 km and has experienced the highest level of warming compared to the rest of the continent (Vaughan et al., 2003). On the other side of the Transantarctic Mountains lies the East Antarctic Ice Sheet, covering about 85 % of the Antarctic Ice Sheet. Most of East Antarctica is grounded well above sea level and has not undergone dramatic changes, unlike what has been observed in West Antarctica (Gardner et al., 2018). About 30 major ice streams drain the Antarctic Ice Sheet, transporting about 90 % of ice and sediment from the interior to the

margins of the ice sheet (Bamber et al., 2000). These ice streams are typically tens of kilometres wide, extend inland up to a thousand of kilometres, and flow at speeds of around 800 m yr^{-1} (Bennett, 2003). Finally, the Antarctic Ice Sheet is fringed by ice shelves – covering an area of 1.6 million km^2 (Fretwell et al., 2013) – which play an important role on the stability of the ice sheet by exerting back-stresses on the grounded ice (Dupont and Alley, 2005).

In the northern hemisphere, the Greenland Ice Sheet is the largest ice-covered land and is about 1000 km wide and 2500 km long. Greenland is surrounded by the North Atlantic subpolar gyre, Baffin Bay, the Arctic Ocean, and the Greenland Sea. Greenland counts more than 200 major outlet glaciers. More than half of these glaciers are tidewater in direct contact with the ocean, while the remainder are land-terminating glaciers or glaciers ending in ice shelves (Moon et al., 2012) with the largest glaciers of the Greenland Ice Sheet - Hellheim, Jakobshavn, and Petermann glaciers - draining to the ocean. Compared to Antarctica, Greenland's glaciers are much narrower, and extend over a width of a few kilometres at their terminus. Greenland's outlet glaciers typically flow at a speed of hundreds of meters per year (though a record velocity of 17 000 m yr^{-1} was recorded at Jakobshavn Isbrae in summer 2012 (Joughin et al., 2014)), discharging about ∼500 Gt of ice to the ocean ever year (King et al., 2020). The Greenland Ice Sheet can be partitioned into ablation and accumulation areas, separated by the equilibrium altitude line (ELA). The ablation zone is defined as the region where surface mass balance is negative at the end of the year and experiences melting every summer. The accumulation area can be further partitioned into the percolation zone, where meltwater can percolate into the snowpack, and the dry snow zone, which never experiences any melt (Benson, 1996). However, this distinction has been challenged in recent years as surface melt extent and duration have increased due to warming temperatures and a persistent negative North Atlantic Oscillation atmospheric circulation pattern (Bevis et al., 2019). In 2012 and 2019 notably, surface melt extended over the highest elevation of the ice sheet (Nghiem et al., 2012; Tedesco and Fettweis, 2020). Furthermore, the ablation area has expanded towards the ice sheet interior in all regions of the ice sheet, especially in North Greenland, where

the ablation zone now covers an area 46 % larger compared to the 1990s (Noël et al., 2019) (Figure 1.3). Chapters 4 and 5 of this thesis both focus on the Greenland Ice Sheet. The former looks at a transect in West Central Greenland, while the latter investigates changes in the Northwest sector of the Greenland Ice Sheet.
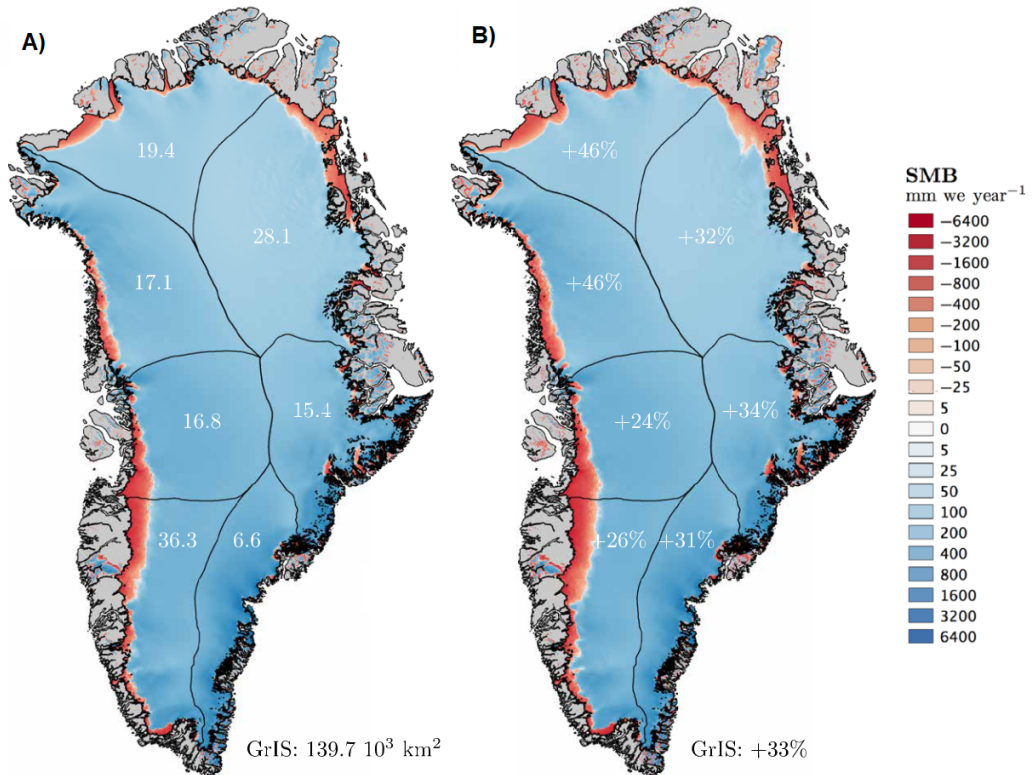
Figure 1.3: Map of SMB averaged over the period a) 1958-1990. Numbers refer to the ablation zone area (103 km^2) for individual sectors of the Greenland Ice Sheet. b) 1997-2011. Numbers refer to the relative ablation zone expansion (%) post-1990s. Reproduced from Noël et al. (2019).

1.1.2 Acceleration of Ice Losses from Antarctica and Greenland during the 'Satellite Era'

Ice sheets gain mass through snowfall accumulation and lose ice through meltwater runoff and solid ice discharge to the ocean through basal melting and iceberg calving. Among the different ice sheet mechanisms, the reaction time to an external perturbation varies from a couple of days to tens of thousands of years. Processes affecting the surface mass balance (SMB) of the ice sheet, such as snow precipitation, surface melting, sublimation, wind-driven sublimation, and refreezing react almost instantly to a climatic change. On the other hand, there is a lag in the response of outlet glaciers, ice streams and ice shelves, ranging from a couple of years to decades or centuries. Other processes such as basal fusion, isostasy, and ice flow occur on very long time scales (>10 000 years) (Rémy and Frezzotti, 2006) (Figure 1.4).
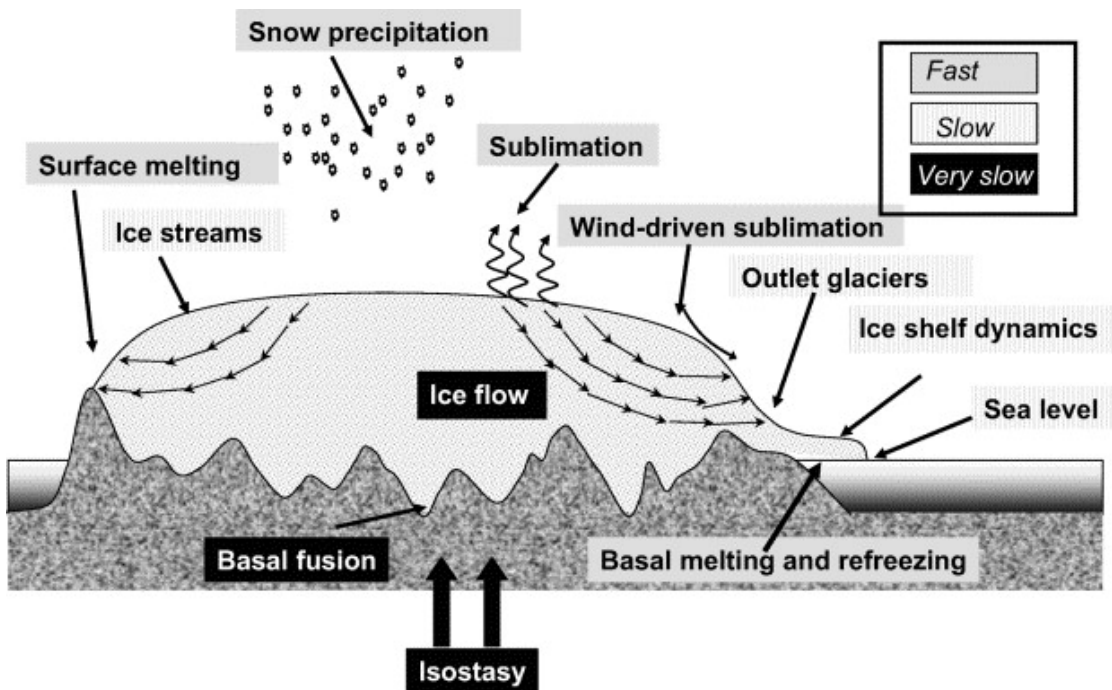
Figure 1.4: Illustration of ice sheet mechanisms. Reproduced from Rémy and Frezzotti (2006).

1. INTRODUCTION

Satellite observations have greatly advanced our understanding of the processes responsible for changes in ice sheet mass, particularly since the launch of a new generation of satellites in the 1990s, starting with the launch of ERS-1 (European Remote Sensing) in 1991. which was capable of mapping the ice sheets up to 82° latitudes. Earth observations have been instrumental in detecting changes in ice sheet flow, thickness or grounding line location. In combination with knowledge of the external forcing at play and numerical modelling, observations of ice imbalance can be attributed to the changing climate or natural variability. Before reviewing changes in mass at the scale of the ice sheets, I present examples of Earth observations of ice imbalance of two key glaciers, Pine Island Glacier in Antarctica and Jakobshavn Isbrae in Greenland.

Pine Island Glacier in West Antarctica is the largest contributor to Antarctica's ice losses, losing 58 Gt yr^{-1} in 2017 (Rignot et al., 2019) and has shown strong decadal variations in its flow, thickness and grounding line location (Figure 1.5). Satellite radar interferometry observations have revealed that between 1992 and 2011, Pine Island grounding line retreated by 31 km (Rignot et al., 2014). Pine Island glacier sped up until 2009, with ice flow velocity reaching peaks of 4000 m yr^{-1} (Joughin et al., 2016) and thinning rates exceeding 5 m yr^{-1} in the central trunk of the glacier close to the grounding line in 2009 (Konrad et al., 2017), after which the grounding line has stabilised (Mouginot et al., 2014). Since then thinning in the fast-flowing trunk of the glacier has reduced by a factor three and the highest rates of thinning are now found instead in areas of slow flow beyond the shear margins (Bamber and Dawson, 2020) (Figure 1.5). Variations in the flow of Pine Island Glacier are thought to be driven by thinning of its ice shelf due to ocean melting (e.g. Christianson et al., 2016; Dutrieux et al., 2014) and calving processes (De Rydt et al., 2021), leading to a reduction in ice shelf buttressing. Furthermore, satellite imagery has revealed the existence of crevasses and open fractures in the ice shelf shear zones during the past decade – first initiated in 1999 and rapidly expanding since 2016. The damage development over Pine Island has progressively weakened the ice shelf, enhancing ice shelf disintegration and promoting further grounding line retreat (Lhermitte et al., 2020).
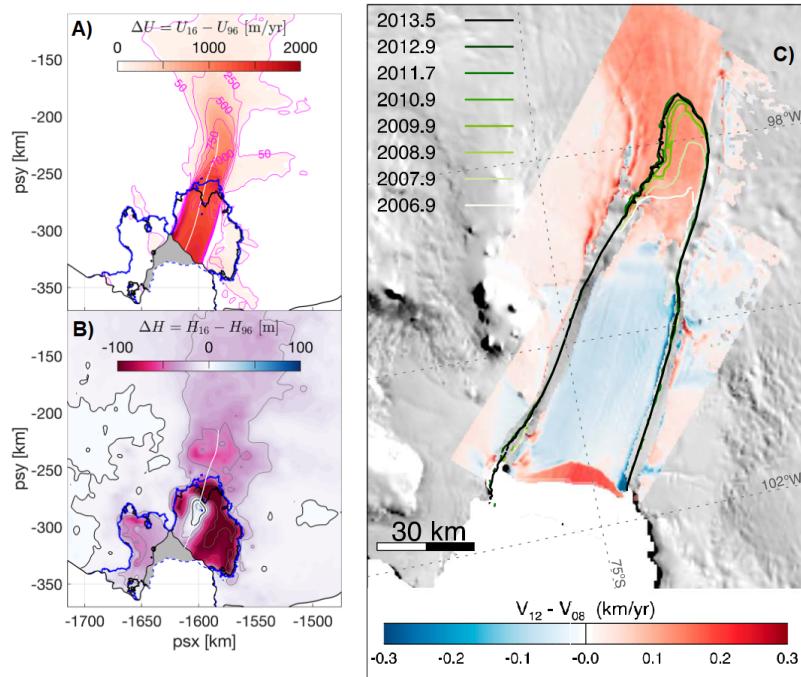
Figure 1.5: a) Changes in Pine Island Glacier flow speed between 1996 and 2016. b) Changes in thickness between 1996 and 2016. The blue line indicates the 2011 grounding line and the grey shaded area represents the loss of ice shelf extent. Reproduced from De Rydt et al. (2021). c) Changes in flow speed between 2008 and 2012. Coloured lines indicate the position of the contour of flow speed at 2.3 km yr^{-1}. Reproduced from Mouginot et al. (2014).

In Greenland, satellite imagery has shown that marine terminating glaciers from all sectors of the ice sheet have experienced pronounced retreat during the past decades, with this retreat likely starting in the 1990s and accelerating since then (Howat and Eddy, 2011). Jakobshavn Isbrae is the largest contributor to sea level rise from the Greenland Ice Sheet, accounting for 6.6 % of the ice sheet total ice losses between 1972 and 2018 (Mouginot et al., 2019). Jakobshavn Isbrae has experienced sustained retreat and thinning for two decades before recently advancing and thickening again. Intrusion of warm water from the Irminger Sea in Jakobshavn Isbra's fjord in 1997 likely triggered the break up of its floating

ice tongue (Holland et al., 2008) and subsequent sped up (Joughin et al., 2008) observed until 2016, when Jakobhavn started re-advancing and thickening due to the cooling of the ocean temperatures in Disko Bay (Khazendar et al., 2019) (Figure 1.6).
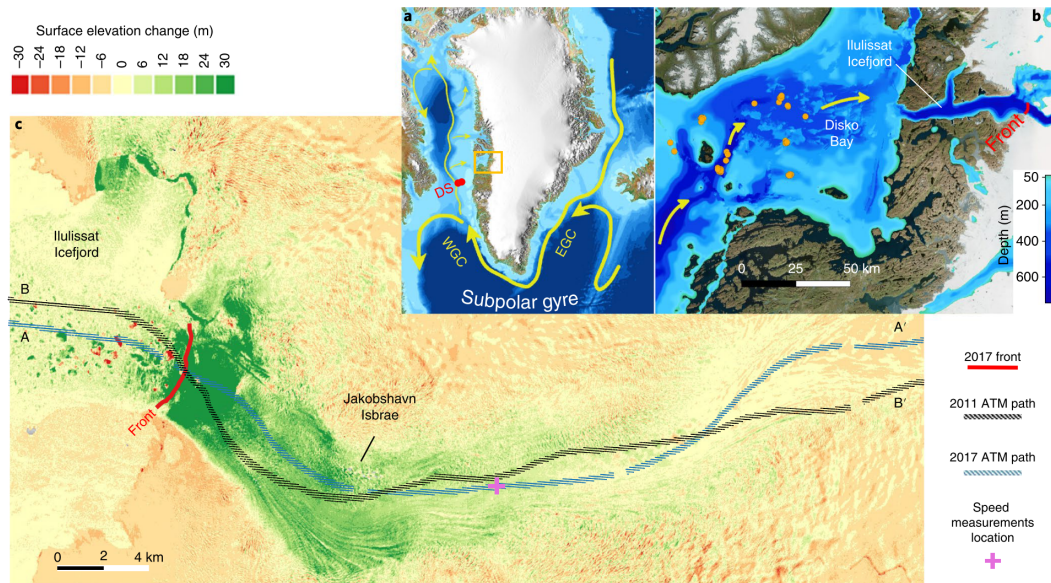
Figure 1.6: a) Location of Jakobshavn Isbrae and Disko Bay and major ocean currents (EGC, East Greenland Current; WGC, West Greenland Current). The red dots mark mooring locations. b) Map of Disko Bay and depth of the ocean and bed below sea level under the ice. Orange dots indicate the location of conductivity-temperature-depth measurements and yellow arrows represent currents transporting warm water though Disko Bay. The red line marks the location of the front of the glacier on 1st May 2017. c) Surface elevation change of Jakobshavn Isbrae main trunk between 2016 and 2017 derived from Ka-band airborne radar (GLISTIN) surveys. Reproduced from Khazendar et al. (2019).

Ice sheet mass balance at the continental scale can be routinely estimated through three methods based on satellite observations: from observations of ice flow velocity combined with estimates of surface mass balance in the mass budget method, from observations of gravitational attraction fluctuations or from repeated altimetry observations of elevation changes – the focus of this thesis. Between 1992 and 2017, the Greenland and Antarctic

Ice Sheets have collectively lost 6.4 trillion tonnes of ice (Shepherd et al., 2020; The IMBIE Team, 2018). Ice losses from the Antarctic Ice Sheet have accelerated during the past decades, rising from 49 $\pm$ 67 Gt yr^{-1} between 1992 and 1997 to 219 $\pm$ 43 Gt yr^{-1} between 2012 and 2017 (The IMBIE Team, 2018) (Figure 1.7). Unlike in Greenland – where ice losses are equally split between ice dynamics and surface processes – most of Antarctica's ice losses are driven by submarine melting and iceberg calving, which lead to glacier speedup (Rignot et al., 2019). 86 % of Antarctica's total ice losses originate from West Antarctica, with the rapid retreat and thinning of Pine Island and Thwaites glaciers due to ocean melting (Rignot et al., 2014; Shepherd et al., 2002). Almost a quarter of West Antarctica is now estimated to be in a state of dynamic imbalance (Shepherd et al., 2019). Ice losses at the Antarctic Peninsula increased by 25 Gt yr^{-1} over the 1992-2017 period following the collapse of the Larsen B Ice Shelf (Rignot et al., 2004). On the other hand, East Antarctica has remained close to a state of balance, recording only a small gain of 5 $\pm$ 46 Gt yr^{-1} between 1992 and 2017 (The IMBIE Team, 2018).

Before the 1990s, the Greenland Ice Sheet was close to a state of balance with mass gain from snowfall accumulation balancing out mass losses from meltwater runoff and solid ice discharge into the oceans (Mouginot et al., 2019). Since then, ice losses have accelerated due to increased ice flow of marine terminating glaciers and increased meltwater runoff, rising from 46 $\pm$ 37 Gt yr^{-1} in the 1990s to 244 $\pm$ 28 between 2012 and 2017 (Shepherd et al., 2020) leading to widespread thinning at the ice sheet margins (McMillan et al., 2016) (Figure 1.7). Ice losses from reduced surface mass balance and increased solid discharge to the oceans contributed equally to total ice losses over the period 1992-2018. In the early 2000s, ice discharge rose sharply primarily driven by the acceleration of outlet glaciers in Northwest and Southeast Greenland (Moon et al., 2012). However, after 2009, the main driver of Greenland's ice losses was the decrease in surface mass balance, which accounted for 84 % of the increase in mass loss, due to increase surface meltwater runoff (Enderlin et al., 2014).
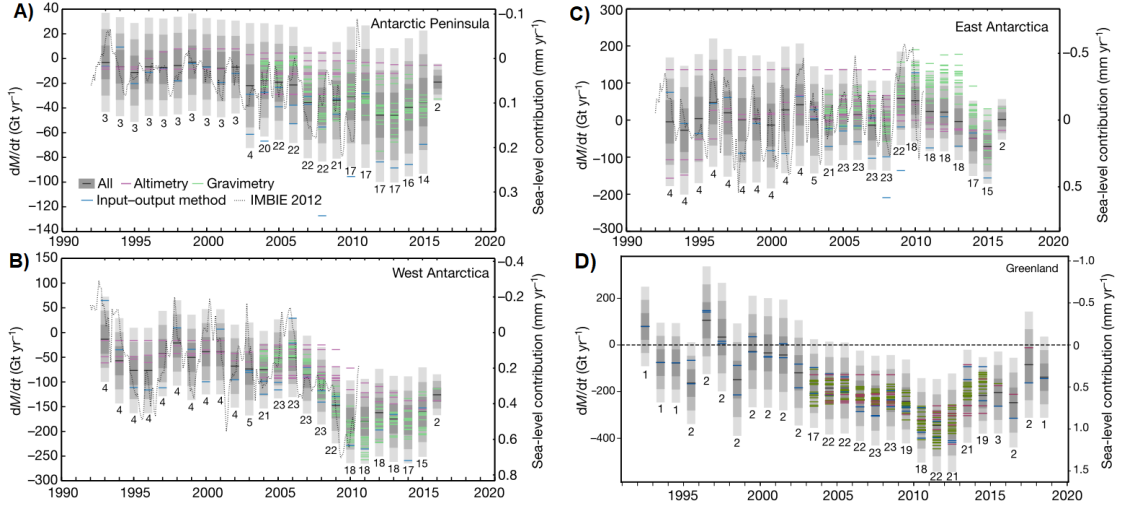
Figure 1.7: Annual rates of mass change of the Antarctic and Greenland Ice Sheets from the Ice Sheet Mass Balance Inter-comparison Exercise (IMBIE). Annual rates of mass change of a) Antarctic Peninsula, b) West Antarctica, c) East Antarctica, d) Greenland. Individual estimates of mass balance from the altimetry, gravimetry and input-output method groups are shown by the coloured lines. The average of the estimates across each measurement technique is marked by the black line. Reproduced from The IMBIE Team (2018) and Shepherd et al. (2020).

1.1.3 Ice Sheets Contribution to Global Sea Level

Between 1992 and 2017, ice losses from Greenland and Antarctica have contributed to 17.8 $\pm$ 1.8 mm to global mean sea level rise (Shepherd et al., 2020; The IMBIE Team, 2018). Together with the other components of the sea level budget (ocean thermal expansion, temporal changes in mass of glaciers, liquid water storage on land, atmospheric vapour and snow mass changes), ice losses from the ice sheets amounted to a global mean sea level rate of 3.0 mm [-1] between 1993 and 2015. While the contributions of all components of the sea level budget slightly increased between 2004-2015 compared to 1993-2004, causing an increase of 0.8 mm yr^{-1} in global mean sea level rate, the most substantial increase came from the Greenland Ice Sheet, whose contribution increased from 0.32 mm yr^{-1} between

1993-2004 to 0.82 mm yr^{-1} between 2004-2015 (Dieng et al., 2017). Ice losses from the Greenland and Antarctic Ice Sheets now represent about a quarter of the total sea level budget, contributing 0.66 mm yr^{-1} and 0.19 mm yr^{-1} to the rate of sea level rise (3.1 mm yr^{-1}) between 2002 and 2017, respectively (Nerem et al., 2018).
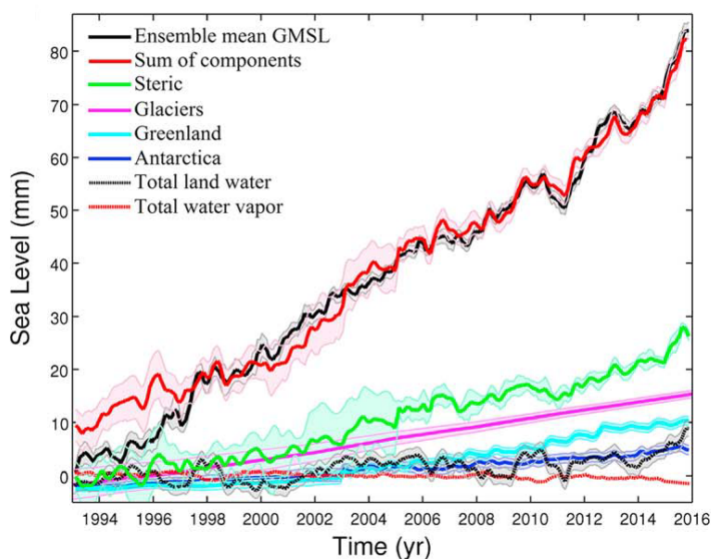
Figure 1.8: Global mean sea level and its components. Reproduced from Dieng et al. (2017).

However, while the values quoted above refer to global mean sea level rise, it is important to note that input meltwater from the ice sheet to the ocean is redistributed unevenly across the globe due to solid earth deformation coupled with gravitational effects, in a pattern named as sea level fingerprint (Farrell and Clark, 1976). When an ice sheet loses ice, it affects the Earth's gravitational field by pulling away the nearby ocean waters, inducing a sea level fall in the vicinity of the ice sheet and a sea level uplift towards faraway coastlines. Sea level change measured at tide gauges have shown large departures from eustatic values, with tide gauges in Europe recording just 40 % of the eustatic value expected from Greenland melting (Mitrovica et al., 2001). Satellite gravimetry, by measuring fluctuations in continental ice and land hydrology masses, has been used to detect the sea

level fingerprints associated with these elements. The sea level fingerprint from continental ice shows the largest drop in sea level in the near field and the largest rise below 40° latitudes (Riva et al., 2010) (Figure 1.9).
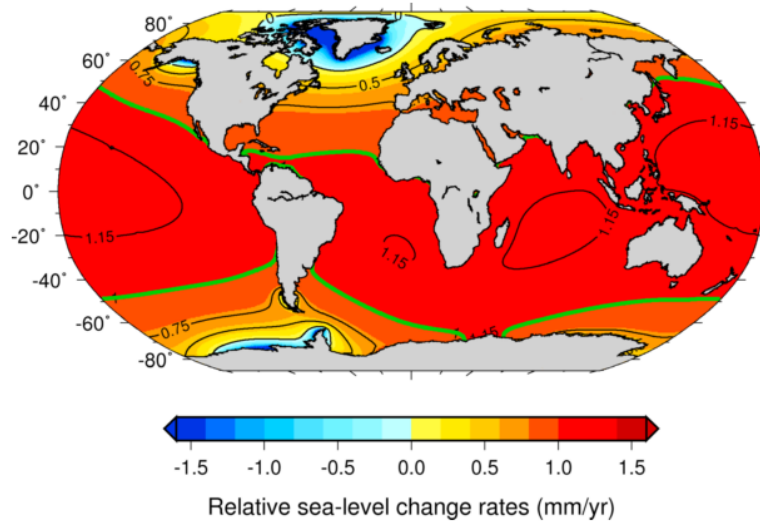
Figure 1.9: Regional sea level rise fingerprint due to the contribution of continental ice, derived from satellite gravity measurements from GRACE. The green line represents the eustatic equivalent of 1 mm yr^{-1}. Reproduced from Riva et al. (2010)

Increase in sea level has direct societal and economic implications. It is estimated that about 110 million people are currently living in low elevation coastal areas below the high tide line, putting them at risk of coastal inundation. It is projected that even under a low carbon emission scenario, a further 80 million would be exposed to coastal flooding if sea level rose by 30 to 80 cm by 2100 (Kulp and Strauss, 2019) (Figure 1.10). To inform governmental policy and plan effective mitigation measures to protect coastal areas, tracking the contribution of the ice sheets to global mean sea level rise is thus crucial (Shepherd and Nowicki, 2017).
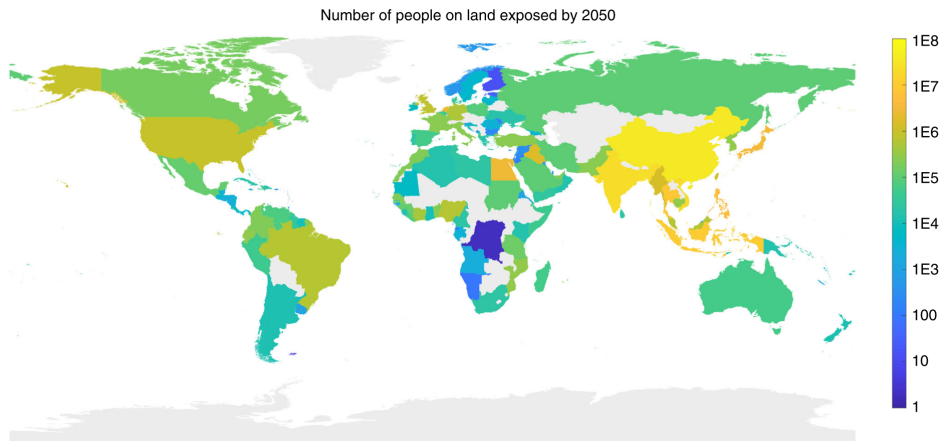
Figure 1.10: Current population on land living below projected high tide line in 2100 assuming intermediate carbon emissions (RCP 4.5). Reproduced from Kulp and Strauss (2019)

The impacts of ice sheets losing mass also have far-reaching impacts on the global climate system. In addition to contributing to global mean sea level rise, mass loss from the ice sheets constitutes an input of freshwater to the ocean, potentially affecting ocean circulation patterns. In the northern hemisphere, meltwater from the Greenland Ice Sheet has been linked to the weakening of the Atlantic meridional overturning circulation (AMOC) (Böning et al., 2016; Caesar et al., 2018). On the other hand, climate simulations of Antarctica's future ice losses have shown that increased meltwater from Antarctica would lead to a warming of the Southern Ocean subsurface, further enhancing melting at the edge of the ice sheet (Golledge et al., 2019). Finally, additional meltwater input from the ice sheets is predicted to enhance global temperature inter-annual variability up to 50 % by 2100, leading to more frequent extreme weather events (Golledge et al., 2019) (Figure 1.11).
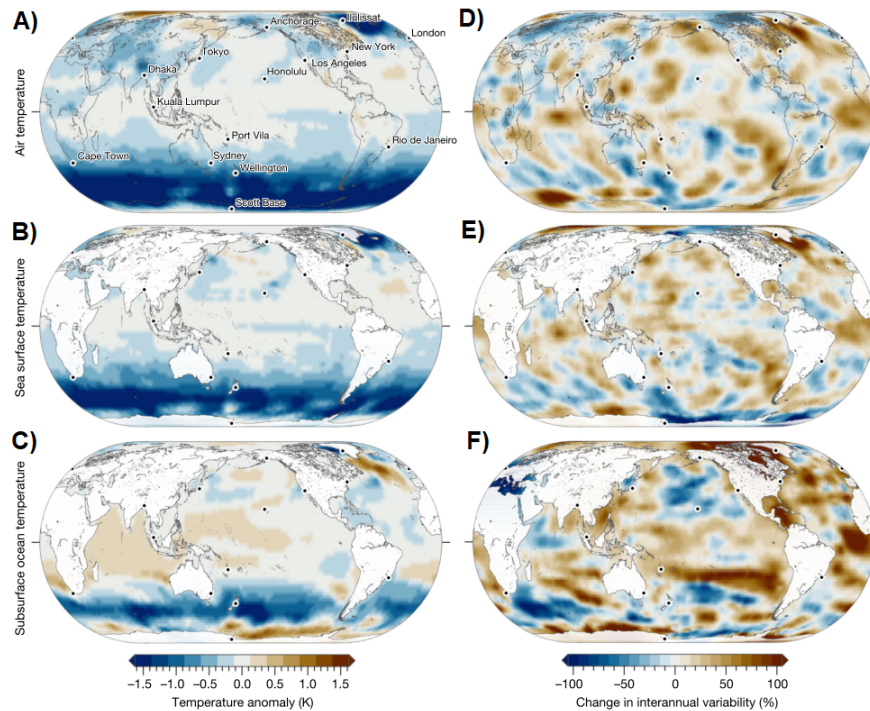
Figure 1.11: Modelled patterns of a) air temperature, b) sea surface temperature and c) subsurface ocean temperature change at 2100 compared to 2000, arising solely from additional input meltwater from the ice sheets under high emissions scenario (RCP 8.5). d) to f) Corresponding magnitude of changes in inter-annual temperature variability by 2100 compared to 2000. Reproduced from Golledge et al. (2019).

1.1.4 Future Projections of Ice Losses

Even under limited warming to less than 1.5°C compared to pre-industrial level, as preconized by the 2015 Paris Climate agreement, the ice sheets will continue to lose mass this century at rates similar to those of the past decade (Pattyn et al., 2018). A simulation of the future evolution of the Greenland Ice Sheet for three Representative Concentration Pathways (RCPs), which uses the Parallel Ice Sheet Model (PISM), shows that the Greenland Ice Sheet will lose up to a quarter (8 to 25 %) of its present-day mass under a low emission scenario (RCP 2.6); up to half (26 to 57 %) of its mass under an intermediate emission scenario (RCP 4.5); and could completely disappear (72 to 100 %) under

the highest emission scenario (RCP 8.5) in a thousand years (Aschwanden et al., 2019) (Figure 1.12). On shorter timescales, a multi-model study predicts that the Greenland Ice Sheet will add between 3 cm (RCP 2.6) and 9 cm (RCP 8.5) to global mean sea level rise by the end of the century (Goelzer et al., 2020).
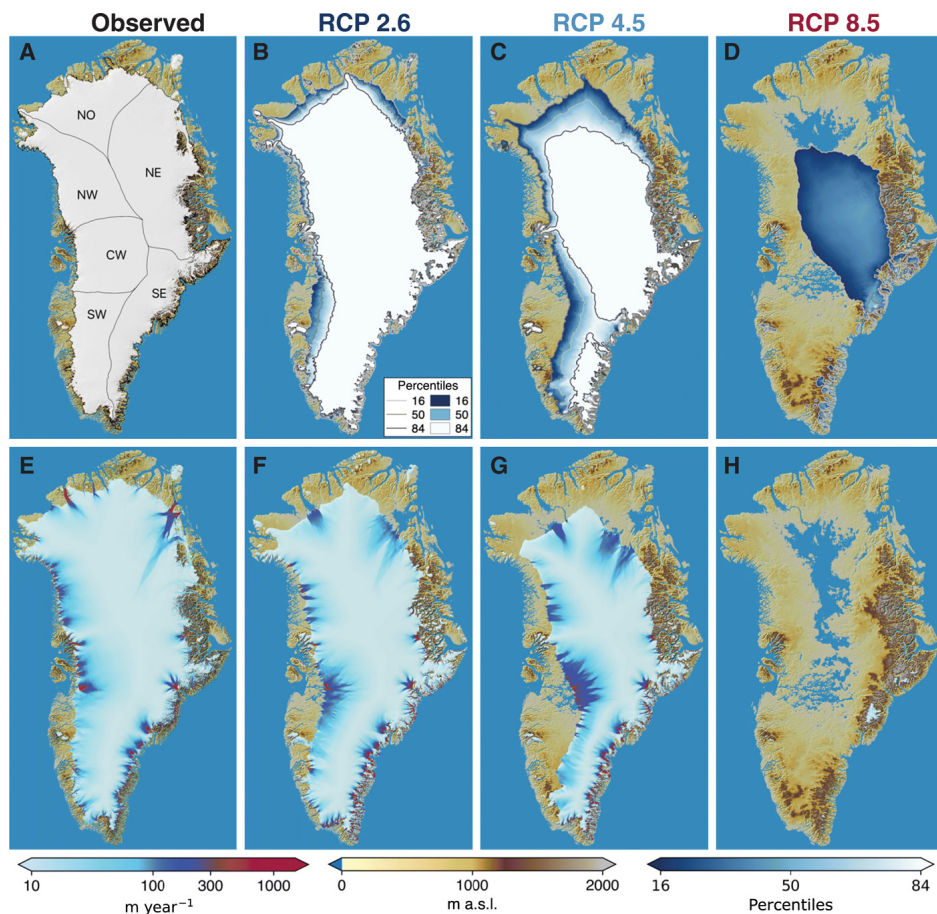
Figure 1.12: a) Observed ice extent in 2008. b) to d) Likelihood of ice cover as percentage of the ensemble simulations with nonzero ice thickness for three RCPs at year 3000. e) Observed surface velocity. f) to h) Simulated surface speed for the corresponding RCP scenarios at year 3000. Reproduced from Aschwanden et al. (2019).

Compared to the Greenland Ice Sheet, it would take much longer for the Antarctic Ice Sheet to disintegrate. For Antarctica to become ice free in a millennium, it would require burning a total of 10,000 Gt of fossil fuel, when by comparison limiting the temperature

increase to 2°C compared to 2010 would require limiting future carbon release to 600 Gt (Winkelmann et al., 2015). However, simulations show that if a threshold of 500 Gt of carbon released in the atmosphere is crossed, West Antarctica would be at risk (Figure 1.13). It is also important to note that models' results show a large spread in Antarctica's future predictions, with simulated contribution to sea level rise between 2015 and 2100 varying from -7.8 cm and +30.0 cm under RCP 8.5 (Seroussi et al., 2020). In a warming climate, snowfall is expected to increase across the continent due to higher moisture in the air (Frieler et al., 2015), which could potentially offset the ice losses from West Antarctica and thus lead to an almost negligible contribution of Antarctica to sea level rise, and even in some models, to a reversal of the current trend. Furthermore, poor knowledge of ocean and ice sheet interactions contributes to higher uncertainties in simulations of future Antarctica Ice Sheet mass balance, as observations of ocean temperatures beneath ice shelves remain sparse (Pattyn and Morlighem, 2020).
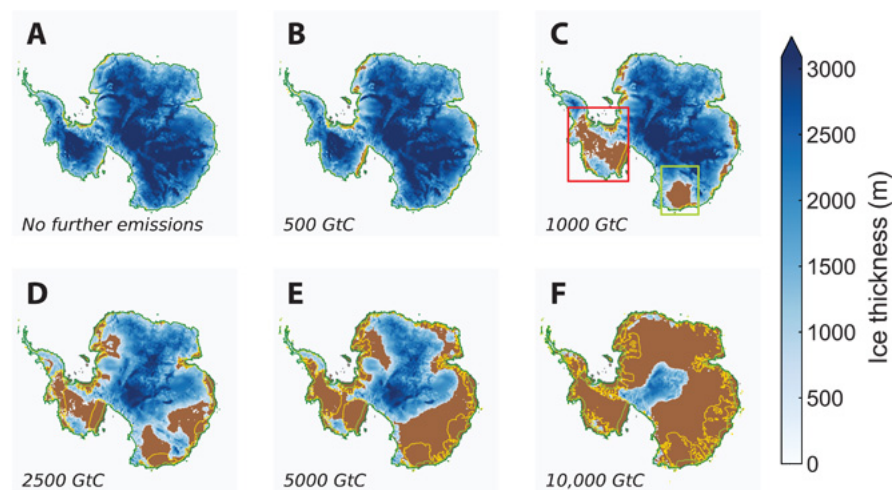
Figure 1.13: Ice thickness of the Antarctic Ice Sheet after 10,000 years. a) present-day thickness, b) to f) after 10,000 years of forcing with cumulative emissions of 500 GtC, 1000 GtC, 2500 GtC, 5000 GtC and 10,000 GtC, respectively. The grounding line position after 100, 300 and 1000 years is indicated in green, light green and yellow, respectively. Reproduced from Winkelmann et al. (2015).

Ice sheets are also suspected to be vulnerable to positive feedback effects - marine ice sheet instability (MISI) (see Section 1.1.1) and marine ice-cliff instability (MICI) – that would lead to a rapid acceleration in mass loss and irreversible retreat of the ice sheets in case of prolonged atmospheric and oceanic warming. However, the vulnerability of the ice sheets to these positive feedback effects remains unclear. Marine ice sheet instability is associated with grounding line retreat on a retrograde bed slope, a mechanism that would reinforce itself as ice thickness increases inland, thus increasing the ice flux as the grounding line retreats further (Ritz et al., 2015). Thwaites and Pine Island Glaciers basins in West Antarctica are suspected to already be undergoing this process (Joughin et al., 2014). On the other hand, marine ice-cliff instability is associated with a collapse of tall ice cliffs ($\approx$90 m) triggered by ice-shelf collapse, inducing a rapid and sustain retreat of the ice sheet (DeConto and Pollard, 2016). While it would lead to a non-linear response of the ice sheets and a more extreme sea level rise contribution, it has not been observed previously and may not be needed to reproduce past sea level rise from the Pliocene (Edwards et al., 2019).

Ice losses from Antarctica and Greenland are the largest sources of uncertainty in projections of future sea level rise (Shepherd and Nowicki, 2017) and are projected to contribute between 21 cm and 1.3 m to global mean sea level rise by 2100 based on the Fifth assessment (AR5) of the Intergovernmental Panel on Climate Change (IPCC) (Church et al., 2013). Compared to the previous IPCC assessment (AR4), which did not include rapid ice dynamic mechanisms, models developed for the AR5 assessment were greatly improved by implementing the approximation of the Stokes equations in order to reproduce rapid changes in the flow of outlet glaciers and ice shelves (Church et al., 2013). Furthermore, considerable improvements in the availability and abundance of observations of ice sheet changes have supported new refinements of ice sheet models through ice sheet models initialisation and validation and data assimilation techniques (Goelzer et al., 2017). For instance, satellite observations of ice sheet mass losses between 2007 and 2017 showed that the ice sheets contributed 12.7 mm to global mean sea level rise over this period, tracking the upper range of the IPCC AR5 projections, which predicts a contribution

to sea level rise between 13.7 and 14.1 mm over the same period (Slater et al., 2020).
However, oceanic forcing of the ice sheets remains a large source of uncertainty, limiting
the ability of models to accurately represent ice-ocean interactions, mainly due to the lack
of observational dataset of ocean temperatures within ice shelf cavities (Colleoni et al.,
2018).

1.2 Processes Leading to Ice Sheet Elevation Change

Fluctuations in ice sheet elevation can arise through a wide variety of processes, including
changes in glacier dynamics ($\dot{h}_{dyn}$), changes in surface mass balance ($\dot{h}_{smb}$), changes in the
firn layer thickness ($\dot{h}_{fc}$), changes in ice sheet hydrology ($\dot{h}_{hydro}$), and changes in the solid
earth height ($\dot{h}_{bedrock}$). Measurements of surface elevation change integrate all of these
processes to measure the total elevation change ($\frac{dh}{dt}$):

$$\frac{dh}{dt} = \dot{h}_{dyn} + \dot{h}_{smb} + \dot{h}_{fc} + \dot{h}_{hydro} + \dot{h}_{bedrock} \qquad (1.1)$$

Not all processes leading to surface elevation change are associated with a change in ice
sheet mass, and it is therefore important to account for these before using elevation changes
to study mass imbalance. Ice-dynamical elevation changes are concentrated over glaciers
and ice streams in the margins of the ice sheet, though ice-thinning originating from these
processes has been shown to spread inland over hundreds of kilometres (Konrad et al.,
2017). Ice-dynamical thinning has been linked to increase in ice flow and grounding line
retreat, most notably in the Amundsen Sea Embayment, where thinning of the order of
several of meters per year has been recorded at Pine Island, Thwaites and Pope-Smith
and Kohler glaciers (e.g. Flament and Remy, 2012; Konrad et al., 2018; Shepherd et al.,
2002; Thomas et al., 2004). On the other hand, thickening has been observed in case
of glacier slowdown, for instance at the Ross Ice Streams in West Antarctica (Joughin
and Tulaczyk, 2002). Fluctuations in surface elevation arising from surface mass balance
fluctuations occur across the whole ice sheets over short time scales. While snowfall accu-
mulation contributes to thickening and has been shown to be the driver of the thickening
observed in East Antarctica (Davis et al., 2005), surface melting, drifting snow sublim-

ation and snow erosion all contribute to surface thinning. Firn processes occur mainly in the interior of the ice sheets, with firn compaction leading to elevation changes of the order of up to tens centimetres per year. Hydrology processes are very localised processes with drainage and filling of supraglacial and subglacial lakes leading to elevation changes of the order of tens meters over short periods of time (e.g. McMillan et al., 2007; Palmer et al., 2015; Smith, Gourmelen, Huth and Joughin, 2017). Finally, solid earth processes, such as glacial isostatic adjustment, occur on very long time scales and the magnitude of the induced elevation changes are small (of the order of millimetres per year) compared to the processes mentioned above (Martín-Español et al., 2016; Wake et al., 2016). Repeated radar or laser altimetry measurements from airborne and satellite platforms allow us to track changes in ice surface elevation over time, and are therefore a powerful tool for studying ice sheet processes. Satellite altimetry, for example, has revealed spatial patterns of surface elevation change at fine (kilometre scale) spatial resolution across the vast majority of the Greenland and Antarctic ice sheets, showing that thinning is concentrated at the margins of the ice sheets (e.g. McMillan et al., 2016; Pritchard et al., 2009; Smith et al., 2020) (Figure 1.14). While the methods for deriving ice sheet surface elevation from altimetry measurements are presented in the next chapter of this thesis, in the following sections I discuss the key processes that lead to changes in ice sheet surface elevation. Surface elevation changes resulting from these processes are not necessarily equivalent to surface elevation changes measured from radar or laser altimeters, as these sensors detect the scattering horizon rather than directly measuring the elevation of the ice sheet surface. This requires assumptions and post-processing procedures of the radar or laser raw data, which I will examine in details in the next chapter.
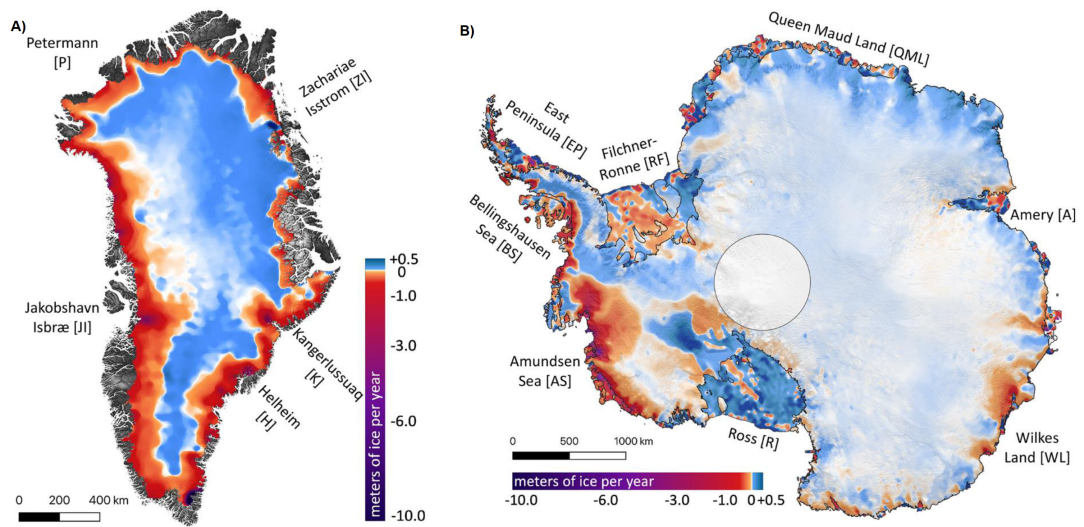
Figure 1.14: Surface elevation change between 2003 and 2019 of a) the Greenland Ice Sheet and b) the Antarctic Ice Sheet derived from ICESat and ICESat-2 satellite laser altimetry. Reproduced from Smith et al. (2020).

1.2.1 Glacier Dynamics

Ice dynamic processes occur over glaciers and ice streams and originate from a change in ice flow. Ice is discharged from the ice sheet to the ocean via basal melting and iceberg calving of marine terminating glaciers and thus interactions between ocean and ice play an essential role in ice sheet mass loss (Joughin et al., 2012).

Calving front retreat and ice shelf thinning can additionally destabilise the grounded ice sheet upstream due to a loss in buttressing to the grounded ice sheet (Dupont and Alley, 2005), leading to glaciers speed up and further thinning (Gudmundsson et al., 2019). Submarine melting of ice shelves and tidewater glaciers' floating ice tongues at the ice-ocean interface leads to ice flow acceleration near the grounding line (Holland et al., 2008), further inducing thinning of the ice upstream (Shepherd et al., 2002) and grounding line retreat (Park et al., 2013). The intrusion of warm subsurface water close to the edge of marine-terminating glaciers and beneath ice shelves is dependent on the bed topography (Seroussi et al., 2017) and submarine melt rates are highly variable both
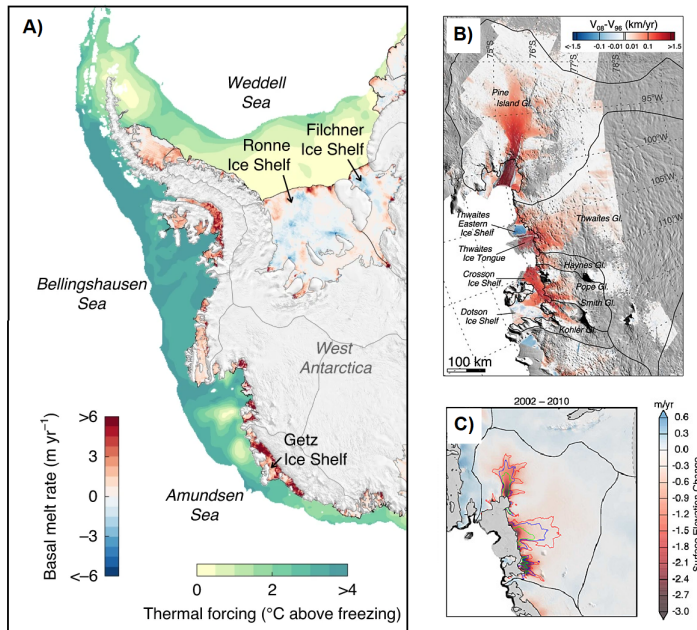
Figure 1.15: a) Basal melt rates of the Amundsen Sea ice shelves averaged between 2010 and 2018 derived from CryoSat-2 satellite radar altimetry. Reproduced from Adusumilli et al. (2020). b) Change in ice flow velocity between 1996 and 2008 from satellite imagery and radar interferometry. Reproduced from Mouginot et al. (2014) c) Surface elevation change between 2002 and 2010 from Envisat satellite radar altimetry from (Flament and Remy, 2012). Reproduced from Sutterley et al. (2014).

spatially (Wilson et al., 2017) and temporally over a range of different time scales from weeks to months (Davis et al., 2018). Ice shelves in the Amundsen and Bellingshausen seas have thinned by up to 18 % of their thickness in 2012 compared to 1994 (Paolo et al., 2015). Cavities under ice shelves promoting the circulation of Circumpolar Deep Water (CWD) have been identified as a trigger for submarine melting, removing more than 300 m of solid ice beneath Smith Glacier between 2002 and 2009 (Khazendar et al., 2016). Consequently, ice dynamic losses are the greatest in this region of Antarctica with a 77 % increase in ice discharge between 1973 and 2013 due to the speed-up of Pine Island, Thwaites, Pope, Smith and Kohler glaciers (Mouginot et al., 2014) and ice thinning over

these glaciers exceed 3 m yr^{-1} (Flament and Remy, 2012) (Figure 1.15).
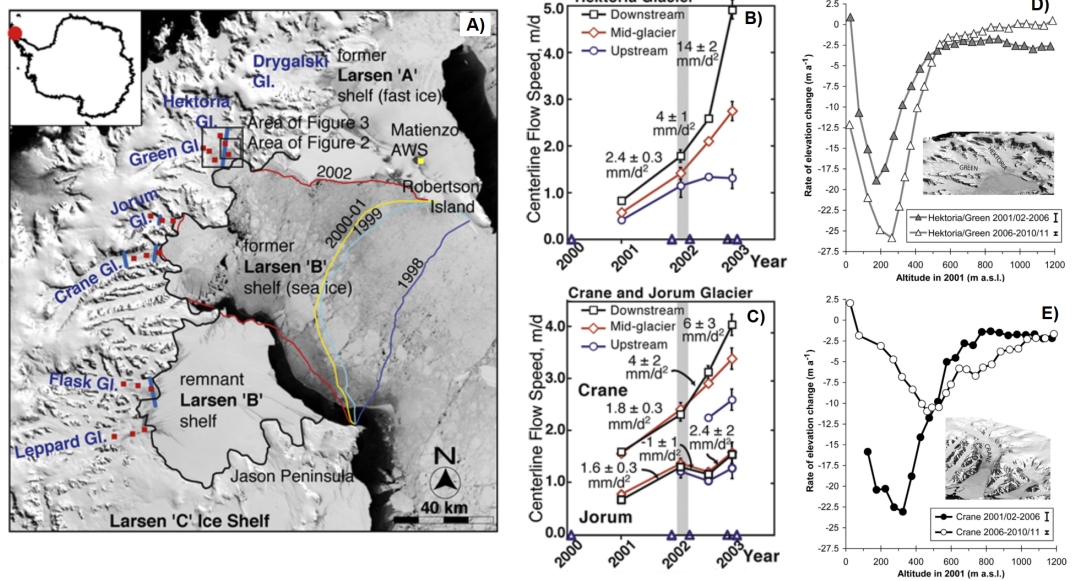
Figure 1.16: a) MODIS image from 1st November 2003 of the Larsen B ice shelf and its tributary glaciers. The coloured lines indicate ice shelf extents from 1998, 1999, 2000 and 2002 and the black line marks the grounding line. b) and c) Hektoria and Crane and Jorum glaciers centreline flow speed derived from Landsat 7 satellite imagery. Grey bars represent the February-March 2002 collapse event. Reproduced from Scambos et al. (2004). d) and e) Hektoria and Crane glaciers rate of elevation change for 50 m altitude bands during 2001/02/-2006 (filled symbols) and 2006-2010/11 (unfilled symbols) derived from ASTER and SPOT5 optical stereo-imagery. Reproduced from Berthier et al. (2012).

In addition to submarine melting, the polar ice sheets lose mass at the margins of the ice shelves and termini of marine glaciers through iceberg calving, releasing chunks of ice to the ocean (Enderlin et al., 2014). Iceberg calving is initiated by the formation of small cracks on the surface of glaciers and ice shelves, further growing into crevasses, a process that can be enhanced through hydro-fracturing of water-filled of crevasses or meltwater undercutting (Benn et al., 2007). Major calving events occurred over the Larsen A and B ice shelves, leading to their disintegration in 1995 and 2002, respectively. These events

induced the speed-up and thinning of the ice shelves' tributary glaciers (Figure 1.16). Following the collapse of the Larsen B ice shelf in the Antarctic Peninsula in 2002, glaciers sped up by a factor two to six due to the loss of buttressing, leading to accelerated mass losses. This was followed by a rapid thinning of these glaciers, with a surface lowering of up to 38 m recorded a year after the ice shelf collapse over a period of only 6 months (Scambos et al., 2004). The thinning of the glaciers has persisted for many years after the ice shelf collapse and propagated further upstream with the 10 m yr^{-1} thinning contour propagating at a speed of 2 km yr^{-1} between 2006 and 2011 (Berthier et al., 2012).

Overall, submarine melting of tidewater glaciers' floating ice tongues and ice shelves accounts for about half of Antarctica dynamic ice losses (Depoorter et al., 2013) and a quarter of Greenland's dynamic ice losses (Benn et al., 2017), with calving losses accounting for the remainder dynamic losses.

1.2.2 Surface Mass Balance

Surface mass balance (SMB) represents the mass gained or lost through processes occurring at the surface of the ice sheet as a consequence of its interactions with the atmosphere. Among these processes, precipitation falling as snow or rain leads to a mass gain while surface melt, meltwater runoff, drifting snow sublimation, and snow erosion all lead to a removal of mass at the surface of the ice sheet (Broeke et al., 2016). Observations of SMB are scarce across the ice sheets and therefore SMB and its individual components are modelled at the continental scale using regional climate models forced by climate reanalyses such as the Regional Atmospheric Climate Model (RACMO) (Noël et al., 2018) or the Modèle Atmosphérique Régional (MAR) (Fettweis et al., 2017).

While snowfall accumulation is by far the main source of mass in both Greenland and Antarctica, the dominant surface ablation process is different for the two ice sheets. In Greenland, surface melt is the predominant ablation process while in Antarctica the main ablation process is drifting snow sublimation. All SMB components exhibit a strong seasonal cycle, and drive the short-term fluctuations in ice sheet volume and mass changes. Surface melt occurs when air temperature is above local freezing point. The Greenland Ice

Sheet coastal region has warmed by +1.7°C and +4.4°C in summer and winter respectively between 1991 and 2019 (Hanna et al., 2021) and thus, the duration of the melt season has significantly increased over the years. In addition to the duration of the melt season, the melt extent has also spread to higher altitudes in the interior of the ice sheet in recent years, with almost the entirety of the surface of the ice sheet melting in 2012 (Nghiem et al., 2012). On the other hand, Antarctica's air temperatures are much lower than in Greenland and only some parts of Antarctica – West Antarctica and the Antarctic Peninsula – experience regular summer melt. However, only a portion of the meltwater produced leaves the ice sheet through runoff. Some meltwater is retained in the firn by capillary forces, refreezes at the surface or below the surface forming ice lenses, is stored in liquid form in firn aquifers or in subsurface lakes or accumulates in depressions present at the surface of the ice sheet to form supraglacial lakes. About half of the total meltwater directly runs off to the ocean in Greenland (van den Broeke et al., 2009) while in Antarctica, runoff is close to zero as almost all surface meltwater refreezes locally (Figure 1.17).
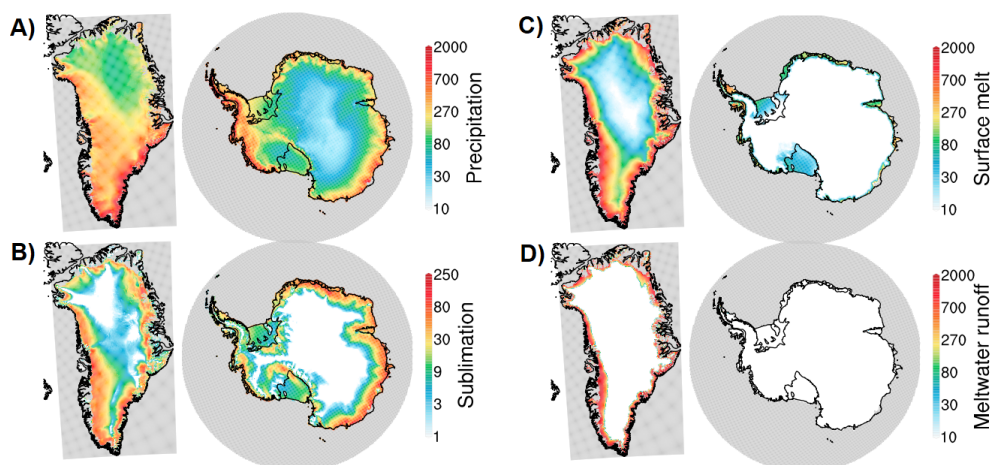
Figure 1.17: Annual mean values of surface mass balance components over the period 1980-2015 from RACMO2 in mm w.e. yr^{-1} on the Greenland and Antarctic Ice Sheets. a) Precipitation, b) Total sublimation (surface sublimation + drifting snow sublimation), c) Surface melt and d) Meltwater runoff. Reproduced from Lenaerts et al. (2019).

SMB fluctuations, by adding or removing mass at the surface of the ice sheet, induce a surface elevation change. Across the whole Greenland Ice Sheet, SMB and firn processes - which I will explore in more details in the next section – accounted for a total surface lowering of 1.96 m between 1980 and 2014 (Kuipers Munneke et al., 2015) (Figure 1.18). Thickening in the interior of the ice sheet can be attributed to snowfall accumulation while at lower elevations, snowfall accumulation is offset by surface melt, except in the South where melt dominates the firn-driven surface lowering. In Antarctica, snowfall accumulation has been correlated to the observed thickening of East Antarctica where surface elevation has increased at a rate of 1.6 cm yr^{-1} between 1992 and 2003 (Davis et al., 2005).
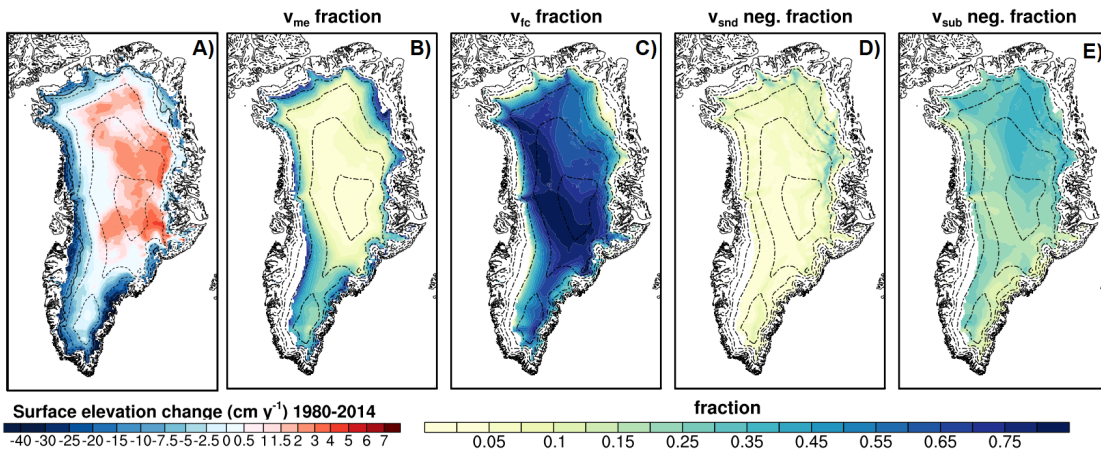
Figure 1.18: Greenland Ice Sheet surface elevation changes arising from SMB and firn processes. a) Modelled average firn thickness change for 1980-2014. The black line marks the equilibrium line. b) to e) Fraction of the surface lowering caused by b) melt, c) firn compaction, d) snowdrift processes and e) sublimation. Reproduced from Kuipers Munneke et al. (2015).

1.2.3 Firn Compaction

Accumulated snow at the surface of the ice sheet compacts into firn – the intermediate stage between snow and glacial ice – thus increasing its density. Snow deposited at the surface of the ice sheet has a density of about 315 kg m^{-3} (Fausto et al., 2018) and contains a large amount of air. As more snow is deposited at the surface, air between firn pore spaces is gradually squeezed out under the action of gravity, progressively increasing the density of the firn. High values of firn air content are found in areas of high accumulation where the firn layer is buried quickly, resulting in a thick firn layer with remaining air bubbles while low values of firn air content are found in regions where surface melting is important (Ligtenberg et al., 2014) (Figure 1.19).
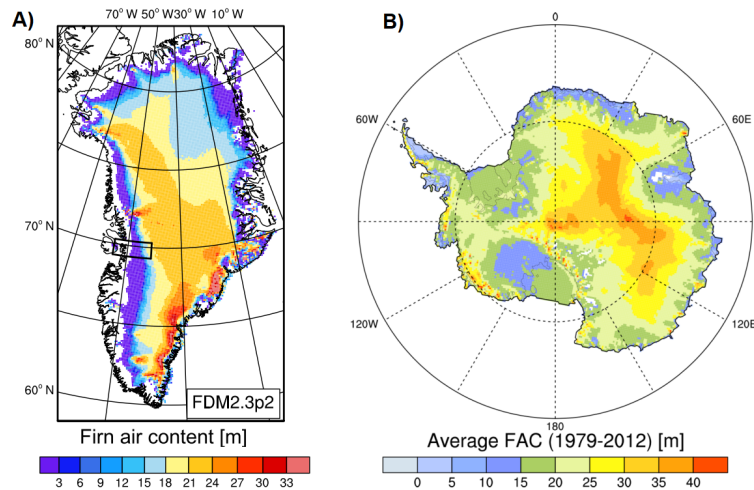
Figure 1.19: a) Greenland Ice Sheet average firn air content for the period 1990-2009. Reproduced from Ligtenberg et al. (2018). b) Antarctic Ice Sheet average firn air content for 1979-2012. Reproduced from Ligtenberg et al. (2014).

Densification of the firn results in a decrease in surface elevation with no associated mass change. Firn and SMB processes drive the seasonal fluctuations in surface elevation change observed from altimeters. Comparisons of surface elevation change observed from Envisat satellite altimetry and modelled elevation change associated with SMB and firn processes have shown that the seasonal fluctuations in the firn layer can explain 31 % of

the seasonal elevation cycle observed from radar altimetry in Antarctica (Ligtenberg et al., 2012), with the firn layer thickness increasing in autumn, winter and spring before rapidly decreasing in summer (Figure 1.20). In addition, modelling firn processes, including firn compaction, meltwater percolation and refreezing, is important as ice lenses (Benson, 1996) or thicker ice slabs can form at depth within the snowpack (Macferrin et al., 2019), altering the backscatter distribution recorded with radar instruments. Therefore, accurate estimates of the firn layer depth and density are important to correct satellite altimetry data for changes in the firn thickness as well as to understand the radar penetration into the snowpack.
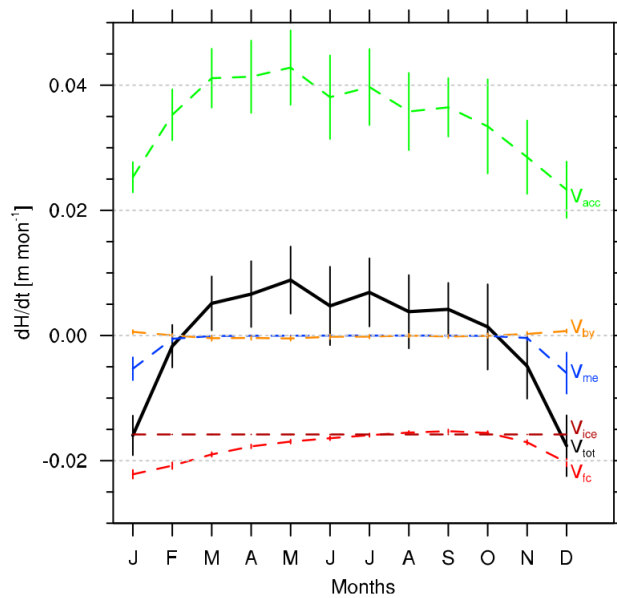
Figure 1.20: Monthly surface elevation changes and its components over the Antarctic Ice Sheet and ice shelves: total elevation change in black (V_{tot}, black), accumulation (V_{acc}, green), firn compaction (V_{fc}), snow melt (V_{me}, blue), vertical downward movement of ice (V_{ice}, brown) and buoyancy effect over ice shelf (V_{by}, orange) simulated by a firn densification model. Reproduced from Ligtenberg et al. (2012).

1.2.4 Ice Sheet Hydrology

Meltwater produced from surface melt is an important input to the ice sheet hydrological system. Meltwater accumulated in supraglacial lakes at the surface of the ice sheet can be delivered to the subglacial drainage system during episodic drainage events of these lakes through moulins or crevasses that propagate from the surface to the bed through hydro-fracturing (Das et al., 2008) (Figure 1.21).
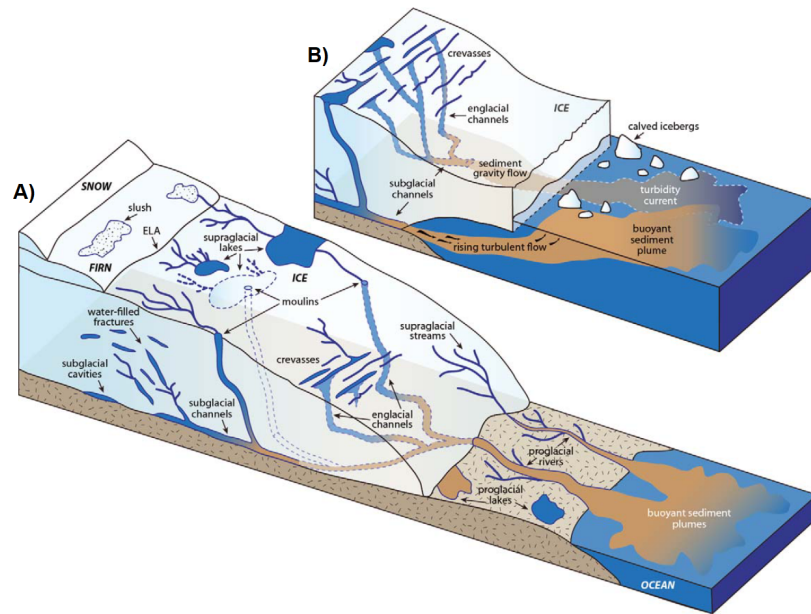
Figure 1.21: Illustration of the Greenland Ice Sheet hydrology system for a a) Land terminating glacier, b) Marine terminating glacier. Reproduced from Chu (2014).

In Greenland, supraglacial lakes form during the melt season across the ablation zone and have spread to higher elevations in recent years in response to warm temperatures and increase in surface melt (e.g. Gledhill and Williamson, 2017; Leeson et al., 2015). There are more than a thousand supraglacial lakes forming on the surface of the Greenland Ice Sheet during the summer months, with a typical size of a few kilometres and a depth between 1 to 15 meters. A large proportion of these lakes are perennial and undergo a cycle of growth and decay (Chu, 2014). Drainage of lakes can create new conduits transporting water

from the surface of the ice sheet to its bed through hydro-fracturing. GPS measurements of surface displacement of North Lake (located south of Jakobshavn Isbrae catchment) before, during and after three rapid drainage events in 2011, 2012 and 2013 show that these events are preceded by an uplift of the ice sheet. The drainage events are initiated by the introduction of meltwater in nearby cracks and moulins generating tensile stress due to the accumulated meltwater, thus provoking an uplift of the surface and promoting the creation of a hydro-fracture beneath the lake (Stevens et al., 2015). Drainage of supraglacial lakes also play a role in enhancing ice sheet dynamics and these events can modulate fluctuations in ice velocity over daily timescales (Shepherd et al., 2009) and seasonal timescales (Palmer et al., 2011). In Antarctica, most of the supraglacial lakes can be found over ice shelves during the ablation season. In East Antarctica, more than 65,000 lakes have been mapped from satellite imagery during the melt season in January 2017, resulting in a cumulative area of more than 1300 km^2 (Stokes et al., 2019). Supraglacial lakes are also a precursor of ice shelf collapse, which as we have seen earlier in Section 1.2.1, plays a major role in ice sheet dynamics. During the two decades prior to the collapse of Larsen B ice shelf, more than 3000 supraglacial lakes formed. The repeated drainage and filling of these lakes caused the ice shelf to flex, enabling the deepening of fractures, eventually leading to the disintegration of the ice shelf (Banwell et al., 2013).

Below the ice sheet surface, subglacial lakes located beneath ice streams and glaciers have been identified through radar echo sounding and altimetry surveys in both Antarctica (Smith, Fricker, Joughin and Tulaczyk, 2017) and Greenland (Bowling et al., 2019). The presence of 60 subglacial lakes has been detected in Greenland from radar sounding and ice-surface elevation changes, roughly distributed in three clusters in north-western, northern and central-eastern Greenland, concentrated towards the ice sheet margin. However, these lakes are less than 6 km in length and only two of these lakes are reportedly active (Bowling et al., 2019). On the other hand, Antarctica counts almost 400 subglacial lakes (Wright and Siegert, 2012) and 124 of these lakes have been found to be active based on a satellite altimetry survey (Smith, Fricker, Joughin and Tulaczyk, 2017). Water can be transported across the subglacial drainage system from one lake to another by floods (Fricker et al.,

2007). This movement of water induces a surface displacement causing elevation anomalies of the order of tens of meters. Satellite altimetry measurements from CryoSat-2 revealed the existence of a system of subglacial lakes beneath Thwaites glacier that drained between 2013 and 2014, inducing a subsidence of up to 20 m, caused by a transfer of 3.7 km^3 of water between subglacial lakes (Smith, Gourmelen, Huth and Joughin, 2017) (Figure 1.22). Subglacial water can be discharged at depth to the ocean, forming a buoyant plume rising up to the ice-ocean interface in case of a marine terminating glacier or a turbidity plume in case of a land terminating glacier (Figure 1.21). Subglacial discharge has been shown to enhance submarine melting at the front of marine terminating glaciers by dragging the warm ocean water close to the ice edge (e.g. Slater et al., 2017; Wood et al., 2021).
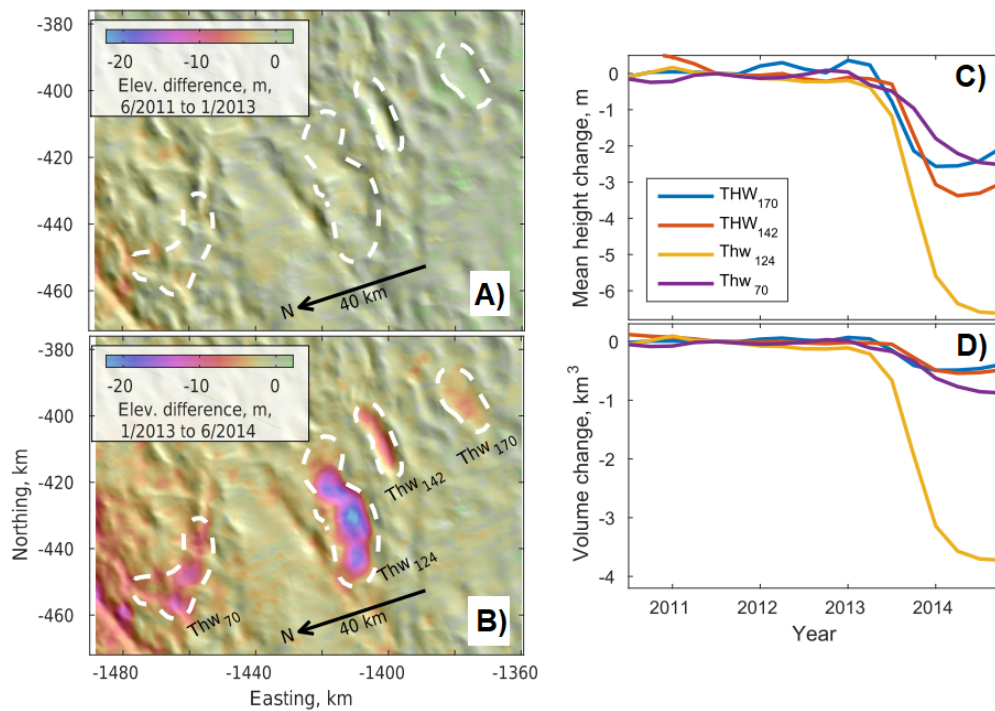
Figure 1.22: a) Elevation change derived from CryoSat-2 satellite altimetry between a) June 2011 and January 2013 and b) January 2013 and June 2014. c) Mean elevation change relative to 1st June 2011 of the four identified lakes outlined on b), d) Corresponding volume change. Adapted from Smith, Gourmelen, Huth and Joughin (2017).

1.2.5 Solid Earth Motion

The underlying bedrock motion induced by the solid Earth's movement results in a surface elevation displacement that is not associated with a mass change. The principal sources of Earth movement are in response to past and present ice mass variability; this motion is the result of the solid Earth's delayed viscoelastic response to past deglaciation – called Glacial Isostatic Adjustment (GIA) – and of the instantaneous elastic response to present-day ice mass changes. While subglacial volcanism, glacial erosion or changes in the mantle properties are also associated with a motion of the bedrock, these phenomena are less known and harder to quantify and we therefore focus here on the vertical motions induced by changes in past and contemporary ice loading. In Greenland, vertical displacement due to the instantaneous elastic response dominates the displacement induced by GIA and is of the order of a couple of millimetres per year compared to up to 10 mm yr^{-1} for the elastic response contribution (Bevis et al., 2012). In the Amundsen Sea Sector, a rapid uplift of 41 mm per year has been measured, linked to a lower viscosity of the mantle beneath this region compared to the global average, inducing a more rapid uplift than previously thought. This rapid uplift of the bedrock rebound potentially has a stabilising effect on ice sheet mass losses from this region (Barletta et al., 2018). To remove the GIA effect on satellite altimetry data, models of the Earth's structure combined with glacial history are used (e.g. Caron et al., 2018; Peltier, 2004) (Figure 1.23).
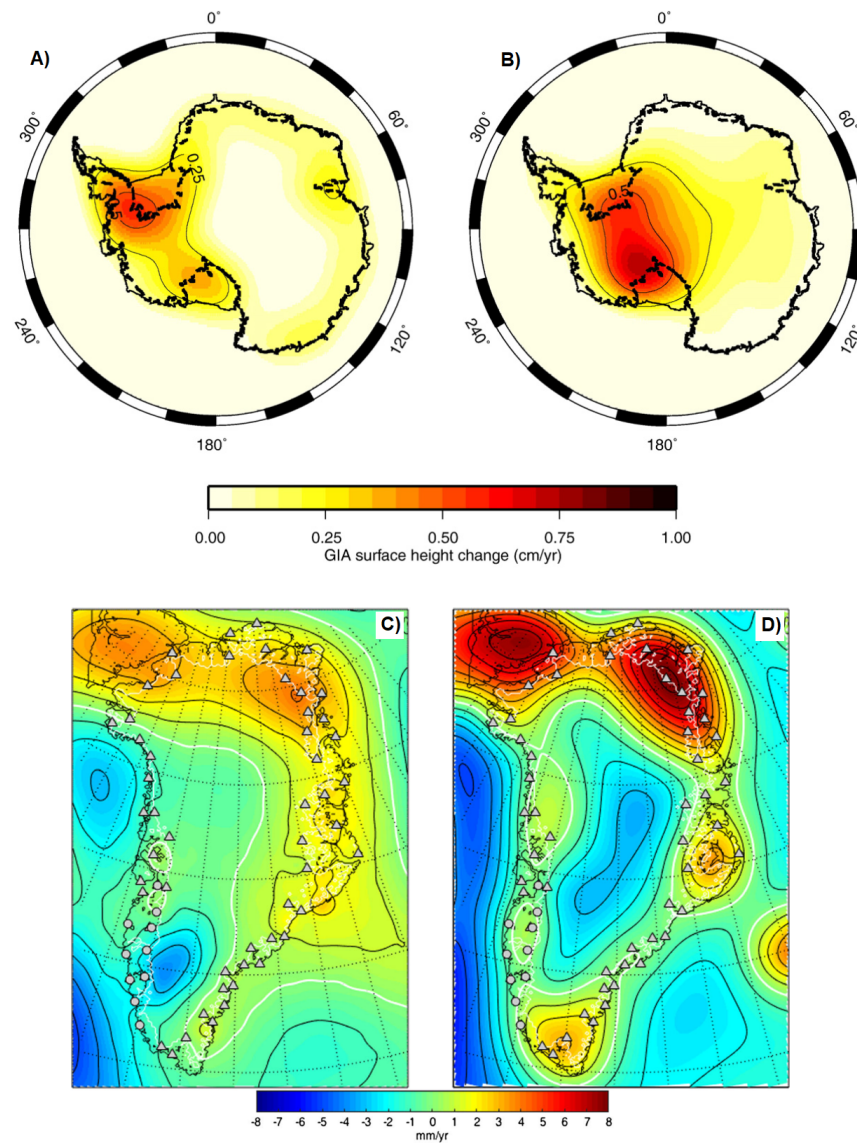
Figure 1.23: GIA surface elevation change rate of the Antarctic Ice Sheet from two ice histories a) IJ05, b) ICE-5G. Reproduced from Riva et al. (2009). GIA surface elevation change rate of the Greenland Ice Sheet from two ice histories c) ICE-6GC, d) Earth model VM5a. Reproduced from Wake et al. (2016).

1.3 Thesis Aim

The aim of this thesis is to improve our ability to detect and interpret changes in the surface elevation of Earth's polar ice sheets using satellite radar altimetry.

1.4 Thesis Objectives

To address the aim of this thesis, the following research objectives are set:

1. Assess the ability to determine ice sheet elevation change using Ka-band radar altimetry. This will be achieved using AltiKa, the first space borne altimeter operating at Ka-band, and contrasting the results to CryoSat-2 and airborne altimetry in West Antarctica.

2. Investigate the link between fluctuations in radar penetration and firn properties. This will be achieved using in-situ firn cores, airborne radar and modelled firn densification outputs in West Central Greenland.

3. Assess the ability of waveform retracking algorithms to mitigate the impact of radar penetration fluctuations on elevation measurements. This will be achieved through a comparison of airborne and satellite radar and laser altimetry in West Central Greenland.

4. Estimate ice sheet mass balance using satellite radar altimetry. This will be achieved using CryoSat-2 measurements in Northwest Greenland in conjunction with independent estimates from satellite gravimetry and the mass budget method.

1.5 Thesis Structure

In Chapter 2, I describe the altimetry principle, the methods I implemented as well as the satellite missions and airborne campaigns from which the analyses presented in this thesis were drawn. In Chapter 3, I present a study in West Antarctica using satellite Ka-band and Ku-band radar altimetry as well as airborne laser altimetry to investigate changes in

surface elevation in this sector of the Antarctic Ice Sheet. In Chapter 4, my attention turns to West Central Greenland where I investigate changes in radar penetration linked with changes in firn properties using airborne radar and laser data and in-situ data collected during the ESA CryoVEx campaigns with the aid of firn densification model outputs. In Chapter 5, I present surface elevation change from CryoSat-2 satellite radar altimetry and compare it to airborne laser altimetry from Operation IceBridge in the Northwest sector of the Greenland Ice Sheet. I estimate the mass imbalance of this sector and compare this result to independent estimates of mass balance from the gravimetry and mass budget techniques. Finally, in Chapter 6, I synthesise the findings of this thesis, place these results in a wider context and discuss potential avenues for future work.

Chapters 3, 4 and 5 have been written as stand-alone papers to facilitate the dissemination of their findings to the research community. Authors contribution statements are included at the start of this thesis. Chapters 3 and 4 have already been published in Geophysical Research Letters and their published format are included as appendixes at the end of this thesis (Appendices C and D).

CHAPTER 2

Tracking Changes in Ice Sheet Surface Elevation using Satellite Radar Altimetry

While the Results Chapters 3 to 5 that follow each have their own Methods section, this chapter provides a broader overview and context of the satellite radar altimetry principle as well as a description of the methods and algorithms I have developed in this thesis to track changes in the elevation of the ice sheets. In this chapter, I start by providing an overview of the altimetry principle before underlining the specific corrections that need to be applied to the altimetry signal over the ice sheets in order to derive surface elevation from the radar echoes. I then summarise the methods I have used to estimate surface elevation change from satellite radar altimetry data. I present the two satellite radar altimetry missions central to this thesis, CryoSat-2 and AltiKa, as well as underline the differences between satellite radar and laser altimetry. Finally, I introduce NASA's Operation IceBridge and ESA's CryoVEx campaigns, which provide airborne and in-situ data to calibrate and validate satellite altimetry data.

2. TRACKING CHANGES IN ICE SHEET SURFACE ELEVATION USING SATELLITE RADAR ALTIMETRY

2.1 Principles of Satellite Radar Altimetry

The first scientific demonstration of the application of satellite radar altimetry can be dated to the SeaSat mission for the observation of the oceans, which was launched in 1978 by NASA, building on the legacy from the previous Skylab and GEOS-3 missions. Despite a short lifetime of only three months, the SeaSat mission demonstrated that it was possible to observe the ocean surface topography from space, providing observations of geostrophic currents, ocean bathymetry and significant wave height (Evans et al., 2005), but also initiated the future developments of radar altimetry for glaciological studies (e.g. Thomas et al., 1983; Zwally et al., 1989). Following this, Geosat was launched in 1985, later followed by the launch of ERS-1 (1991), TOPEX/Poseidon (1992), ERS-2 (1995), Geosat Follow-on (GFO) (1998), Jason-1 (2001), Envisat (2002), Jason-2 (2008), CryoSat-2 (2010), AltiKa (2013), Jason-3 (2016), Sentinel-3 (2016) and Sentinel-6 (2020). The success achieved in satellite oceanography altimetry encouraged the application of radar altimetry to land ice surfaces, which is complicated by the pronounced topography of the ice sheets. ERS-1 was the first mission with the explicit aim of monitoring the polar ice sheets, surveying Greenland and Antarctica up to $81.5°$ latitudes – compared to the Jason or TOPEX/Poseidon satellites which cover only the southern part of the Greenland Ice Sheet –, thus providing the opportunity to map the surface elevation change of almost the whole Antarctic Ice Sheet for the first time (Wingham et al., 1998).

The surface elevation measurement E above a reference ellipsoid is the combination of the measurement of the satellite altitude A above the same reference ellipsoid and the measurement of the distance between the satellite and the sensed surface on the ground, called the range R (Figure 2.1):

$$E = A - R \tag{2.1}$$

In addition to these two quantities, several instrumental and geophysical corrections need to be applied to the range measurement. Instrumental corrections account for the variations in the centre of gravity of the satellite, internal noise of the instrument etc. These corrections are estimated based on periodic on-board calibration and are already applied

by the Space Agencies in the Level 1B data.[1]. On the other hand, geophysical corrections account for the processes affecting the radar signal propagation in the atmosphere and for the processes affecting the target point location such as oscillations due to tides. These geophysical corrections are delivered in the data product but need to be added to the range measurement by the user. The geophysical corrections that need to be applied over land ice surfaces as well as the other specific corrections to the ice sheets, including land ice retracking correction and corrections for the surface slope effect and radar penetration in the snowpack, are described in details in Section 2.2 of this chapter.
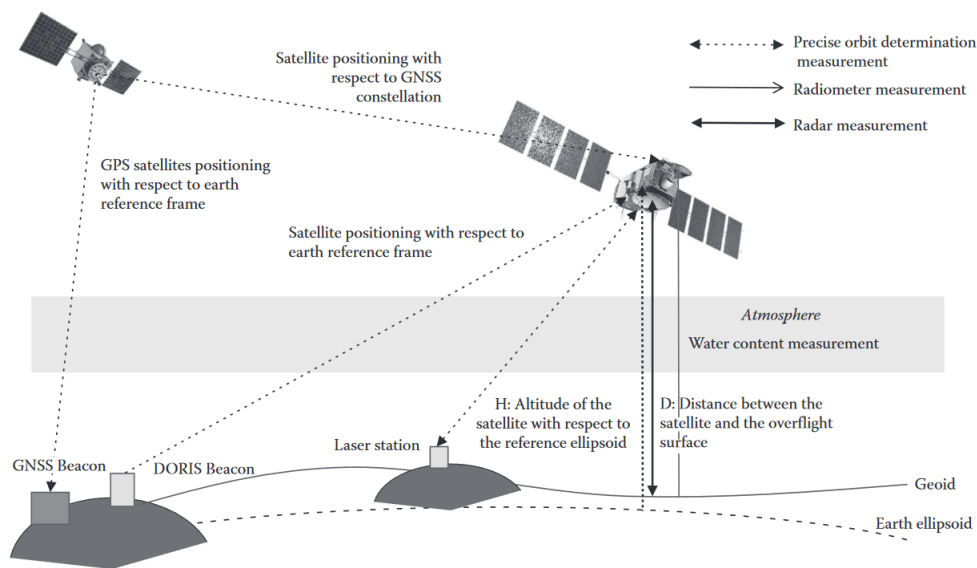
Figure 2.1: Illustration of the satellite radar altimetry principle. Reproduced from Escudier et al. (2018).

---

[1]Data are processed into different levels from raw instrument data to geophysical parameters Level 1B (L1B) data refer to data that have been processed to sensor units (e.g. radar waveforms), Level 2 (L2) data to data that have been processed into geophysical parameters (e.g. surface elevation) and Level 3 (L3) data to variables that have been mapped onto a grid (e.g. rates of elevation change).

2. TRACKING CHANGES IN ICE SHEET SURFACE ELEVATION USING SATELLITE RADAR ALTIMETRY

2.1.1 Altitude Determination

To measure the surface elevation of the terrain surveyed, the position of the satellite needs to be precisely determined. The precise orbit determination (POD) is usually achieved through a combination of a GPS (Global Positioning System), Doris (Doppler Orbitography and Radiopositioning Integrated by Satellite), or laser telemetry tracking systems on-board the satellite (Figure 2.1) combined with dynamical modelling. A GPS receiver system embarked on-board the satellite provides continuous tracking of the satellite's position, receiving signals from up to 12 satellites of the GNSS constellation. The Doris system is based on the Doppler shift measured between the signal transmitted by the ground beacons and the signal received on-board the satellite, from which the velocity and trajectory of the satellite is deduced. Finally, a laser retro-reflector instrument acts as a target for laser tracking by reflecting the laser pulse emitted from ground stations back. Contrary to the GPS and Doris systems which provide continuous tracking of the satellite's position, laser telemetry is limited by the number of laser ground stations and by the sensitivity of the laser signal to weather conditions and is therefore mainly used for the refinement and validations of the orbits determined using the GPS or Doris systems. Thanks to advances in POD, the real-time position of the satellite can now be achieved with an accuracy typically between 2 to 10 cm and after a period of 30-day, this is further refined and delivered with an accuracy of about 1 cm.

2.1.2 Range Determination

Radar altimeters transmit electromagnetic pulses at regular intervals defined by the pulse repetition frequency (PRF) travelling at the speed of light towards the Earth's surface in the nadir direction and records the travel time it takes to reach the Earth's surface and back (two-way travel time). The range measurement is the product of the speed of light c and the two-way travel time t_{twt} of the radar signal divided by two:

$$R = \frac{ct_{twt}}{2} \qquad (2.2)$$

To achieve a high resolution in the range measurement, radar altimeters use the deramp technique, first implemented on SeaSat. Radar altimeters send a chirp linearly modulated in frequency of length τ, centred around the frequency of the altimeter (Ku-band for CryoSat-2 and Ka-band for AltiKa), sweeping over a bandwidth B. When the chirp is generated, two copies of the chirp are taken. The first one is transmitted, while the second one – the deramping chirp – is delayed by the expected return time of the transmitted chirp and slightly shifted in frequency. The return signal from the surface consists of many discrete chirps, coming from the different scatterers present within the surface illuminated by the altimeter, each with a slightly different delay time. The deramping chirp is mixed with this backscattered signal and the frequency of this mixing product is proportional to the difference in frequency between the deramping chirp and the backscattered echo, from which the range is deduced. The range resolution ΔR can be written as:

$$\Delta R = \frac{c\tau}{2} = \frac{c}{2B} \tag{2.3}$$

The range resolution of CryoSat-2 is 47 cm in LRM mode and 23 cm in SARIn mode and the range resolution of AltiKa is 31 cm.

The echo received by the altimeter originates from the ground surface illuminated by the radar, which corresponds to the footprint of the antenna beam. The total area illuminated by the altimeter on the Earth's surface is called the beam-limited footprint and is dependent on the satellite altitude and the antenna beam width θ. The width of the beam-limited footprint can be written as:

$$F_b = 2Atan(\frac{\theta}{2}) \tag{2.4}$$

For CryoSat-2, the width of the beam-limited area varies between 13.2 and 14 km along-track and 14.9 and 15.8 km across-track. For AltiKa, the width of the beam-limited area is 8 km.

The pulse-limited footprint corresponds to the ground area illuminated around the point of closest approach (POCA) and is defined as the area illuminated by the leading edge of the pulse until the time when the trailing edge first intersects the surface (Figure

2.2). For a conventional pulse-limited altimeter, the pulse-limited footprint is dictated by the length of the pulse (or bandwidth) and is a circular area that can be approximated as:

$$F_p = \sqrt{Ac\tau} = \sqrt{\frac{Ac}{B}} \tag{2.5}$$

In CryoSat-2 LRM mode, the pulse-limited footprint corresponds to a circular area of diameter 1.65 km and AltiKa, which operates only in LRM mode, has a pulse-limited footprint of 1.4 km.

In SARIn mode, CryoSat-2 can be viewed as a beam-limited altimeter. The footprint of a beam-limited altimeter is dictated by the width of the beam. In SARIn mode, CryoSat-2 uses delay-doppler interferometry to sharpen the altimeter footprint in the along-track direction, which results in a smaller footprint of 1.65 km across-track and 0.305 km in the along-track direction. While all radar altimeters are pulse-limited altimeters, at the exception of CryoSat-2 which can be approximated as a beam-limited altimeter when it is operating in SAR or SARIn modes, laser altimeters such as the instruments on board ICESat and ICESat-2 are beam-limited altimeters and have a footprint smaller than 100 m. In SAR and SARIn mode, the pulse-Doppler limited footprint in the along-track direction is dependent on the altitude of the satellite, the pulse repetition frequency (PRF), the velocity of the platform and the wavelength used:

$$F_{p,x} = A\frac{\lambda}{2N\nu}PRF \tag{2.6}$$

The shape and magnitude of the echo (or waveform) recorded by the altimeter corresponds to all the reflections comprised within the footprint of the altimeter as a function of time. The power received by the altimeter corresponds to the surface illuminated on the ground, which varies during the impulsion and recording time. Shortly after the emission of the pulse, the only signal recorded by the altimeter is a low-magnitude signal corresponding to thermal noise from the instrument and from reflections from the atmosphere. Once the signal reaches the surface, the altimeter illuminates a circular area widening over time, reaching points away from nadir. This results in a gradual increase in power, corresponding to the leading edge part of the waveform. The power then starts decreasing
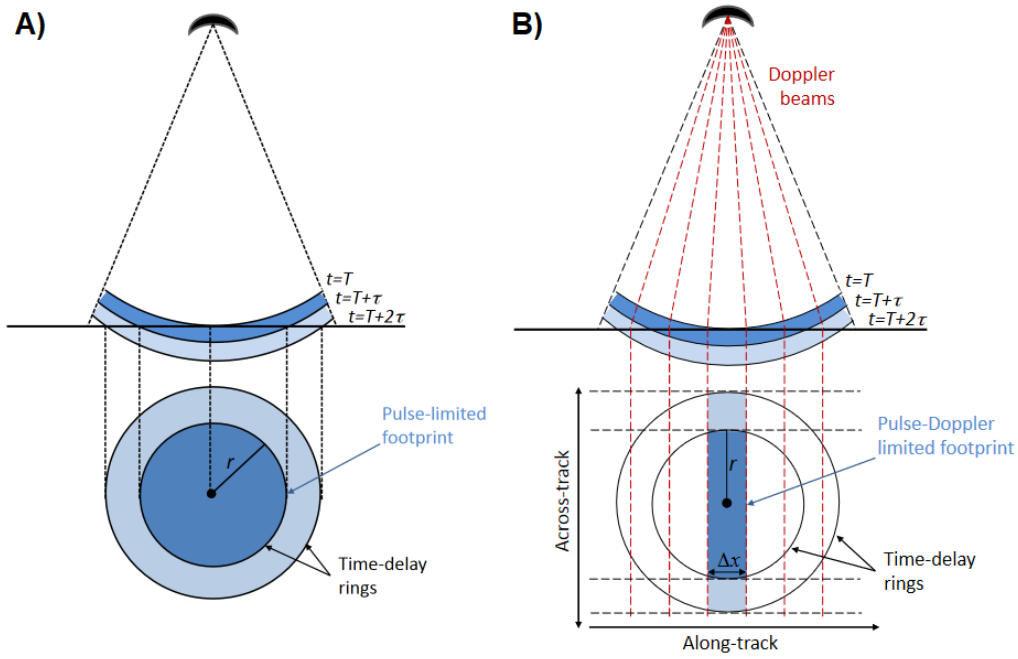
Figure 2.2: Illumination geometry and footprint plan view of the a) Pulse-limited footprint, b) Pulse-Doppler-limited footprint. Reproduced from Scagliola (2013).

progressively and the ground footprint corresponds to an annular ring of increasing radius but constant surface, corresponding to the trailing edge part of the waveform (Figure 2.3).

The ideal waveform corresponds to the Brown model, which is an idealised waveform for flat surfaces. In the Brown model, the averaged returned waveform P is the convolution of three components, the transmitted pulse $P_t(t)$, the average flat surface response $S(t)$ and the probability density function distribution of local scatterers in the radar footprint $I(t)$ (Brown, 1977):

$$P(t) = P_t(t) * S(t) * I(t) \tag{2.7}$$

However, this is further complicated by the roughness of land ice surfaces as well as by the penetration of the radar wave into the snowpack, which implies that the echo over ice surfaces is the sum of both surface and volume scattering. In the next section, I present the corrections dedicated to the altimetry signal over land ice surfaces.
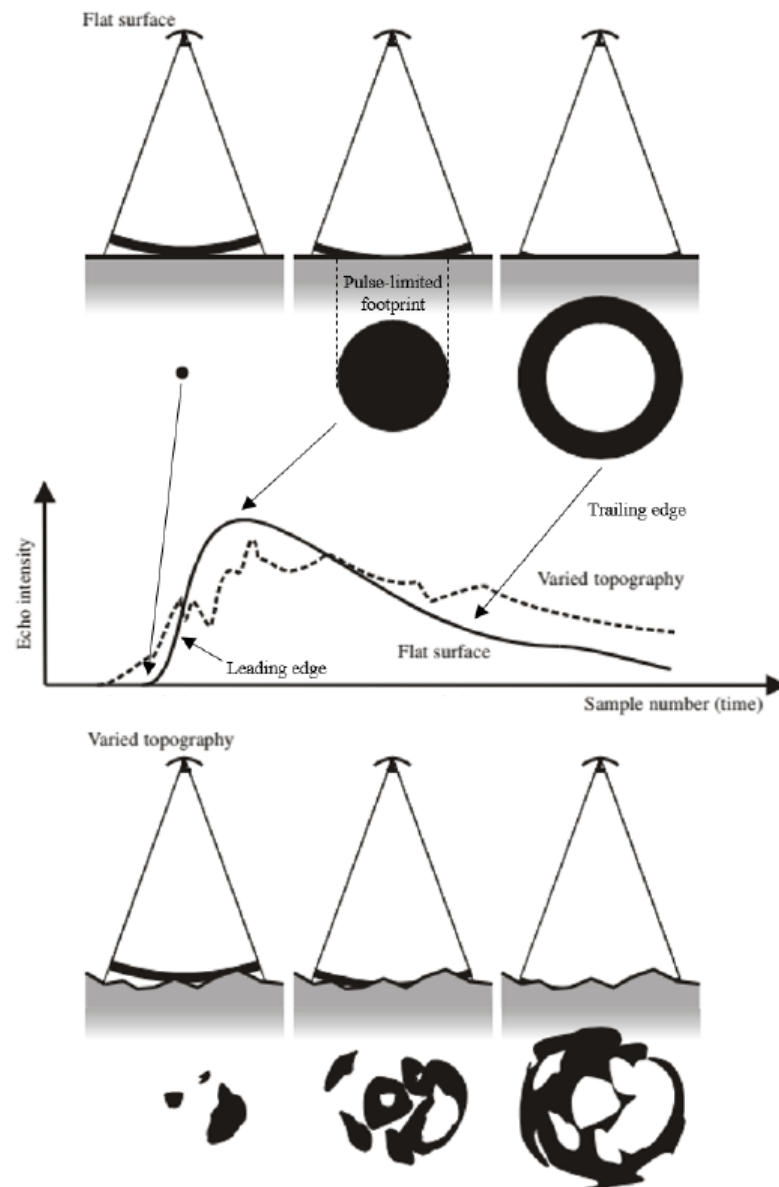
Figure 2.3: Area illuminated through time and corresponding waveform recorded over a flat surface (top) and a non-penetrating rough surface (bottom). Reproduced from Woodhouse (2006).

2.2 Corrections to the Altimetric Signal over the Ice Sheet Surface

In order to derive surface elevation from the radar waveforms, it is necessary to correct the radar signal for atmospheric and tidal effects, to develop specific retracking algorithms to account for the pronounced topography of the ice sheets as well as specific corrections for the surface slope induced error and for the penetration of the radar signal into the snowpack. In this section, I review the different processing steps involved in deriving surface elevation (Level 2) from radar waveforms (Level 1B). The processing chain I implemented in this thesis is illustrated on Figure 2.4 with the different steps being described in the following paragraphs.
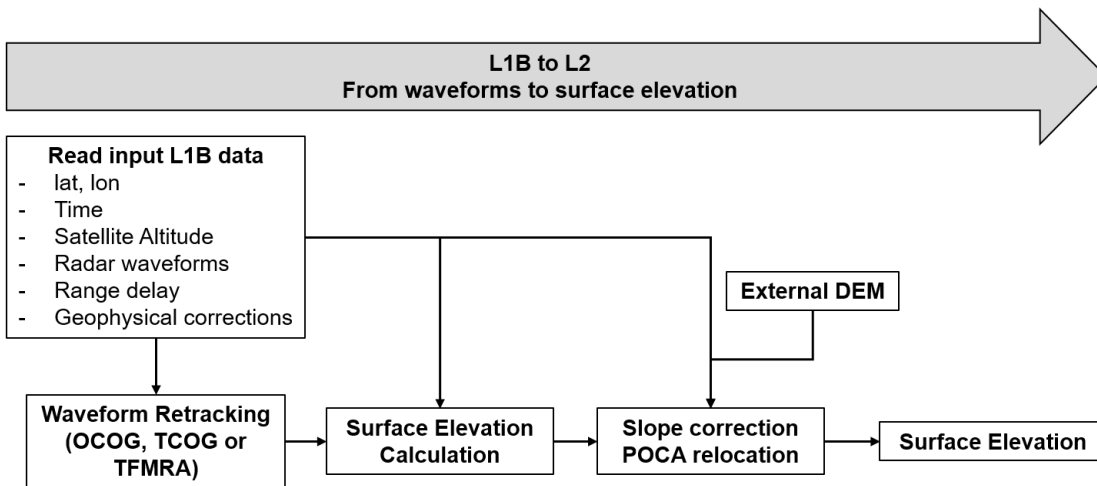
Figure 2.4: Processing scheme to derive surface elevation over the ice sheets from the radar waveforms

2.2.1 Geophysical Corrections

The propagation of the radar signal is slightly delayed when it travels through the ionosphere and troposphere and thus the range measurement must be adjusted for this delay. The ionospheric correction accounts for the presence of free electrons in the ionosphere; the dry tropospheric correction accounts for the presence of dry neutral gases – such as oxygen

and nitrogen – in the atmosphere; and the wet tropospheric correction for the presence of water vapour, which delay the propagation of the radar signal with respect to the speed of light. The magnitude of these corrections is usually estimated through modelling or by using data from a dual-frequency radiometer carried on the same platform as the altimeter in case of the wet tropospheric correction. It is important to note that the ionospheric effects are much lower on Ka-band than Ku-band with the ionospheric correction being inversely proportional to the square of the frequency (Steunou et al., 2015). In addition to these atmospheric corrections, the range measurement needs to be further corrected for tidal effects which induce a deformation of the Earth's crust. The ocean loading tide correction accounts for the deformation of the Earth's crust due to the weight of the ocean tides; the solid earth tide correction accounts for the deformation of the Earth's crust due to the combined gravitational pull of the Sun and Moon; and the geocentric polar tide originates from variations in the Earth's rotation axis. The magnitude of these tidal effects are estimated using dedicated models. The typical magnitude of these geophysical corrections are given in Table 2.1 below.

Table 2.1: Typical range of the different geophysical corrections applied over the grounded ice sheet. Adapted from Bouzinac (2012) and Bronner et al. (2016).

Geophysical correction	Magnitude	Source of the correction	
		CryoSat-2	**AltiKa**
Ionosphere	6 - 12 cm (Ku) 0.3 - 3.6 cm (Ka)	Global ionospheric map (GIM)	GIM
Wet troposphere	0 - 50 cm	ECMWF model	Radiometer or ECMWF model
Dry troposphere	170 - 250 cm	ECMWF model	
Ocean loading tide	± 2 cm	FES2004 model	FES2012 or GOT4.8 model
Solid Earth tide	± 30 cm	Cartwright model	
Geocentric polar tide	± 2 cm	Wahr (1985)	

2.2.2 Echo Retracking

The radar echo is recorded by the altimeter within a fixed number of tracking gates or range bins. The reflections from the surface are recorded within a pre-set range window, whose position is continuously adjusted on-board to account for the variations in the range in order to maintain track of the received echoes. The range window of CryoSat-2 consists of 128 range bins in LRM mode and 512 range bins in SARIn mode, which is equivalent to 60 m and 240 m in range, respectively. The range window of AltiKa counts 128 range bins, equivalent to 40 m in range. The on-board processor uses a fixed nominal tracking gate (63/255 for CryoSat-2 LRM/SARIn and 51 for AltiKa) to compute the range. However, in practice, the waveform is not exactly centred on the nominal tracking gate in the analysis window, but is slightly shifted. To remedy this and precisely locate the tracking gate corresponding to the point of closest approach, a ground processing technique called echo retracking is used. The retracking procedure provides a correction to the range measurement, calculated as the offset between the nominal tracking point and the leading edge of the waveform.

Several algorithms – both empirical and analytical retrackers – dedicated to ocean, sea ice and land ice surfaces have been developed. The CryoSat-2 product contains range estimates from three different retrackers for the LRM waveforms – Ocean Customer Furnished Item (Ocean CFI), University College London Land Ice (UCL) and Offset Centre Of Gravity (OCOG) – and for the SARIn waveforms, a dedicated retracker that fits the waveform to a modelled SAR waveform is provided (Wingham et al., 2006). On the other hand, in the AltiKa product, four different retracking algorithms – ICE-1, ICE-2, Sea Ice and Ocean – are used to generate range estimates (Figure 2.5).

There is a large variety of retracking algorithms available in the literature with different sensitivities to the waveform shape. The waveform shape is affected by the surface slope and roughness and in the case of continental ice, the shape of the waveform is a result of both surface and volume scattering as the radar pulse penetrates into the snowpack layers (Ridley and Partington, 1988). The Ocean retracker implemented on the ground-processing scheme of AltiKa consists of a MLE4 fit from second order to the Brown model
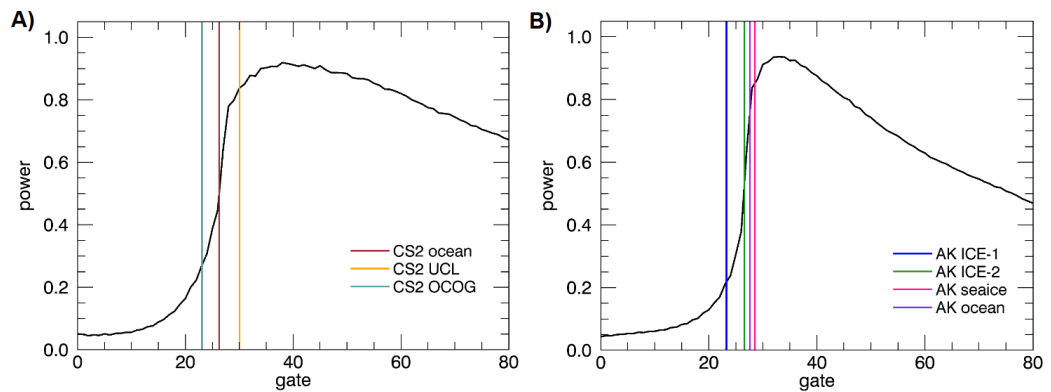
Figure 2.5: Example waveform recorded by a) CryoSat-2 (LRM) and b) AltiKa in West Antarctica. The leading edge position identified from the different retrackers available in the two satellite products are marked by the coloured lines. The waveforms have been averaged along-track and shifted by 27 gates.

(Amarouche et al., 2004; Brown, 1977). The ICE-2 retracker attempts to fit the measured waveform to a modified Brown model waveform adapted to continental ice (Légrésy et al., 2005). The ICE-2 algorithm assumes that for continental ice, the leading edge part of the waveform does not affect the trailing edge part of the waveform contrary to oceanic waveforms and therefore, the two parts of the waveform can be fitted separately. The ICE-1 retracker is an OCOG-based retracker, which determines the centre of gravity of the waveform based on its power distribution (Davis, 1997; Wingham et al., 1986). The Sea Ice retracker is a threshold retracker designed for peaky waveforms that are usually recorded over sea ice. A threshold is applied to the maximum amplitude of the waveform to determine the leading edge position (Laxon, 1994). The CryoSat-2 OCOG retracker is a threshold-based OCOG retracker, similar to ICE-1. Both the Ocean CFI and UCL Land Ice retracking algorithms are model fits to the Brown model. The retracking correction and the resulting height estimate is dependent on the algorithm chosen. In the example presented on Figure 2.5, all of the retrackers give a slightly different leading edge position with a maximum difference of 5 gates for AltiKa between the ICE-1 and Sea Ice retrackers and 7 gates for CryoSat-2 OCOG/UCL, corresponding to a difference of approximately
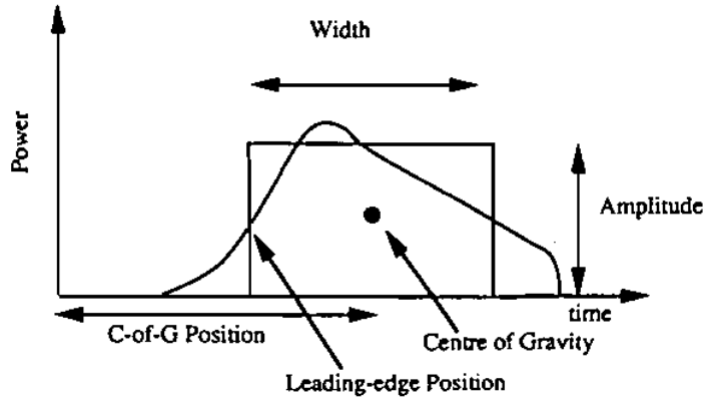
Figure 2.6: Illustration of the OCOG retracking algorithm. Reproduced from Bamber (1994).

1.6 m and 3.3 m between the resulting height estimates respectively.

While the retracked range estimates are available from the Level-2 satellite products, I have implemented three commonly used land ice retrackers in this thesis – the OCOG, TCOG (available in the AltiKa and CryoSat-2 products) and TFMRA algorithms – that I use to analyse airborne radar waveforms in Chapter 4. In the next paragraphs, I detail the implementation of these three retrackers.

The OCOG Retracker

The OCOG retracker is an empirical model, which determines the centre of gravity of the waveform COG and its amplitude A by fitting a rectangular box to the waveform (Wingham et al., 1986) (Figure 2.6). The leading edge position LEP is calculated from the centre of gravity and width W of this box.

For a waveform with N samples, P_i the power recorded in the ith bin, n_1 and n_2 the number of aliased bins at the start and end of the waveform, the amplitude A, width W and centre of gravity COG are given by:

$$A = \sqrt{\frac{\sum_{i=1+n_1}^{N-n_2} P_i^4(t)}{\sum_{i=1+n_1}^{N-n_2} P_i^2(t)}} \tag{2.8}$$

49

$$W = \frac{\sum_{i=1+n_1}^{N-n_2} P_i^2(t)}{\sum_{i=1+n_1}^{N-n_2} P_i^4(t)} \tag{2.9}$$

$$COG = \sqrt{\frac{\sum_{i=1+n_1}^{N-n_2} i P_i^2(t)}{\sum_{i=1+n_1}^{N-n_2} P_i^2(t)}} \tag{2.10}$$

Finally, the leading edge position is defined as:

$$LEP = COG - \frac{W}{2} \tag{2.11}$$

The OCOG retracker is a robust retracker and is the basis of the Threshold retracker (TCOG), which I describe in the next paragraph, and is also used as the initial guess in the Ocean CFI waveform fitting procedure. However, as all samples of the waveform are used to find the leading edge position, it is sensitive to both surface and volume scattering.

The TCOG Retracker

The Threshold retracker (TCOG) is based on the parameters estimated by the OCOG retracker but instead defines the leading edge position as the first range bin to exceed a certain threshold of the OCOG amplitude (Davis, 1997). The retracking position is then linearly interpolated between the bins adjacent to the threshold crossing to improve the precision of the retracking procedure. This offers the advantage of focusing the waveform procedure to the first part of the waveform, which minimises the contribution of volume scattering in the determination of the leading edge position. The ICE-1 retracker, implemented in AltiKa ground processing segment, and the retracker confusingly labelled as 'OCOG' in the CryoSat-2 ground processing segment both use this algorithm with a threshold set at 30 % of the OCOG amplitude.

TFMRA

The Threshold First Maximum Retracker (TFMRA) is another threshold retracking algorithm but instead of finding the centre of gravity of the waveform, it finds the first local maximum of the waveform exceeding a certain threshold level. The procedure is described in details in Helm et al. (2014) and is summarised briefly here. The algorithm proceeds

by oversampling and smoothing the waveform, before calculating the first derivatives of the power to find the first local maxima exceeding the set threshold. Finally, the leading edge position is defined as the first range bin exceeding the threshold level at the leading edge of the first local maxima and is linearly interpolated in the same manner as in the TCOG algorithm.

2.2.3 Surface Slope Correction

As we have seen, a radar altimeter illuminates an area of several kilometres on the ground. However, over the ice sheets, the terrain topography is far from homogeneous within the footprint of the altimeter and fluctuations in the surface elevation can reach up to tens of meters over a few kilometres. This has important consequences on the signal recorded by the altimeter as the point of closest approach is shifted upwards from the sub-satellite nadir point when the surface is inclined. The difference between the range to the sub-satellite nadir point and the range to the impact point is the slope-induced error. The magnitude of the slope-induced error Δh_{slope} can be approximated for small slope angles α as:

$$\Delta h_{slope} \approx \frac{A\alpha^2}{2} \tag{2.12}$$

This shows that the slope error is proportional to the square of the surface slope (Brenner et al., 1983) and can therefore be very large and it is in fact the largest source of error on the surface elevation measurement. The magnitude of the surface slope over the ice sheets ranges typically between 0.1° to 1.5°, which corresponds to a vertical error of 1 m to 275 m or a lateral shift of 1 to 21 km in the point of closest approach. To correct for the error induced by the surface slope, several geometrical corrections have been developed. The three main corrections are the direct method, intermediate method, and the relocation method (Figure 2.7). In the following paragraphs, I briefly describe each of these methods and in particular the relocation method, which I have implemented and further developed to correct AltiKa surface elevation change measurements in Chapter 3. Finally, it is important to remark that all of these slope correction methods require the use of an external Digital Elevation Model (DEM). DEMs – such as the RAMP DEM (Liu et al.,
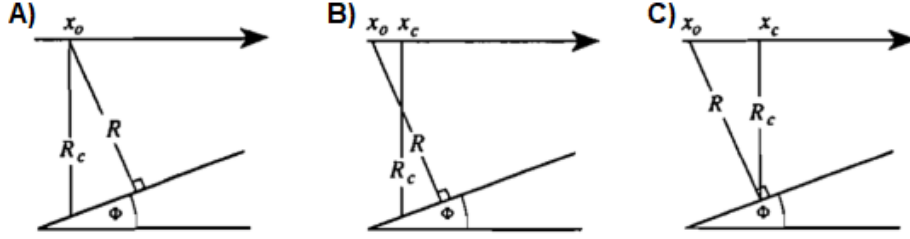
Figure 2.7: Illustration of the principles of the three slope corrections. a) Direct Method, b) Intermediate Method, c) Relocation Method. x_0 and R are the initial satellite position along-track and the measured range, and x_C and R_C are the corrected along-track position and range. Φ is the slope angle. Reproduced from Bamber (1994).

2015) for Antarctica or the GIMP DEM (Howat et al., 2015) for Greenland – are usually generated by combining multiple remote sensing datasets from satellite and airborne radar and laser altimetry, satellite optical and radar imagery and aerial photogrammetry to ensure a complete coverage of the ice sheets. In recent years, DEMs created exclusively from CryoSat-2 satellite altimetry data have also been generated by taking advantage of the interferometric mode of CryoSat-2 in the steep margins of the ice sheets, which improved the coverage over the ice sheets compared to previous satellite radar altimetry missions (e.g. Helm et al., 2014; Slater et al., 2018). The contemporaneity of the datasets used in the compilation of the DEM as well as the DEM spatial resolution both play an important role in the accuracy and precision of the slope correction, especially in the steep margins of the ice sheets (Levinsen et al., 2016).

The Direct Method of Slope Correction

In the Direct Method, the range measurement at nadir is corrected without being shifted laterally with the aid of an external DEM. An effective surface is fitted using a quadratic function to the a-priori DEM over the ground area that encloses the pulse-limited footprint of the altimeter (Brenner et al., 1983; Roemer et al., 2007):

$$z(x, y) = a_h + a_x x + a_y y + a_{xx} x^2 + a_{xy} xy + a_{yy} y^2 \tag{2.13}$$

Where x and y are the horizontal coordinates centred around the nadir sub-satellite point and a_h, a_x, a_y, $a_x x$, $a_y y$ are the coefficients of the fit. From the parameter estimation of the quadratic fit, the slope angle of the effective surface is calculated as:

$$\alpha = \sqrt{a_x^2 + a_y^2} \tag{2.14}$$

Finally, the corrected range R_c is computed from the measured range R based on the slope angle as:

$$R_c = \frac{R}{cos(\alpha)} \tag{2.15}$$

This approach can be further refined by considering the curvature C (Rémy et al., 1989) calculated as:

$$C = 2(a_x^2 a_{xx} + a_x a_y a_{xy} + a_y^2 a_{yy})\alpha^{-2} \tag{2.16}$$

In this case, the corrected range is calculated as:

$$R_c = \frac{R\alpha^2}{2(1 - R(C - \frac{1}{r_E + a_h}))} \tag{2.17}$$

where r_E is the Earth radius

In addition to its easy implementation, the Direct Method also facilitates the calculation of temporal elevation changes through crossovers or repeat-track methods compared to the other two slope correction methods as the original location of the measurements is retained. However, simply correcting the range measurement without relocating it to its true location can cause interpretation errors, as the geophysical parameters are not attributed to their actual locations (Hurkmans et al., 2012).

The Intermediate Method of Slope Correction

The Intermediate Method finds the point on the ground between the nadir point and the true impact point for which the range measurement is correct and relocates the measurement to that point. This method thus provides a correction on the location of the measurement rather than on the range measurement itself (Rémy et al., 1989). Similarly to the Direct Method, an effective surface is fitted within the pulse-limited footprint of

the altimeter (Eq. 2.13) and the slope angle of the plane is computed from the parameters estimated during the plane fitting stage (Eq. 2.14). Finally, the lateral displacement D from the satellite nadir point is calculated as:

$$D = R tan(\frac{\alpha}{2}) \tag{2.18}$$

The Intermediate Method results in lower errors than the Direct Method (Rémy et al., 1989). However, the relocation of the range measurement is not to the true impact point, but somewhere in-between the nadir point and the true impact point, and therefore the geophysical signals are attributed to an artificial location where the range measurement is correct.

The Relocation Method of Slope Correction

Contrary to the two previous slope corrections, the relocation method finds the true impact point – the point of closest approach – within the beam-limited footprint of the altimeter, correct and relocate the range measurement to this location. Rather than assuming a constant slope angle within an effective surface, the full topography within the altimeter footprint is taken into account. Here, I detail the implementation of the relocation procedure. First, the DEM segment centred around the sub-satellite nadir position (x_{sat},y_{sat},z_{sat}) that falls within the beam-limited footprint is extracted in order to identify the location of the point of closest approach. To improve the precision of the relocation procedure, the DEM segment is resampled at a finer resolution. The locations and elevation of the DEM pixels within the beam-limited footprint are denoted (x_{blf},y_{blf},z_{blf}). The corresponding DEM elevation of the nadir point $z_{blf,nadir}$ is extracted and the DEM elevation relative to the DEM elevation at nadir is written as:

$$dz_{dem} = z_{blf} - z_{blf,nadir} \tag{2.19}$$

The horizontal distance of each point in the beam-limited footprint from the nadir sub-satellite point is calculated as:

$$d_{nadir} = \sqrt{(x_{blf} - x_{sat})^2 + (y_{blf} - y_{sat})^2} \tag{2.20}$$

Next, the surface geometry parameters – the slope angle (Eq. 2.21) and the surface parallel distance (Eq. 2.22) – for each point in the beam-limited footprint can be written as:

$$\alpha = 90 - Atan(\frac{dz_{dem}}{d_{nadir}}) \tag{2.21}$$

$$d_{surf,parallel} = \sqrt{d_{nadir}^2 + dz_{DEM}^2} \tag{2.22}$$

Using the law of cosines, the range from the satellite to each point of the beam-limited footprint is given by:

$$R_{dem} = \sqrt{A_{dem}^2 + d_{surf,parallel}^2 - 2.A_{dem}.d_{surf,parallel}.cos(\alpha)} \tag{2.23}$$

where $A_{dem} = A - z_{blf,nadir}$ is the satellite altitude above the DEM

The point of closest approach is identified by calculating the corresponding range of each point within the beam-limited footprint to the satellite using Eq. 2.23 and selecting the point for which the Euclidean distance between the satellite and the DEM is the smallest:

$$R_{poca}(x_{poca}, y_{poca}, z_{poca}) = min(R_{dem}) \tag{2.24}$$

Finally, the coordinates of the identified point of closest approach are used to compute the offset Δz to add to the measured elevation measurement and the relocation distance D:

$$\Delta z = z_{poca} + R_{poca} - A \tag{2.25}$$

$$D = \sqrt{(x_{poca} - x_{sat})^2 + (y_{poca} - y_{sat})^2} \tag{2.26}$$

Compared to GNSS field measurements in East Antarctica, the Relocation method results in smaller errors compared to the Direct and Intermediate methods (Schröder et al., 2017). This is therefore the method that I implemented in Chapter 3 of this thesis to correct AltiKa surface elevation measurements for the slope-induced errors. However, AltiKa's beam-width footprint is smaller than previous altimeter (0.6°), which enables a more precise elevation measurement as the beam-limited footprint is smaller, however it also limits AltiKa's ability to survey terrain where the slope angle exceeds the antenna half beam-width. This is particularly limiting over the ice sheet margins where the slope is

usually high. Rather than excluding the measurements that are being relocated outside the beam-limited footprint – which could result in excluding important measurements over the rapidly thinning glaciers – I iterate the relocation procedure by increasing the search radius in step of 1 km, which is equivalent to increasing the beam-limited footprint in increments of 1 km. As the power received by the altimeter decreases outside the 3-dB antenna beam-width, the measurements relocated outside the beam-limited footprint are expected to be noisier. However, through a comparison to coincident airborne laser altimetry, I demonstrate in Chapter 3 that the benefit of retaining more measurements outweighs the small increase in noise level.

2.2.4   Penetration of Radar Signal

A further complication over the ice sheets is the penetration of the radar wave into the snowpack. The radar penetration depth is dependent on both the physical properties of the medium and the frequency of the sensor. At Ku-band, the radar signal is estimated to penetrate between 5 and 12 m below the ice sheet surface whereas at Ka-band, this is reduced to only 10 to 70 cm below the surface (Rémy et al., 2015). As a consequence, the radar waveform is the sum of a surface and volume echo (Ridley and Partington, 1988). The surface echo is modulated by the snow density and surface roughness while the volume echo is the result of ice grain size and internal layering in the snowpack (Rémy et al., 2014). The contributions of the surface and volume echoes both affect the radar waveform parameters (Figure 2.8). The slope of the leading edge is related to the surface roughness, with smooth surfaces having a steep leading edge and rough surfaces a shallower leading edge. This directly affects the retracking procedure as the precise location of the surface is determined from the identification of the first interaction of the surface from the leading edge part of the waveform as we have seen in Section 2.2.2. On the other hand, the trailing edge part of the waveform is related to the penetration depth. The slope of the trailing edge is linked to the scattering properties of the medium observed, with a rapid tailing off when scattering is limited to surface scattering and a slow tailing off when there is additional volume scattering due to the penetration of the radar signal into

the snowpack (Lacroix et al., 2008). The contributions of surface and volume scattering to the radar echo are spatially and temporally variable (Adodo et al., 2018). As the ratio between surface and volume scattering affects the shape of the echo, it impacts the retracking procedure, introducing a bias on the surface elevation measurements retrieved from the radar echoes.
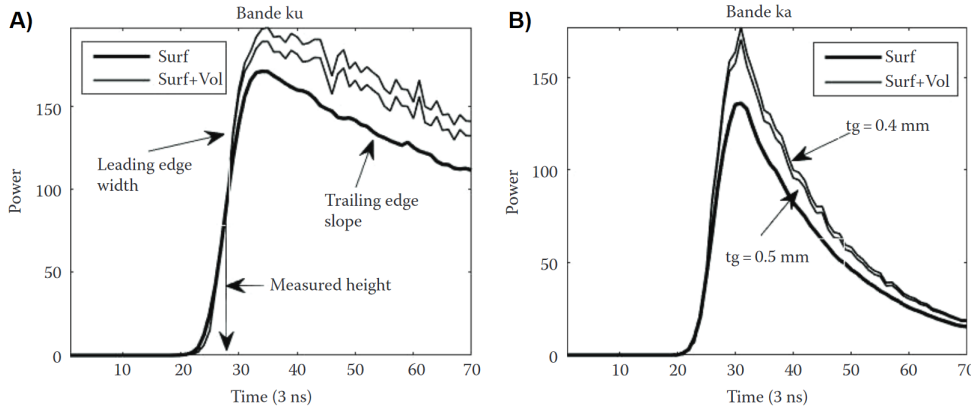
Figure 2.8: Simulated waveform at a) Ku-band and b) Ka-band showing the surface echo ('Surf') and the sum of a surface and volume echo ('Surf + Vol') with two snow grain sizes: tg = 0.4 and 0.5 mm. Reproduced from Rémy et al. (2017).

Inter-annual and seasonal changes in the snowpack properties thus entail fluctuations in radar elevation measurements. Time-series of radar elevation change over the Greenland Ice Sheet exhibit a pronounced seasonal cycle in surface elevation of the order of tens of centimeters following the annual cycle of surface melt, snow accumulation and compaction (Davis and Segura, 2001; Khvorostovsky, 2012). Seasonal fluctuations are also visible in time-series extracted over the Antarctic Ice Sheet, where the seasonal cycle in elevation change modelled from firn processes has been compared against temporal changes derived from Envisat, showing that a third of the seasonal variations in radar elevation can be explained by the seasonal cycle of firn processes with both signals having the same phase (Ligtenberg et al., 2012). Irregular and episodic changes in the snowpack properties can further bias surface elevation time-series retrieved from radar altimetry. This issue was illustrated during the Greenland melt event of 2012, following which a thickening of 56 ±

26 cm of the interior of the ice sheet over a period of only 5 months was observed from CryoSat-2 (Nilsson et al., 2015) (Figure 2.9). However, this step in elevation change was caused by the formation of a refrozen ice layer at the surface of the ice sheet following the melt event rather than being an actual elevation change caused by snowfall accumulation.
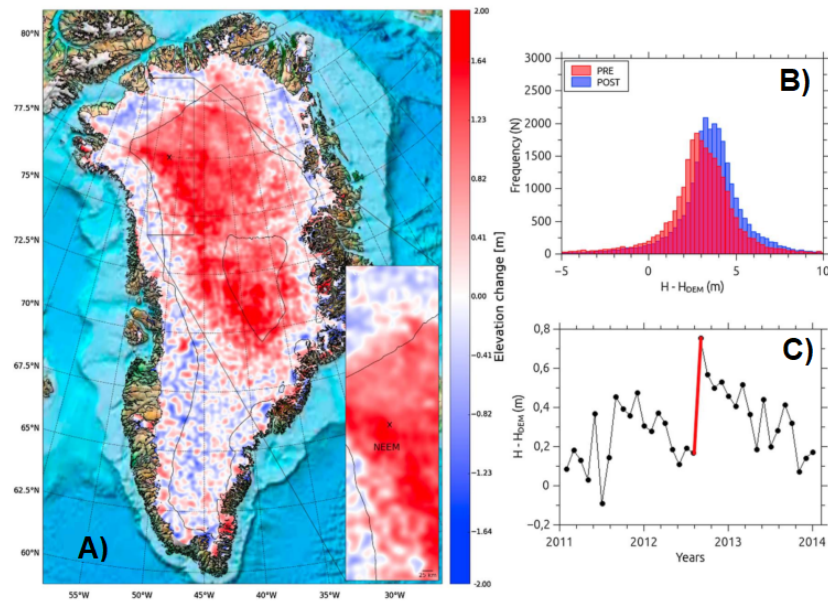
Figure 2.9: a) Surface elevation change difference between the periods May-June 2012 and August-September 2012 from CryoSat-2. b) Histogram of elevation difference to a DEM before and after the 2012 melt event around the local site NEEM shown in the inset on (a). c) Time-series of elevation change at local site NEEM. Reproduced from Nilsson et al. (2015).

The choice of the retracking algorithm can play an important role in mitigating the effect of radar penetration on radar surface elevation measurements and this is further explored in Chapter 4 of this thesis. For instance, different thresholds have been proposed to limit the calculation of the leading edge position to only the very first part of the radar waveform in order to minimize the contribution of volume scattering on the range determination (Davis, 1993). More recently, Slater et al. (2019) proposed another method to correct for changes in radar penetration depth by explicitly calculating the contribution

of surface and volume scattering to the radar waveform and the effective penetration depth using a waveform deconvolution model (Arthern et al., 2001). Other methods account for the effect of changing snowpack properties in the calculation of time-series of elevation change rather than correcting the surface elevation measurement itself, by examining correlations between temporal changes in waveform parameters and surface elevation changes. In this thesis, I adopt the latter method, which is described further in the following section.

2.3   Deriving Ice Sheet Thickness Change from Satellite Altimetry Data

By repeatedly surveying the surface of the ice sheets with satellite altimetry, it is possible to estimate temporal changes in surface elevation across the ice sheets. Radar altimeters measure the integrated change in surface elevation, which arises from a combination of different physical processes – changes in glacier dynamics, surface mass balance, firn layer thickness, ice sheet hydrology or solid Earth height (described in Chapter 1) – as well as from the remaining effect of radar penetration and fluctuations in the surface and snowpack properties. In this section, I describe the principal methods to derive surface elevation changes from repeated radar altimetry elevation measurements: the crossover, repeat-track and plane fit methods. The processing scheme I implemented in order to derive surface elevation change (Level L3) from surface elevation measurements (Level L2) is shown on Figure 2.10.
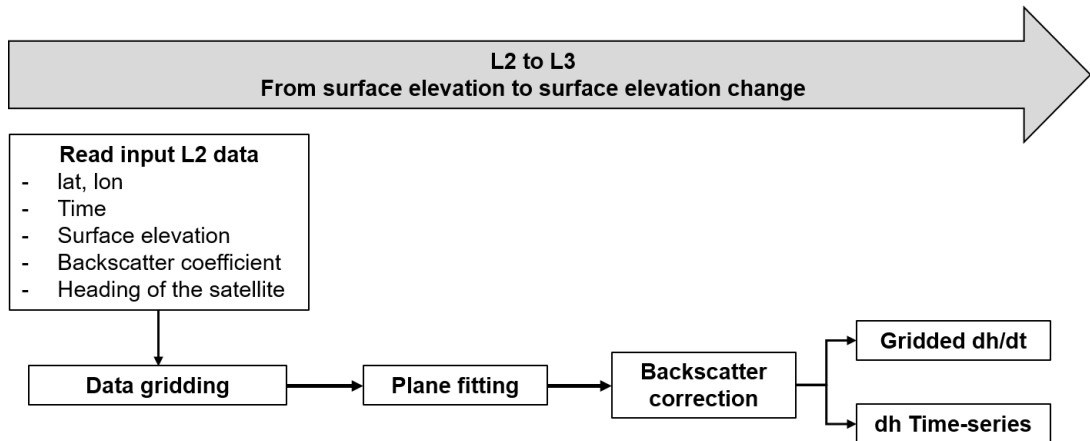
Figure 2.10: Processing scheme to derive surface elevation change over the ice sheets from repeated surface elevation measurements.

2.3.1   Ice Sheet Elevation Changes from Crossover Analysis

The very first method employed to derive surface elevation change of the ice sheet is based on the analysis of differences in elevation at crossover points, where ascending and descending orbits cross each other (e.g. Wingham et al., 1998; Zwally et al., 1989) (Figure 2.11). The elevation difference at crossover points is calculated by linearly interpolating the elevation measurements from the two nearest records on each satellite track. To construct a time-series of elevation change, a reference satellite repeat-cycle is crossed against all the other cycles. The elevation difference dH between orbit passes at t_1 and t_2 is calculated as:

$$dH = H(t_2) - H(t_1) + \epsilon \tag{2.27}$$

where ϵ is the associated error arising from orbital errors, noise in the measurement or penetration of the radar wave into the snowpack.
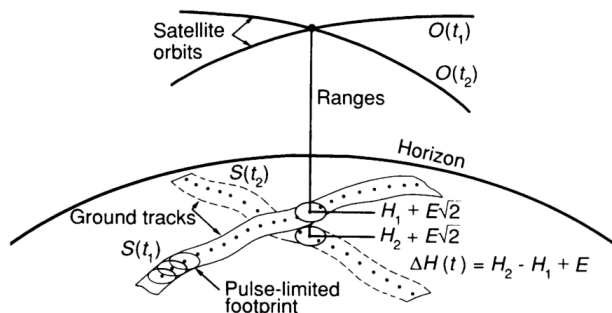
Figure 2.11: Illustration of the crossover technique. Reproduced from Zwally et al. (1989).

By differencing elevation measurements at crossover locations, where the spacecraft is in the same position, the slope error cancels out. This is the main advantage of the crossover technique as it yields a high accuracy in the derived surface elevation change. However, restricting the calculation of surface elevation changes to crossover points does not provide a complete a coverage of the ice sheets (Figure 2.12), and therefore limits the subsequent derivation of volume change or mass balance from crossover points.
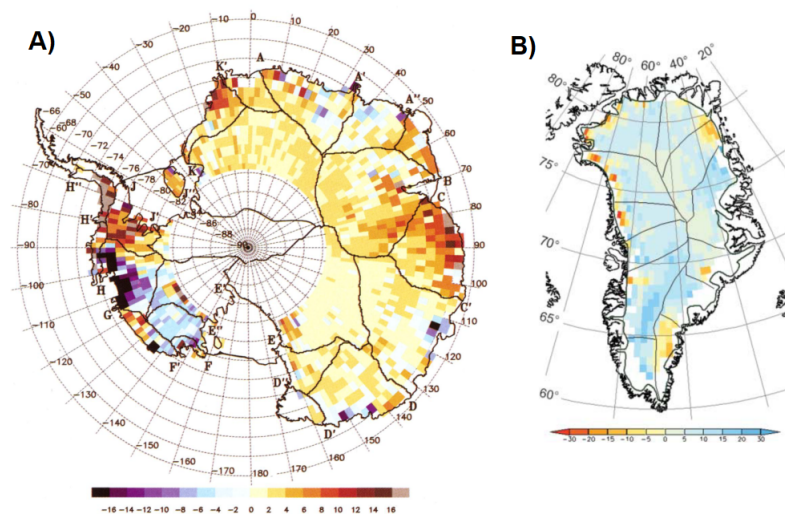
Figure 2.12: Surface elevation change (in cm yr^{-1}) derived using the crossover technique using ERS-1/2 data between 1992 and 2003 over the a) Antarctic and b) Greenland Ice Sheet. Reproduced from Davis et al. (2005) and Johannessen et al. (2005).

2.3.2   Ice Sheet Elevation Changes from Repeat-track and Plane-fit Methods

To make full use of all the surface elevation measurements along the satellite tracks, rather than only using the measurements at crossover locations, the repeat-track method was developed. In the repeat-track method, the satellite tracks within successive orbits are split into segments of kilometre-scale. The repeat-track method provides a large increase in data points, from 60 000 crossovers over the Antarctic Ice Sheet to more than 1.5 million measurements during the Envisat mission (Flament and Remy, 2012). This type of analysis is well suited for satellite missions with a repeat-orbit, such as ERS or Envisat, but another approach is required for CryoSat-2 drifting orbit, which has a repeat cycle of 369 days. The plane-fit method was developed to account for CryoSat-2 ground track spacing at high latitudes. The plane-fit method is a modification of the repeat-track method and is based on the grouping of data based on their spatial proximity with no distinction between tracks (McMillan et al., 2016) (Figure 2.13). As the plane-fit method is well suited to CryoSat-2 and AltiKa's drifting orbit, this is the method I employ in this thesis to calculate surface elevation changes.

In order to isolate the temporal fluctuations in elevation, a least-square model is fitted to the elevation measurements that fall within each segment along-track in the repeat-track method or within each grid cell in the plane-fit method. Different multi-parameters models have been proposed to model the fluctuations of elevation within each segment or grid cell. All these models include the mean of the heights recorded by the satellite z_m, a quadratic function of the coordinates of the measurements relative to the grid cell centre (x, y) and a linear function of the observation acquisition time t relative to the middle of the time-series. In addition, models also include a dependence on the heading of the satellite s to account for the anisotropic dependence of the surface elevation measurement due to the radar polarization and wind-induced small-scale topography of the firn (Armitage et al., 2014; Rémy et al., 2006).

$$z(x, y, t, s) = z_m + a_0 x + a_1 y + a_2 x^2 + a_3 y^2 + a_4 xy + a_5 s + a_6 t \qquad (2.28)$$

2.3 Deriving Ice Sheet Thickness Change from Satellite Altimetry Data

In order to account for changes in the waveform shape arising from the radar penetration in the snowpack, waveform parameters such as the leading edge width (LeW), backscatter coefficient (Bs) or trailing edge slope (TeS) can be further included in the model fit (Flament and Remy, 2012; Simonsen and Sorensen, 2017):

$$z(x, y, t, s, LeW, Bs, TeS) = z_m + a_0 x + a_1 y + a_2 x^2 + a_3 y^2 + a_4 xy + a_5 s + a_6 t + a_7 LeW + a_8 Bs + a_9 TeS$$

(2.29)

Alternatively, the derived surface elevation change measurements obtained from Eq. 2.28 can be corrected after the least-square fitting procedure by removing the surface elevation changes that are correlated with a change in backscatter (McMillan et al., 2016). In this case, the final corrected surface elevation change dh_c can be written in each grid cell as:

$$dh_c(t) = dh(t) - dBs(t) \frac{dh}{dBs}$$

(2.30)

Finally, in addition to generate time-series of elevation change within each grid cell, rates of elevation change are calculated using a linear regression in time.
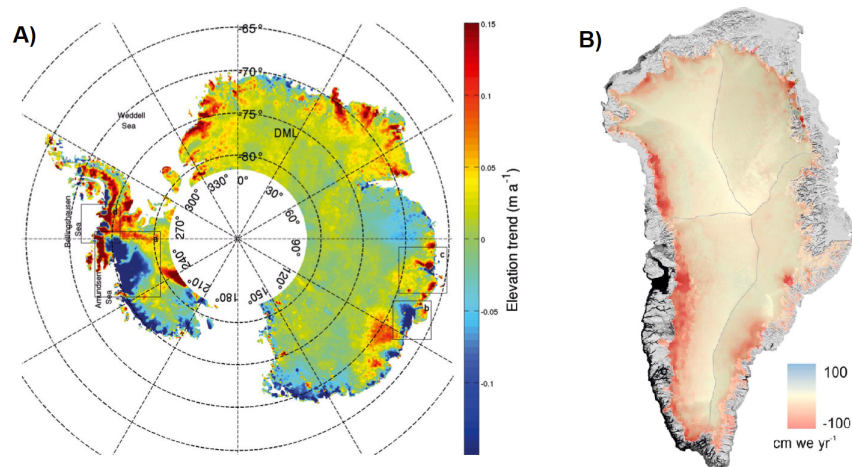
Figure 2.13: a) Surface elevation change derived using the repeat-track method over the Antarctic Ice Sheet from Envisat data between 2002 and 2010. Reproduced from Flament and Remy (2012). b) Surface elevation change derived using the plane-fit method over the Greenland Ice Sheet from CryoSat-2 data between 2011 and 2014. Reproduced from McMillan et al. (2016).

2.4 Satellite Altimetry Missions

This thesis focuses on exploiting data from the CryoSat-2 and AltiKa missions to improve elevation change retrievals from satellite radar altimetry. Here, I provide an overview of these two missions as well as an overview of the satellite laser altimetry missions ICESat and ICESat-2 in order to underline the main differences between radar and laser altimetry.

2.4.1 CryoSat-2

CryoSat-2 was launched in April 2010 and is the first satellite radar altimetry mission dedicated to the observations of the Polar Regions. To maximise the number of observations acquired over the Polar Regions, CryoSat-2 was placed on a non-synchronous orbit with an inclination of 92°, resulting in coverage up to 88° N/S and reducing the pole hole data gap from 2,831,000 km^2 to only 157,000 km^2 compared to ERS-1/2, Envisat or AltiKa. SIRAL, the altimeter carried on-board CryoSat-2, operates in three different modes that

are switched on depending on the type of surface surveyed (Wingham et al., 2006) (Figure 2.14). Over the ice-free ocean and smooth interior of the ice sheets, CryoSat-2 uses the Low-Resolution mode (LRM), operating in a similar manner as previous radar altimeters. Over sea ice, CryoSat-2 uses SAR processing to increase the along-track resolution. Finally, over the ice sheet margins, the ice caps and mountain glaciers, CryoSat-2 operates in SAR interferometric mode (SARIn) by employing a second receiving antenna in addition to SAR processing to improve both the along-track resolution and the location of the echo over steep terrains. The phase difference between the two receiving antennas is used to estimate the across-track surface slope angle in order to directly identify the point of closest approach and correct the range measurement for the slope-induced error, instead of applying a slope correction to the data with an external DEM. The principal characteristics of the LRM and SARIn modes, employed over the Greenland and Antarctic Ice Sheets, are summarised in Table 2.2.
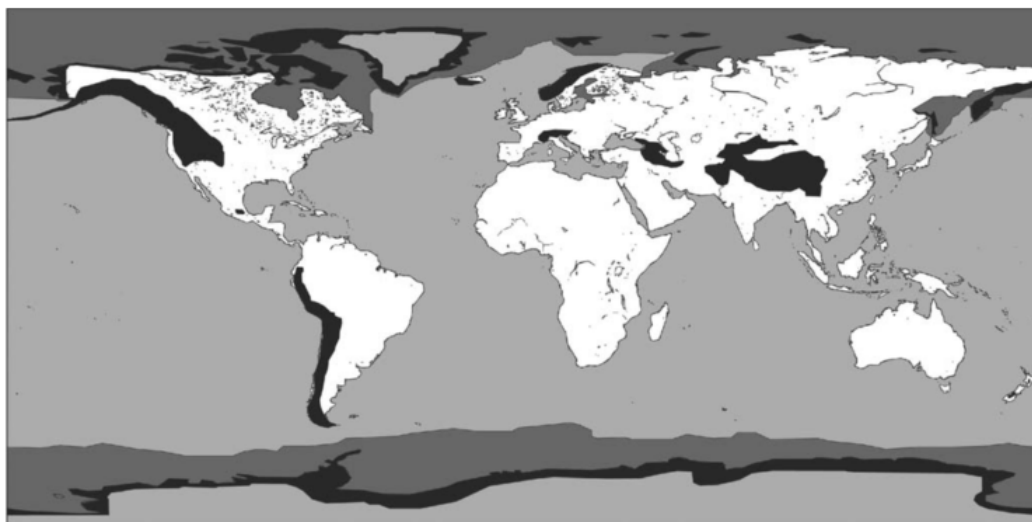
Figure 2.14: Mode acquisition mask of CryoSat-2. CryoSat-2 operates in LRM mode over the ocean and the interior of the ice sheets (light grey), in SAR mode over sea ice (grey) and in SARIn mode over the ice sheet margins and ice caps (black). Reproduced from Wingham et al. (2006).

2.4.2 AltiKa

SARAL was launched in February 2013 as part of a collaboration between CNES and ISRO, embarking the first space-borne altimeter operating at Ka-band, AltiKa. AltiKa was placed on the same sun-synchronous orbit as ERS-1/2 and Envisat and covers the poles up to latitudes of 81.5° N/S. However, from 4th July 2016, AltiKa was moved to a drifting orbit in order to reduce the stress on the satellite's reaction wheels and extend the lifetime of the satellite. Since then, the repetitive ground tracks are no longer maintained. The primary aim of AltiKa is to provide observations over the oceans, with a secondary focus on the monitoring of the Polar Regions. AltiKa is a conventional pulse-limited altimeter but delivers a better performance compared to previous pulse-limited altimeters with a higher PRF of 4 kHz for a better along-track sampling and a higher bandwidth of 480 MHz, resulting in a vertical accuracy of 31 cm and a reduced pulse-limited footprint of 1.4 km. The smaller 3 dB antenna beam width of AltiKa (0.6°) results in a smaller beam-limited footprint of 8 km (Verron et al., 2015). As we have seen in Section 2.2.4, the higher frequency of Ka-band compared to Ku-band offers new opportunities to better understand the interactions of the radar wave into the snowpack. The main instrument's characteristics of AltiKa are summarised in Table 2.2.

2.4.3 Satellite Laser Altimetry

While radar altimetry is the focus of this thesis, both radar and laser altimetry have been used to track changes in the ice sheets topography (e.g. Pritchard et al., 2009; Smith et al., 2020; Sørensen et al., 2018). In this section, I discuss differences between radar and laser altimetry, underlining the strengths and limitations of each technique.

Compared to satellite radar altimetry, which has been used for almost three decades to study the Greenland and Antarctic Ice Sheets, satellite laser altimetry is relatively new. The Ice, Cloud and Land Elevation Satellite (ICESat) was launched in January 2003 but stopped operating in October 2009 after the failure of its last laser instrument. The Geoscience Laser Altimeter System (GLAS) is the lidar system embarked on ICESat. The GLAS instrument consists of three lasers, which have been operated one at a time during

Table 2.2: Summary of the principal instrumental characteristics of CryoSat-2 and AltiKa.

	CryoSat-2		AltiKa
	LRM	**SARIn**	
Launch date	8th April 2010		25th February 2013
Altitude	730 km		800 km
Inclination	92°		98.55°
Latitude limits	88°		81.5°
Repeat cycle	369 days		35 days until July 2016
Centre frequency	13.575 (Ku-band)		35.75 GHz (Ka-band)
Bandwidth	320 MHz	40 MHz	480 MHz
PRF	1.97 kHz	17.8 kHz	4 kHz
Antenna 3 dB beam width	1.08° (along-track) x 1.20° (across-track)		0.6 °
Along-track sampling	250 m		175 m
Range resolution	47 cm	23 cm	31 cm
Waveform samples	128	512	128
Tracking window size	60 m	240 m	40 m

18 episodic campaigns ranging between 12 to 55 days in duration covering latitudes up to 86° N/S, after it appeared that the lasers were affected by manufacturing defects in the laser diode pump arrays (Abshire et al., 2005). More recently, ICESat follow-on, ICESat-2 embarking the Advanced Topographic Laser Altimeter System (ATLAS) was launched in September 2018. ATLAS is a photon-counting laser altimeter that generates six beams arranged in pairs, which enables the determination of the cross-track surface slope angle as well as a better ground coverage. ICESat-2 has a 91-day repeat orbit and samples the poles up to 88° latitudes (Markus et al., 2017).

The main difference between radar and laser altimetry is related to the nature of the measurement itself. While both measure the range, radars are sensitive to the contrast in

dielectric properties of the medium illuminated, while lasers are sensitive to the upper optical surface at the top of the snow surface. As the radar signal can penetrate below the ice sheet surface, it is sensitive to variations in both the surface and snowpack properties that can cause changes in the dielectric contrast of the snowpack unlike laser data. However, laser data are more sensitive to atmospheric conditions and cannot penetrate through the cloud cover, limiting the data acquisition in the presence of thick clouds or blowing snow (Palm et al., 2011). On the other hand, radar altimeters provide measurements in all weather conditions.

Other differences between radar and laser altimetry relate to the different footprints of the instruments. Satellite laser altimeters have a much smaller footprint of the order of tens of meters – ICESat and ICESat-2 have a footprint of only 65 m and 14.5 m, respectively – compared to satellite radar altimeters. The smaller footprint of laser altimeters results in a finer precision of the range measurement to the decimal level than that of radar altimeters. Another advantage to a smaller footprint is that the slope-induced errors are negligible on laser data (Brenner et al., 2007). However, laser data are more sensitive to mispointing errors and are also sensitive to high-energy returns over highly reflective surfaces, which can saturate the detection system resulting in errors of the order of tens of centimetres (Sun et al., 2017; Tilling et al., 2020).

2.5 Calibration and Validation of Satellite Altimetry Missions using Data from Airborne Altimetry Campaigns

To calibrate and validate data acquired from satellite radar and laser altimeters, several airborne campaigns over the Greenland and Antarctica Ice Sheets have been organised. These campaigns provide a very good dataset with which to compare satellite data against, as well as to test the feasibility of future satellite missions. In this section, I give an overview of NASA's Operation IceBridge and ESA's CryoVEx campaigns.

2.5.1   NASA's Operation IceBridge

To bridge the gap between ICESat and ICESat-2, NASA started the Operation IceBridge program, aiming at mapping the Polar Regions from aircraft platforms. Operation IceBridge operations started in 2009 and ended in November 2019, one year after the successful launch of ICESat-2. A dozen of different instruments including two laser altimeters (the Airborne Topographic Mapper (ATM) and the Land and Vegetation and Ice Sensor (LVIS)), several radar instruments (a snow radar, an accumulation radar, an ice-penetrating radar and a Ku-band altimeter) as well as several mapping instruments (a gravimeter, a magnetometer and optical and infrared cameras) were flown during these campaigns. The ATM instrument was flown during all annual IceBridge campaign over both Greenland and Antarctica, which allows the derivation of surface elevation change over the flight lines overflown or crossed between different annual campaigns. The ATM dataset can therefore be used to compare both surface elevation (Data Product ILATM1B) and surface elevation change measurements (Data Product IDHDT4) to estimates derived from satellite radar altimetry. In this thesis, I use data acquired with the ATM instrument to compare to satellite radar altimetry data from CryoSat-2 and AltiKa in Chapters 3 and 5.

2.5.2   ESA's CryoVEx campaigns

In preparation for the CryoSat mission, ESA started a series of airborne campaigns in 2004. In total, 9 airborne surveys were organised in 2004, 2006, 2008, 2011, 2012, 2014, 2016, 2017 and 2019 over the Greenland Ice Sheet as well as one survey over the Antarctic Ice Sheet in 2018. While these surveys are not as comprehensive as surveys from Operation IceBridge, they nonetheless provide some valuable datasets to understand the physical processes responsible for variations in radar altimetry returns. The aircraft flown during the CryoVEx campaigns carries both a laser and radar instrument, which allows the simultaneous acquisition of elevation measurements from radar and laser altimetry. The radar altimeter used is a Ku-band radar, called ASIRAS, designed to mimic the SIRAL altimeter on-board CryoSat-2. It operates at a central frequency of 13.5 GHz with a bandwidth of 1.0 GHz and range resolution of 0.109 m (Cullen, 2010). The laser instrument

is a laser scanner, which surveys the ice sheet in a 400 m wide swath at a raw resolution of 0.7 m x 0.7 m (at a nominal flying altitude of 300 m) with an accuracy of 0.1 m. In addition to these two instruments, a Ka-band radar, KAREN, was also flown in 2016 and 2017. KAREN has a bandwidth of 0.5 GHz and a range resolution of 0.165 m. Finally, these airborne campaigns have sometimes been organised in conjunction with a coincident in-situ campaign in the ice sheet, in order to collect data on the snowpack properties to help the interpretation of the airborne radar. In 2016, 2017 and 2019, a field campaign was organised on the ice sheet along the EGIG line in West Central Greenland. This location was surveyed during several campaigns and there are therefore extensive airborne and in-situ datasets over this region, which is analysed in Chapter 4 of this thesis.

CHAPTER 3

Ice Sheet Elevation Change in West Antarctica From Ka-band Satellite Radar Altimetry

3.1 Abstract

Satellite altimetry has been used to track changes in ice sheet elevation using a series of Ku-band radars in orbit since the late 1970's. Here, we produce an assessment of higher-frequency Ka-band satellite radar altimetry for the same purpose, using SARAL/AltiKa measurements recorded over West Antarctica. AltiKa elevations are 3.8 ± 0.5 and 2.5 ± 0.1 m higher than those determined from airborne laser altimetry and CryoSat-2, respectively, likely due to the instruments' coarser footprint in the sloping coastal margins. However,

AltiKa rates of elevation change computed between 2013 and 2019 are within 0.6 ± 2.4 and 0.1 ± 0.1 cm yr^{-1} of airborne laser and CryoSat-2, respectively, indicating that trends in radar penetration are negligible. The fast-flowing trunks of the Pine Island and Thwaites Glaciers thinned by 117 ± 10 and 100 ± 20 cm yr^{-1}, respectively, amounting to a 9 % reduction and a 43 % increase relative to the 2000's.

3.2   Introduction

Satellite radar and laser altimetry have been widely used to derive ice sheet surface elevation and elevation change in Antarctica (e.g. Bamber et al., 2009; Pritchard et al., 2009; Schröder et al., 2019; Shepherd et al., 2019; Slater et al., 2018; Wingham et al., 1998) and in Greenland (e.g. McMillan et al., 2016; Sørensen et al., 2018) to quantify their contributions to global sea level rise. Radar altimeters transmit pulses of electromagnetic radiation towards the Earth's surface and record the two-way travel time of the signal as well as the magnitude and the shape of the backscattered echo (waveform). The waveform shape is related to the average terrain and scattering properties of the Earth surface area illuminated by the altimeter footprint which, in turn, is determined by the sensor design (Brown, 1977). The leading-edge position of the waveform can be deduced with the aid of an echo retracking algorithm (Davis, 1997; Légrésy et al., 2005), and is typically used as a range adjustment to improve the precision of the surface elevation measurement. The AltiKa sensor has operated on the ISRO/CNES SARAL satellite since 2013, and is the first space-borne radar altimeter transmitting at Ka-band (37 GHz, 0.8 cm wavelength) frequencies. In this study, we look at the strengths and weaknesses of this new dataset for cryosphere studies. In theory, Ka-band radar has a reduced penetration depth within ice sheet surfaces when compared to the Ku-band sensors (13.5 GHz, 2.3 cm wavelength) due to the scattering losses dominating in Ka-band (with a scattering coefficient $\sim$57 times higher than in Ku-band) over absorption losses, and this has been supported by comparisons between the degree of radar backscattering recorded by AltiKa and Envisat over Antarctica (Adodo et al., 2018; Rémy et al., 2015). Reduced signal penetration may

potentially lead to better measurements of the ice sheets surface height. Previous studies have looked at the possibility of deriving elevation and elevation change in Antarctica (Suryawanshi et al., 2019) and Greenland (Yang et al., 2018) from AltiKa but their analyses were limited to only three years of data and did not include a comparison to Ku-band measurements. Here, we compute elevation and changes in the elevation of West Antarctica using 5 years of data acquired by AltiKa between March 2013 and March 2019. The main objectives of this study are to (i) assess the capability of AltiKa to measure elevation and elevation change in West Antarctica by comparing these estimates to contemporaneous airborne laser altimetry observations recorded by Operation IceBridge (OIB) and (ii) compare the Ka-band measurements to CryoSat-2 satellite Ku-band measurements to investigate whether the different frequencies of the two instruments lead to significant differences in elevation or elevation change.

3.3   Data and Methods

We use 51 million range measurements recorded by AltiKa between March 2013 and March 2019 to compute elevation change across the Amundsen Sea Sector of West Antarctica, a region that has exhibited widespread thinning (Flament and Remy, 2012; Shepherd et al., 2002) due to ice dynamical imbalance (Mouginot et al., 2014; Rignot et al., 2019). The range measurements were derived from 63 cycles of the AltiKa Sensor Geophysical Data Record (SGDR-T), and include corrections for dry tropospheric delay, wet tropospheric delay, ionosphere delay, solid earth tide, ocean loading tide and pole tide. The AltiKa data were acquired along the same 35-day repeat orbit as ERS-1/2 and Envisat until July 2016, date at which the satellite was moved to a drifting orbit because of technical issues on the reaction wheels (Verron et al., 2018). This change of orbit did not affect the data availability or quality. Although AltiKa is a pulse-limited radar altimeter of similar design to Envisat, its operating bandwidth of 500 MHz allows for a higher pulse-repetition frequency (4 kHz), which results in a closer along-track sampling, a narrower beam width (0.6°), and a smaller (8 km diameter) ground footprint (Steunou et al., 2015; Verron et al.,

2015).

To assess the performance of AltiKa, we compare the retrieved elevation and elevation change to satellite Ku-band altimetry data from CryoSat-2. CryoSat-2 is operating since 2010 and has been widely used to map the elevation and elevation change of the Greenland and Antarctic ice sheets (Helm et al., 2014; Nilsson et al., 2016). It offers improved spatial coverage and resolution relative to previous pulse-limited altimeter missions, thanks to its high (92°) orbital inclination, its long-repeat drifting orbit, and – in coastal regions – its Synthetic Aperture Radar Interferometric Radar Altimeter (SARIn) mode (Wingham et al., 2006). Over the interior of the ice sheets, CryoSat-2 operates as a traditional pulse-limited altimeter, known as Low-Resolution Mode (LRM).

Elevation measurements over the ice sheets need to be adjusted for the effects of the ice sheet surface slope, which typically ranges from 0.1° to 1.5° in Antarctica, introducing a 1.4 to 20.9 km lateral shift in the point of closest approach (Brenner et al., 1983; Levinsen et al., 2016; Rémy et al., 1989) or, equivalently, a 1.2 to 274.2 m error in the estimated elevation if the measurement was assumed to be originating from nadir. CryoSat-2 elevation measurements from Product L2I are corrected for this slope-induced error unlike AltiKa SGDR-T elevation measurements. To correct for this we apply a geometrical translation (Roemer et al., 2007) that relocates echoes to the point of closest approach, using the same digital elevation model (Liu et al., 1999) employed in the ESA CryoSat-2 Level-2 processing chain to ensure a like-for-like comparison with CryoSat-2. In total, 76.1 % of echoes fall within AltiKa's beam-limited footprint. However, the remainder are in areas of high slope that tend to be located near to the ice sheet margin, which is a region of geophysical interest. To include these, we iterate the slope correction by artificially increasing the ground footprint diameter in three 1 km intervals, and this procedure allows us to retain 20.5 % more echoes (96.6 % in total).

We applied waveform retracker corrections to the AltiKa and CryoSat-2 range measurements to improve their precision. The shape of pulse limited satellite radar altimeter waveforms is dependent on the instrument specifications, the surface topography, and on the degree of surface and volume scattering (Ridley and Partington, 1988). One aim of

retracking algorithms is to mitigate the effects of volume scattering, which occurs if the radar pulse penetrates below the physical surface – as is common over ice sheets (Michel et al., 2014; Nilsson et al., 2015). Retracking algorithms achieve this by identifying the location of the surface echo within the waveform, which is itself the sum of scattering from all elements illuminated by the transmitted pulse. A selection of retracker corrections are present within the AltiKa SGDR (ICE-1, ICE-2, Sea Ice and Ocean retrackers) and the CryoSat L2I (OCOG, Ocean CFI, UCL Land Ice retrackers) products and, for consistency, we pick similar ones for both missions. We choose Threshold Centre of Gravity (TCOG) based retracking algorithms (Wingham et al., 1986): the ICE-1 retracker for AltiKa and the OCOG retracker for CryoSat-2 LRM waveforms. Only one waveform retracker (the Wingham/Wallis model fit) is available for CryoSat-2 data acquired in SARIN mode, and so we use this correction for those data (Bouzinac, 2012).

We apply the same methodology to derive elevation and elevation change from AltiKa and CryoSat-2 (McMillan et al., 2016). The data are collated within 5 km by 5 km square grid cells, and a multi-parameter least-square model fit is applied to retrieve the mean elevation and the mean rate of elevation change within each cell. The model fit accounts for the fluctuations in the heights recorded by the satellite, due to the horizontal location, the heading of the satellite, and time. We apply an additional correction on elevation change based on the correlation of elevation and backscattered power to account for temporal variability of the snowpack properties which can induce a spurious elevation change associated with changes in surface and volume scattering (Davis and Ferguson, 2004; Simonsen and Sorensen, 2017). We estimate the uncertainty in elevation from the departure between the heights recorded by the satellite and in our model fit. Errors in gridded rates of elevation change are estimated as the 1-sigma uncertainty from the linear fit, and errors over larger regions are computed as the sum in quadrature of this and the standard deviation of the elevation change measurements at each epoch over the contributing grid cells. Finally, we exclude grid cells where the time span of measurements is less than 2.5 years, where the magnitude of the elevation change rate exceeds 10 m yr^{-1}, where the root-mean-square of the residuals exceeds 10 m, or where the proportion of

ascending and descending orbits is not evenly balanced.

To evaluate the accuracy of the AltiKa data, we use contemporaneous and coincident measurements of ice sheet elevation and elevation change acquired during NASA's Operation IceBridge (OIB) surveys. We use surface elevation measurements recorded by the NASA's Airborne Topographic Mapper (ATM) (Studinger, 2014, updated 2018*a*) (ILATM icessn) and elevation change rates derived from repeated ATM elevation measurements (Studinger, 2014, updated 2018*b*) (IDHDT).

3.4 Results

3.4.1 Comparison Between Ka-Band Satellite Altimetry and Airborne Laser Altimetry

We computed the average surface elevation (Figure 3.1a) and the average rate of surface elevation change (Figure 3.1d) across the Amundsen Sea Sector between 2013 to 2019 from the AltiKa measurements alone. The region is an area of known dynamical imbalance (Joughin et al., 2014; Mouginot et al., 2014; Rignot, 2008) where rapid ice thinning has occurred across the coastal margins in the vicinity of its fast-flowing outlet glaciers (Shepherd et al., 2002). Altogether, AltiKa is able to map 60.7 % of 5 km square grid cells within the study area (up to 81.5°), and most data gaps are small so that 95.7 % of the basin has an adjacent measurement at this resolution. However, in areas of high slope, AltiKa struggles to track the ice sheet surface because of the instrument's smaller beam-width and of the smaller range window explored ($\sim$40 m compared to $\sim$60 m in LRM and $\sim$120 m in SARIn for CryoSat-2). Furthermore, due to AltiKa's 35-day repeat cycle, the track spacing is wider compared to CryoSat-2 and only half (48.1 %) of grid cells falling on fast-flowing ice (v $\geq$ 250 m yr^{-1}) are surveyed. For comparison, the interferometric altimeter of CryoSat-2 is able to survey 92.7% of the same ice (McMillan et al., 2017).

First, we compare AltiKa elevation measurements to the OIB measurements to evaluate their accuracy (Figures 3.1b and 3.1c). To compare the elevation data, we interpolated the satellite data to the time and location of the airborne measurements using the coefficients
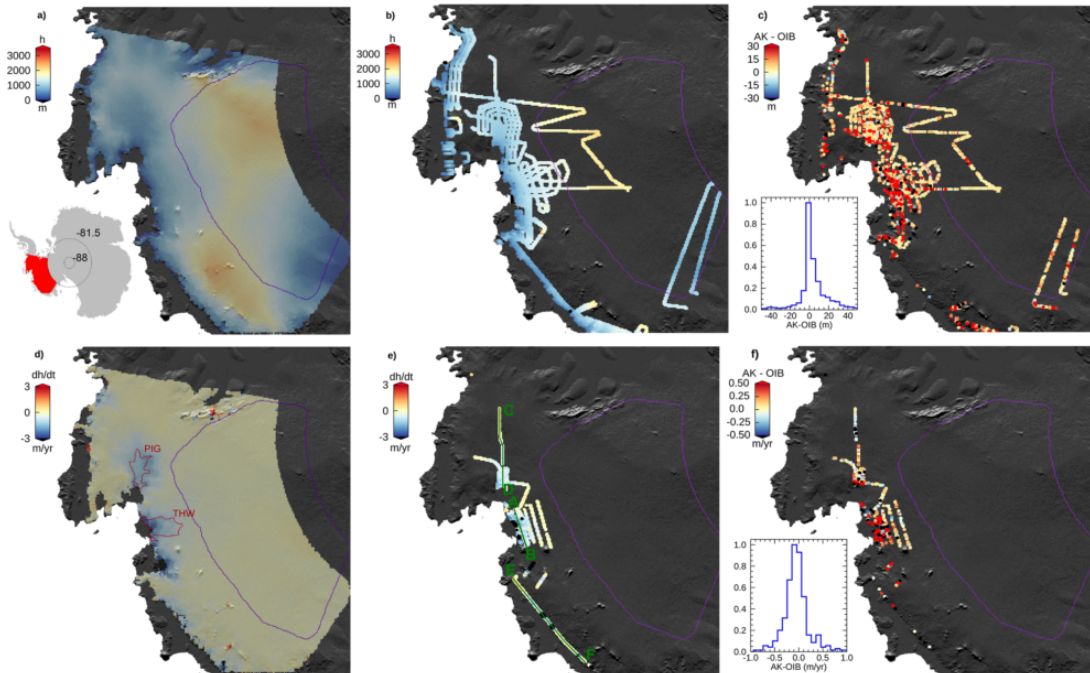
Figure 3.1: a) Average elevation of the Amundsen Sea Sector determined from AltiKa Ka-band satellite radar altimetry between March 2013 and March 2019, h, b) average elevation from Operation IceBridge airborne laser altimetry, c) elevation difference between AltiKa and airborne laser altimetry, d) average rate of elevation change from AltiKa, dh/dt, e) average rate of elevation change from Operation IceBridge, f) difference between rates of elevation change between AltiKa and airborne laser altimetry. The size of the OIB data has been increased for better visualization. A 25 km x 25 km median filter is applied to fill small gaps in the AltiKa data. The inset on (a) represents the location of the study area in Antarctica. Insets on (c) and (f) are histograms of the difference between AltiKa and OIB in the recorded elevation and rates of elevation change, respectively. Purple line shows the boundary between CryoSat-2 LRM and SARIn acquisition modes, green lines show OIB flight lines (A to B, C to D and E to F), and the red outlines mark the central trunks of the Pine Island (PIG) and Thwaites (THW) Glaciers defined by a 250 m/yr contour from ice velocity data (Rignot et al., 2011).

of the multi-parameter model fits, and we then computed the median difference within the 1,654 AltiKa data grid cells that contained at least five airborne measurements. We compare both the uncorrected and relocated AltiKa elevation measurements to OIB to assess the quality of our iterative slope correction. The uncorrected AltiKa measurements are positively biased with a median difference relative to OIB of 6.2 ± 0.5 m and associated standard deviation of 19.2 m. With our iterative relocation, the median difference is reduced to 3.8 ± 0.5 m with a standard deviation of 20.8 m. The OIB measurements are concentrated around the ice sheet margins (Figure 3.1b), with 55.9 % of the data collected over surfaces with a slope higher than AltiKa's half antenna aperture ($0.3°$) where the median and standard deviation of the difference to OIB are 5.5 ± 0.8 m and 23.4 compared to 2.3 ± 0.5 m and 12.2 m in low slope areas. This larger departure from the OIB dataset in areas of slope exceeding $0.3°$ illustrates the trade-off between the beam width footprint of a radar altimeter and the slope of the terrain surveyed. There are advantages to a smaller footprint (e.g. a shaper waveform), however when the surface slope exceeds half the antenna aperture, the point of closest approach is shifted outside the beam footprint where the power is significantly lower. This does not apply to laser altimeters such as ICESat-1/2, which have footprints of the order of tens of meters over which the surface slope variations can be neglected. This could explain the positive bias and relatively high dispersion as 50.6 % of the echoes used in the comparison to OIB are scattered from beyond the instrument's $0.3°$ beam-limited footprint – 23.9 % of the total number of echoes across the study area – introducing an increased standard deviation in the difference to OIB of 17.8 m compared to 16.6 m when considering only the points within the $0.3°$ beam limited footprint. We also examine this elevation bias in terms of surface slope and roughness (Figure 3.2). The differences between AltiKa and OIB exceeding 10 m are recorded in areas of slope higher than $0.4°$ and of surface roughness higher than 7 m. The presence of crevasses from which the returned echo is more complex could also potentially bias the elevation measurements recorded (Lacroix et al., 2007; Partington et al., 1987).

We also compared rates of surface elevation change computed from AltiKa data to those determined from the OIB measurements over 327 grid cells common to both datasets and
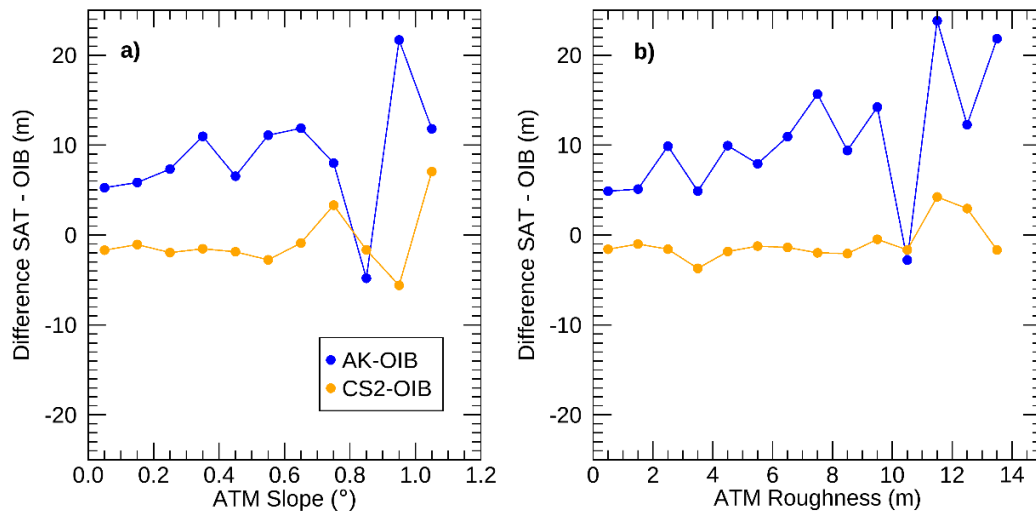
Figure 3.2: Difference between satellite rates of elevation change and airborne laser altimetry rates of elevation change as a function of a) surface slope and b) surface roughness.

falling within the CryoSat-2 SARIn mask (Figures 3.1e and 3.1f). Without a backscatter correction applied, the median difference between AltiKa and OIB rates of elevation change is -5.5 $\pm$ 2.5 cm yr^{-1} with an associated standard deviation of 43.0 cm yr^{-1}. Across this subset of grid cells, the backscatter correction applied to AltiKa elevation change is 4.8 cm yr^{-1} on average with a standard deviation of 30.7 cm yr^{-1} and across the study area as a whole, the magnitude of this correction is 1.0 cm yr^{-1} with a standard deviation of 16.5 cm yr^{-1}. Applying this correction leads to a better agreement with the laser altimetry rates of elevation change with a median difference of -0.6 $\pm$ 2.4 cm yr^{-1} and standard deviation of 42.7 cm yr^{-1}. This analysis shows that there is far better agreement between the OIB and AltiKa measurements of elevation change in comparison to elevation.

3.4.2 Comparison Between Ka Band and Ku Band Satellite Altimetry

As a second test, we compared the AltiKa estimates of ice sheet surface elevation to independent estimates derived from CryoSat-2, to investigate potential differences in the degree of signal penetration recorded by each sensor. At the 3,580 common grid cells that

contained at least five airborne measurements, the median difference between CryoSat-2 and OIB measurements of elevation is -0.7 $\pm$ 0.2 m, consistent with previous studies (Slater et al., 2018). By comparison, the median difference between AltiKa and CryoSat-2 (computed as AltiKa - CryoSat-2) elevation data at 27,192 coincident grid cells is 2.5 $\pm$ 0.1 m, which confirms that AltiKa elevations are on average positively biased. Because the AltiKa bias is present in comparisons to both OIB and CryoSat-2, and because there is little evidence of bias between OIB and CryoSat-2, we do not believe it is associated with differences in the degree of radar penetration. Rather, the largest differences are in areas of high slope and roughness, suggesting this bias is related to the different instrument characteristics and in particular to the different footprint sizes and acquisition modes.

Next, we compared AltiKa and CryoSat-2 estimates of ice sheet surface elevation change to examine whether the positive bias in AltiKa elevation measurements is also present in the rates of elevation change recorded by AltiKa. This comparison also extends the area over which the AltiKa data can be evaluated with respect to independent observations, as the OIB data are limited to a small ($\leq 2\%$) portion of the mainly coastal Amundsen Sea Sector. Across the region as a whole, the rate of elevation change recorded by AltiKa and CryoSat-2 averages 5.3 $\pm$ 1.0 cm yr^{-1} and 8.2 $\pm$1.2 cm yr^{-1} lowering between 2013 and 2019, respectively. Within the coastal margins (the SARIn mask of CryoSat-2, see Figure 3.1d), the average rate of surface lowering recorded by AltiKa and CryoSat-2 is 14.4 $\pm$ 1.6 cm yr^{-1} and 18.1 $\pm$ 2.0 cm yr^{-1} whereas in the interior (the LRM mask of CryoSat-2), the surface elevation increased at an average rate of 0.6 $\pm$ 0.6 cm yr^{-1} and 1.3 $\pm$ 1.0 cm yr^{-1}, respectively. At 27,192 common locations, the median difference between AltiKa and CryoSat-2 measurements of surface elevation change is -0.1 $\pm$ 0.1 cm/yr with an associated standard deviation of 11.5 cm yr^{-1}. This difference is small, and comparable to or smaller than the differences between each instrument and the OIB data themselves (-0.6 $\pm$ 2.4 cm yr^{-1} between AltiKa and OIB and -8.1 $\pm$ 1.5 cm yr^{-1} between Cryosat-2 and OIB, at 327 common grid cells). We also compute the robust dispersion estimate (RDE) of the difference between AltiKa and CryoSat-2 as defined by Smith, Gourmelen, Huth and Joughin (2017). The RDE is 3.5 cm yr^{-1} and shows that although local differences

exceeding 20 cm yr^{-1} do occur (e.g. Figure 3.4), the small regional differences suggest that there is no significant bias in either AltiKa and CryoSat-2 estimate of elevation change in this particular sector of Antarctica where the changes are dominated by changes in ice dynamics. Other factors that may be responsible for local differences between AltiKa and CryoSat-2 include differences in the low-level satellite data processing chains and differences in the satellite radar acquisition modes, and without equal treatment of these factors it is not possible to further isolate the potential effects of radar signal penetration.

We also compared AltiKa and Cryosat-2 rates of elevation change to Operation IceBridge along continuous sorties flown by the aircraft, to examine changes over diverse terrain in more detail: one along Thwaites Glacier, one along the centreline of Pine Island Glacier and another following approximately the ice sheet grounding line inland of the Getz Ice Shelf (Fig. 3.1e). Along the Thwaites sortie, AltiKa records fewer measurements than Cryosat-2 but both sensors have comparable performances with RMS differences of 0.58 m yr^{-1} and 0.54 m yr^{-1}, respectively (Figure 3.3a). AltiKa and CryoSat-2 perform similarly well along the Pine Island Glacier sortie, yielding RMS differences of 0.22 m yr^{-1} and 0.21 m yr^{-1} relative to OIB, respectively (Figure 3.3b). Along the Getz Ice Shelf sortie, however, AltiKa performs poorly due to the presence of steep and rough terrain, and acquires 9 times fewer measurements (Figure 3.3c). Although there is rapid thinning at several outlet glaciers, AltiKa fails to detect this, and records a RMS difference of 2.85 m yr^{-1} relative to OIB. This highlights the limits of AltiKa, which struggles to track surfaces in areas of complex terrain with rapidly changing slopes because of its smaller beam footprint and tracking window size, which are not very suited for high slope areas such as the ice sheet margins. Thus, deriving total volume change from AltiKa might be challenging, as most of the ice losses are occurring in the areas least well sampled by AltiKa. By comparison, the SARIn mode of CryoSat-2 performs extremely well despite the challenging terrain, tracking local thinning at a series of outlet glaciers along the sortie, with an RMS difference of 0.43 m yr^{-1} relative to OIB.
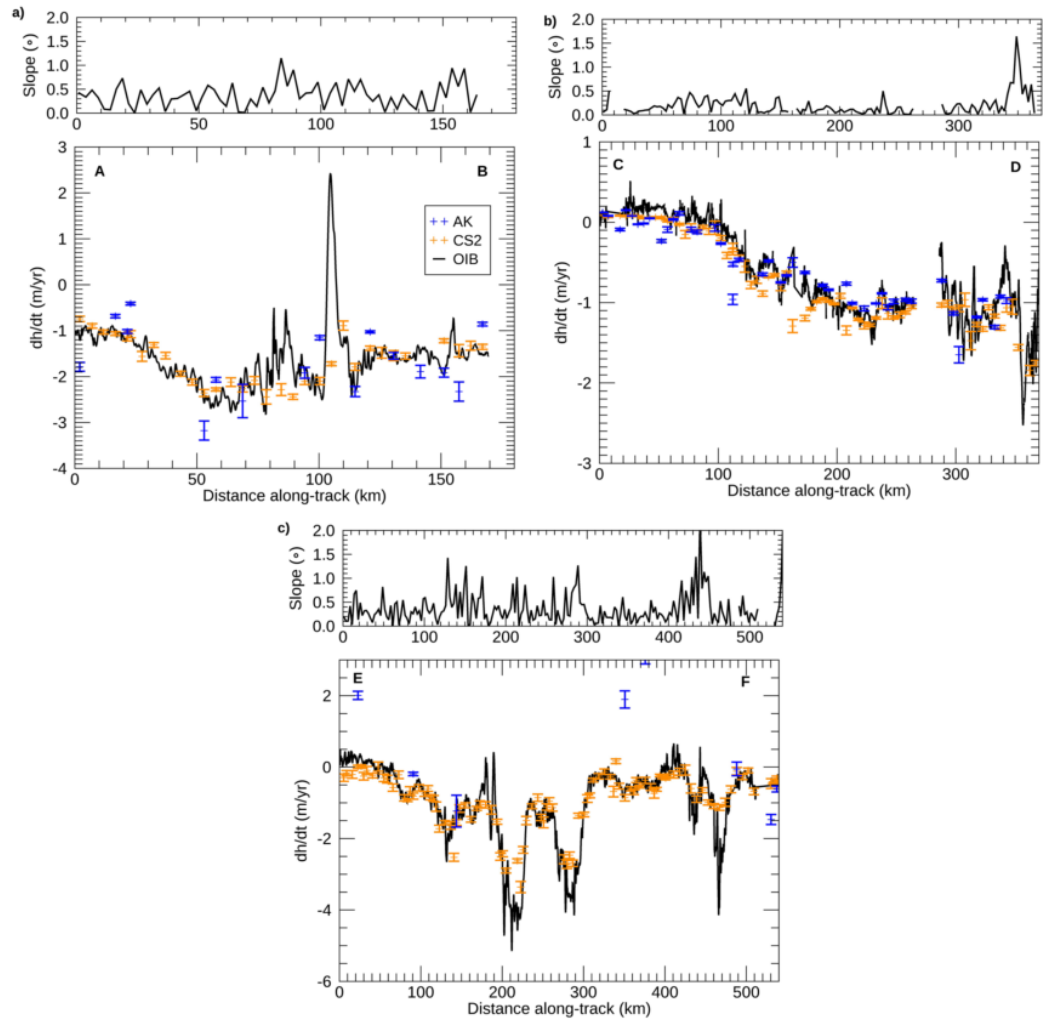
Figure 3.3: Rates of elevation change profiles from Operation IceBridge ATM, AltiKa and CryoSat-2 and ATM surface slope profiles a) along airborne sorties of Thwaites Glacier from A to B, b) Pine Island Glacier from C to D and c) at the Getz Ice Shelf grounding line from E to F (locations shown on Figure 3.1e).
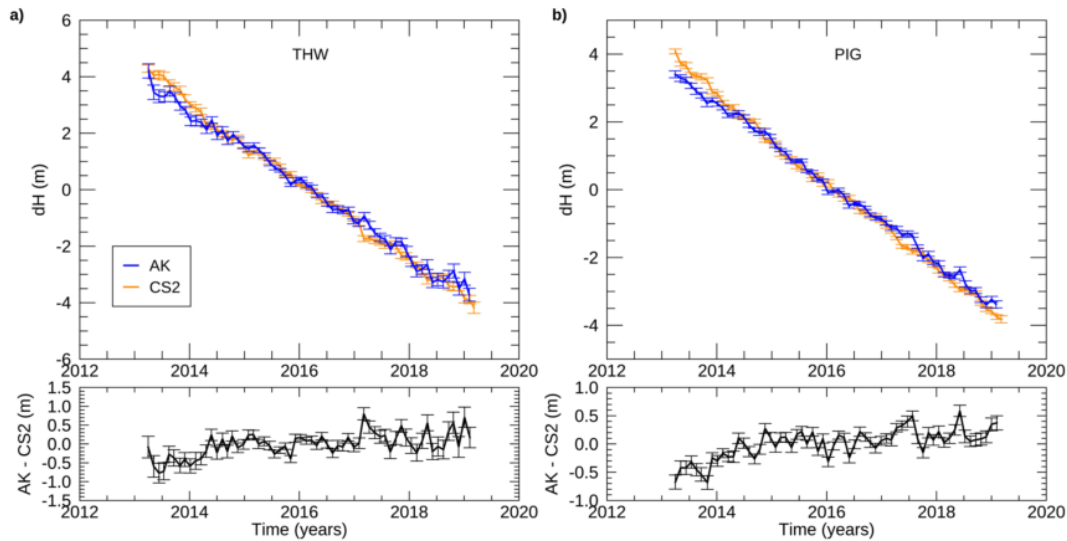
Figure 3.4: Time series of elevation change over a) Thwaites Glacier and b) Pine Island Glacier fast-flowing trunks (shown on Figure 3.1d) from AltiKa and CryoSat-2 and elevation change difference.

We also examined temporal variations in the surface elevation of the fast-flowing sections of Thwaites (Figure 3.4a) and Pine Island Glaciers (Figure 3.4b) recorded by AltiKa and CryoSat-2 to assess to which extent AltiKa can be used to examine elevation change trends at the scale of individual glaciers. Previous studies have identified rapid and increasing rates of surface lowering across the fast-flowing trunks of the Thwaites and Pine Island Glaciers (Shepherd et al., 2001; Wingham et al., 2009). This signal reflects glacier thinning associated with widespread ice dynamical imbalance (Konrad et al., 2017). Observations recorded by AltiKa show that the surface at Thwaites Glacier has lowered at a rate of 100 ± 20 cm yr^{-1} between 2013 and 2019 and thinning exceeded 50 cm yr^{-1} at distances up to 173 km from the grounding line. Over Pine Island Glacier, AltiKa recorded a rate of elevation change of 117 ± 9 cm yr^{-1} over the same period with thinning spreading inland up to 363 km from the glacier's terminus. Thinning rates recorded at these two glaciers peaked at 343 ± 33 cm yr^{-1} and 216 ± 9 cm yr^{-1} at Thwaites and Pine Island Glaciers, respectively. We compared these Ka-band observations with CryoSat-2

data. Over Thwaites Glacier, CryoSat-2 is recording a rate of elevation change of 136 $\pm$ 14 cm yr^{-1} showing that AltiKa is slightly underestimating the elevation trend at this particular glacier, likely because AltiKa surveys only 45 % of the glacier, compared to an almost complete coverage of Thwaites Glacier (97 %) by Cryosat-2. On the other hand, the elevation change trend recorded by Cryosat-2 at Pine Island Glacier is in close agreement with AltiKa with a rate of 128 $\pm$ 9 cm yr^{-1}.

3.5   Discussion and Conclusion

We provide observations of ice sheet surface elevation change from Ka-band satellite radar altimetry. Using SARAL/AltiKa measurements and a least-square model fit, we map ice thinning across the Amundsen Sea Sector of West Antarctica between March 2013 and March 2019, and we evaluate these estimates using two independent datasets – Operation IceBridge airborne laser altimetry and CryoSat-2 satellite Ku-band radar altimetry. In general, the AltiKa, IceBridge, and CryoSat-2 data are in excellent agreement, with difference in elevation and elevation change in the range -59 to 68 m and -110 to 114 cm yr^{-1} for 99.7% of the data, respectively. We surmise that the small positive bias in elevation between AltiKa and IceBridge is related to AltiKa's coarser ground footprint and the sloping terrain of the study region. The slope correction we applied to the AltiKa dataset reduced this bias by 63% but a small residual slope effect remains. Despite being less suited to survey the ice sheets surface than CryoSat-2 because of its orbit inclination and smaller beam width compared to the magnitude of the slope found in the margins of the ice sheet, AltiKa is still able to detect elevation change with good levels of agreement with both airborne laser altimetry and Cryosat-2. The very small difference in elevation trends between AltiKa and IceBridge, and CryoSat-2 and IceBridge, is an indicator that trends in radar altimeter penetration are negligible in this region. Although deriving total volume change from AltiKa might be challenging, as it does not sample parts of the ice sheet margins where the surface slope and roughness are high with a sufficient spatial coverage, it is still able to detect changes in the surface elevation of Thwaites and Pine

Island Glaciers for instance. The new Ka-band altimetry record presented in this study reveals that the surface elevation at Thwaites and Pine Island Glaciers has reduced by 7.9 ± 1.1 m and 6.8 ± 0.5 m respectively between 2013 and 2019 with a change in elevation of 2.5 ± 0.8 m and 2.3 ± 0.3 m in the last two years (2017-2019) of our survey. These additional two years of data added by our study to the long altimetry record already available show that the surface elevation lowering on Pine Island and Thwaites Glacier has continued at a similar pace compared to the 2013-2017 period. However, compared to surface elevation change estimates recorded during the 2000's from a combination of ERS-2 and Envisat (Shepherd et al., 2019), the rate of elevation change over the fast-flowing section of Thwaites Glacier has increased by 43% and decreased by 9% over Pine Island Glacier compared to the AltiKa record from 2013 to 2019. Overall, our study highlights the capability of AltiKa, the first space borne Ka-band altimeter, for measuring surface elevation change in West Antarctica.

This page intentionally left blank.

CHAPTER 4

Surface Melting Drives Fluctuations in Ku-airborne Radar in West Central Greenland

4. SURFACE MELTING DRIVES FLUCTUATIONS IN KU-AIRBORNE RADAR IN WEST CENTRAL GREENLAND

4.1 Abstract

Greenland Ice Sheet surface melting has increased since the 1990s, affecting the rheology and scattering properties of the near-surface firn. We combine firn cores and modelled firn densities with seven years of CryoVEx airborne Ku-band (13.5 GHz) radar profiles to quantify the impact of melting on microwave radar penetration in West-Central Greenland. Although annual layers are present in the Ku-band radar profiles to depths up to 15 m below the ice sheet surface, fluctuations in summer melting strongly affect the degree of radar penetration. The extreme melting in 2012, for example, caused an abrupt 6.2 ± 2.4 m decrease in Ku-band radar penetration. Nevertheless, retracking the radar echoes mitigates this effect, producing surface heights that agree to within 13.9 cm of coincident airborne laser measurements. We also examine two years of Ka-band (34.5 GHz) airborne radar data and show that the degree of penetration is half that of coincident Ku-band.

4.2 Introduction

In recent decades, increased melting at the surface of the Greenland Ice Sheet (Broeke et al., 2016) has had a marked impact on rates of runoff (Enderlin et al., 2014; van Angelen et al., 2014) and glacier flow (van de Wal et al., 2008), and has also affected the structure of the near surface firn owing to the redistribution and refreezing of surface meltwater (de la Peña et al., 2015; Machguth et al., 2016). These processes, and the associated changes in firn properties, present challenges for satellite radar altimetry surveys of the ice sheet mass balance when converting observations of volume change to mass change (McMillan et al., 2016). Surface melting has a large impact on the firn stratigraphy and density as meltwater can refreeze at the surface, or percolate into the snowpack and refreeze to form ice lenses (Benson, 1996), or refreeze in between already existing ice layers and form thicker ice slabs (Macferrin et al., 2019). Ice cores provide records of density and stratigraphy at point locations (Mosley-Thompson et al., 2001) and firn densification models provide estimates of densities across the ice sheet (e.g. Kuipers Munneke et al., 2015). Radars have also been widely used over glaciers and ice sheets to map their structure (MacGregor

et al., 2015), calculate accumulation rates (Miège et al., 2013), and track changes in their elevation (Shepherd et al., 2019).

Radar systems transmit electromagnetic pulses and record the amplitude and time delay of the waves scattered back from discontinuities in the dielectric properties. Their echoes are sensitive to density variations in the firn column, and the firn structure can reveal continuous internal scattering horizons, corresponding to isochrones (Hawley et al., 2006). Both ground-based (Brown et al., 2012) and airborne radar, such as the snow radar flown during NASA Operation IceBridge (Koenig et al., 2016; Medley et al., 2013; Montgomery et al., 2020) or the European Space Agency's Airborne SAR/Interferometric Radar Altimeter System (ASIRAS) operating at Ku-band (de la Peña et al., 2010; Helm et al., 2007; Overly et al., 2016; Simonsen et al., 2013), have been used to track isochrones and derive accumulation rates. Unlike ground-based and airborne radar, satellite radar measurements lack the vertical resolution to resolve the internal structure of the firn column due to the smaller bandwidth and coarser spatial resolution of the radar footprint. Nonetheless, satellite radar altimeters are sensitive to variations in the firn properties as the radar signal penetrates into the snowpack. Additionally, the radar signal penetration is frequency-dependent. At present, two frequencies are used by satellite radar altimeters: Ku-band (13.5 GHz) is used by CryoSat-2 and Sentinel 3A/B, and Ka-band (37 GHz) is used by AltiKa. Studies have shown that at Ku-band the radar signals can penetrate up to $\sim$15 m into firn, while the penetration depth of higher frequency Ka-band radars is reduced to $\sim$ 0.5 m (Rémy et al., 2015). The altimeter echo recorded is therefore a combination of surface and volume scattering (Ridley and Partington, 1988). The ratio between surface and volume scattering varies spatially and temporally according to changes in the surface and subsurface properties, and may impact the height retrieval from radar altimeters (Simonsen and Sorensen, 2017).

In this study, we use airborne Ku-band radar data acquired using the ASIRAS instrument, Ka-band radar data acquired using the KAREN radar (the MetaSensing Ka-band altimeter), airborne laser data, shallow firn cores ($\leq$ 6 m), and firn density models to characterise and assess the impact of spatial and temporal fluctuations in the properties

89

of the near-surface firn in West Central Greenland. This study is performed along the glaciological transect established during the Expéditions Glaciologiques Internationales au Groenland (EGIG) in 1958 (Renaud et al., 1963). The EGIG line extends from the ablation zone at the Western margin of the ice sheet, across the percolation and dry snow zones to the Summit, and further towards the Eastern margin and is therefore a representative location of density variations across the Greenland Ice Sheet (Parry et al., 2007).

4.3 Data and Methods

The EGIG line (Figure 4.2a) has been surveyed for more than a decade as part of ESA's Cryosat Validation Experiment (CryoVEx). According to previous in-situ investigations of snow density and stratigraphy, EGIG line sites T3 to T21 lie in the percolation zone with site T21 marking the start of the dry snow zone (Morris and Wingham, 2011; Scott et al., 2006). In this study, we use data collected between 2006 and 2017 over a ~ 675 km transect of the EGIG line, starting about 14 km from Ilullissat airport at an elevation of 157 m above sea level (m.a.s.l.), 115 km before site T1, and ending 149 km beyond site T41 at an altitude of 2956 m.a.s.l.

4.3.1 Shallow Firn Cores

Shallow firn cores were collected in October 2016 (T1, T4, T5) and April 2017 (T5, T9, T12, T19, T30, T41) (Table 4.1). A Kovacs coring system with a drill barrel of 9 cm diameter was used to extract shallow ice cores down to ~ 6 m to obtain firn density and stratigraphy. A detailed stratigraphy analysis of the ice cores was performed by illuminating the ice cores and taking photographs to identify the snow and ice layers. The density was measured by dividing the ice core into several sections and measuring each section's bulk weight and length. We attribute an uncertainty of 10 % on the firn cores bulk density (Fausto et al., 2018).

Table 4.1: Date of collection and coordinates of firn cores

Site	Date	Latitude (N)	Longitude (W)
T1_16	27/10/2016	69.731	-48.133
T4_16	27/10/2016	69.811	-47.510
T5_16	25/10/2016	69.851	-47.253
T5_17	30/03/2017	69.852	-47.550
T9_17	31/03/2017	70.020	-46.306
T12_17	31/03/2017	70.176	-45.345
T19_17	31/03/2017	70.470	-43.564
T30_17	01/04/2017	70.850	-40.500
T41_17	30/03/2017	71.079	-37.920

4.3.2 Firn Densification Models

These in-situ density measurements are used to evaluate two firn densification models (Figure 4.1): (1) the stand-alone Institute for Marine and Atmospheric research Utrecht Firn Densification Model (IMAU-FDM) (Ligtenberg et al., 2011, 2018), forced at the surface by RACMO (Noël et al., 2018). IMAU-FDM simulates the density and temperature in a vertical, 1-dimensional firn column through time at a vertical resolution of 5 cm; and (2) the CROCUS snow model (Brun et al., 1992) embedded in the Modèle Atmosphérique Régional (MAR) (version 3.10 Fettweis et al., 2017, 2020) to derive the MAR firn densification model (MAR-FDM). CROCUS simulates the transfer of mass and energy between a fixed number of layers of snow, firn or ice with a vertical resolution varying from 5 cm to 500 cm.
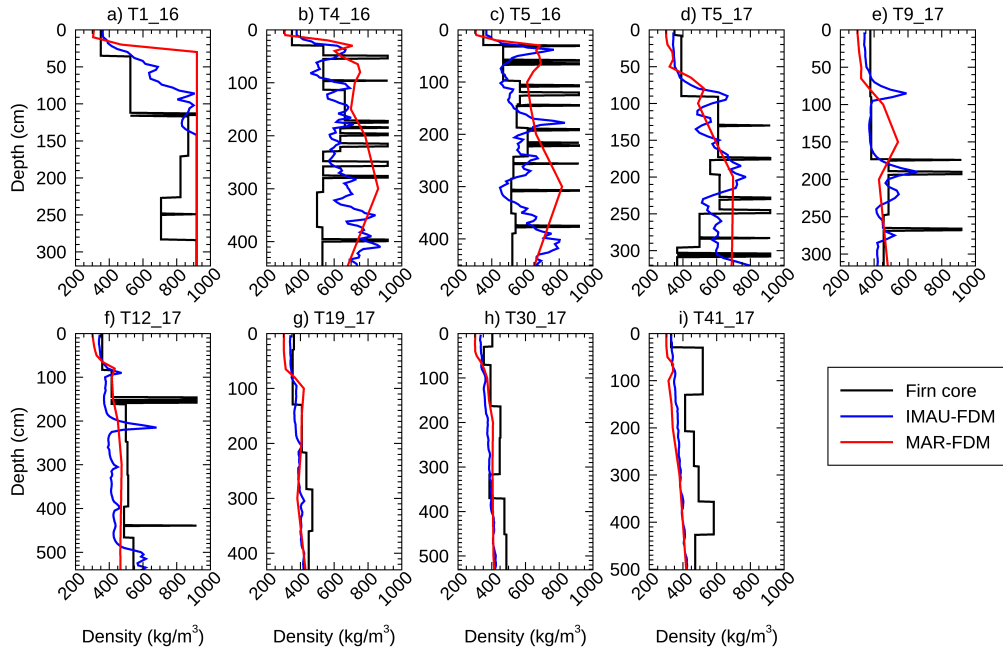
Figure 4.1: Depth-density profiles at each site from the shallow firn cores, IMAU- and MAR-FDMs.

4.3.3 Airborne Radar Data

Airborne radar data were collected in 2004, 2006, 2008, 2011, 2012, 2014, 2016 and 2017, along segments of the EGIG line of varying length. For all CryoVEx airborne surveys, the same aircraft and instrumental setup were used, which includes an airborne laser scanner (ALS), the ASIRAS radar, and the KAREN radar in two surveys in 2016 and 2017. The ALS is a Riegl LMS-Q140-i60 laser scanner operating at 904 nm (red), which gives surface heights in 0.7 m intervals across a 300 m wide swath with an accuracy of 0.1 m (Skourup et al., 2019). ASIRAS is a Ku-band radar designed as a prototype for the SIRAL altimeter on board CryoSat-2 operating at a central frequency of 13.5 GHz with a bandwidth of 1.0 GHz, range resolution of 0.109 m in air and a nominal footprint size of 10 m across-track and 3 m along-track at a flight elevation of ∼300m a.g.l. (Cullen, 2010). KAREN is a Ka-band radar altimeter operating at a central frequency of 34.5 GHz – the same frequency

used by AltiKa – with a bandwidth of ∼0.5 GHz, range resolution of 0.165 m in air and a footprint size of 10 m across-track and 5 m along-track (version 'levc'). Data acquired when the aircraft roll angle exceeded ±1.5°were discarded.

Retracking and Calibration

We applied three different retracking algorithms to locate the ice sheet surface in the radar echoes as different processing strategies have been shown to affect the elevation measurements when the radar penetration depth varies (Slater et al., 2019). We used (1) an offset centre of gravity (OCOG) retracker (Wingham et al., 1986), (2) a 30 % threshold centre of gravity (TCOG) retracker (Davis, 1997) similar to the retracker implemented in CryoSat-2 ground segment, and (3) a 50 % threshold first maximum retracking algorithm (TFMRA, Helm et al., 2014). Each retracker's performance was evaluated by comparing their elevations to those recorded by the ALS, after calibrating ASIRAS and KAREN relative to the ALS along runway over-flights, using search radii of 3 and 5 m, respectively (Table 4.2). The calibration offsets account for the different positions of the radar and laser sensors in the aircraft and are calculated for each campaign by comparing radar and laser surface elevation measurements recorded over runway overflights across Greenland where both radar and laser reflect to the same surface. This calculation is therefore dependent on the retracker used and thus, we compute this correction for all three retrackers used in this study.

Conversion of radar two-way travel time to depth

We aligned each radar waveform to the ice sheet surface and took the mean radar waveforms in 1 km segments along-track to reduce noise. We converted the radar two-way travel time to depth using a depth-density profile from the MAR output:

$$v_{firn} = \frac{c}{\sqrt{\epsilon_{firn}}} \tag{4.1}$$

where c is the speed of light in vacuum, v_{firn} the speed of light in firn, ϵ_{firn} the dielectric permittivity of the firn We estimate the dielectric permittivity of the firn using Looyenga

Table 4.2: Calibration offsets for ASIRAS and KAREN calculated for each campaign.

Radar	Year	OCOG (m)	TCOG (m)	TFMRA (m)
ASIRAS	2006	3.39	3.35	3.42
ASIRAS	2008[1]	*	*	*
ASIRAS	2011	3.47	3.43	3.50
ASIRAS	2012	3.61	3.57	3.62
ASIRAS	2014	3.78	3.68	3.81
ASIRAS	2016	3.49	3.45	3.50
ASIRAS	2017	3.58	3.57	3.63
KAREN	2016	-0.40	-0.51	-0.33
KAREN	2017	0.03	-0.07	0.13

[1] ASIRAS data for the calibration offset computation were not available

(1965) from the modelled density-depth profile at every location i along the EGIG line transect for each depth bin j defined in the model:

$$\epsilon_{firn}^{MAR}(i,j) = (1 + \frac{\rho_{firn}(i,j)}{\rho_{ice}}(\epsilon_{ice}^{\frac{1}{3}} - 1))^3 \qquad (4.2)$$

where ϵ_{ice} is the dielectric permittivity of pure ice, $\rho_{ice}(i,j)$ is the integrated density at location i of the firn column from the surface up to depth j and ρ_{ice} is the density of ice

The velocity of the radar wave in the modelled firn column v_{firn}^{MAR} (corrected for the propagation delay in snow and firn) is deduced from equations 4.1 and 4.2. We calculate the associated uncertainty in the derived velocity by assuming an uncertainty of 15 % in the modelled density based on the comparison to the in-situ measurements:

$$\sigma_{v_{firn}^{MAR}} = \frac{3A}{2} \frac{\delta\rho}{1 + \rho_{firn}(i,j).A} \qquad (4.3)$$

with the constant A defined as:

$$A = \frac{1}{\rho_{ice}}(\epsilon_{ice}^{\frac{1}{3}} - 1) \qquad (4.4)$$

Finally, the radar two-way travel time is converted to depth by interpolating the firn velocity-depth profile from the model and the final uncertainty is calculated as:

$$\delta d = |d|\sqrt{(\frac{\delta twt}{twt})^2 + (\frac{\delta v}{v})^2} \qquad (4.5)$$

by assigning an uncertainty in radar travel time of two travel time bins in the radar travel time: $\delta twt_{ASIRAS} = 1.17$ ns and $\delta twt_{KAREN} = 2.6$ ns

The IMAU-FDM and MAR densities of the top 15 m of the firn column are in close agreement (r=0.99) and using either of these models to convert the radar time delay to a depth leads to similar estimated depths with a mean difference of 2.2 cm and standard deviation of 9.5 cm.

Tracing algorithm to detect internal layers in ASIRAS Ku-band radar

The internal layers present within each ASIRAS profiles were traced in an automated way. To do this, we first applied a logarithmic scale to enhance the deeper layers and we then removed a Gaussian filtered echogram to sharpen each image. Our tracing algorithm is based on the detection of waveform peaks above a power of 15 counts. For each peak detected, we applied a peak-following algorithm (Fahnestock et al., 2001) in both directions along-track to obtain a potential layer across each echogram. This algorithm starts at one peak, proceeds to the adjacent location along-track, and then searches for the range bin within the chosen waveform that records the maximum power within 5 bins centred on the bin identified from the previous location along-track. We grouped the potential layers based on their respective distances to their centroids – defined in the accumulation zone where the layers are the most stable – and, for each location along-track, we kept the mode and the standard deviation of the ensemble of layers found to identify a final layer per cluster. We checked that the final layers were all distinct and at least 15 km long, and we resolved their chronology relative to the surface (de la Peña et al., 2010; Hawley et al., 2006).
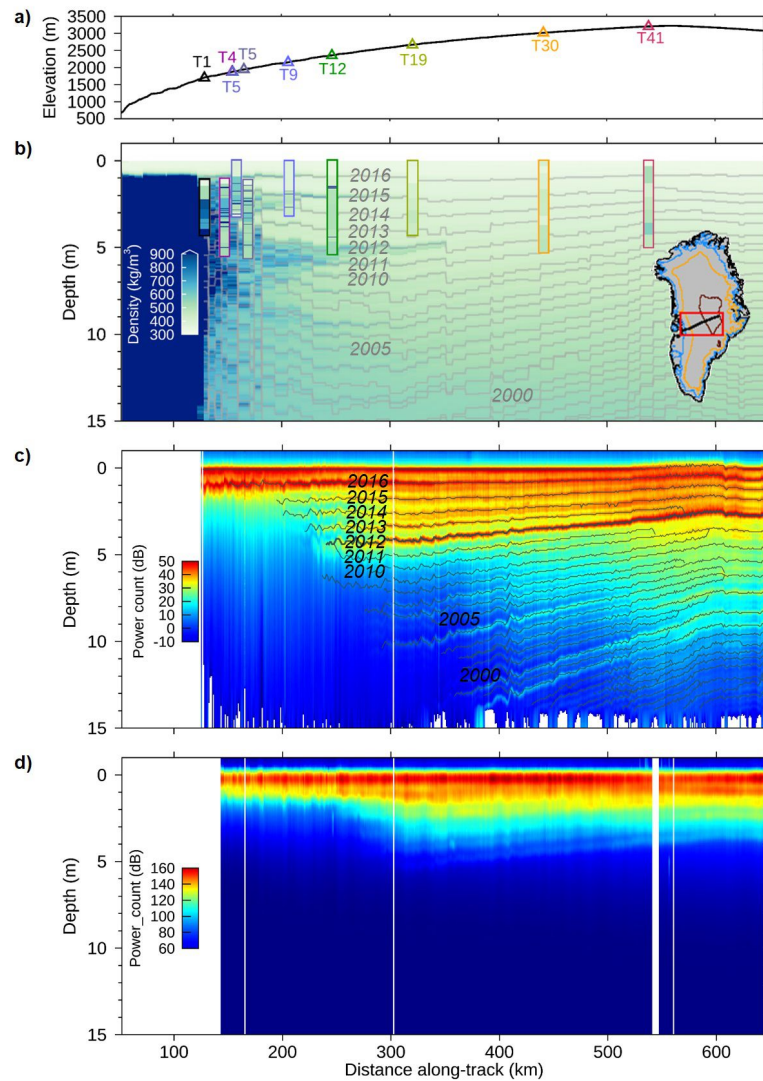
Figure 4.2: a) Elevation profile along the EGIG line. b) IMAU-FDM density profile (31/03/2017) and firn core densities. The isochrones traced from IMAU-FDM are indicated by grey lines. The firn cores from 2016 are offset by the net SMB relative to 2017. The inset shows the location of the study area. c) ASIRAS Ku-band radar profile. The traced layers are indicated by black lines. d) KAREN Ka-band radar profile. The two radar profiles were acquired on 31/03/2017 and 01/04/2017. Along-track distance is relative to Ilulissat airport.

4.4 Results

We evaluated the modelled firn densities by comparison to those measured in the shallow cores (Figure 4.1). The IMAU- and MAR-FDM densities are highly correlated with the cores ($r = 0.93$ and 0.89, respectively) and show good overall agreement, with root-mean-square differences (RMSD) of 64 kg m^{-3} and 104 kg m^{-3}, respectively (Figure 4.3a). However, we note a spatial pattern in the difference between the in-situ and modelled densities. At sites below 2000 m (T1 to T5), IMAU-FDM overestimates firn density by 10 % on average and underestimates firn density by 11 % at higher elevation sites. MAR-FDM exhibits a similar bias, with an overestimation of 21 % on average at sites below 2000 m, and an 11 % underestimation of firn density at higher elevation sites. The largest departure from the firn cores is recorded for both models at site T1, located at an elevation of 1698 m in the low percolation zone. At this site, we measured a total of 40 cm of ice from the firn core while IMAU- and MAR-FDM simulated a total of 188 cm and 294 cm of ice in the corresponding firn column, indicating that the firn ice content is overestimated in the lower section of the EGIG line (Figure 4.1).

The ASIRAS radar profiles across the EGIG line (Figure 4.2c) show a clear sequence of internal layers starting at an elevation of ∼2200 m, which we attribute to melt and refreezing in the percolation zone and to autumn hoar in the dry snow zone. We compare the distribution and sequence of internal-layers present within the 2017 ASIRAS profile to isochrones derived from the 2017 IMAU-FDM firn density and chronology. We identify annual isochrones in the IMAU-FDM profile by locating the maximum firn density in data of the same age. The ASIRAS internal layers and IMAU-FDM chronology are highly correlated ($r = 0.99$, Figure 4.3b) with a robust dispersion estimate (RDE) of 71 cm. However, compared to the radar layers, IMAU-FDM annual isochrones are consistently found deeper in the firn column, with a systematic bias of 17.1%. The bias between the modelled isochrones and the observed layers accumulates with depth, shifting the distribution of annual layers compared to the radar observations. After adjusting the IMAU-FDM isochrones for this systematic bias, the radar layers and modelled isochrones
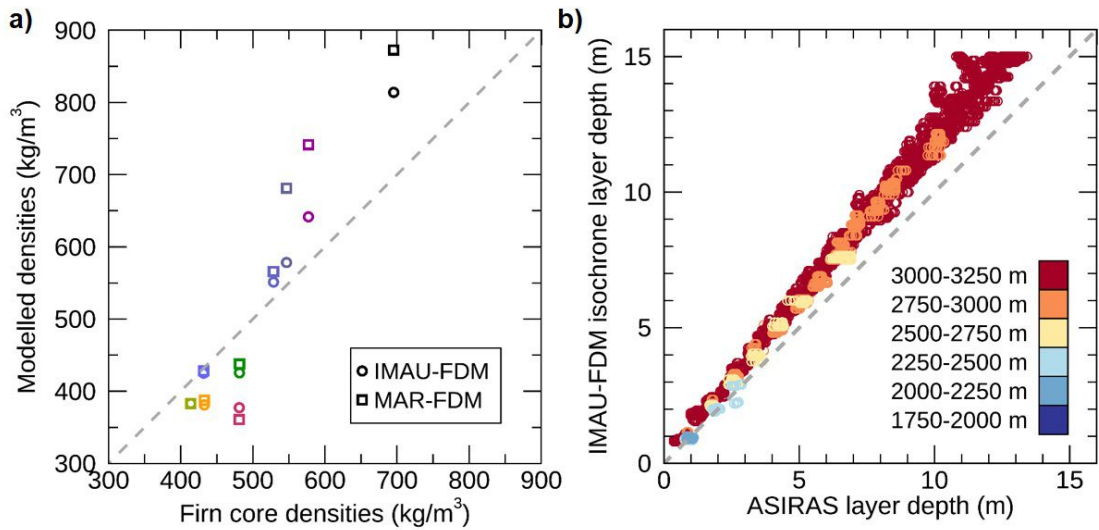
Figure 4.3: a) Scatterplot of firn core densities versus model (IMAU- and MAR-FDM) densities. b) Scatterplot of the IMAU-FDM isochrones depths versus ASIRAS internal layers depths.

are well-aligned with an overall RDE of 26 cm and RMSEs of 14 cm for the top 2016 isochrone and 21 cm for the 2012 isochrone. The close agreement between the sequence and depth of the ASIRAS internal layers with the IMAU-FDM chronology leads us to conclude they are recording the same physical features.

The layers recorded in the ASIRAS profiles show marked inter-annual variability, with a clear transition after 2012 (Appendix A). Until 2012, the top two isochrones are the strongest peaks in the radar return. Afterwards in 2014, however, the strongest peaks correspond to the surface layer and the 2012 isochrone. In 2016 and 2017, even though the 2012 isochrone is located deeper in the snowpack, the associated waveform peak remains relatively high – at 33 % and 29 % of the maximum peak respectively. The strong dielectric contrast of the 2012 melt layer – reducing the energy transmitted to the deeper firn column – is linked to the formation of an ice lens following the intense melt event of that year (Nghiem et al., 2012). This attenuation of the radar backscatter is seen in both the percolation and the dry snow zone. In the percolation zone, we recorded a 1 cm thick

ice lens at a depth of 4.4 m in the firn core collected at site T12 in 2017 (at an elevation of 2352 m). This layer is aligned with the 2012 isochrone measured at a depth of 4.4 ± 0.2 m in ASIRAS data collected in the same year. At elevations above 2500 m and prior to the melt event in 2012, the Ku-band radar records significant power (above 1% of the maximum surface return) to a depth of 11.5 ± 1.3 m below the ice sheet surface (Figure 4.6a). After the melt event, the attenuation in the firn column is mainly driven by the strong reflection at the 2012 melt layer and as a result, the degree of radar penetration is reduced to 5.3 ± 2.0 m in 2014 and 7.5 ± 2.0 m in 2017. The strong reduction in radar penetration coincides with a peak in the density anomaly recorded by IMAU-FDM of 32.9 kg m^{-3} and by MAR-FDM of 63.0 kg m^{-3}, which demonstrates that the near-surface firn densities and degree of the radar penetration are linked (Figure 4.6b).

We observe strong spatial variations in the degree of radar penetration into the near-surface firn along the EGIG line (Figure 4.4). In all years, few or no internal-layers are present in the ASIRAS data in the ablation and percolation zones below $\sim$2200 m, after which their abundance begins to increase with surface elevation as the firn density falls. The number of layers with significant power (above 10% of the maximum surface return) varies in a similar manner to the OCOG retracker width, indicating that strong near-surface scattering has masked scattering at depth. In the ablation and percolation zones, water percolates into the winter snow and new ice lenses or layers are formed each year, preventing the radar signal from penetrating deep into the firn. This process leads to a reduction of the OCOG width, because the main scattered energy is concentrated nearer the ice sheet surface. In all years, the OCOG retracker width and the number of layers show a tendency to increase with elevation and reach maxima at the highest elevation of the transect. However, the maximum number of layers visible and the maximum OCOG retracker width vary from year to year; in 2014 for example, the maxima of both parameters above 2500 m are more than three times lower than in 2012. Furthermore, compared to 2012, the range of variations in OCOG width is reduced by 86% in 2014 over the same section, which shows that spatial variations in volume scattering are also less prominent after the 2012 melt event.

Figure 4.4: a) Number of layers above 10 % of the maximum surface return. b) OCOG width. c) Depth at which power falls below 1 % of the maximum surface return.

We evaluate the impact of volume scattering fluctuations on the performance of three alternative radar retrackers – OCOG, TCOG and TFMRA. Both the TCOG and TFMRA retrackers track the very first peak recorded by the radar altimeter and identify the surface at similar locations with a mean difference of 7.1 cm and standard deviation of 1.9 cm. On the other hand, the OCOG retracker follows the centre of gravity of the radar echoes. At elevations above 3000 m, the scattering horizon is shifted towards the snow surface after the melt event in 2014 compared to 2012, resulting in a 73 cm increase in the altimetry range measurement using the OCOG retracker. We compare the heights from each of the retrackers to the ALS heights (Figure 4.5). Over a total of 2496 km of flights acquired on five different years, the mean difference between the ALS and OCOG heights was 107 cm, with a standard deviation of 55 cm (Table 4.3). By comparison, the TCOG and TFMRA retracked heights are in far better agreement with the ALS data, with mean differences of 14 cm and 20 cm, and standard deviations of 20 cm and 21 cm, respectively. Despite the large fluctuations in volume scattering that have occurred along the EGIG line as a consequence of changes in the snowpack structure, the TCOG and TFMRA retracking of radar heights is stable, demonstrating that these algorithms are effective methods of mitigating the impact of radar penetration variations.

Table 4.3: Comparison of airborne laser and ASIRAS elevation measurements. Mean and standard deviation of the difference between ALS and ASIRAS (cm). The quality of the ALS data was not sufficient for this comparison in 2008 and 2014.

Date	ALS-OCOG	ALS-TCOG	ALS-TFMRA	Number of km surveyed
2006	96.0 ± 34.1	13.4 ± 24.0	21.1 ± 25.3	575
2011	99.2 ± 33.6	9.7 ± 17.6	13.3 ± 13.5	514
2012	108.0 ± 51.7	13.8 ± 21.0	20.5 ± 21.4	562
2016	78.8 ± 52.4	29.3 ± 15.0	37.6 ± 17.1	287
2017	139.6 ± 73.8	10.4 ± 13.6	15.6 ± 17.1	558
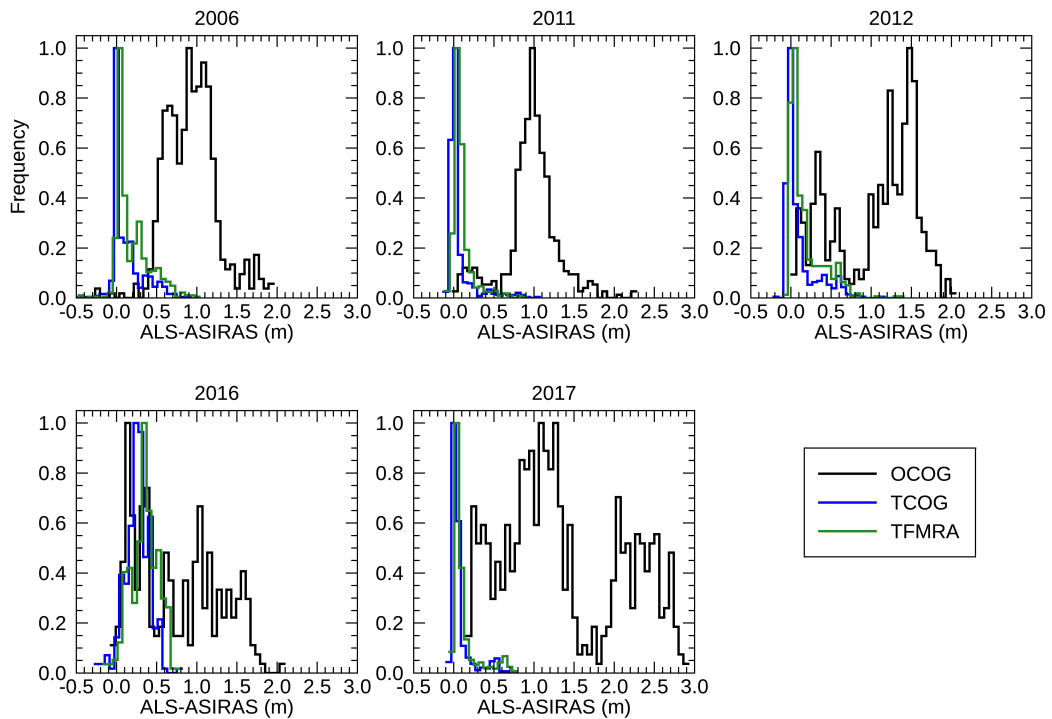
Figure 4.5: Histograms of the difference between airborne laser scanner and Ku-band radar
surface heights (ALS-ASIRAS).

4.5 Discussion

The two firn densification models we have tested at the EGIG line are able to reproduce
the mean density of the shallow firn column with typical differences of 10 % (IMAU) and
15 % (MAR-FDM) by comparison to in-situ measurements. At site T1 in particular, the
firn ice content is largely overestimated by the models with more than 59 % and 92 % of
the total length of the firn core simulated as ice by IMAU- and MAR-FDM respectively,
compared to only 13 % from the field observations (Figure 4.1). This indicates that
surface melt and refreezing might not be quantified properly in the lower percolation zone
of the EGIG line. However, using the density measured from the firn cores or the density
outputs from either of these models to convert the radar travel time to depth leads to mean
differences within 13 cm. Nevertheless, small biases in modelled firn density do accumulate

with depth, offsetting the vertical distribution of annual ice layers (Figure 4.3b). We also investigate to which extent firn densification models are able to capture the distribution of annual melt layers within the firn column compared to radar-derived layers. This requires a firn model with a fine vertical resolution, such as the IMAU-FDM, to resolve the different layers, which are typically spaced between 30 cm to 100 cm apart. Although the chronology and spatial distribution of isochrones derived from the IMAU-FDM show good agreement with the internal layers detected by ASIRAS, there is a systematic bias of 17.1 % between the two data sets, which we suspect is due to an underestimation of the firn densification rate. This shows that capturing the density variability in the firn column is more challenging than simulating the mean density of the column as suggested by firn model inter-comparison studies (Vandecrux et al., 2018; Verjans et al., 2019).

We link the sharp reduction in the degree of radar penetration depth after 2012 to the 2012 melt event. Over elevations of 2500 m, the 2012 isochrone is recorded in the Ku-band altimetry echoes at a depth of 1.5 ± 0.2 m with a significant power of 82 % of the maximum surface return and in 2014 at a depth of 3.7 ± 0.2 m with a significant power of 60 % (Figure 4.6a). To analyse these fluctuations in radar penetration depth, to fluctuations in the intensity of surface melting, we calculate the density anomalies from IMAU- and MAR-FDMs. The density anomaly from IMAU-FDM is derived from the 2017 firn column density and chronology data averaged between 300 and 600 km along-track (at elevation above $\sim$2500 m). The chronology in the firn column is defined as the age of the different layers on 31st March 2017 (date of the 2017 CryoVEx campaign). We convert the age of the different layers to decimal years and we exclude the first three layers defined in the model due to some spurious behaviour caused by inter- and extrapolation of the age profile. We average the density and date fields along-track over the 300 km section of the EGIG line to obtain a density time series. Finally, we detrend this time series with a quadratic fit to account for firn compaction. To derive the density anomaly from MAR-FDM, which lacks the vertical resolution to resolve the density in the column through time, we extract a time series of the integrated density of the top 1 m using modelled daily density from 2006 through to 2017. We average the integrated density
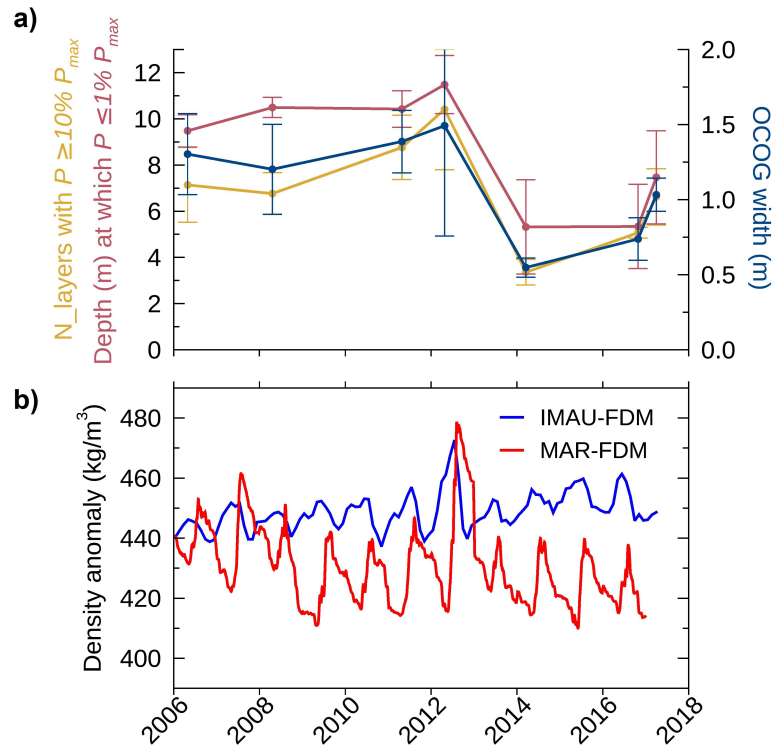
Figure 4.6: a) Temporal variations of the mean of three proxies for penetration depth derived from ASIRAS radar profiles presented on Figure 4.4 over the section 300-600 km along-track. Error bars indicate the standard deviation. b) Density anomaly from IMAU- and MAR-FDMs centred around the mean over the same section.

over the transect extending between 300 and 600 km along-track (at elevation above 2500 m). Finally, we detrend this time series by removing the mean density calculated over the whole time period 2006-2017. From the derivation of these density anomalies, we found that over the same part of the transect, the melt layer is captured by the IMAU- and MAR-FDM with a high density peak after the 2012 summer, which is double the density of the previous summer's peak. In general, when surface melting occurs, the degree of radar penetration into the near surface firn reduces sharply. The density fluctuations recorded above 2500 m in 2012 are the largest since 2006 (Figure 4.6b) and coincide with the fluctuations in radar penetration recorded in the same year. This is shown by the 63

% decrease in the OCOG width, the 68 % reduction in the number of layers with a high power return, and the 6.2 ± 2.4 m decrease in the radar penetration depth. Such density fluctuations lead to instantaneous upwards (towards the surface) shifts in the distribution of power within the radar echo, followed by gradual downwards (away from the surface) returns to pre-melt conditions. These saw-tooth variations in radar penetration lead to aliased fluctuations in the elevation of the scattering surface, explaining effects that have been highlighted (and corrected for) in analyses of satellite radar altimetry (McMillan et al., 2016; Nilsson et al., 2015; Slater et al., 2019).

We explored two approaches to mitigate the impact of these density fluctuations on surface elevation derived from radar altimetry. First, we found that the application of threshold waveform echo retracking is able to provide estimates that agreed to within 20 cm of coincident laser altimetry. We also examined the sensitivity of higher-frequency Ka-band radar data to volume scattering, as an alternative means of mitigating firn density fluctuations (Appendix B). At higher frequencies, surface scattering is relatively stronger than volume scattering, and we find that the penetration depth is smaller at Ka-band than Ku-band. For example, in 2016 and 2017, although significant power was recorded in ASIRAS Ku-band radar at depths of up to 6.8 ± 0.3 m below the surface along the high altitude section of the EGIG line (300 to 600 km), the corresponding KAREN Ka-band radar penetration was 3.4 ± 0.3 m. We also compared Ka-band surface elevation estimates to those recorded by the ALS (Figure 4.7) . Over a total of 782 km of KAREN flight tracks, the mean difference between the KAREN and laser data, when using OCOG, TCOG and TFMRA retracking algorithms, was 16.0 cm, 12.5 cm and 15.6 cm respectively, with standard deviations of 10.8 cm, 10.9 cm and 11.3 cm (Table 4.4). A more detailed assessment of the Ka-band penetration depth was not possible due to the reduced bandwidth of KAREN compared to ASIRAS, which prevents internal layering from being resolved (Figure 4.2d).

Table 4.4: Comparison of airborne laser and KAREN elevation measurements. Mean and standard deviation of the difference between ALS and KAREN (cm).

Date	ALS-OCOG	ALS-TCOG	ALS-TFMRA	Number of km surveyed
2016	24.7 ± 15.9	21.6 ± 15.7	25.8 ± 15.4	236
2017	12.2 ± 3.2	8.6 ± 3.5	11.1 ± 3.8	546
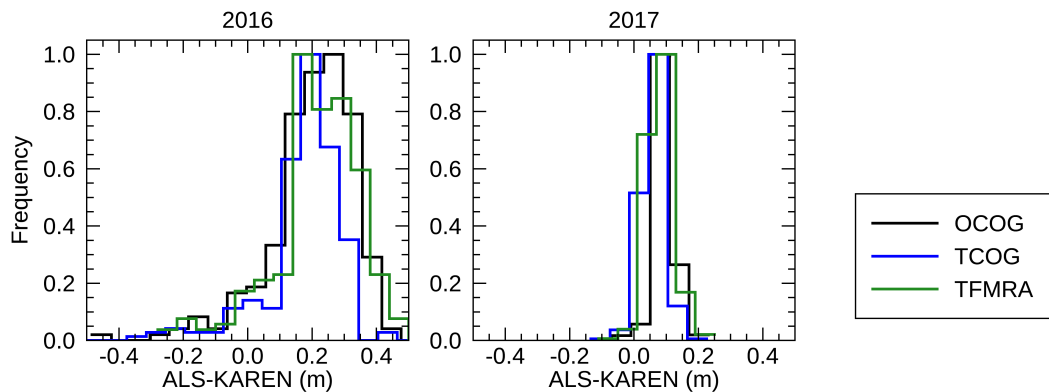
Figure 4.7: Histograms of the difference between airborne laser scanner and Ka-band radar surface heights (ALS-KAREN).

4.6   Conclusion

We present an extensive and coincident set of near-surface firn density and airborne radar and laser measurements acquired between 2006 and 2017 along the EGIG line in West Central Greenland. Using these data, we examine the impacts of firn density fluctuations on spatial and temporal variations in the scattering of airborne ASIRAS Ku-band radar waveforms. The largest fluctuations in radar penetration over this period are recorded after 2012 with an abrupt decrease of 6.2 ± 2.4 m in the Ku-band radar penetration. We link this decrease in radar penetration to the density fluctuations associated with the 2012 extreme melt event. As the frequency and extent of extreme melt events is likely to increase in the coming decades (Hall et al., 2013), the effects of fluctuations in radar

penetration are an important consideration for satellite radar altimetry. We find that simple methods of threshold retracking are efficient at mitigating this effect on Ku-band airborne radar data and the impact of such events are likely to last for a shorter period of time on Ka-band data due to its reduced penetration depth.

This page intentionally left blank.

CHAPTER 5

Changes in Northwest Greenland Ice Sheet Elevation and Mass

The work presented in this chapter was prepared as a manuscript to be submitted as:

Citation: Otosaka, I. N., Shepherd, A., Groh, A.: Changes in Northwest Greenland Ice Sheet Elevation and Mass.

Author contributions: I. N. Otosaka led the study, processed and analysed the data and wrote the manuscript supervised by A. Shepherd. A. Groh provided the gravimetry data and the solid Earth corrections. A. Shepherd commented on the manuscript.

5.1 Abstract

About a third of Greenland's total ice losses come from the Northwest sector, a sector that includes a large number of marine-terminating outlet glaciers, which have all experienced widespread retreat triggered by ocean-induced melting. Here, we derive changes in surface elevation, volume and mass in the Northwest sector of the Greenland Ice Sheet using a decade of CryoSat-2 observations. We find an average elevation change rate of 18.7 $\pm$ 0.4 cm yr^{-1}, with rapid thinning at the ice sheet margins at a rate of 42.7 $\pm$ 0.9 cm yr^{-1}. We compare our CryoSat-2 rates of elevation change to airborne laser altimetry

data from Operation IceBridge. Overall, there is a good agreement between the two datasets with a mean difference of 6.5 ± 0.5 cm yr^{-1} and standard deviation of 31.1 cm yr^{-1}. We further compute volume change, which we convert to mass change by testing three alternate density models and we find that the Northwest sector has lost 386 ± 3.7 Gt of ice between July 2010 and July 2019. We compare our mass balance estimate to independent estimates from gravimetry and the mass budget method across different spatial scales. First, we compare the different estimates by splitting the sector into two and four regions. While our altimetry estimate is the least negative across all regions, the gravimetry and mass budget estimates alternate in recording the largest ice losses. We further compare mass changes derived from altimetry and the mass budget method within 73 glacier basins of the Northwest sector. We find a high correlation of 0.81 between rates of mass change from altimetry and the mass budget method, with the highest differences recorded in Steenstrup-Dietrichson and Kjer Gletscher basins. Our comparisons show that the spatial pattern of the differences between mass balance estimates is complex, suggesting that discrepancies between techniques do not solely originate from one single region or technique. Finally, we explore several factors that could potentially bias our altimetry mass balance estimation, by investigating differences between satellite radar and airborne laser altimetry, the dependency on grid spatial resolution and the impact of using different density models.

5.2   Introduction

Changes in ice sheet mass manifest as changes in thickness, glacier flow and gravitational attraction. These parameters can be measured from space and used to derive mass changes independently from each other. Thickness changes are measured from repeated laser or radar altimetry measurements of surface elevation from either airborne or space borne platforms. Altimetry-derived elevation changes are then converted to mass change using a density model (McMillan et al., 2016) or by correcting for firn height changes estimated with an external model (Zwally et al., 2011). Gravity measurements are recorded from

satellite gravimetry and are converted to a mass change using mass concentration units (mascons) or spherical harmonics (Velicogna et al., 2020). Finally, ice flow at outlet glaciers is measured from interferometric satellite synthetic radar aperture (InSAR) and is combined with ice thickness observations and surface mass balance models to estimate ice sheet mass changes in the so-called 'mass budget method' (Mouginot et al., 2019). Estimates of ice sheet mass balance from these three geodetic techniques have been aggregated (e.g. Shepherd et al., 2020) to assess their agreement and to produce a reconciled ice-sheet-wide scale estimate of Greenland's mass balance. Although a regional inter-comparison has been performed for the Amundsen Sea sector in West Antarctica (Sutterley et al., 2014), this has yet to be done at the basin scale for Greenland.

The Greenland Ice Sheet is a major contributor to global mean sea level rise, contributing about 20 % to the global mean sea level rise since 1993 (WCRP Global Sea Level Budget Group, 2018) despite only storing 10 % of Earth's total ice on land – about 3 million km^3 of ice (Morlighem et al. 2017). In recent years, ice losses from the Greenland Ice Sheet have accelerated, rising from 34 Gt yr^{-1} in the 1990s to 244 Gt yr^{-1} between 2012 and 2017 (Shepherd et al., 2020) as a consequence of widespread retreat (King et al., 2020) and thinning (Pritchard et al., 2009) of outlet glaciers of the Greenland Ice Sheet. About a third of Greenland's total ice losses come from the Northwest sector, which has been contributing a total of 4.4 mm to global mean sea level rise since 1972 (Mouginot et al., 2019). The Northwest sector includes a large number of marine-terminating outlet glaciers, which have all experienced widespread retreat triggered by ocean-induced melt (Wood et al., 2018). Glaciers retreat was first observed from aerial photographs between 1985 and 1993 (Kjær et al., 2012), and another period of sustained retreat between 2000 up to at least 2015 was observed from satellite optical imagery (Bunce et al., 2018; Howat and Eddy, 2011). However, the pattern of retreating and thinning of the different glaciers is complex and suggests that their response to oceanic forcing is strongly modulated by their bed topography (Morlighem et al., 2019) and fjord geometry (Carr et al., 2013).

In this chapter, we estimate elevation and volume change of the Northwest Greenland Ice Sheet using a decade of CryoSat-2 observations between 2010 and 2020 and evaluate

these estimates with airborne laser altimetry from NASA's Operation IceBridge. We then use this new dataset to derive mass change over the Northwest sector and compare this new result to existing mass balance estimates from gravimetry and the mass budget method. Finally, we investigate the potential sources of the discrepancies between the three mass balance solutions and we outline further avenues to explore the origins of these differences.

5.3 Data

We use 24.4 million observations from CryoSat-2 between July 2010 and July 2020 to compute changes in ice sheet elevation in North Western Greenland, using the drainage basin delineations as defined in Mouginot et al. (2019). The Northwest sector is divided into 74 basins with 63 tidewater glaciers and 11 land-terminating glaciers, over an area of 27 thousand km^2. The novel design of CryoSat-2, launched in 2010, offers many advantages for observing the polar regions compared to previous radar altimeters. CryoSat-2 operates as a traditional pulse-limited altimeter in the interior of the ice sheet using the so-called Low Resolution Mode (LRM). Over the more rugged terrain of the coastal margins of the ice sheet, it uses the Synthetic Aperture Radar Interferometric mode (SARIn). In addition to this novel interferometric mode, CryoSat-2 benefits from a high orbital inclination allowing measurements to be collected up to latitudes of $\pm 88°$ and from a long-repeat drift orbit (369-day, with a 30-day sub-cycle), which maximises the number of orbit crossovers at the poles (Wingham et al., 2006). We use CryoSat-2 Baseline D elevation measurements from the L2i product obtained by applying the on-board TCOG retracker (Davis, 1997) on the LRM waveforms in the interior of the ice sheet and the Wingham-Wallis retracker on the SARIn waveforms over the margins of the ice sheet. We correct the elevation measurements for dry tropospheric delay, wet tropospheric delay, ionosphere delay, solid Earth tide, ocean loading tide, and pole tide.

5.4 Methods and Results

In this section, we present the methodology we develop to derive surface elevation change, volume change, and mass change from CryoSat-2 elevation measurements in the Northwest sector and the resulting estimates of these three parameters. First, we derive surface elevation change using a least-square model fit and we validate the resulting rates of elevation change using airborne laser altimetry from Operation IceBridge. Using these elevation change data, we derive volume change and compare our results to airborne laser altimetry in the ablation zone, where airborne measurements are dense enough to measure volume change. Finally, we test different density scenarios to convert volume change to mass change and present our new mass balance estimate.

5.4.1 Ice Sheet Surface Elevation Change

We compute surface elevation changes from CryoSat-2 elevation measurements in square grids of 5 km x 5 km, 2500 m x 2500 m, and 10 km x 10 km to investigate the dependency of elevation changes to grid resolution. We fit a multi-parameter least-square model to the observed elevation measurements within each grid cell of the form:

$$z(x, y, t, s) = z_m + a_0 x + a_1 y + a_2 x^2 + a_3 y^2 + a_4 xy + a_5 s + a_6 t \qquad (5.1)$$

with z_m is the mean of the heights recorded by the satellite falling within the grid cell considered, x,y, the coordinates relative to the grid cell centre, s the heading of the satellite (ascending or descending orbit), and t the time relative to the centre of the time period.

The fitting is iterated until the modelled heights are within 2 standard deviations of the heights recorded by the altimeter or until only 15 measurements are left. The temporal change in elevation dh_{uc} is calculated from Eq. 5.1 for each surface height measurement z_{obs} acquired within the considered grid cell as:

$$dh_{uc}(t) = z_{obs} - (z_m + a_0 x + a_1 y + a_2 x^2 + a_3 y^2 + a_4 xy + a_5 s) \qquad (5.2)$$

Eq. 5.2 thus provides a time-series of elevation change within each grid cell calculated with reference to the centre of the time period so that $dh_{uc}(t = t_{mid}) = 0$. This elevation change

time-series is then adjusted using a backscatter correction to ensure that elevation changes correlated with backscatter changes are removed as they likely emerge from changes in the ice sheet surface properties rather than actual elevation changes (Davis and Ferguson, 2004). The corrected elevation change time-series $dh_c(t)$ within each grid cell is computed as:

$$dh_c(t) = dh_{uc}(t) - dBs(t)\frac{dh}{dBs} \tag{5.3}$$

where $dBs(t)$ is the time-series of backscatter change within the same grid cell and $\frac{dh}{dBs}$ is the slope of the linear fit between the elevation changes and backscatter changes

Finally, we derive rates of elevation changes (dh/dt) in each grid cell with a linear regression in time.

We correct our gridded rates of elevation change for the vertical crustal displacement induced by the solid Earth's response to ice mass variability. We correct for the combined effect of the solid earth's delayed response to past changes in ice distribution – called Glacial Isostatic Adjustment (GIA) – and of the viscoelastic response to present-day ice mass changes. The former correction is computed using the GIA simulation from Caron et al. (2018). The latter correction is calculated using Green's function ((Farrell, 1972) and requires knowledge of the recent ice mass changes. Here, we use as input the mass balance estimate computed in Section 5.4.3 of this chapter (and corrected for GIA). After the elastic uplift correction is computed, we iterate our mass balance estimation to include this new correction. In the Northwest sector, the GIA rate ranges from -2.8 mm yr^{-1} to 3.9 mm yr^{-1}, with an average subsidence rate of 1.1 mm yr^{-1}, while the elastic rebound rate ranges between 0.3 mm yr^{-1} and 15.7 mm yr^{-1}, with an average uplift rate of 2.4 mm yr^{-1}. Lastly, we estimate the uncertainty in dh/dt as the 1-sigma uncertainty from the fit, as it is more conservative than the uncertainty derived from the formal uncertainties. Figure 5.1 illustrates the processing applied in a SARIn and in a LRM grid cell.
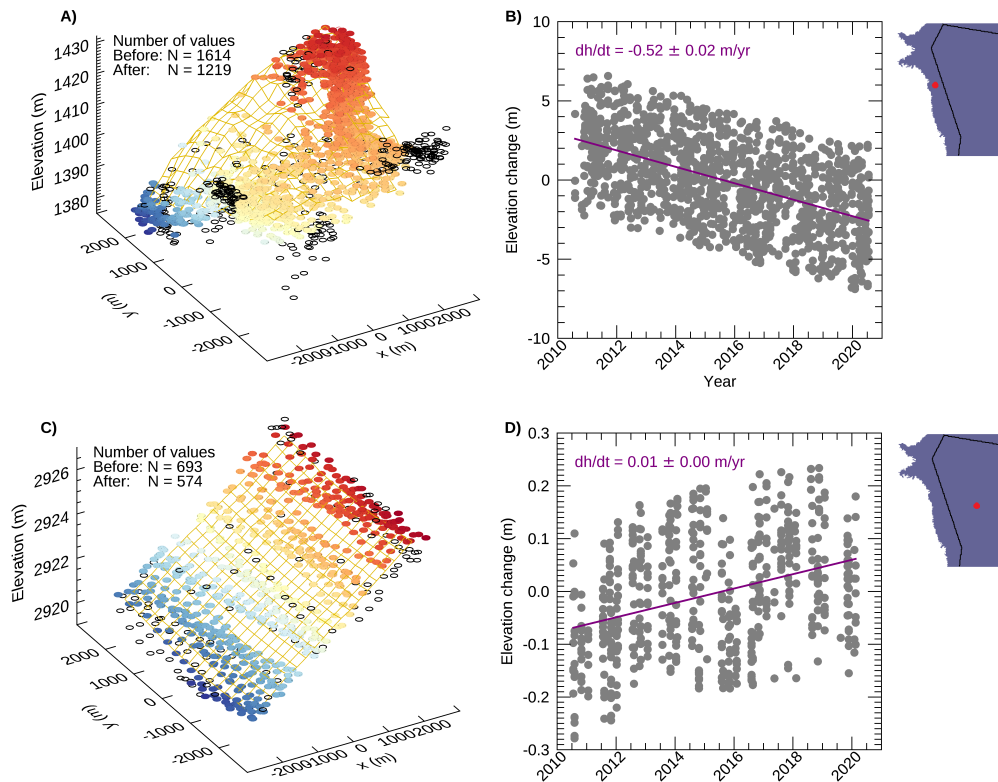
Figure 5.1: Example of the plane fit method in one 5 km x 5 km grid cell located in the SARIn area (top row) and LRM area (bottom row). a) and b) Modelled surface from the plane fit and CryoSat-2 surface elevation measurements. The circles represent the CryoSat-2 surface elevation measurements used in the plane fitting process. The coloured circles represent the surface heights retained after the different iterations and the black circles the points excluded. The x and y coordinates refer to the middle of the grid cell. b) and d) Time-series of elevation changes with respect to the centre of the time period ($t_{ref} = 2015.5$) for the same grid cells. The linear fit and elevation change rate are indicated in purple. The location of the grid cells is marked by the red circle and the boundary between LRM and SARIn areas is marked by the black line on the inset maps.

In addition to gridded rates of elevation change, we produce elevation change time-series within 60-day epochs at the sector and glacier drainage basin level. For each grid

cell of the selected region and at each time step, we calculate the cumulative elevation change (with respect to the centre of the time-series) as the mean of the elevation change within the 60-day epoch and correct the resulting elevation change for GIA and elastic uplift. The magnitude of the solid earth corrections at each time step is computed as the uplift/subsidence rate multiplied by the epoch duration, assuming that the GIA and elastic rebound rates are constant over the study period. We then take the final elevation change of the total area at each time step as the mean of the grid cells contributing to the area of interest. At each epoch (except at the very beginning of the CryoSat-2 record during its commissioning phase), almost 40 %, 70 % and 90 % of the Northwest sector is surveyed – compared to only 20 %, 40 % and 60 % over 30-day epochs at grid resolutions of 2.5 km, 5km and 10 km, respectively. We fill in the elevation change map using an inverse distance weighting interpolation with a radius of 25 km and a power of 2. There is a trade-off between spatial and temporal samplings: shorter epochs offer the advantage of preserving the short-term fluctuations in elevation change, while longer epochs offer the advantage of reducing the number of grid cells that need to be filled. Here, we choose an epoch duration of 60-day as a compromise between spatial and temporal samplings and to compare all three grid resolutions consistently, we select the same epoch duration for all three resolutions. This epoch choice is short enough to preserve the seasonality observed in elevation changes while limiting the unobserved areas. Figure 5.2 illustrates the choice of the epoch duration at 5 km. We find that not accounting for unobserved areas leads to an underestimation in total elevation change in the Northwest sector of 9.2 cm, 6.8 cm and 17.7 cm between 2010 and 2020 at 2.5 km, 5 km, and 10 km, respectively. Predecessors of CryoSat-2 and AltiKa have a repeat cycle and therefore the epoch duration should match the satellite cycle. In Chapter 3, we compute time-series of elevation change in the Amundsen Sea Sector from AltiKa and CryoSat-2 within 35-days epoch to match AltiKa repeat cycle. In Antarctica, Shepherd et al. (2019) have calculated elevation changes from CryoSat-2 within 3-month epochs as there are no seasonal fluctuations in elevation changes in Antarctica compared to Greenland. In Greenland, McMillan et al. (2016) and Nilsson et al. (2016) among others have derived elevation changes from CryoSat-2 at monthly

intervals.

Finally, the uncertainty in elevation change $\sigma_{dh,obs}$ at a surveyed grid cell (i,j) and epoch (t) is estimated as the combination of the errors arising from the noise at the grid cell level σ_{noise}, the backscatter correction σ_{ps}, the GIA correction σ_{gia}, and the elastic uplift σ_{ela} correction. We assume these sources of errors to be uncorrelated and sum them in quadrature as:

$$\sigma_{dh,obs_{i,j}}(t) = \sqrt{\sigma_{noise_{i,j}}^2 + \sigma_{pc_{i,j}}^2 + \sigma_{gia_{i,j}}^2 + \sigma_{ela_{i,j}}^2} \tag{5.4}$$

However, the combined GIA and elastic rebound corrections result in an alteration of the elevation change at each epoch smaller than 1 mm (0.2 mm) and we therefore neglect the uncertainty associated to the solid earth corrections. The uncertainty associated with the measurement imprecision is estimated as the standard error (SE) of the elevation change measurements within the grid cell and epoch considered. The uncertainty associated with the backscatter correction is computed as the standard error of the magnitude of the correction. Eq. 5.4 can then be written as:

$$\sigma_{dh,obs_{i,j}}(t) = \sqrt{SE[dh_{c_{i,j}}(t)]^2 + SE[dh_{c_{i,j}}(t) - dh_{uc_{i,j}}(t)]^2} \tag{5.5}$$

At unobserved grid cells – where we use an inverse distance weighting scheme to estimate the elevation change using the n grid cells located within a 25 km radius – we estimate the error $\sigma_{dh,interp}$ by cross-validation using the jackknife procedure (Quenouille, 1956). Similarly to the bootstrapping procedure, the jackknife procedure is a resampling technique; however it proceeds by omitting one observation from the original set instead of replacing it. Here, we repeat the interpolation n times, each time removing one data point in turn, and we calculate the standard error as the standard error of the resulting n jackknife estimates $\hat{dh}$ (each calculated using $n - 1$ grid cells):

$$\sigma_{dh,interp_{i,j}}(t) = \sqrt{\frac{n-1}{n}VAR(\hat{dh}_{i,j})} \tag{5.6}$$

Finally, to obtain a single error per epoch across the selected area, the errors from the N contributing grid cells at each epoch are propagated as:

$$\sigma_{dh}(t) = \frac{\sqrt{\sum_0^{N-1} \sigma_{dh_{i,j}}(t)^2}}{N} \tag{5.7}$$

Lastly, errors at each epoch are cumulatively summed in quadrature to get errors on the cumulative elevation change.
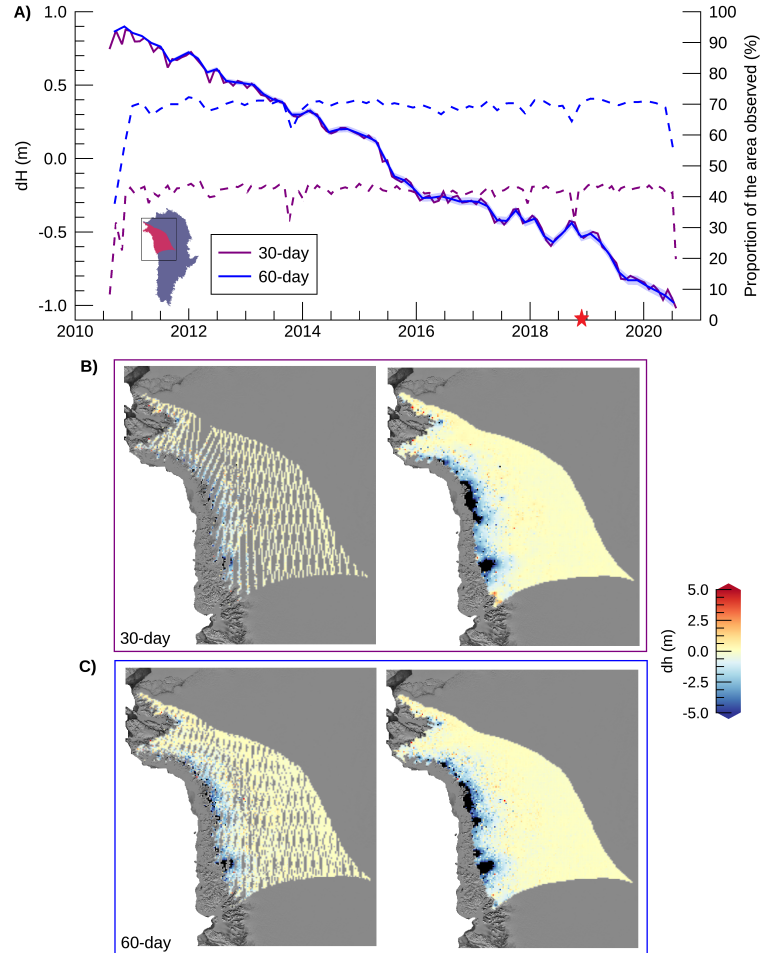
Figure 5.2: a) Elevation change time-series (with reference to the centre of the time period $t_{ref} = 2015.5$) and percentage of the Northwest sector area surveyed by CryoSat-2 using a 30-day and 60-day epochs. b) Example given at one epoch ($t = 2018.77$, marked with a red star on (a)). Map of the elevation change between $t = 2018.77$ and t_{ref} and same version of this map but interpolated with inverse distance weighting at 30-day epoch and 60-day epoch, respectively. c) Same as (b) but using a 60-day epoch. The inset on (a) shows the location of the Northwest sector.

Over the Northwest sector, the average surface lowering rate was 18.7 $\pm$ 0.4 cm yr^{-1} between 2010 and 2020 (Figure 5.3). All of the thinning is concentrated around the margins of the ice sheet, where the surface is lowering at a rate of 42.7 $\pm$ 0.9 cm yr^{-1} (SARIn mask, Figure 5.3b). On the other hand, elevation changes in the interior of the ice sheet are small and we record there a rate of elevation change of -0.3 $\pm$ 0.3 cm yr^{-1} (LRM mask, Figure 5.3c). While elevation changes around the margins of the ice sheet are largely dominated by the thinning of outlet glaciers, changes in the interior of the ice sheet arise due to a combination of snowfall accumulation and fluctuations in radar penetration depth. The radar signal can penetrate in the firn up to several meters below the snow surface and is therefore sensitive to any ice lenses in the structure of the near surface firn resulting from strong melt events as seen in Chapter 4 of this thesis. We find an elevation change increase of 25 cm in the LRM region after the 2012 melt event, due to the formation of an ice lens that shifted the main scattering horizon upwards (Nilsson et al., 2015). However, these fluctuations are short-lived and, over the course of a decade, cancel out each other. Several procedures have been implemented to correct for the effect of the 2012 melt event, including applying an empirical step change correction (McMillan et al., 2016) or a deconvolution procedure to the radar waveforms to estimate and correct for the penetration depth (Slater et al., 2019). However, as we expect the scattering horizon to recover progressively over the course of a decade, applying a step change function to correct for the effect of the 2012 melt event would only be appropriate when looking at short time periods within only a couple of years after the melt event. Applying a deconvolution procedure to the LRM CryoSat-2 data is out of the scope of this chapter as we only focus on Level-2 data.
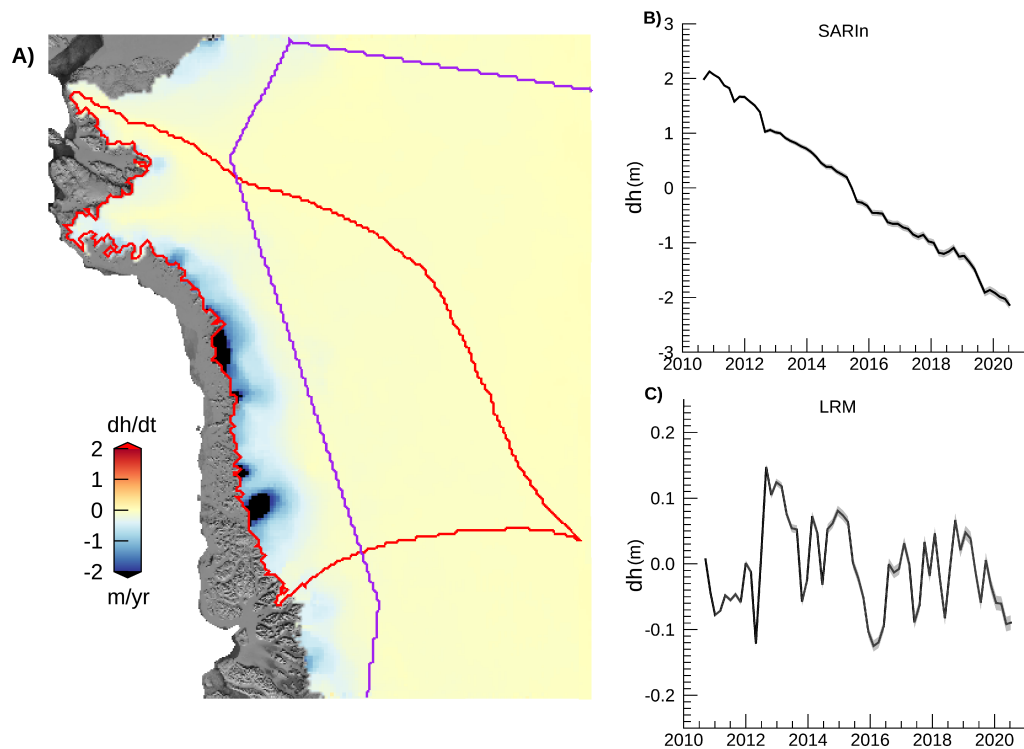
Figure 5.3: a) CryoSat-2 surface elevation change rates from 2010 to 2020. The purple line marks the boundary between SARIn and LRM modes of CryoSat-2. The red line marks the boundary of the Northwest Greenland region used in this chapter. The map has been smoothed using a 25 km x 25 km median filter for better visualisation. b) Elevation change time-series over the SARin area of the Northwest sector. c) Elevation change time-series over the LRM area of the Northwest sector. The elevation change time-series refer to the centre of the survey time period.

To evaluate the rates of surface elevation changes determined from CryoSat-2 (Figure 5.3a), we compare them to independent estimates derived from NASA's Operation IceBridge airborne topographic mapper (ATM). We use rates of elevation changes from Operation IceBridge (Product IDHDT4 provided by the National Snow and Ice Data Center (NSIDC)), which are derived from overlapping or crossing flight lines flown during two different annual campaigns (Figure 5.4) (Studinger, 2014, updated 2018*b*).
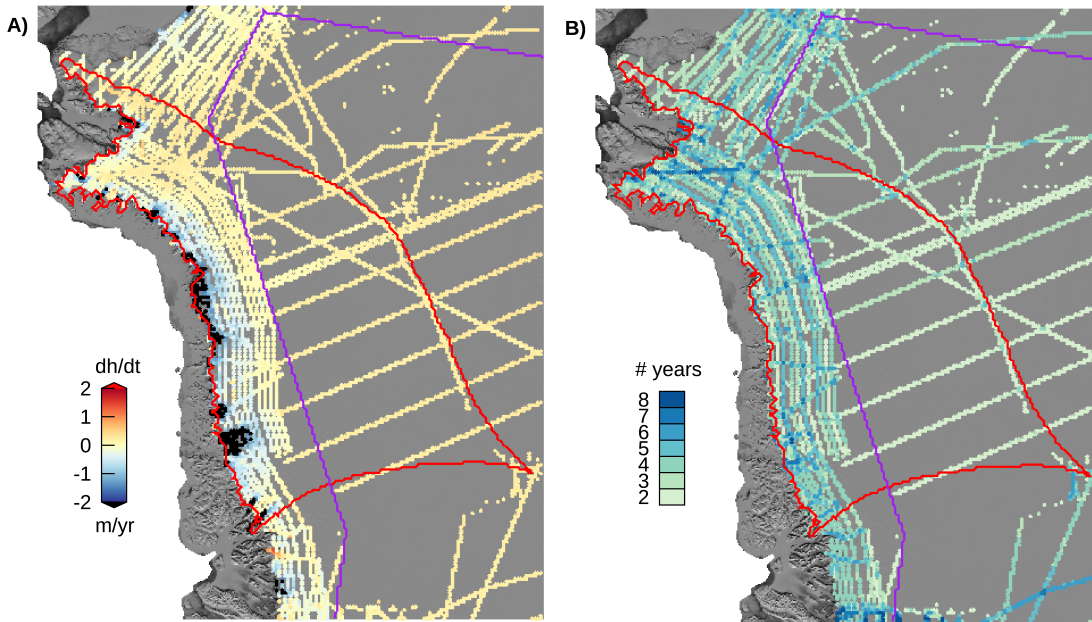
Figure 5.4: a) Operation IceBridge surface elevation change rates computed from surveys conducted between 2010 and 2018. b) Number of years during which at least one airborne survey was conducted.

As Operation IceBridge campaigns are typically conducted between March and May of each year with additional summer surveys conducted in 2015, 2016 and 2017, the resulting elevation rates are typically computed over shorter time periods than those derived from CryoSat-2. In addition, the airborne data are of inferior temporal sampling by comparison to CryoSat-2, which records elevation measurements all year long. To ensure that we compare airborne and satellite surface elevation rates computed over the same time intervals, we limited the CryoSat-2 elevation change time-series to the periods used in the derivation of the airborne laser rates. To do this, we fitted first-, second- and third-degree polynomial functions in time to the CryoSat-2 elevation data and selected the order that resulted in the lowest root-mean-square (RMS) departure. Rates of elevation change were then computed as the slope between the polynomial fits at the start and end dates used in the computation of the Operation IceBridge rates of elevation change. We then use this set of CryoSat-2 elevation change rates to compare to Operation IceBridge data.

5. CHANGES IN NORTHWEST GREENLAND ICE SHEET ELEVATION AND MASS

In total, it was possible to compare CryoSat-2 and Operation IceBridge rates of elevation change within 3,331 grid cells distributed across the Northwest sector. The majority (72 %) of grid cells were located in the SARIn mask of CryoSat-2, and the remainder fell within the LRM mask (Figure 5.5a). A first-order (linear) polynomial fit was selected over 49 % of the grid cells, and a quadratic fit was selected over the remaining 51 % because the cubic fit systematically resulted in higher RMS departure (Figure 5.5b). We find a good agreement between satellite radar and airborne laser data with a mean difference of 6.5 ± 0.5 cm yr^{-1} and a standard deviation of 31.1 cm yr^{-1} (Figures 5.5c and 5.5d). When comparing over the LRM and SARIn regions separately, we find mean differences of 3.1 ± 0.2 cm yr^{-1} and 7.8 ± 0.7 cm yr^{-1}, respectively. This level of agreement is consistent with previous studies, with McMillan et al. (2016) reporting a mean difference to Operation IceBridge of 3 cm yr^{-1} and Simonsen and Sorensen (2017) a mean difference of 9 cm yr^{-1} across the whole Greenland Ice Sheet between 2010 and 2014.
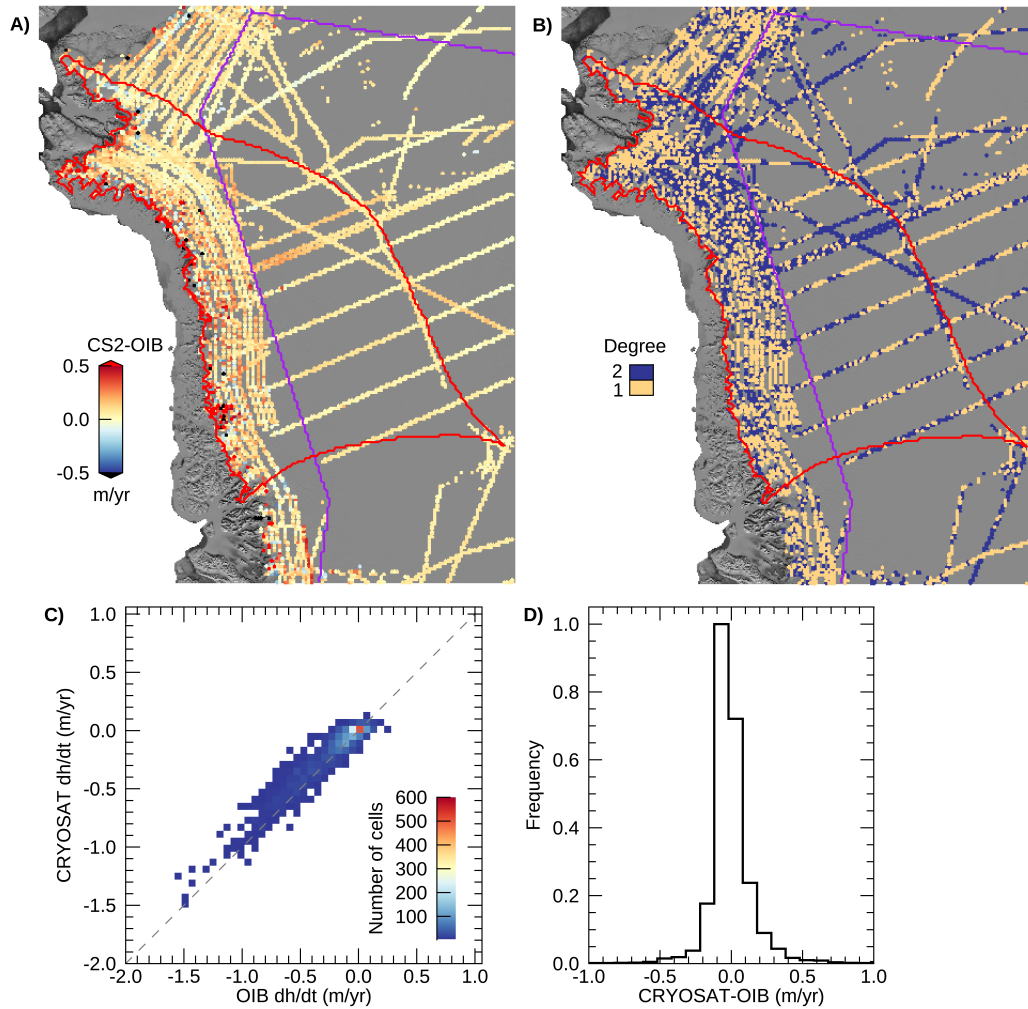
Figure 5.5: a) Difference in surface elevation change rates between CryoSat-2 satellite radar altimetry and Operation IceBridge airborne laser altimetry. b) Map indicating whether a linear fit or quadratic fit was applied to the CryoSat-2 elevation change time series. c) Scatterplot of CryoSat-2 and Operation IceBridge rates of elevation change over the Northwest sector. d) Histogram of the difference between Cryosat-2 and Operation IceBridge rates of elevation change over the Northwest sector.

5.4.2 Ice Sheet Volume Change

We compute volume change, dV, from CryoSat-2 by multiplying elevation change recorded within each grid cell (i,j) by the corresponding grid cell area A at each epoch t:

$$dV_{i,j}(t) = A_{i,j}.dh_{i,j}(t) \tag{5.8}$$

The associated uncertainty is simply derived by multiplying the uncertainty in elevation change by the grid cell area:

$$\sigma_{dV_{i,j}}(t) = A_{i,j}.\sigma_{dh_{i,j}}(t) \tag{5.9}$$

We record a total volume change of 496.4 $\pm$ 4.1 km^3 between 2010 and 2020 in the Northwest sector. We further examine the volume change spatial distribution by dividing the Northwest sector into three elevation bands (Figure 5.6). At elevations below 2000 m, volume change is most important due to the thinning of the outlet glaciers and accounts for 92.7 % of the sector's total volume change, with a volume change rate of -49.8 $\pm$ 0.6 km^3 yr^{-1}. At elevations ranging between 2000 m and 2700 m, volume change is only a small portion (4.6 %) of the sector's total volume change with a volume change rate of -1.6 $\pm$ 0.3 km^3 yr^{-1}. At elevations higher than 2700 m, we find that the area is stable with a volume change rate of 0.2 $\pm$ 0.1 km^3 yr^{-1}.
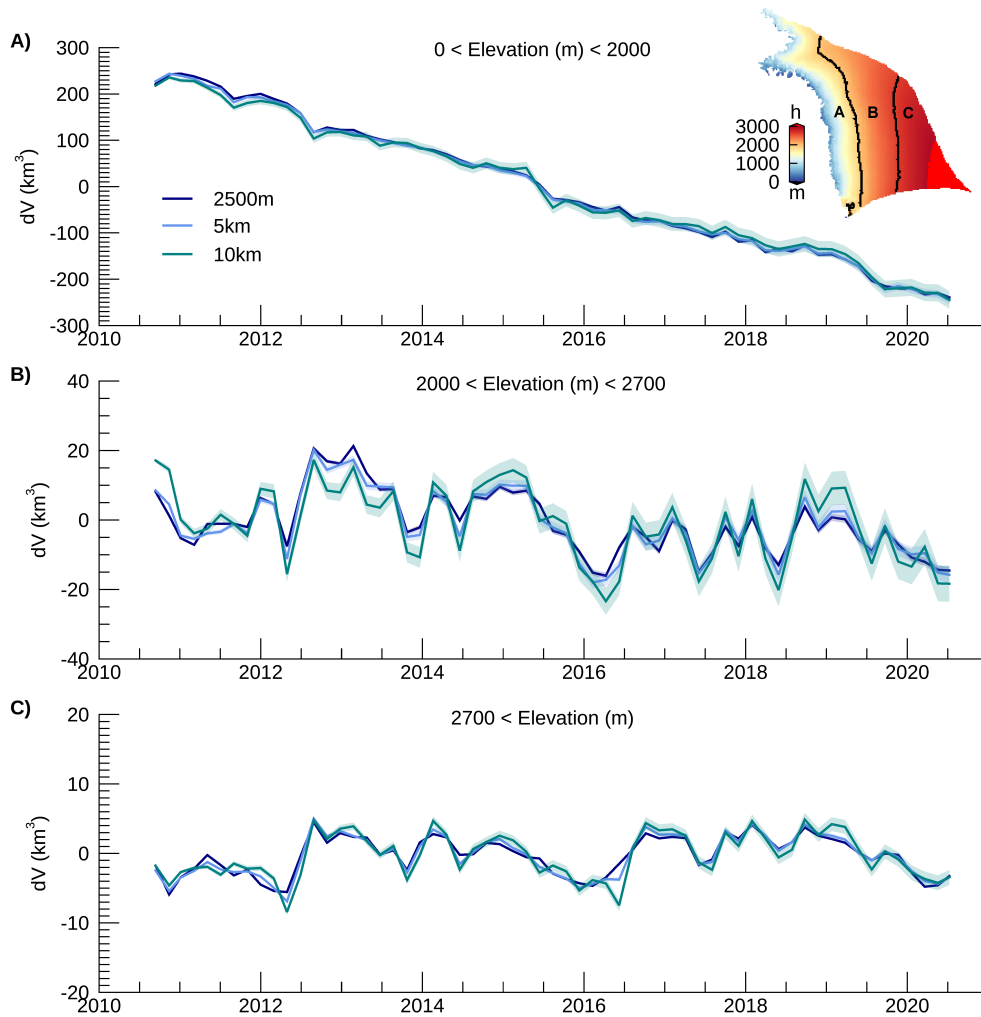
Figure 5.6: Volume change time-series from CryoSat-2 over three elevation bands processed at different grid resolutions (2.5 km (blue), 5 km (sky blue), 10 km (teal)). Associated uncertainties are shown by the corresponding coloured shaded envelopes. a) at elevation below 2000 m, b) at elevations between 2000 m and 2700 m, c) at elevations higher than 2700 m. The inset map on (a) shows the elevation in the Northwest sector and the three different elevation bands defined.

We compare volume change derived from CryoSat-2 with Operation IceBridge data in the ablation zone where the laser airborne measurements are dense enough to derive

volume change (Figure 5.7). We define the ablation zone as the area where the mean annual surface mass balance from 2010 to 2020 is negative, using surface mass balance data from the regional climate model MAR (Modèle Atmosphérique Régional, version 3.10). The ablation zone covers 16 % of the Northwest sector, with the main part located along the coastal margins and the remainder at the northern tip of the sector.
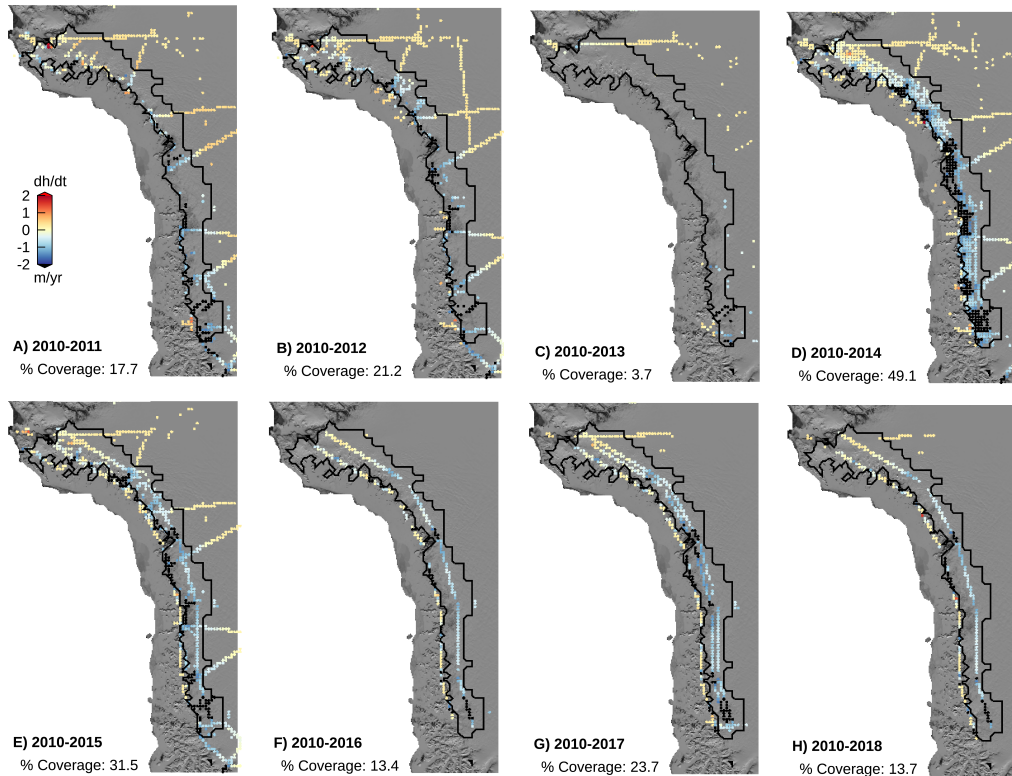
Figure 5.7: Operation IceBridge rates of elevation change maps interpolated with least-square collocation computed a) between 2010 and 2011, b) between 2010 and 2012, c) between 2010 and 2013, d) between 2010 and 2014, e) between 2010 and 2015, f) between 2010 and 2016, g) between 2010 and 2017, h) 2010 and 2018. The black line marks the ablation zone. The proportion of the area sampled by Operation IceBridge is indicated on each map.

We derive a volume change time-series from Operation IceBridge measurements at two grid resolutions (1 km x 1 km and 5 km x 5 km) from rates of elevation change com-

puted from pairs of annual campaigns, taking the 2010 campaign as reference. Operation IceBridge elevation change maps cover between 13 % to 49 % of the main coastal ablation region, except for elevation changes computed between 2010 and 2013 which cover only 4 % of this area and that we therefore exclude from the final volume change time series. We interpolate the Operation IceBridge rates of elevation change maps using least-square collocation similarly to Nilsson et al. (2016). Finally, we derive volume change from Operation IceBridge by multiplying the rates of elevation change by the time interval separating the two campaigns and the corresponding grid cell area. The associated uncertainty is derived as the standard error of the elevation change across the area, multiplied by the grid cell area. Despite covering only a small portion of the sector (13.2 %), the main ablation region over which we perform the comparison between CryoSat-2 and Operation IceBridge volume change estimates is the region where 64.6 % of the sector's total volume change is recorded. Furthermore, as changes in the ablation zone occur at the density of ice, any disagreement between satellite radar and airborne altimetry volume change estimates are important to consider as it would lead to a large bias in mass change.

We find a good agreement between CryoSat-2 and Operation IceBridge volume change measurements over the coastal ablation zone (Figure 5.7). We find volume change rates of -36.8 $\pm$ 0.5 km^3 yr^{-1}, -35.5 $\pm$ 0.6 km^3 yr^{-1}, -34.6 $\pm$ 0.8 km^3 yr^{-1} from CryoSat-2 at 2.5 km, 5 km and 10 km grid resolution and volume change rates of -36.1 $\pm$ 0.3 km^3 yr^{-1} and -36.4 $\pm$ 1.4 km^3 yr^{-1} from Operation IceBridge at 1 km and 5 km grid resolution between 2011 and 2018, respectively.

We note that volume change estimates from both datasets show a slight dependency on the resolution of the grid used, becoming more negative with finer scale resolution grids. This suggests that both datasets could be undersampling changes in the area as using larger grid cell sizes could average out some important small-scale spatial variations in elevation and volume change. Based on this comparison, we choose to keep the CryoSat-2 estimates computed at the finer resolution grid (2500 m x 2500 m) as it is in closest agreement with the airborne altimetry data and is likely to minimize the issue of the undersampling compared to the other grid resolutions used in this chapter. Furthermore, as many glaciers

in the Northwest sector are of relatively small drainage area (40 smaller than 1000 km^2), a finer grid resolution is better suited to observe changes at these small outlet glaciers. However, this analysis is limited by the reduced temporal sampling and spatial coverage of the airborne laser altimetry dataset compared to our satellite radar altimetry dataset. Our volume change estimates from Operation IceBridge are computed annually (compared to bi-monthly for CryoSat-2) and have been heavily interpolated spatially across this region, which could therefore bias our volume change estimates from airborne laser altimetry.
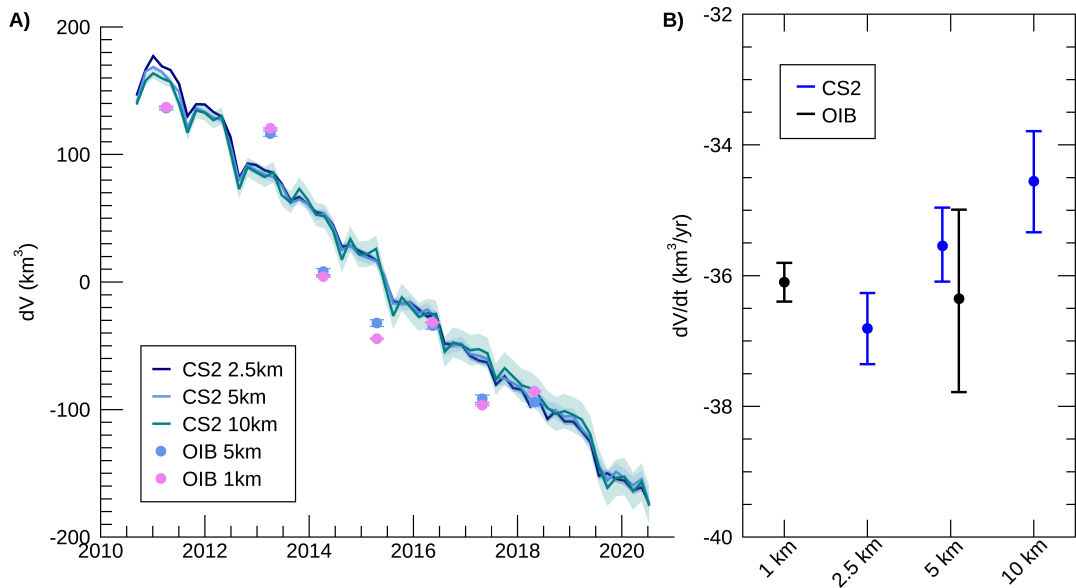
Figure 5.8: a) Volume change time-series over the coastal ablation region from CryoSat-2 and Operation IceBridge processed at different grid resolutions. CryoSat-2 time-series are displayed with coloured lines and the associated uncertainties are shown by the corresponding coloured shaded envelopes. Operation IceBridge time-series are displayed with coloured dots. b) Volume change rates (CryoSat-2 in blue and Operation IceBridge in black) versus spatial resolution of the grid used. Associated errors are shown with error bars.

5.4.3 Ice Sheet Mass Change

Finally, we derive mass change, dM, from CryoSat-2 volume change within each grid cell as:

$$dM_{i,j}(t) = \rho_{i,j}(t).dV_{i,j}(t) \qquad (5.10)$$

To estimate mass change, the density ρ associated with the volume change needs to be estimated. We assume that all volume changes in the ablation zone occur at the density of ice (917 kg m^{-3}) and we test three different density model approaches for the interior of the ice sheet (Models 1, 2, and 3), illustrated on Figure 5.9. In Model 1 we simply assign the interior of the ice sheet to the density of snow (450 kg m^{-3}). In Model 2, we further divide the interior of the ice sheet into percolation and dry snow zones based on the intensity and frequency of melting. We define the dry snow zone over the area where melting does not exceed 5 mm water equivalent on any day using MAR model outputs from 2010 to 2020 but excluding 2012 in this record, as exceptional melting extended up to the dry snow during summer 2012 (Nghiem et al., 2012). The remainder of the interior of the ice sheet is defined as the percolation zone. The dry snow zone covers only 4 % of the Northwest sector, while the percolation covers 80 % of this sector. We assign the percolation and dry snow zones to densities of 488 kg m^{-3} and 400 kg m^{-3} respectively, following (McMillan et al., 2016). In Model 3, we allow the density in the interior of the ice sheet to vary in time and space based on the density output from MAR. However, MAR densities are only available up to September 2020 and therefore we only compute mass change from Model 3 until this date. At each epoch, we compute the integrated density of the first top meter of the firn column within each grid cell to convert CryoSat-2 volume change to mass change.

The uncertainty in mass change, σ_{dM}, is computed based on the uncertainty in volume change defined in the previous section (itself derived from the uncertainty in elevation change from Section 5.4.1) and from the uncertainty in density as:

$$\sigma_{dM_{i,j}}(t) = |dM_{i,j}(t)|.\sqrt{(\frac{\sigma_{dV_{i,j}}(t)}{dV_{i,j}(t)})^2} \qquad (5.11)$$

For Models 1 and 2, we define the uncertainty associated to the density σ_ρ as the standard

deviation of the top 1-m of the firn column density from MAR in each of the defined facies of the sector. We find standard deviations of 114.1 kg m^{-3}, 63.8 kg m^{-3}, 65.3 kg m^{-3} and 3.8 kg m^{-3} for the ablation, interior of the ice sheet, the percolation and dry snow zones, respectively. For Model 3, we define the uncertainty in the density at each epoch in a similar manner as the standard deviation of the 1-m firn column density within each grid cell. Using temporally and spatially variable densities (Model 3) to compute mass change from volume change results in higher mass losses than when assigning fixed densities over the different facies of the Northwest sector (Models 1 and 2). We note however that based on our findings in Chapter 4, the standard deviation might be an underestimate of the density error, especially in some parts of the ice sheet. We have shown in Chapter 4 that the densities from MAR in West Central Greenland are overestimating the firn density by 21 % in the lower percolation zone and underestimating the density by 11 % in the higher percolation zone compared to in-situ firn cores.
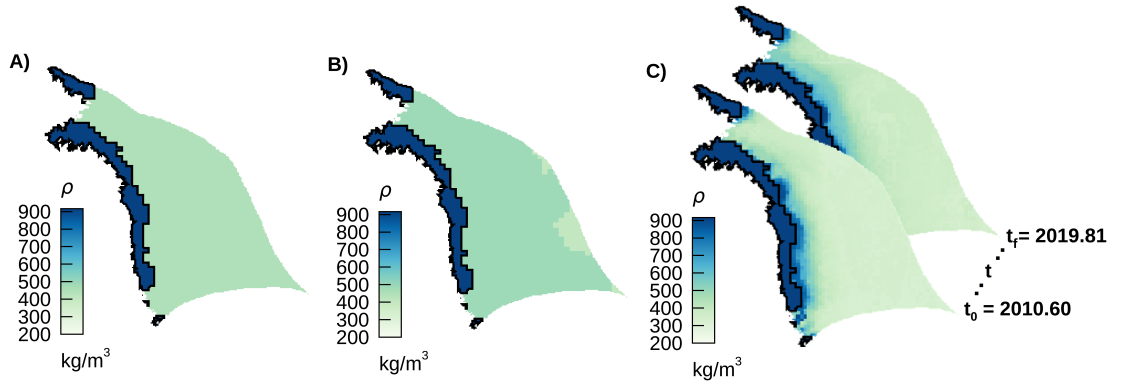
Figure 5.9: Illustrations of the three density models defined in this study. a) Model 1 assigning the interior of the ice sheet to the density of snow, b) Model 2 further partitioning the interior of the ice sheet into percolation and dry snow zones, c) Model 3 using time- and space-varying densities from MAR. The black line marks the extent of the ablation zone where the density is set to that of ice in all three models.

We compute mass change over the Northwest sector using these three density models. We find that the Northwest sector has lost mass at a rate of 40.5 $\pm$ 0.6 Gt yr^{-1}, 41.1 $\pm$

0.6 Gt yr^{-1}, and 41.3 $\pm$ 0.6 Gt yr^{-1} between July 2010 and September 2019 from Models 1, 2 and 3, respectively. The first two density models offer the advantage, by relying on fixed densities, of not requiring up-to-date densities from an external firn densification models. On the other hand, they ignore the spatial and temporal variability in firn density. Furthermore, as in recent years melting has increased at the surface of the Greenland Ice Sheet, the division of the ice sheet into ablation, percolation and dry snow zones might not be valid anymore as it has been observed that melt has extended up to the dry snow zone in 2012 for example (Nghiem et al., 2012). We therefore select Model 3 as our final estimate of mass balance.

We further examine CryoSat-2 mass change in each of the different glacier basins (except for one basin that is smaller than 6.3 km^2) to be resolved within our CryoSat-2 mass balance solution (Figure 5.10). Between July 2010 and July 2019, the Northwest sector has lost a total of 386.0 $\pm$ 3.7 Gt, with all glaciers losing ice over this period. The largest losses are recorded at Upernavik-Isstrom-N (-4.6 $\pm$ 0.2 Gt yr^{-1}), followed by Steenstrup-Dietrichson (-2.9 $\pm$ 0.1 Gt yr^{-1}) and Kjer Gletscher (-2.9 $\pm$ 0.1 Gt yr^{-1}). We find that between the 2011-2014 period and the 2014-2017 period, ice losses increased by 8.2 % and have stabilized over the 2017-2020 period. The largest increase in mass loss occurred at Hayes Gletscher-N-NN (+2.1 Gt), Kong Oscar Gletscher (+1.7 Gt), and Gade-Morell (+1.6 Gt) glaciers with an increase of more than 1.5 Gt between 2011-2014 and 2014-2017.
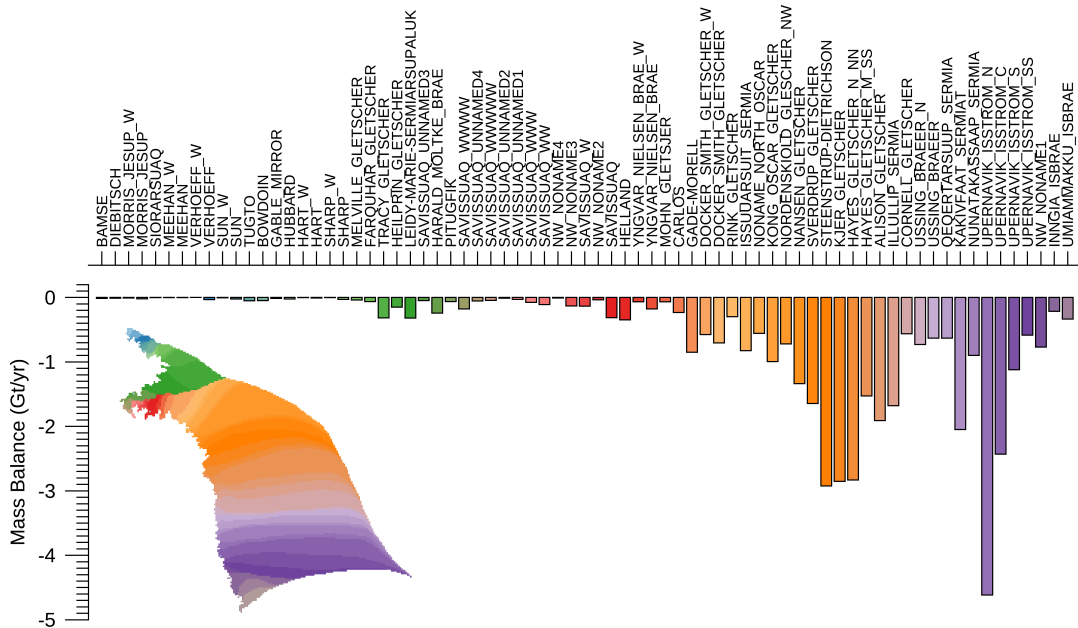
Figure 5.10: Mass change rate between July 2010 and July 2019 for each individual glacier drainage basin of the Northwest sector. The basins have been ordered by latitudes. The colours of the bars refer to the location of the basins as shown on the inset map.

5.5   Discussion

In this section, we compare our mass balance results to independent estimates from gravimetry and the mass budget method. We investigate the spatial variability of the differences in mass balance between these three geodetic techniques by looking at differences across different spatial scales. Finally, we identify potential sources of biases in our altimetry mass balance solution.

5.5.1   Comparison to Independent Estimates of Ice Sheet Mass Balance

We compare our mass balance solution with independent mass balance estimates from gravimetry from Groh and Horwath (2016) and the mass budget method from Mouginot et al. (2019) (Figure 5.11). These two independent estimates were computed using the

same basin delineations; however, both estimates include mass losses from Greenland's peripheral glaciers and ice caps (GICs) unlike our CryoSat-2 estimates. An estimate based on surface mass balance (SMB) modelling is available for GICs in the Northwest sector from Mouginot et al. (2019) and we thus add this signal to our CryoSat-2 time-series. Based on this estimate, the ice caps in the Northwest sector have lost ice at a rate of 1.3 ± 0.1 Gt yr^{-1}. Between July 2010 and July 2019, the mass budget estimate is the most negative with a mass change rate of -66.7 $\pm$ 1.0 Gt yr^{-1}, followed by the gravimetry estimate with a rate of -57.2 $\pm$ 2.2 Gt yr^{-1} and our CryoSat-2 estimate with a rate of -41.7 $\pm$ 0.2 Gt yr^{-1} (including the GICs).
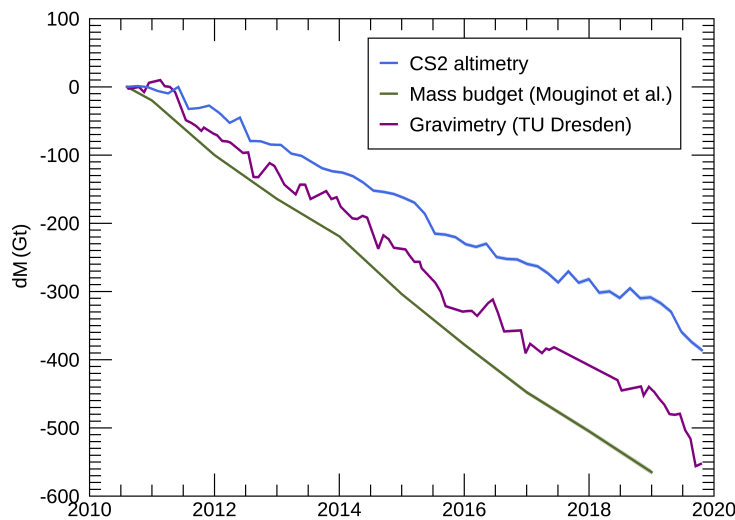
Figure 5.11: Time-series of mass change of the Northwest sector of the Greenland Ice Sheet since July 2010 from CryoSat-2 satellite altimetry, satellite gravimetry, and the mass budget method.

We further compare these mass balance estimates across different spatial scales in order to look at the spatial variability in the differences. First, we compare our altimetry solution to the gravimetry and mass budget estimates across the sector divided into two and four regions of similar size (Figure 5.12). For this comparison, we do not include the

5. CHANGES IN NORTHWEST GREENLAND ICE SHEET ELEVATION AND MASS

GICs in our CryoSat-2 estimate and in the mass budget estimate as we only have a mass balance estimate for the ensemble of GICs of the whole Northwest sector rather than a spatially varying estimate of the GICs. When divided into two regions, we found that CryoSat-2 underestimates mass losses across the two regions (Figure 5.12a). Gravimetry and the mass budget method are in close agreement in the southern region (region 2) with rates of -34.4 $\pm$ 1.1 Gt yr^{-1} and -32.3 $\pm$ 1.1 Gt yr^{-1} respectively but a large difference of 6.8 Gt yr^{-1} is recorded in the northern region (region 1). We further divide each of these two regions into two sub-regions to further isolate the areas exhibiting large differences (Figure 5.12b). In sub-region 1a, the gravimetry estimate is the most negative among all estimates, likely due to the inclusion of the large ice cap located in the northernmost part of the sector. In sub-region 1b, we find that CryoSat-2 and gravimetry both estimate a similar rate of mass loss of $\sim$10 Gt yr^{-1} while the rate of mass loss from the mass budget method is twice as large. This shows that most of the difference between gravimetry and the mass budget method recorded in region 1 actually originates from the southern half of this region (sub-region 1b). On the other hand, in sub-region 2a, CryoSat-2 and the mass budget method are in better agreement than with the gravimetry estimate. Finally, in sub-region 2b, CryoSat-2 largely underestimates mass losses compared to both gravimetry and the mass budget method. This comparison reveals that differences between estimates are highly variable spatially, suggesting that discrepancies between techniques do not solely originate from one single region or technique.
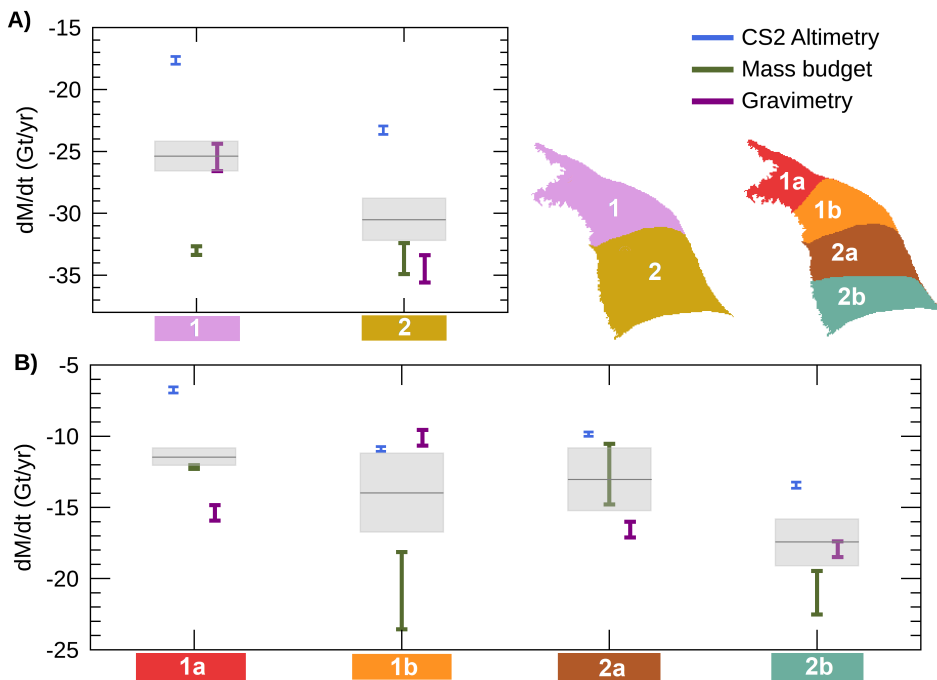
Figure 5.12: Comparison of CryoSat-2 altimetry, gravimetry and mass budget mass balance estimates in the Northwest sector divided into a) two and b) four parts. The different regions (1 and 2) and sub-regions (1a, 1b, 2a, 2b) defined in this comparison are shown on the inset maps. The grey box represents the reconciled mass balance estimate with the solid grey line indicating the average of the altimetry, gravimetry and mass budget mass balance estimates. The height of the grey box indicates the corresponding uncertainty calculated as the average of the three estimates' uncertainties.

Second, we compare mass balance estimates from CryoSat-2 altimetry and the mass budget method in each individual glacier basin as the higher resolution of these two techniques enable us to compute mass balance of individual glacier drainage basins. Differences between mass budget and altimetry estimates exceed 0.5 Gt yr^{-1} in 19 basins, with the mass budget method estimating larger ice losses than our CryoSat-2 estimate in 17 of these basins. The largest differences are recorded in Steenstrup-Dietrichson and Kjer Gletscher basins – the basins in which we have recorded the largest ice mass losses after Upernavik-

Isstrom-N according to our CryoSat-2 estimates – with differences of -4.4 Gt yr^{-1} and -3.0 Gt yr^{-1}, respectively (Figure 5.13). Overall, we find a correlation coefficient (r^2) of 0.81 between our CryoSat-2 estimates and the mass budget estimates (Figure 5.14a).
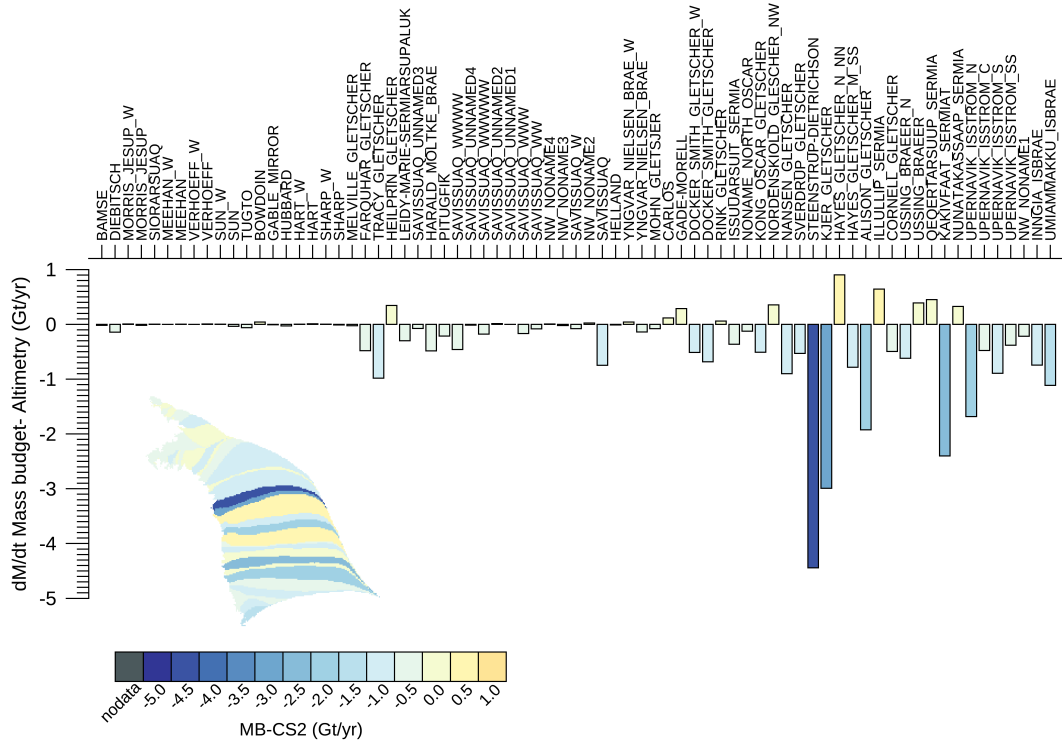
Figure 5.13: Comparison of mass change rates between CryoSat-2 altimetry and the mass budget method in the Northwest sector divided into individual glacier drainage basins. The colours of the bars refer to the difference in dM/dt between mass budget and altimetry estimates as shown on the inset map.

To investigate the origins of these differences, we examine which datasets were included in the compilation of the mass budget estimates. The ice discharge component of the mass budget is computed from observations of ice velocity and ice thickness change at a defined flux gate. However, in some basins, observations of ice velocity or thickness change are not always available and in the absence of data, steady state conditions are assumed, which could bias the discharge estimates. In Mouginot et al. (2019) dataset, no velocity

or thickness change data were used in the computation of the discharge estimates of 26 basins. 9 basins had velocity data but no thickness change data and 2 basins (Steenstrup-Dietrichson and Morris-Jesup) had thickness change data but no velocity data (Figure 5.14a). As we record the largest differences in Steenstrup-Dietrichson, we believe that the absence of velocity data in this basin could explain the large bias between the altimetry and mass budget method at this particular basin. If we remove Steenstrup-Dietrichson and Morris-Jesup estimates from this comparison, the correlation coefficient between our dataset and the mass budget method slightly increases to 0.83. We also examine whether the differences between the two methods could arise from a lack of CryoSat-2 observations close to the grounding line where ice losses are generally greater. To do this, we look at the area sampled by CryoSat-2 within 25 km from the coast as a measure of the spatial coverage of CryoSat-2 close to the grounding line (Figure 5.14b). In each glacier drainage basin, at least 30 % of the coastal area is sampled by CryoSat-2. Furthermore, in 68 out of 74 basins, at least half of the coastal area is surveyed by CryoSat-2, with this proportion reaching 75 % in 21 basins, suggesting that the spatial coverage of CryoSat-2 cannot be the only factor leading to significant differences with the mass budget method.
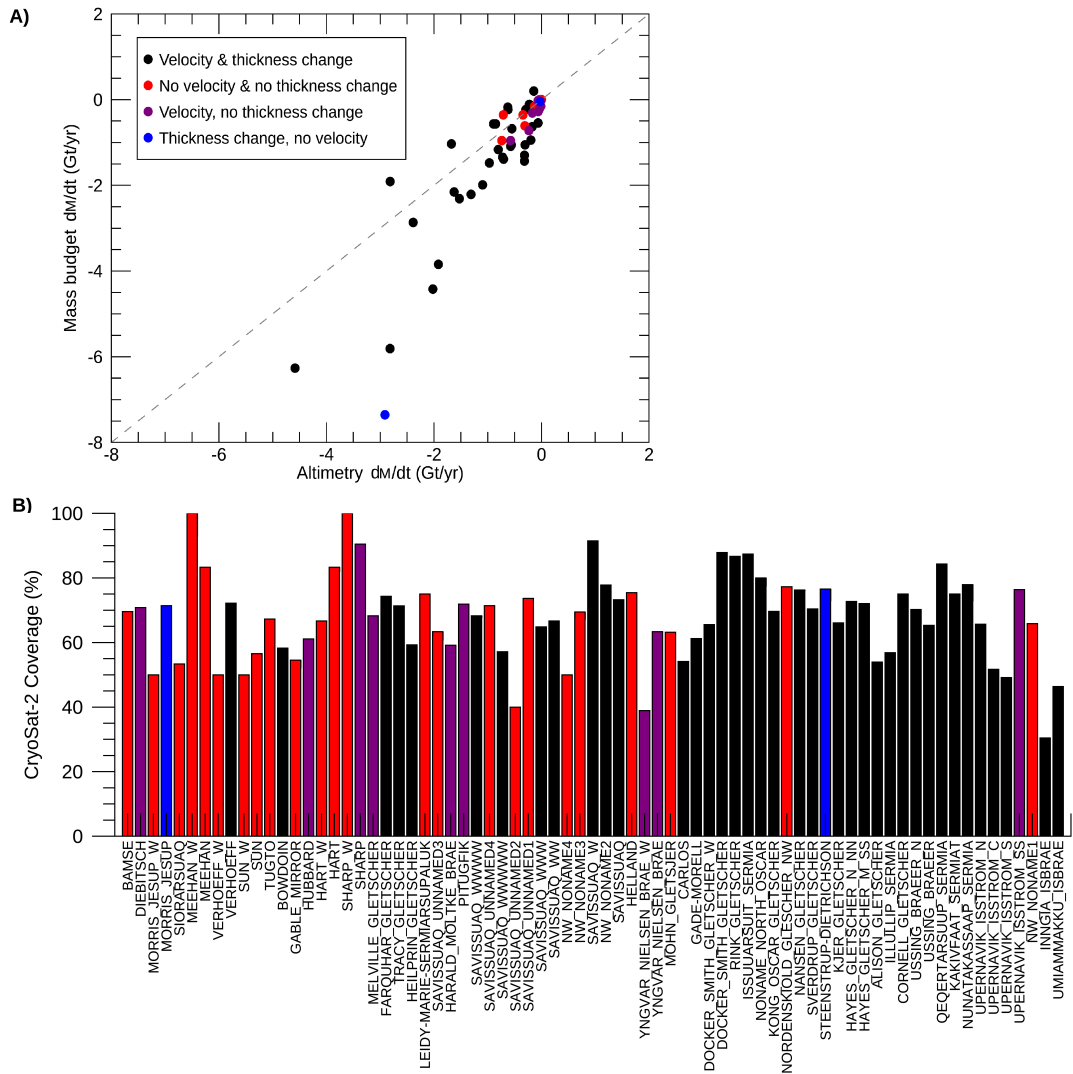
Figure 5.14: a) Scatterplot of mass change rates computed from the mass budget method and from our altimetry estimate. The colours of the points indicate what data were used in the computation of the corresponding mass budget estimate, b) Percentage coverage of CryoSat-2 within 25 km from the coast for each glacier drainage basin of the Northwest sector. The names of the basins have been coloured with the corresponding colour from the scatterplot.

5.5.2 Potential Sources of Bias

We have found that there are large differences between mass balance estimates derived from satellite radar altimetry, satellite gravimetry and satellite velocity measurements in the Northwest sector, with our CryoSat-2 estimate underestimating ice losses compared to the other two techniques. While other studies (Shepherd et al., 2020) have also found that mass balance estimates from satellite radar altimetry are generally less negative compared to other techniques, we outline here some potential sources of bias that could affect our mass balance estimate. Here, we discuss potential biases in our elevation, volume and mass change estimates.

While we have found an overall good agreement between satellite radar and airborne laser altimetry rates of elevation change with a mean difference of 6.5 ± 0.5 cm yr^{-1}, there remain important localized differences in the margins of the ice sheet that could therefore lead to a significant mass change underestimation in our CryoSat-2 solution. To estimate the magnitude of this potential underestimation, we interpolate the difference map between CryoSat-2 and Operation IceBridge rates of elevation change (Figure 5.5a) to produce an empirical correction of our CryoSat-2 rates of elevation change. We limit this analysis to the SARIn area where the airborne measurements are dense enough and where ice losses are concentrated. We find that this empirical correction leads to an additional volume change of 14.9 km^3 yr^{-1} across the SARIn area of the sector. We further convert this volume change to mass change by applying fixed densities from our density model 2 (as the empirical correction that we compute is not time dependent, we cannot apply our density model 3). This results in an additional mass loss of 11.8 Gt yr^{-1}, bringing our altimetry solution much closer to gravimetry and mass budget estimates. The origins of the differences between satellite radar and airborne laser altimetry remain to be explored and are out of the scope of this chapter but these differences likely originate from fluctuations in radar penetration into the snowpack, or from CryoSat-2 sampling issues in areas of high-relief topography. While this simple approach – based on the assumption that Operation IceBridge provides unbiased measurements of surface elevation changes compared to CryoSat-2 – ignores temporal variations in the bias between satellite radar

and airborne laser altimetry, it provides an indication of the impact such a bias would have on mass balance derived from satellite radar altimetry.

In this study, we have corrected our elevation change measurements for the solid earth's response to past and contemporary changes in ice load but we have found that the magnitude of the GIA and elastic uplift corrections is very small (less than 1 cm) and therefore are unlikely to lead to significant differences in mass balance. However, we have not corrected our elevation changes for the effect of firn compaction. Firn elevation changes due to firn compaction are not associated with a mass change and therefore need to be accounted for before converting volume to mass change using a firn density model. This correction is not included in this study as no up-to-date firn model outputs are available to compute this correction, but it has been estimated that this correction correspond to a volume change of -19 km^3 yr^{-1} for the whole of the Greenland Ice Sheet between 2003 and 2008 (Sørensen et al., 2011).

A key parameter in calculating mass balance from satellite altimetry is the density used to convert our observed volume change to mass change. Here, we have tested three density models in this chapter. However, we have found that using either of these density models leads to similar mass change rates with maximum differences of the order of 1 Gt yr^{-1}, which are insufficient compared to the magnitude of the differences with other mass balance estimates. Therefore, we conclude that while density is an important parameter, it cannot solely explain the underestimation of ice losses compared to gravimetry and the mass budget method.

Finally, when comparing ice sheet mass balance estimates, the inclusion of the peripheral glaciers and ice caps needs to be considered as not all techniques can isolate mass losses from the GICs. The gravimetry estimate includes the peripheral ice caps as they cannot be isolated from the ice sheet due to the coarse resolution of the GRACE and GRACE-FO sensors. We used the estimate from Mouginot et al. (2019) to include the GICs mass balance in our CryoSat-2 solution, however this estimate might be an underestimation of the GICs ice losses, as we have seen that in the northern half of the sector, differences between gravimetry and mass budget exceed this estimate. If the GICs contri-

bution is underestimated, it would bring the mass balance estimates from altimetry and the mass budget method closer to the gravimetry solution.

5.6   Conclusion

In this chapter, we derive surface elevation change, volume change and mass change from CryoSat-2 in the Northwest sector of the Greenland Ice Sheet between 2010 and 2020. We find that all glaciers have lost ice over this period with an overall rate of mass loss of 41.3 $\pm$ 0.6 Gt yr^{-1}. We compare our altimetry mass balance estimate to independent estimates from gravimetry and mass budget method. This comparison shows that mass losses measured from CryoSat-2 data are underestimated compared to the other techniques, which recorded a mass loss rate of -57.2 $\pm$ 2.2 Gt yr^{-1} and 66.7 $\pm$ 1.0 Gt Gt yr^{-1}, respectively. We further investigate differences between mass balance estimates spatially by splitting the Northwest sector into different regions and individual glacier drainage basins. Finally, we identify potential sources of biases in our estimation of elevation change, volume change and mass change from CryoSat-2. While there is a good overall agreement between satellite radar and airborne laser altimetry rates of elevation change, we find that local differences in the coastal margins of the ice sheet can lead to significant underestimation of ice sheet volume and mass change and could help explain the departure of the radar altimetry mass balance from the other geodetic techniques. However, this remains to be further explored by closely examining radar penetration fluctuations and satellite sampling against airborne laser altimetry data.

This page intentionally left blank.

CHAPTER 6

Conclusion, Synthesis and Future Work

The aim set at the beginning of this thesis was to improve our ability to detect and interpret changes in the elevation of Earth's polar ice sheets using satellite radar altimetry. In the preceding three chapters, I have met this aim using satellite and airborne Ka-band and Ku-band altimetry data to detect surface elevation and elevation changes across Antarctica and Greenland. In Chapter 3, I have shown that Ka-band satellite altimetry from AltiKa is fit to retrieve surface elevation and elevation change in West Antarctica. I demonstrated that AltiKa is detecting trends in elevation change similar to those derived from Ku-band satellite altimetry from CryoSat-2, apart in some specific areas of the ice sheet margins, such as the Getz ice shelf grounding line, where AltiKa struggles to sample the steep terrain compared to CryoSat-2. After demonstrating the ability of Ka-band satellite altimetry for measuring surface elevation changes, I examined the sensitivity of airborne radar data to surface melt and firn stratigraphy in West Central Greenland in Chapter 4 to assess their relative performance and to further explore differences between Ka- and Ku-band data. I investigated means of mitigating the impact of radar penetration fluctuations on retrieved surface heights and showed that applying threshold retracking methods results in surface heights in good agreement with coincident airborne laser altimetry data. Finally, in Chapter 5, I used a decade of CryoSat-2 Ku-band satellite altimetry data to detect

surface elevation changes in the Northwest sector of the Greenland Ice Sheet and estimate the mass imbalance of this region. Thanks to the long CryoSat-2 record and to its SARIn acquisition mode, which allows for dense observations in the margins of the sector where the topography of the terrain is complex, I further partitioned the mass change into the individual glacier basins of the Northwest sector, showing that all glacier basins lost ice during the past decade.

In this final chapter, I firstly summarise the main findings from each piece of work. I then present a synthesis of these findings and discuss their significance before underlining key areas of future work that have emerged from the results presented here.

6.1   Summary of Main Results

The different pieces of work comprised in this thesis are presented in the chronological order they have been undertaken. As the main priority of this thesis was to explore the potential of Ka-band altimetry data over the ice sheets, I started by assessing trends in surface elevation derived from Ka-band satellite altimetry against coincident Ku-band satellite and laser airborne data, before exploring differences between Ka- and Ku-band more closely using data from field campaigns in West Central Greenland. Finally, I used a decade of CryoSat-2 data to estimate the mass imbalance of the Northwest Greenland Ice Sheet. I compared estimates of elevation change from CryoSat-2 satellite altimetry and airborne laser altimetry in the Northwest sector of the Greenland Ice Sheet and produced a mass balance estimate in the individual glacier basins of this region by making use of the high temporal and spatial sampling of CryoSat-2. The later chapters of this thesis were developed based on the findings of the earlier chapters and inversely, with more time, the earlier chapters could also be revisited based on the knowledge gained from the later chapters.

6.1.1 Ice Sheet Elevation Change in West Antarctica from Ka-band Satellite Radar Altimetry

In Chapter 3, I assessed the potential of higher frequency Ka-band data for mapping elevation and elevation changes of the ice sheets. I used AltiKa Ka-band satellite altimetry data to derive surface elevation and elevation change in West Antarctica between 2013 and 2019, producing the first extensive map of West Antarctica surface elevation change from Ka-band satellite altimetry. Ka-band (36 GHz, 0.8 cm) has a reduced penetration depth compared to the traditional Ku-band (13.5 GHz, 2.3 cm) used by the other altimeters (Rémy et al., 2015). Given that the signal scatters closer to the surface at Ka-band than at Ku-band, the reduced penetration depth at Ka-band might potentially lead to more reliable surface elevation and elevation change measurements. I evaluated these estimates of elevation and elevation change through comparisons to airborne laser altimetry from Operation IceBridge. I showed that there is a good agreement in terms of surface elevation with a mean difference of 3.8 ± 0.5 m, which is half that of the difference when a slope correction is not applied. In terms of surface elevation change, the mean difference between Ka-band satellite altimetry and airborne laser altimetry is 0.6 ± 2.4 cm yr^{-1}. I further compared these estimates to CryoSat-2 Ku-band satellite altimetry and found that there are only minor differences in both elevation and elevation change with mean differences of 2.5 ± 0.1 m and 0.1 ± 0.1 cm yr^{-1}, respectively (Figure 6.1). This demonstrates that trends in radar penetration are minor in this sector of this ice sheet as differences between Ka-band and Ku-band satellite altimetry and airborne laser altimetry are small. The main challenge of using AltiKa for the study of the ice sheets is not related to its different penetration depth, but rather to its smaller antenna beam width ($0.6°$) and smaller range window (40 m against 120 m for CryoSat-2 operating in SARIN mode), which limits the number of valid elevation measurements acquired over the steep margins. This effect can be seen in some specific regions of the margins of the ice sheet, for instance along the Getz ice shelf grounding line, where AltiKa records 9 times fewer measurements than CryoSat-2. From this new Ka-band satellite altimetry dataset, I have shown that surface elevation is lowering at rates of 117 ± 10 cm yr^{-1} and 100 ± 20 cm yr^{-1} between 2013 and 2019 over

145

Pine Island and Thwaites Glaciers, respectively. Compared to surface elevation change recorded in the 2000s and estimated from ERS-2 and Envisat from Shepherd et al. (2019), the rate of surface lowering has risen by 43 % at Thwaites Glacier but has slow down by 9 % at Pine Island Glacier (Figure 6.1). The reduced pace of thinning of the main trunk of Pine Island Glacier was also later confirmed by Bamber and Dawson (2020) and has been linked to the weakening in the ocean forcing (Dutrieux et al., 2014).
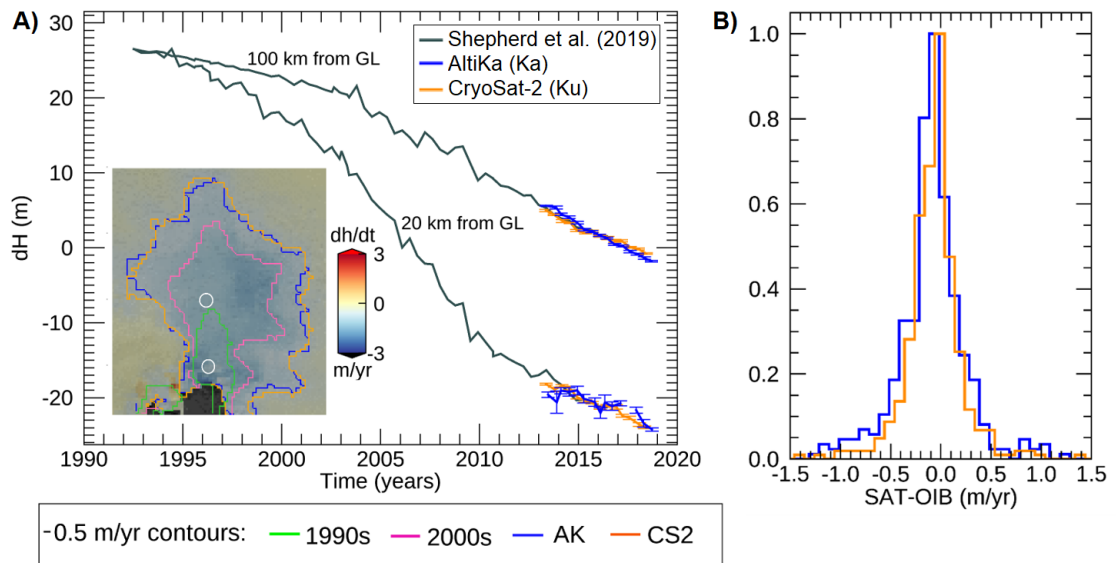
Figure 6.1: Time series of elevation change at a) Pine Island Glacier from AltiKa, CryoSat-2 and from a combination of ERS, Envisat, and CryoSat-2 data (Shepherd et al., 2019). The locations of the selected pixels are indicated by the white circles on the AltiKa map of average rate of elevation change in the insets. The 0.5 m yr^{-1} contours of rates of surface lowering from the 1990s, the 2000s and from the AltiKa and Cryosat-2 datasets used in this study are marked by the coloured lines on the maps. b) Histograms of the difference in rates of elevation change between satellite Ka-band and Ku-band radar and airborne laser altimetry from Operation IceBridge.

This work highlights the potential of Ka-band satellite altimetry for mapping changes in the surface elevation of the ice sheets. To further explore differences between Ka-band

and Ku-band data, my attention now turns to a close examination of a transect in West Central Greenland by analysing a decade of airborne radar and laser data in combination with in-situ firn density measurements and firn densification model outputs.

6.1.2 Correlated Fluctuations in Ku-band Airborne Radar Penetration and Surface Melting in West Central Greenland

In Chapter 4, I examined the spatial and temporal variability in Ku-band airborne radar profiles acquired over the EGIG line in West Central Greenland from data acquired during the ESA CryoVEx field campaigns between 2006 and 2017. By tracing annual melt layers in the radar profiles, I showed that there are large variations in the radar scattering horizon spatially – across the ablation, percolation and dry snow accumulation sections of the EGIG line – and temporally with high inter-annual variability. The largest fluctuations are found between 2012 and 2014, with a radar penetration depth reduction of 6.2 ± 2.4 m, owing to a shift of the main scattering horizon closer to the surface. Using firn cores collected during the field campaigns and modelled outputs from firn densification models, I demonstrated that these fluctuations are correlated with fluctuations in surface melting. After evaluating two firn densification models with in-situ firn density measurements – showing that they agree with RMSEs of 104 kg m^{-3} and 64 kg m^{-3} for MAR and IMAU-FDM, respectively – I linked the strong reduction in radar penetration observed after 2012 to fluctuations in firn density (Figure 6.2). The reduction in radar penetration depth coincides with a peak in summer density, which is twice the density from previous years, underlining the anomalous character of the 2012 melt event. While the impact of the 2012 melt event had been shown on CryoSat-2 satellite altimetry in the interior of the ice sheet (Nilsson et al., 2015; Slater et al., 2019), this piece of work provides the first direct evidence of the origins of these fluctuations by using a combination of airborne data, field data and outputs from firn densification models.

Fluctuations in radar penetration can have a large impact on retracked surface heights. Nilsson et al. (2015) showed that the 2012 melt event induced a step in elevation of 89 ± 49 cm in the dry snow zone of the Greenland Ice Sheet from CryoSat-2 satellite altimetry.
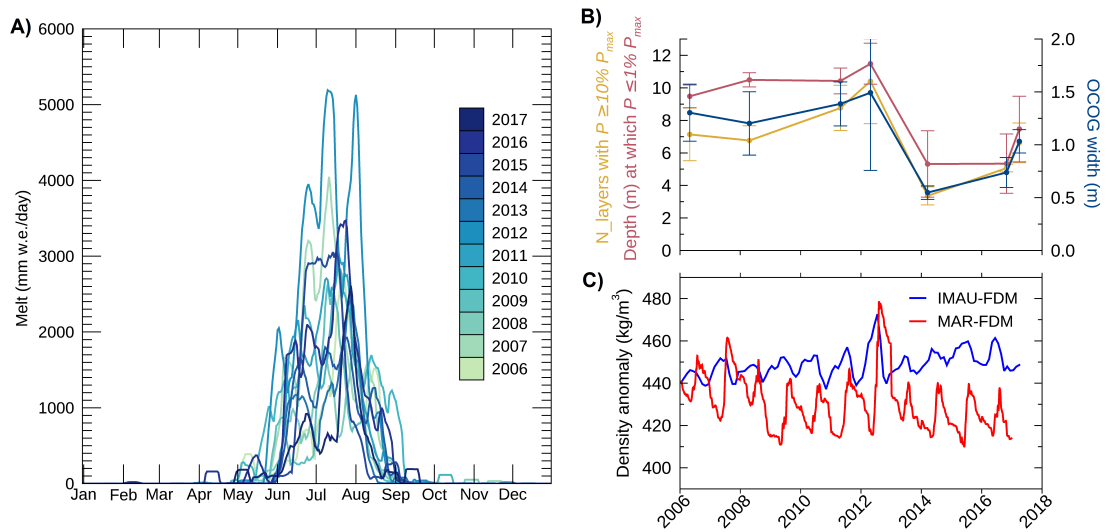
Figure 6.2: a) Total daily melt along the EGIG line from MAR regional climate model. A 10-day moving average has been applied to the time-series to reduce noise. b) Fluctuations in airborne Ku-band radar penetration shown by three parameters derived from radar echoes. c) Density anomaly from the MAR- and IMAU firn density models (FDM).

Several approaches have been proposed to mitigate this effect on CryoSat-2 satellite altimetry data, such as applying a deconvolution procedure to the radar waveforms to correct for penetration depth (Slater et al., 2019). Here, I assessed three different retrackers and their ability to mitigate fluctuations in radar penetration through comparisons to coincident airborne laser altimetry data. I showed that applying threshold retracking algorithms results in surface heights in good agreement within 13.9 cm from coincident laser data. I further investigated the potential of higher frequency Ka-band data as a means of mitigating the impact of fluctuations in surface melting on retracker surface heights. As Ka-band penetration depth is reduced compared to Ku-band, the impact of an anomalous melt layer on Ka-band data would last over shorter timescales compared to Ku-band. To verify this assumption, I investigated the sensitivity of Ka-band data to volume scattering fluctuations. Despite this analysis being limited to one year, I found that all three retrackers provide similar results – within 16 cm from the coincident laser data – suggesting that

Ka-band data are less sensitive to the choice of the retracking algorithm due to its reduced penetration depth (Figure 6.3).
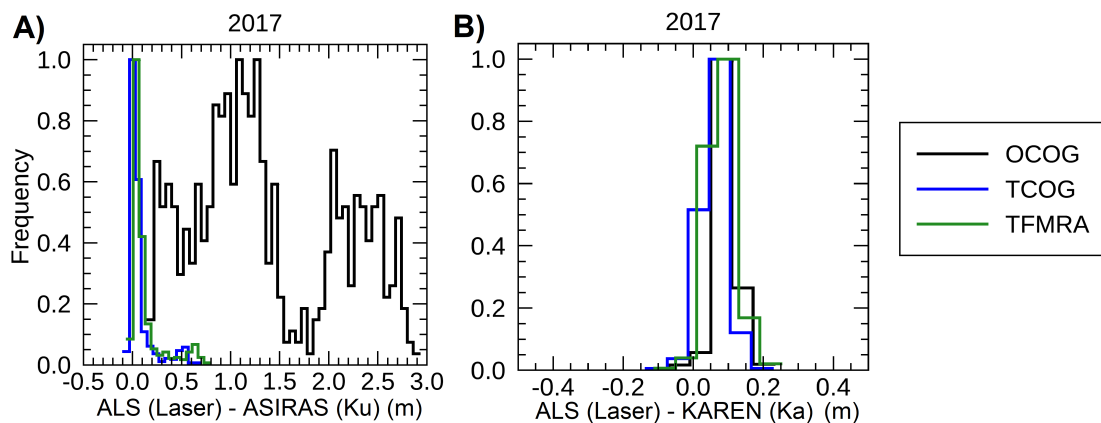
Figure 6.3: Histograms of the difference between airborne radar and airborne laser altimetry surface heights during the 2017 campaign. a) Airborne laser scanner - Ku-band radar ASIRAS, b) Airborne laser scanner - Ka-band radar KAREN. The radar data were retracked using three different retracking algorithms (OCOG, TCOG and TFMRA) indicated by the coloured lines.

In that chapter, I showed that there are large fluctuations in radar penetration but that threshold retracking methods can be effectively applied to mitigate the impact of these fluctuations on retracked surface heights. In the following chapter, I compared surface elevation changes from CryoSat-2 Ku-band satellite altimetry and Operation IceBridge airborne laser altimetry in Northwest Greenland and estimated the mass balance of this sector. I further compared this altimetry mass balance estimate to independent estimates from gravimetry and the mass budget method and investigated the potential sources of discrepancies between the different techniques.

6.1.3 Changes in the Elevation and Mass of the Northwest Sector of the Greenland Ice Sheet

In Chapter 5, I derived surface elevation change from a decade of CryoSat-2 satellite altimetry data between 2010 and 2019 in the Northwest sector of the Greenland Ice Sheet. The Northwest sector is the only region of the Greenland Ice Sheet that has experienced sustained acceleration in ice discharge since the early 2000s (King et al., 2020), triggered by ocean forcing (Wood et al., 2021), and accounts for a third of the total mass loss of Greenland (Mouginot et al., 2019). This sector counts a large number of marine-terminating glaciers, which have the potential to experience widespread inland thinning diffusion due to their bed topography (Felikson et al., 2021), potentially explaining the sustained increase in discharge. I derived surface elevation change from a decade of CryoSat-2 data in this sector and found that the surface is lowering at a rate of 18.7 ± 0.4 cm yr^{-1} during this period, with the margins of this region thinning at more than twice this pace (42.7 ± 0.9 cm yr^{-1}). I compared these estimates to airborne laser altimetry from Operation IceBridge estimates and found an overall good agreement with a mean difference of 6.5 ± 0.5 cm yr^{-1} and standard deviation of 31.1 cm yr^{-1} (Figure 6.4).

After correcting these elevation changes for the glacial isostatic adjustment and the instantaneous elastic response of the solid Earth to contemporaneous ice changes, I estimated the mass balance of this sector. I found that Northwest Greenland lost a total of 386.0 ± 3.7 Gt between 2010 and 2019, with only 8 glacier basins – out of the 68 basins of the sector surveyed – contributing to more than half of this mass loss (Figure 6.5).

I compared this mass balance estimate to estimates from gravimetry and the mass budget method and found that the altimetry solution is the least negative, both at the sector scale and when the region is split into two or four regions. I further compared the altimetry and mass budget estimates in individual glacier basins as both these methods allow for finer spatial resolution. There is a high correlation between the two techniques. While the mass budget method directly estimates discharge in 35 basins from velocity and thickness change data, steady-state conditions are assumed for the remainder of the basins. I also explored potential sources of biases in my altimetry estimate. I found that
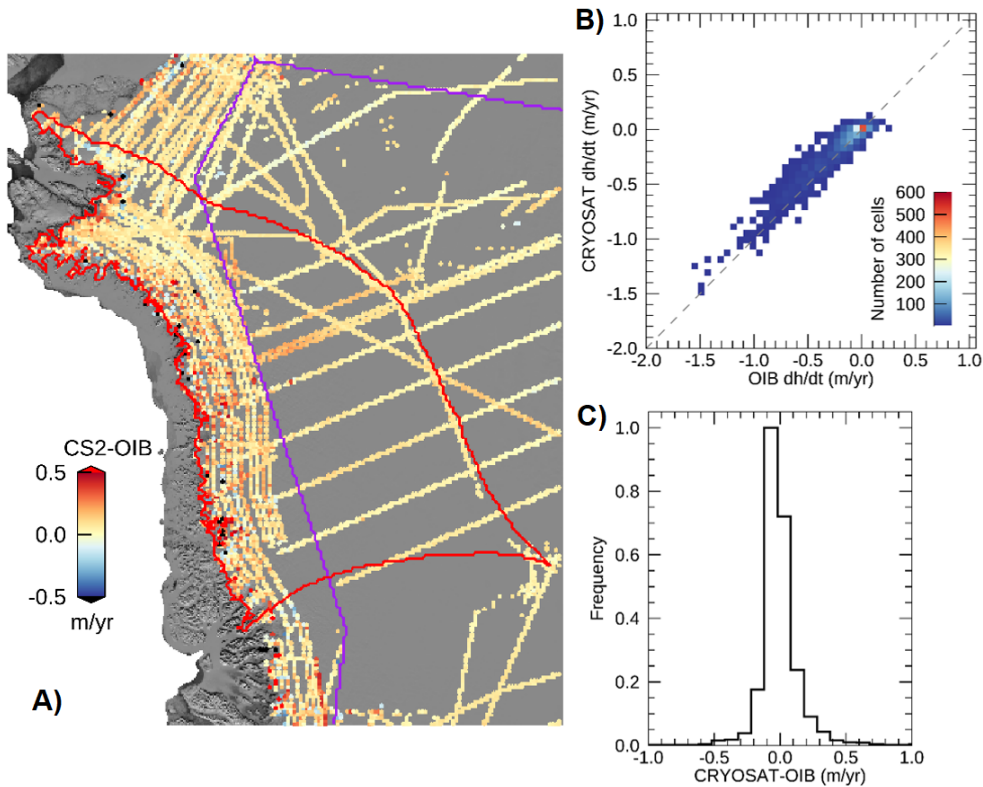
Figure 6.4: a) Difference between CryoSat-2 Ku-band and Operation IceBridge airborne laser altimetry rates of elevation change. b) Scatterplot of CryoSat-2 rates of elevation change against Operation IceBridge rates of elevation change. c) Histogram of the difference between CryoSat-2 and Operation IceBridge rates of elevation change.

the largest source of discrepancy could potentially be explained by a bias between radar and laser retrievals of surface elevation change, which can account for an additional mass loss of 11.8 Gt yr^{-1}, using a simple empirical correction based on extrapolating differences between airborne laser and satellite radar altimetry.
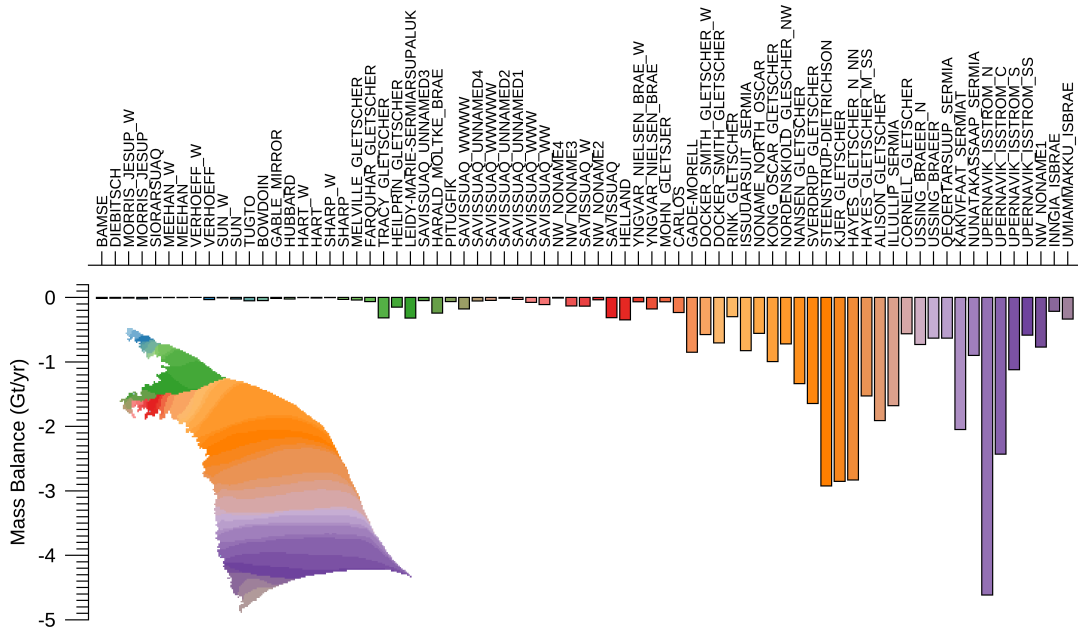
Figure 6.5: CryoSat-2 mass balance estimates per glacier basin.

In this chapter, I showed that Northwest Greenland has lost mass at a rate of 41.3 $\pm$ 0.6 Gt yr^{-1} between 2010 and 2019 from CryoSat-2 satellite altimetry. However, I showed that there are significant differences between altimetry, gravimetry and the mass budget method mass balance estimates in Northwest Greenland. The spatial pattern of the differences between the different geodetic techniques is complex, suggesting that the differences cannot be solely attributed to a particular region or technique.

6.2 Synthesis of Principal Findings

In this thesis, I have developed methods and created new datasets in order to improve our ability to detect and interpret changes in the elevation of Earth's polar ice sheets using Ka-band and Ku-band satellite altimetry. In this section, I will first show how this has contributed to demonstrating the potential of Ka-band AltiKa satellite altimetry for detecting trends in surface elevation change. Next, I investigated the effect of radar

penetration depth on surface elevation and elevation change measurements by comparing Ka- and Ku-band data in Antarctica and Greenland from satellite and airborne platforms. Finally, I will show that the new datasets I have created using AltiKa and CryoSat-2 data underline significant areas of ice sheet imbalance in West Antarctica and Northwest Greenland.

6.2.1 Demonstration of the Potential of Ka-band Satellite Altimetry to Track Changes in the Ice Sheets' Shape

In this thesis, I have demonstrated the potential of the new higher-frequency AltiKa altimeter for tracking changes in the ice sheets shape. AltiKa is the first space borne mission using the higher frequency Ka-band and interest in using this higher frequency for both oceanic and cryospheric studies has been growing in the last decades (Verron et al., 2015). One advantage of Ka-band is its reduced penetration in the snowpack below the ice sheet surface compared to Ku-band (Rémy et al., 2015). Another advantage is the smaller antenna of Ka-band, which lowers the cost of a satellite mission using Ka-band compared to an equivalent mission using Ku-band. There has been a number of studies on the combination of Ka- and Ku-band over sea ice to derive snow depth (e.g. Guerreiro et al., 2016; Lawrence et al., 2018), but land ice has received limited attention in comparison.

To retrieve surface elevation and elevation changes using AltiKa data, I have implemented new methods to accommodate for the altimeter's instrumental characteristics and spatial sampling. First, in Chapter 3, I developed a slope correction method to correct AltiKa Ka-band surface elevation data for slope-induced errors. This new correction, based on Roemer et al. (2007), takes into account the fact that AltiKa has a smaller aperture (0.6°) than other altimeters (CryoSat-2's antenna aperture is twice that of AltiKa), resulting in the retainment of 20.5 % more surface height measurements compared to the regular slope correction. This slope correction led to an agreement of AltiKa surface heights with coincident airborne laser data to within 3.8 ± 0.5 m in West Antarctica, compared to a median difference of 6.2 ± 0.5 m when a slope correction is not applied. Second, to estimate changes in surface elevation, I have applied a least-square model fit for estim-

ating surface elevation changes on both AltiKa Ka-band and CryoSat-2 Ku-band data in Chapters 3 and 5. Using the plane-fitting method (McMillan et al., 2016) maximises the spatial coverage of the derived elevation change field compared to the crossover method and is more adapted to AltiKa's drifting orbit phase (which began in July 2016) than the repeat-track method. This was the first application of such a model fit on Ka-band satellite data. I showed in Chapter 3 that this led to a coverage of 60.7 % of the West Antarctica basin with only small gaps in-between tracks. I also assessed the performance of AltiKa with respect to contemporaneous CryoSat-2 Ku-band data and showed that AltiKa detects similar surface elevation trends than those derived from CryoSat-2 with a mean difference of 0.1 ± 0.1 cm yr^{-1}.

While trends in surface elevation from AltiKa have not been studied in detail before this thesis, the potential of AltiKa for monitoring the oceans, inland water bodies and sea ice has already been demonstrated. Over the open ocean, the vast majority of AltiKa data (99.5 %) results in valid measurements of sea surface heights and AltiKa has a similar level of performance than Ku-band Jason-2 data in terms of both sea surface heights differences at crossovers and along-track sea level anomalies (Prandi et al., 2015). Furthermore, close to the coast – where radar echoes are easily distorted by the presence of land, complicating sea surface height retrievals from satellite altimetry – the smaller footprint (1.4 km against 1.7 km) and higher along-track sampling (31 cm against 47 cm) of AltiKa compared to Jason-2 results in a higher number of measurements. In the Northwestern Mediterranean Sea, AltiKa provides denser near shore observations compared to Jason-2 with improved quality with respect to tide gauge measurements (Birol and Niño, 2015). Similarly, over inland water bodies, such as rivers and lakes, the smaller footprint of AltiKa is also better suited for surveying these relatively small features than previous Ku-band altimeters, providing water level time series with reduced noise compared to Ku-band Envisat data (Schwatke et al., 2015). Finally, over sea ice, differences between AltiKa and Ku-band CryoSat-2 freeboard measurements arise from the different radar penetration depths of Ka- and Ku-band (Armitage and Ridout, 2015), which can be further used to derive snow depth on top of sea ice floes (Guerreiro et al., 2016; Lawrence et al., 2018). While the main

benefit of AltiKa over these surfaces is its smaller footprint, which results in better quality measurements, this proves more complicated over the ice sheets where the topography of the terrain can vary by up to tens of meters over only a few kilometres causing the radar echoes to originate outside AltiKa's narrow beam-limited footprint. This implies that in the margins of the ice sheet, the smaller antenna beam width of AltiKa, rather than providing higher quality measurements, limits the retrievals of surface elevation. However, as I have demonstrated in Chapter 3, this can be mitigated by adapting the slope correction algorithm to allow the relocation of surface elevation measurements outside the beam-limited footprint of AltiKa.

6.2.2 Exploring Differences in Penetration Depth between Ka- and Ku-band over the Ice Sheets

While differences between Ka- and Ku-band satellite data over the oceans and inland water bodies are driven by the difference in the sensors' characteristics, over sea ice and land ice, the radar signal can penetrate below the actual snow surface. Thus, differences between Ka- and Ku-band surface elevation and freeboard measurements are related to differences in radar penetration. Over Arctic sea ice, differences in freeboard between AltiKa, CryoSat-2, and airborne laser altimetry from Operation IceBridge have been used to show that Ka- and Ku-band radar range to a different scattering horizon over both first year and multi-year sea ice. CryoSat-2 penetrates up to the ice surface over first-year sea ice and through the majority of the snow layer on multi-year sea ice, while AltiKa echoes originate from the midpoint of the snow layer in both cases (Armitage and Ridout, 2015).

Unlike over sea ice, where there is a clear snow-ice interface with a snow layer that does not typically exceed 40 cm in the Arctic and 100 cm in the Antarctic in thickness, the ice sheets are covered by a layer of firn of up to tens of meters in the interior of the ice sheets. In Chapter 4, I have demonstrated that radar data are sensitive to melt layers formed during past summers by examining a long record of Ku-band airborne radar data in West Central Greenland. The spatial and temporal variations in surface melting induce strong fluctuations in the radar waveforms shape and penetration depth. The

largest variation in radar penetration is linked to the formation of an ice lens following the 2012 melt event, with a shift of the radar main scattering horizon upwards closer to the snow surface, resulting in a sudden decrease in Ku-band radar penetration of 6.2 $\pm$ 2.4 m. In 2017, the 2012 melt layer was still visible in the Ku-band radar profile, buried at a depth of 4.4 $\pm$ 0.2 m. While our Ka-band airborne data record is limited to 2016 and 2017 only, which limits our analysis of the sensitivity of higher-frequency data to extreme melt events, I showed that over these two years, radar penetration at Ka-band is reduced by half compared to that of coincident Ku-band. I have further assessed the ability of different retracking algorithms to mitigate the impact of radar penetration fluctuations on surface height retrievals and have shown that threshold retracking methods results in a good agreement with airborne laser data to within 13.9 cm for Ku-band data and 15.6 cm for Ka-band data.

While fluctuations in radar penetration are evident in Greenland where surface melt occurs every summer, in Antarctica where surface melt is limited to the margins of the ice sheet, this effect is less visible. In Chapter 3, I have shown that trends in surface elevation change in West Antarctica derived from Ka-band AltiKa are in good agreement with both Ku-band CryoSat-2 (within 0.1 $\pm$ 0.1 cm yr^{-1}) and airborne laser altimetry (within 0.6 $\pm$ 2.4 cm yr^{-1}), suggesting that trends in penetration depth over this region are minor. However, when comparing Ku-band CryoSat-2 and airborne laser altimetry data, I found differences in rates of elevation change of the same magnitude in both West Antarctica (Chapter 3) and Northwest Greenland (Chapter 5), with differences of 8.1 cm yr^{-1} and 6.5 cm yr^{-1}, respectively. This shows that differences between Ku-band satellite radar and airborne laser altimetry over both ice sheets seem to be larger than differences with Ka-band AltiKa satellite. Yet, differences between satellite radar and airborne laser cannot be solely interpreted as the effect of radar penetration. Other factors such as the different footprint sizes between satellite radar and airborne laser instruments, the operational mode of the satellite radar altimeter (LRM or SARIn), as well as the slope and roughness of the terrain all play a role in the differences between satellite radar and airborne radar data.

Finally, this work also fits in with the development of the European Space Agency high-priority candidate mission CRISTAL (Copernicus Polar Ice and Snow Topography Altimeter) mission, which will employ both Ka- and Ku-band frequencies (Kern et al., 2020), allowing for new opportunities to further develop the work presented in this thesis.

6.2.3 Detecting Ice Sheet Imbalance from Satellite Radar Altimetry

Finally, I have used the methods and datasets I developed throughout this thesis to study in details two key regions of the Antarctic and Greenland Ice Sheets that are exhibiting significant imbalance. In Chapter 3, I estimated surface elevation changes in West Antarctica using Ka-band and Ku-band satellite altimetry data and showed that the surface is lowering at a rate of 8.2 ± 1.2 cm yr^{-1} between 2013 and 2019 across this region. By extending the surface elevation time-series in time compared to previous studies (Shepherd et al., 2019), I have shown that the pace of surface elevation lowering at Pine Island Glacier fell by 9 % compared to the 2000s, while it increased by 43 % at Thwaites Glacier. The slowdown of Pine Island Glacier was also observed in a later study (Bamber and Dawson, 2020), confirming the complex pattern of thinning of Pine Island Glacier.

In Chapter 5, I used a decade of CryoSat-2 data to examine changes in the elevation and mass of the Northwest sector of the Greenland Ice Sheet. This sector is of critical importance as about a third of Greenland's ice losses come from the Northwest sector, contributing 4.4 mm to global mean sea level rise since 1972 (Mouginot et al., 2019). As this region counts a large number of relatively narrow marine-terminating glaciers in steep terrain, I made use of the dense observations provided by the SARIn acquisition mode of CryoSat-2 to derive surface elevation change and estimate the mass imbalance of this region. I showed that this sector is losing mass at a rate of 41.3 ± 0.6 Gt yr^{-1}, contributing 0.11 mm yr^{-1} to global mean sea level rise between 2010 and 2019. I further partitioned the mass change within each of the 74 glacier drainage basins of the Northwest sector, showing that all basins have lost ice over this period. This geographical partitioning in individual basins allows for a direct comparison with the mass budget method at a higher resolution than previous comparisons which have been performed either by considering the whole

ice sheets (e.g. Shepherd et al., 2020) or large regions of the ice sheets (e.g. Sutterley et al., 2014; Velicogna et al., 2020). A comparison at a finer resolution helps isolate differences geographically and identify more precisely the areas exhibiting similarities and differences. By applying this approach in Chapter 5, I showed that the bias between CryoSat-2 and the mass budget method in Steenstrup-Dietrichson basin likely originates from the absence of ice velocity observations in the computation of the discharge estimate in the mass budget method in this particular basin. Therefore, this approach can further help reconcile differences between independent estimates of mass balance.

6.3 Recommendations for Future Work

In this section, I underline areas of future research that have emerged from the results of this thesis. First, I consider comparing surface elevation changes derived from AltiKa and CryoSat-2 data across the Greenland Ice Sheet where seasonal fluctuations in surface mass balance are more important that in Antarctica based on the findings from Chapters 3 and 4 in order to retrieve firn properties from space. I then consider investigating biases between satellite radar and laser airborne altimetry based on Chapter 5. Finally, I consider combining data from AltiKa, CryoSat-2 and Operation IceBridge to create a multi-mission time series of elevation changes in the Antarctic Peninsula, where the steep terrain complicates the altimetry retrievals of surface elevation and elevation change.

6.3.1 Retrieving Firn Properties from Dual Frequency Radar Altimetry Ka-/Ku-band across the Greenland Ice Sheet

In Chapter 3, I demonstrated that surface elevation trends derived from Ka-band AltiKa satellite altimetry were in good agreement with CryoSat-2 Ku-band satellite altimetry and airborne laser altimetry in West Antarctica. A quarter of this region is now in a state of dynamic imbalance (Shepherd et al., 2019) and thinning rates recorded over the glaciers of the Amundsen Sea Embayment – Pine Island, Thwaites and Pope Smith and Kohler glaciers – typically exceed 3 m yr^{-1} over their main trunks (e.g. McMillan et al., 2014;

Pritchard et al., 2009). This dynamic thinning signal is very large and might mask out differences between Ka- and Ku-band signals related to radar penetration.

The Greenland Ice Sheet is a good candidate to further explore differences between Ka- and Ku-band surface elevation trends (Figure 6.6) as the Greenland Ice Sheet experiences large spatial and temporal variations in surface mass balance, as we have seen in Chapter 4. Comparing surface elevation changes arising from surface mass balance and firn processes simulated by a firn densification model (Kuipers Munneke et al., 2015) to Ka- and Ku-band elevation trends across the Greenland Ice Sheet could potentially help us infer properties of the firn pack and how these properties can affect radar penetration.
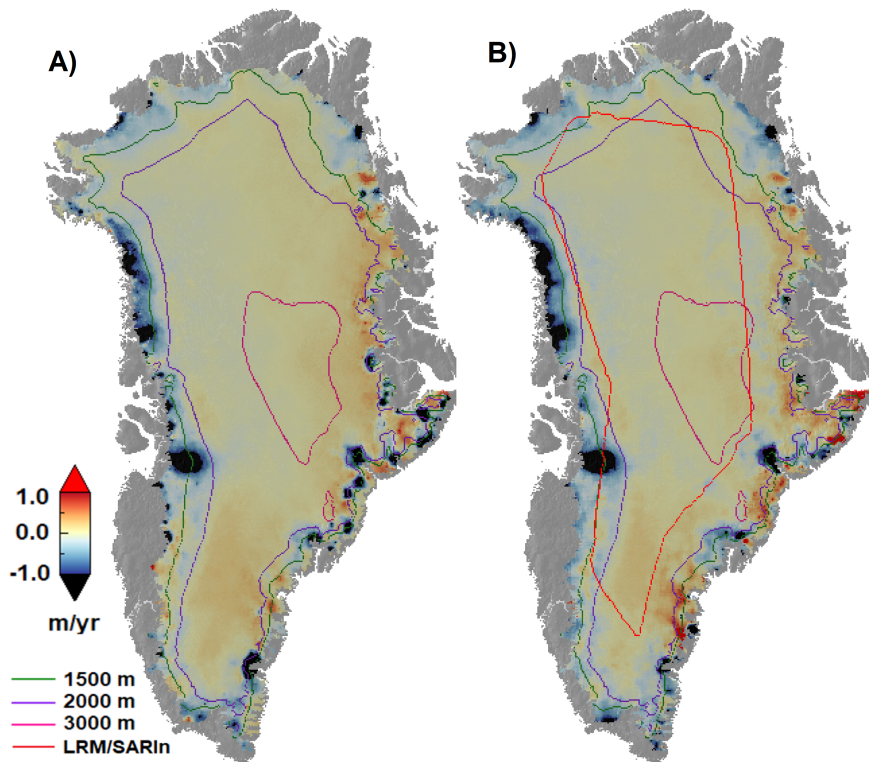
Figure 6.6: Greenland Surface Elevation Change between March 2013 and April 2017 from a) AltiKa Ka-band satellite altimetry, b) CryoSat-2 Ku-band satellite altimetry.

In particular, snowfall accumulation and surface melting are the two main surface mass balance processes leading to a surface elevation change and both these components vary

in time and space across the ice sheet. Snowfall is the highest in Southeast Greenland, which receives about 30 % of Greenland's total snow accumulation (Miège et al., 2013) and accumulation rates in this region have been derived from Operation IceBridge snow radar data (Montgomery et al., 2020) and simulated by firn densification models (e.g. Fettweis et al., 2017; Noël et al., 2018). In addition to snowfall accumulation, I have shown in Chapter 4 that surface melting has a large impact on radar scattering horizon, with the 2012 unprecedented melt event causing a shift of the scattering horizon towards the ice sheet surface and a sudden decrease in radar penetration. While AltiKa was launched after the 2012 melt event, surface melting was also substantial in summer 2019 (Tedesco and Fettweis, 2020) and investigating the impact of extensive surface melt on Ka- and Ku-band data would also help improve our radar altimetry retrievals of surface elevation and elevation changes and better characterise uncertainties from variable scattering horizon.

6.3.2 Investigating Potential Biases between Satellite Radar and Laser Altimetry in Greenland from CryoSat-2 and Operation IceBridge

Based on Chapter 5, in which I have shown that there are significant differences between mass balance estimates derived altimetry, gravimetry and the mass budget method in Northwest Greenland, I investigated the possibility that there exists a bias between radar and laser surface elevation changes. Here, I propose to extend this work by examining differences between CryoSat-2 Ku-band satellite altimetry and Operation IceBridge airborne laser altimetry across the whole Greenland Ice Sheet to understand the origin of this bias. Determining the origin of this bias and correcting the CryoSat-2 surface elevation change for this effect is crucial for accurately estimating the mass balance of the Greenland Ice Sheet. Several factors, such as the sensors' different footprint sizes, the different sampling pattern between satellite and airborne campaigns, the topography of the terrain or the Ku-band radar penetration (or a combination of these factors), could explain the bias between satellite Ku-band radar and airborne laser altimetry.

While CryoSat-2 has a footprint size of 1.6 km in LRM mode and a reduced footprint size of 0.3 km along-track and 1.6 km across-track in SARIn mode (Wingham et al., 2006),

Operation IceBridge airborne topographic mapper has a footprint of only ∼1 m. This implies that Operation IceBridge can resolve much smaller features than CryoSat-2 and could potentially lead to differences between the satellite radar and airborne laser data. Another factor inherent to any airborne campaign to take into account is the sampling pattern of the terrain. As the airborne campaigns are limited by weather conditions, personnel availability, time and other logistics constraints, the campaigns' foremost priority is to survey the fast-flowing parts of the ice sheet in the margins of the ice sheet that are rapidly changing, unlike satellites, which systematically revisit the terrain and provide measurements across the whole ice sheet. Furthermore, it is important to remark that the majority of the airborne data are collected in areas of high slope where CryoSat-2 surface elevation measurements are more likely to be affected by slope-induced errors. Finally, unlike laser signal, which is reflected by the snow surface, Ku-band radar signal can penetrate up to 15 m below the snow surface, potentially contributing to the differences between laser and radar surface elevation changes.

While in Chapter 5, I have only investigated the possibility of the bias between laser and radar surface elevation change in Northwest Greenland and estimated the impact of such a bias by extrapolating the differences in space, the differences appear to vary in time and across the Greenland Ice Sheet (Figure 6.7). Making use of a decade of coincident data between CryoSat-2 and Operation IceBridge is a unique opportunity to further explore differences between radar and laser surface elevation trends and has important implications for determining ice sheet mass balance. This analysis could be further used as a benchmark to assess the different processing steps applied in the CryoSat-2 processing chain, such as the different retracking algorithms or the backscatter correction used to correct the elevation changes for the temporal variations in the snowpack properties.
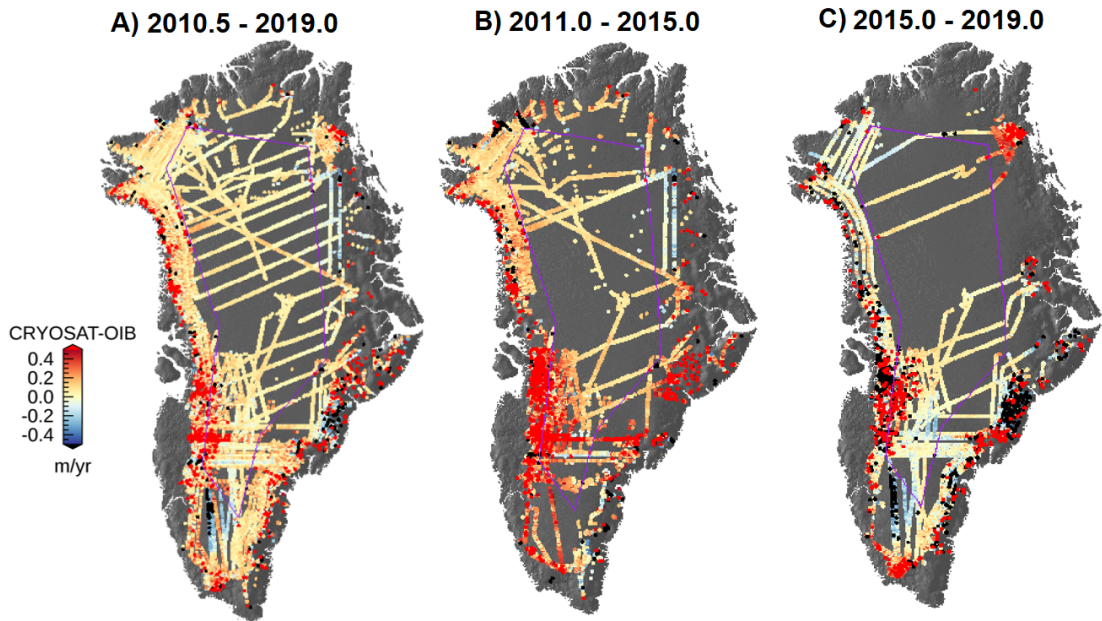
Figure 6.7: Difference in surface elevation change between CryoSat-2 Ku-band satellite altimetry and Operation IceBridge airborne laser altimetry. Difference in rates of surface elevation change calculated between a) 2010.5 and 2019, b) 2011.0 and 2015.0, c) 2015.0 and 2019.0. The boundary between LRM and SARIn modes of CryoSat-2 is indicated by the purple line.

6.3.3 Applying the Methods Developed in this Thesis to other Regions of Concern

The methods I developed in this thesis to detect changes in surface elevation of the ice sheets from satellite radar altimetry could also be applied to other regions of concerns. In Chapter 5, I derived surface elevation and mass changes of the Northwest sector of the Greenland Ice Sheet. This region counts a large number of small-terminating glaciers, which are challenging to observe from satellite radar altimetry. However, by using CryoSat-2 data, I have shown that it is possible to detect changes within the individual glacier basins of this sector. The same approach could be applied to the Antarctic Peninsula, a mountainous region with steep terrain. Dynamic thinning has been reported

over several glaciers in the Southern Peninsula from CryoSat-2 (Wouters et al., 2015), however satellite radar altimetry data coverage is too sparse in the Northern Peninsula to derive surface elevation changes, which also limits the ability of deriving a mass balance estimate of the Antarctic Peninsula from satellite radar altimetry (Shepherd et al., 2019). The entire Antarctic Peninsula was covered in its entirety for the first time using satellite laser altimetry data from ICESat, showing that the pattern of surface elevation change is complex across the Peninsula, with tributary glaciers of the former Larsen ice shelf and Georges VI ice shelf undergoing significant thinning exceeding several meters per year, while small glaciers around the Bellinghausen Sea coast are thickening (Pritchard et al., 2009). However, this has not yet been achieved using satellite radar altimetry as radar altimetry data are affected by large slope-induced errors, which limits the ability of radar altimetry to survey the Antarctic Peninsula. Nonetheless, detailed patterns of thickness changes of the ice shelves of the Antarctic Peninsula have been derived from satellite radar altimetry (e.g. Adusumilli et al., 2018; Paolo et al., 2015), and therefore, having a more comprehensive record of elevation changes over the grounded ice sheet would also help investigate changes over the ice shelves together with changes of their tributary glaciers.

Using CryoSat-2 between 2010 and 2019 and applying the same processing steps as in Chapters 3 and 5 of this thesis to derive surface elevation changes over the Antarctic Peninsula, results in a coverage of 80 % of the area at a 5 km resolution. However, as this region counts some very small outlet glaciers, deriving elevation change at a fine spatial resolution is necessary but only 49 % of the area is surveyed at a resolution of 1 km, with very few data recovered in the northern drainage basins of the Peninsula (Figure 6.8). This CryoSat-2 dataset could be supplemented with data from AltiKa, by applying the same slope correction scheme as developed in Chapter 3, in order to retain a larger proportion of AltiKa data in regions of high slope compared to other slope correction algorithms. Furthermore, as I have extensively compared data from Ka-band AltiKa, Ku-band CryoSat-2 and Operation IceBridge in West Antarctica and Northwest Greenland and showed that all three datasets detect trends in surface elevation within 8 cm yr^{-1}, including data from Operation IceBridge to complement the satellite radar

altimetry datasets would enable to further maximise the data coverage across the Antarctic Peninsula. Therefore, combining data from CryoSat-2, AltiKa and Operation IceBridge to create a multi-mission time-series of elevation changes would improve the spatial coverage of this region and help identify and understand glaciological changes of the Antarctic Peninsula.
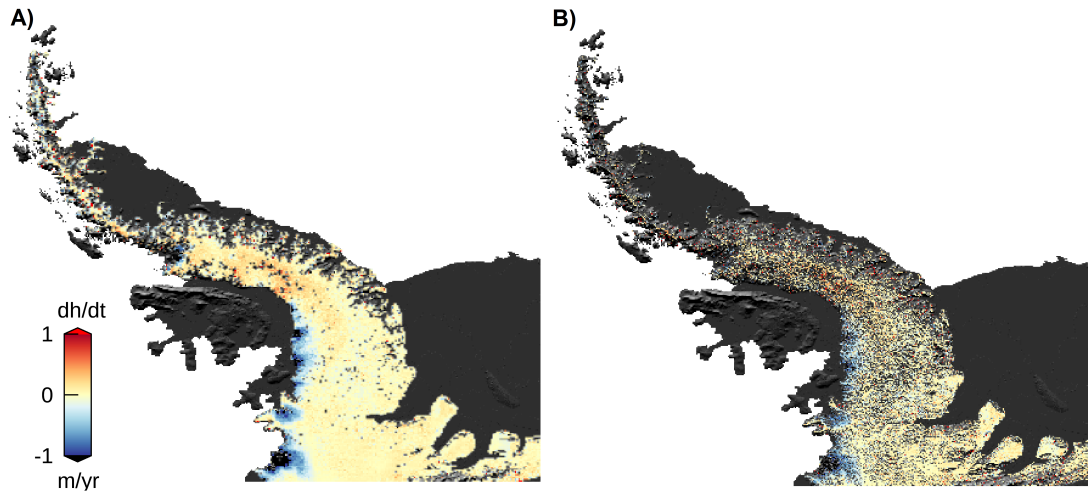
Figure 6.8: Antarctic Peninsula rates of surface elevation change from CryoSat-2 between 2010 and 2019 at a) 5 km resolution and b) 1 km resolution.

6.4   Concluding Remarks

Since the 1990s, satellite radar altimeters have enabled us to monitor changes in the surface elevation of the Greenland and Antarctica Ice Sheets (Schröder et al., 2019; Sørensen et al., 2018), providing critical information on their contributions to global mean sea level rise (Shepherd et al., 2020; The IMBIE Team, 2018) and constraining numerical simulations of future ice sheet mass losses (Nias et al., 2019). The altimeters on board, the ground segment processing of the satellite data, and the methods to derive and interpret geophysical signals from these data have all been refined throughout the years (e.g. Flament and Remy, 2012; Helm et al., 2014; McMillan et al., 2016; Slater et al., 2019),

further improving our ability to detect changes in the surface of the ice sheets. In this thesis, I have developed methods and datasets to contribute to this effort, using data from Ka-band AltiKa and Ku-band CryoSat-2. I have derived surface elevation and surface elevation changes over West Antarctica using AltiKa, demonstrating the ability of AltiKa to track changes in the ice sheets' shape, with sufficient coverage to examine recent changes at Pine Island and Thwaites Glaciers (Otosaka et al., 2019). I investigated the impact of surface melting on fluctuations in radar penetration in West Central Greenland and assessed methods to mitigate this effect on surface elevation retrievals using a new dataset of airborne and in-situ measurements combined with firn densification model outputs (Otosaka et al., 2020). Finally, I estimated the mass imbalance of the Northwest sector of the Greenland Ice Sheet from a decade of CryoSat-2 satellite altimetry, making use of the dense observations of CryoSat-2 in the margins of the ice sheet to estimate the mass loss in individual glacier basins (Otosaka et al., 2021). The methods and datasets derived in this thesis could be further extended back in time with data from the ERS-1/2 and Envisat historical missions and could also be combined with contemporaneous data from Sentinel-3 or ICESat-2 to further improve the spatial and temporal resolution of surface elevation changes estimates of the polar ice sheets.

This page intentionally left blank.

Appendix A

ASIRAS Ku-band Radar Profiles along the EGIG line

27/10/2016

31/03/2017 - 01/04/2017

169
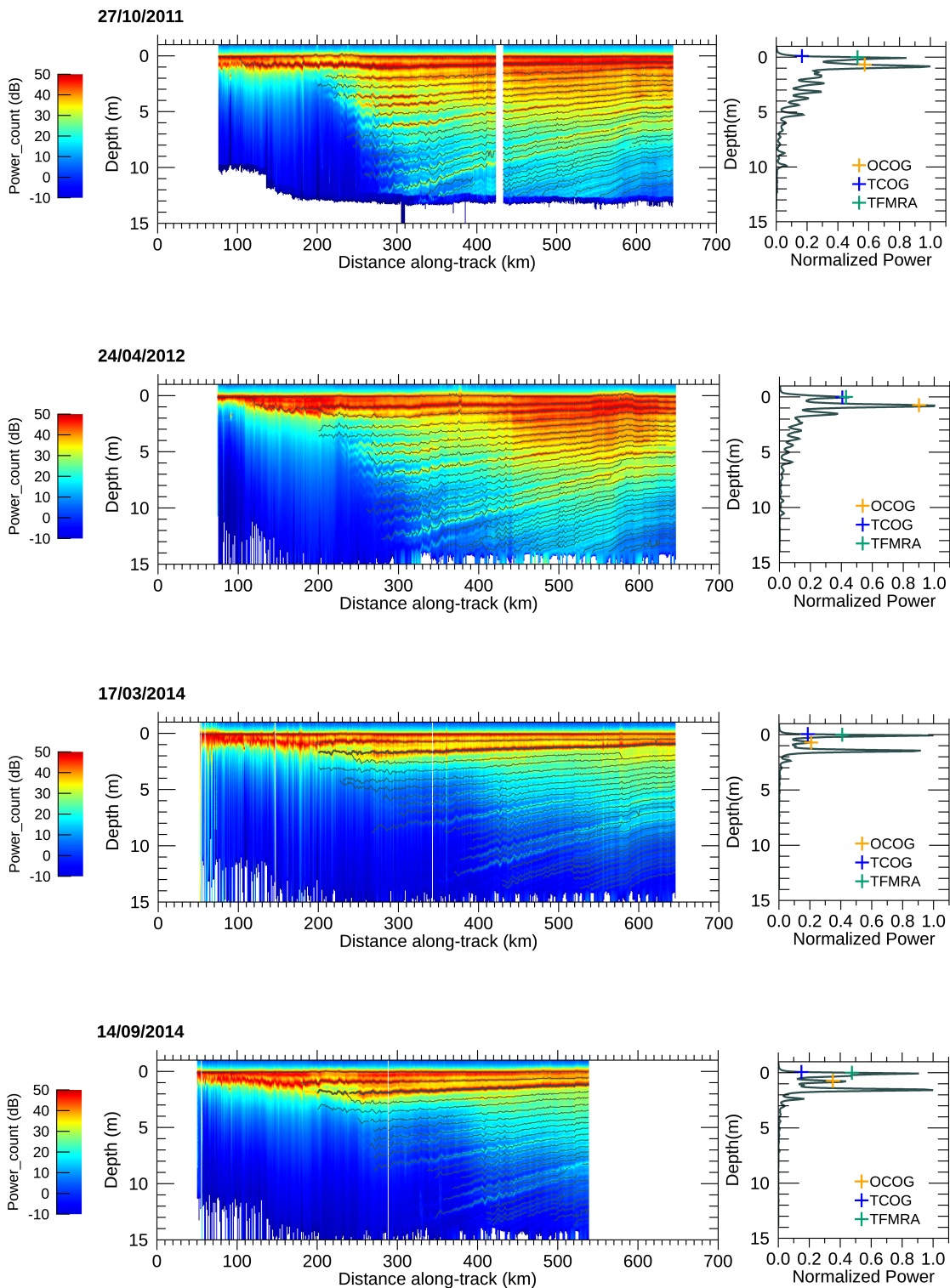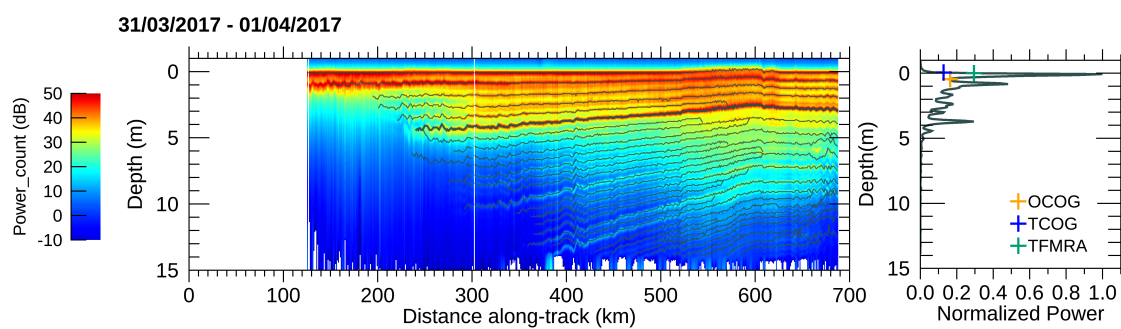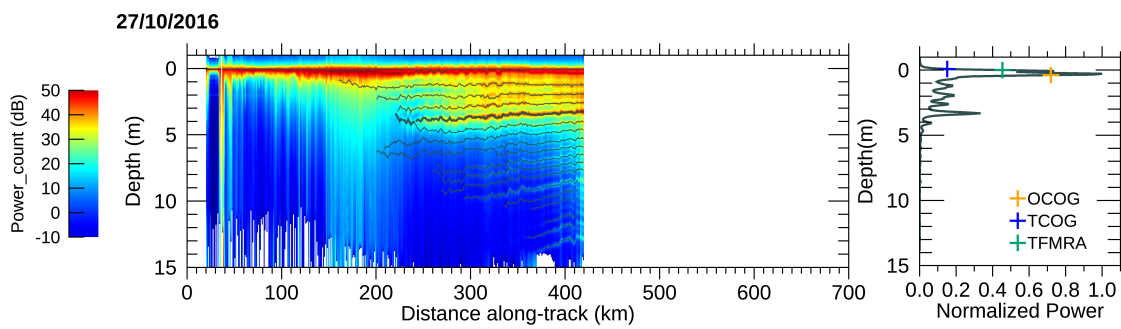
This page intentionally left blank.

Appendix B

KAREN Ka-band Radar Profiles along the EGIG line

This page intentionally left blank.

APPENDIX C

Ice Sheet Elevation Change in West Antarctica

From Ka-Band Satellite Radar Altimetry

Geophysical Research Letters

Ice Sheet Elevation Change in West Antarctica From Ka-Band Satellite Radar Altimetry

Inès Otosaka[1] [ID], Andrew Shepherd[1] [ID], and Malcolm McMillan[2] [ID]

[1]Centre for Polar Observation and Modelling, School of Earth and Environment, University of Leeds, Leeds, UK, [2]Centre for Polar Observation and Modelling, Lancaster University, Lancaster, UK

Abstract Satellite altimetry has been used to track changes in ice sheet elevation using a series of Ku-band radars in orbit since the late 1970s. Here, we produce an assessment of higher-frequency Ka-band satellite radar altimetry for the same purpose, using SARAL/AltiKa measurements recorded over West Antarctica. AltiKa elevations are 3.8 ± 0.5 and 2.5 ± 0.1 m higher than those determined from airborne laser altimetry and CryoSat-2, respectively, likely due to the instruments' coarser footprint in the sloping coastal margins. However, AltiKa rates of elevation change computed between 2013 and 2019 are within 0.6 ± 2.4 and 0.1 ± 0.1 cm/year of airborne laser and CryoSat-2, respectively, indicating that trends in radar penetration are negligible. The fast-flowing trunks of the Pine Island and Thwaites Glaciers thinned by 117 ± 10 and 100 ± 20 cm/year, respectively, amounting to a 9% reduction and a 43% increase relative to the 2000s.

Plain Language Summary Satellite altimeters transmitting 2.3 cm radio waves have been used to track changes in the shape of Earth's polar ice sheets since the late 1970s. In this study, we demonstrate the capability of a new altimeter mission—SARAL/AltiKa—to survey ice in western Antarctica using shorter, 0.8 cm radio waves. AltiKa measures changes in elevation across most of the ice sheet to within 0.6 cm/year of airborne and satellite sensors. Since the late 2000s, thinning of Thwaites Glacier has risen from 70 to 100 cm/year, but thinning of Pine Island Glacier has fallen from 128 to 117 cm/year.

1. Introduction

Satellite radar and laser altimetry have been widely used to derive ice sheet surface elevation and elevation change in Antarctica (e.g.,Bamber et al., 2009 ; Pritchard et al., 2009 ; Schröder et al., 2019 ; Shepherd et al., 2019 ; Slater et al., 2018 ; Wingham et al., 1998) and in Greenland (e.g.,McMillan et al., 2016 ; Sandberg Sørensen et al., 2018) to quantify their contributions to global sea level rise. Radar altimeters transmit pulses of electromagnetic radiation toward the Earth's surface and record the two-way traveltime of the signal and the magnitude and the shape of the backscattered echo (waveform). The waveform shape is related to the average terrain and scattering properties of the Earth surface area illuminated by the altimeter footprint, which, in turn, is determined by the sensor design (Brown, 1977). The leading edge position of the waveform can be deduced with the aid of an echo retracking algorithm (Davis, 1997; Legresy et al., 2005) and is typically used as a range adjustment to improve the precision of the surface elevation measurement.

The AltiKa sensor has operated on the ISRO/CNES SARAL satellite since 2013 and is the first space-borne radar altimeter transmitting at Ka-band (37 GHz, 0.8 cm wavelength) frequencies. In this study, we look at the strengths and weaknesses of this new data set for cryosphere studies. In theory, Ka-band radar has a reduced penetration depth within ice sheet surfaces when compared to the Ku-band sensors (13.5 GHz, 2.3 cm wavelength) due to the scattering losses dominating in Ka-band (with a scattering coefficient ~57 times higher than in Ku-band) over absorption losses, and this has been supported by comparisons between the degree of radar backscattering recorded by AltiKa and ENVISAT over Antarctica (Adodo et al., 2018; Rémy et al., 2015). Reduced signal penetration may potentially lead to better measurements of the ice sheets surface height. Previous studies have looked at the possibility of deriving elevation and elevation change in Antarctica (Suryawanshi et al., 2019) and Greenland (Yang et al., 2018) from AltiKa, but their analyses were limited to only 3 years of data and did not include a comparison to Ku-band measurements. Here, we compute elevation and changes in the elevation of West Antarctica using 5 years of data acquired by AltiKa between March 2013 and March 2019. The main objectives of this study are to (i) assess the capability of

AltiKa to measure elevation and elevation change in West Antarctica by comparing these estimates to contemporaneous airborne laser altimetry observations recorded by Operation IceBridge (OIB) and (ii) compare the Ka-band measurements to CryoSat-2 satellite Ku-band measurements to investigate whether the different frequencies of the two instruments lead to significant differences in elevation or elevation change.

2. Data and Methods

We use 51 million range measurements recorded by AltiKa between March 2013 and March 2019 to compute elevation change across the Amundsen Sea Sector of West Antarctica, a region that has exhibited widespread thinning (Flament & Remy, 2012; Shepherd et al., 2002) due to ice dynamical imbalance (Mouginot et al., 2014; Rignot et al., 2019). The range measurements were derived from 63 cycles of the AltiKa Sensor Geophysical Data Record (SGDR-T) and include corrections for dry tropospheric delay, wet tropospheric delay, ionosphere delay, solid Earth tide, ocean loading tide, and pole tide. The AltiKa data were acquired along the same 35-day repeat orbit as ERS-1/2 and ENVISAT until July 2016, date at which the satellite was moved to a drifting orbit because of technical issues on the reaction wheels (Verron et al., 2018). This change of orbit did not affect the data availability or quality. Although AltiKa is a pulse-limited radar altimeter of similar design to ENVISAT, its operating bandwidth of 500 MHz allows for a higher pulse-repetition frequency (4 kHz), which allows a closer along-track sampling, a narrower beam width (0.6°), and a smaller (8 km diameter) ground footprint (Steunou et al., 2015; Verron et al., 2015).

To assess the performance of AltiKa, we compare the retrieved elevation and elevation change to satellite Ku-band altimetry data from CryoSat-2. CryoSat-2 is operating since 2010 and has been widely used to map the elevation and elevation change of the Greenland and Antarctic ice sheets (Helm et al., 2014; Nilsson et al., 2016). It offers improved spatial coverage and resolution relative to previous pulse-limited altimeter missions, thanks to its high (92°) orbital inclination, its long-repeat drifting orbit, and—in coastal regions—its Synthetic Aperture Radar Interferometric Radar Altimeter (SARIn) mode (Wingham et al., 2006). Over the interior of the ice sheets, CryoSat-2 operates as a traditional pulse-limited altimeter, known as Low-Resolution Mode (LRM).

Elevation measurements over the ice sheets need to be adjusted for the effects of the ice sheet surface slope, which typically ranges from 0.1° to 1.5° in Antarctica, introducing a 1.4 to 20.9 km lateral shift in the point of closest approach (Brenner et al., 1983; Levinsen et al., 2016; Remy et al., 1989) or, equivalently, a 1.2 to 274.2 m error in the estimated elevation if the measurement was assumed to be originating from nadir. CryoSat-2 elevation measurements from Product L2I are corrected for this slope-induced error unlike AltiKa SGDR-T elevation measurements. To correct for this, we apply a geometrical translation (Roemer et al., 2007) that relocates echoes to the point of closest approach, using the same digital elevation model (Liu et al., 1999) employed in the ESA CryoSat-2 Level-2 processing chain to ensure a like-for-like comparison with CryoSat-2. In total, 76.1% of echoes fall within AltiKa's beam-limited footprint. However, the remainder are in areas of high slope that tend to be located near to the ice sheet margin, which is a region of geophysical interest. To include these, we iterate the slope correction by artificially increasing the ground footprint diameter in three 1 km intervals, and this procedure allows us to retain 20.5% more echoes (96.6% in total).

We applied waveform retracker corrections to the AltiKa and CryoSat-2 range measurements to improve their precision. The shape of pulse limited satellite radar altimeter waveforms is dependent on the instrument specifications, the surface topography, and on the degree of surface and volume scattering (Ridley & Partington, 1988). One aim of retracking algorithms is to mitigate the effects of volume scattering, which occurs if the radar pulse penetrates below the physical surface—as is common over ice sheets (Michel et al., 2014; Nilsson et al., 2015). Retracking algorithms achieve this by identifying the location of the surface echo within the waveform, which is itself the sum of scattering from all elements illuminated by the transmitted pulse. A selection of retracker corrections are present within the AltiKa SGDR (ICE-1, ICE-2, and Sea Ice and Ocean retrackers) and the CryoSat L2I (OCOG, Ocean CFI, and UCL Land Ice retrackers) products, and, for consistency, we pick similar ones for both missions. We choose Threshold Centre of Gravity based retracking algorithms (Wingham et al., 1986): the ICE-1 retracker for AltiKa and the OCOG retracker for CryoSat-2 LRM waveforms. Only one waveform retracker (the Wingham/Wallis model fit) is available for CryoSat-2 data acquired in SARIN mode, and so we use this correction for those data (ESA, 2012).

We apply the same methodology to derive elevation and elevation change from AltiKa and CryoSat-2 (McMillan et al., 2014). The data are collated within 5 km by 5 km square grid cells, and a multiparameter least squares model fit is applied to retrieve the mean elevation and the mean rate of elevation change within each cell. The model fit accounts for the fluctuations in the heights recorded by the satellite, due to the horizontal location, the heading of the satellite, and time. We apply an additional correction on elevation change based on the correlation of elevation and backscattered power to account for temporal variability of the snowpack properties, which can induce a spurious elevation change associated with changes in surface and volume scattering (Davis & Ferguson, 2004; Simonsen & Sandberg Sørensen, 2017). We estimate the uncertainty in elevation from the departure between the heights recorded by the satellite and in our model fit. Errors in gridded rates of elevation change are estimated as the 1-sigma uncertainty from the linear fit, and errors over larger regions are computed as the sum in quadrature of this and the standard deviation of the elevation change measurements at each epoch over the contributing grid cells. Finally, we exclude grid cells where the time span of measurements is less than 2.5 years, where the magnitude of the elevation change rate exceeds 10 m/year, where the root-mean-square of the residuals exceeds 10 m or where the proportion of ascending and descending orbits is not evenly balanced.

To evaluate the accuracy of the AltiKa data, we use contemporaneous and coincident measurements of ice sheet elevation and elevation change acquired during NASA's OIB surveys. We use surface elevation measurements recorded by the NASA's Airborne Topographic Mapper (ATM; Studinger, 2014a; ILATM icessn) and elevation change rates derived from repeated ATM elevation measurements (Studinger, 2014b; IDHDT).

3. Results

3.1. Comparison Between Ka-Band Satellite Altimetry and Airborne Laser Altimetry

We computed the average surface elevation (Figure 1a) and the average rate of surface elevation change (Figure 1d) across the Amundsen Sea Sector between 2013 and 2019 from the AltiKa measurements alone. The region is an area of known dynamical imbalance (Joughin et al., 2014; Mouginot et al., 2014; Rignot, 2008) where rapid ice thinning has occurred across the coastal margins in the vicinity of its fast-flowing outlet glaciers (Shepherd et al., 2002). Altogether, AltiKa is able to map 60.7% of 5 km square grid cells within the study area (up to 81.5°), and most data gaps are small so that 95.7% of the basin has an adjacent measurement at this resolution (see Figure S1 in the supporting information). However, in areas of high slope, AltiKa struggles to track the ice sheet surface because of the instrument's smaller beam width and of the smaller range window explored (~40 m compared to ~60 m in LRM and ~120 m in SARIn for CryoSat-2). Furthermore, due to AltiKa's 35-day repeat cycle, the track spacing is wider compared to CryoSat-2 and only half (48.1%) of grid cells falling on fast-flowing ice ($v > 250$ m/year) are surveyed. For comparison, the interferometric altimeter of CryoSat-2 is able to survey 92.7% of the same ice (McMillan et al., 2017).

First, we compare AltiKa elevation measurements to the OIB measurements to evaluate their accuracy (Figures 1b and 1c). To compare the elevation data, we interpolated the satellite data to the time and location of the airborne measurements using the coefficients of the multiparameter model fits, and we then computed the median difference within the 1,654 AltiKa data grid cells that contained at least five airborne measurements. We compare both the uncorrected and relocated AltiKa elevation measurements to OIB to assess the quality of our iterative slope correction. The uncorrected AltiKa measurements are positively biased with a median difference relative to OIB of 6.2 ± 0.5 m and associated standard deviation of 19.2 m. With our iterative relocation, the median difference is reduced to 3.8 ± 0.5 m with a standard deviation of 20.8 m. The OIB measurements are concentrated around the ice sheet margins (see Figure 1b), with 55.9% of the data collected over surfaces with a slope higher than AltiKa's half antenna aperture (0.3°) where the median and standard deviation of the difference to OIB are 5.5 ± 0.8 m and 23.4 compared to 2.3 ± 0.5 m and 12.2 m in low slope areas. This larger departure from the OIB data set in areas of slope exceeding 0.3° illustrates the trade-off between the beam width footprint of a radar altimeter and the slope of the terrain surveyed. There are advantages to a smaller footprint (e.g., a shaper waveform); however, when the surface slope exceeds half the antenna aperture, the point of closest approach is shifted outside the beam footprint where the power is significantly lower. This does not apply to laser altimeters such as IceSat-1/2, which have footprints of the order of tens of meters over which the surface slope variations can be neglected. This could explain the positive bias and relatively high dispersion as 50.6% of the echoes used in the comparison to OIB are scattered

Figure 1. (a) Average elevation of the Amundsen Sea Sector determined from AltiKa Ka-band satellite radar altimetry between March 2013 and March 2019, h; (b) average elevation from Operation IceBridge airborne laser altimetry; (c) elevation difference between AltiKa and airborne laser altimetry; (d) average rate of elevation change from AltiKa, dh/dt; (e) average rate of elevation change from Operation IceBridge; and (f) difference between rates of elevation change between AltiKa and airborne laser altimetry. The size of the OIB data has been increased for better visualization. A 25 km × 25 km median filter is applied to fill small gaps in the AltiKa data. The inset on (a) represents the location of the study area in Antarctica. Insets on (c) and (f) are histograms of the difference between AltiKa and OIB in the recorded elevation and rates of elevation change, respectively. Purple line shows the boundary between CryoSat-2 LRM and SARIn acquisition modes, green lines show OIB flight lines (A to B, C to D and E to F), and the red outlines mark the central trunks of the Pine Island (PIG) and Thwaites (THW) Glaciers defined by a 250 m/year contour from ice velocity data (Rignot et al., 2011).

from beyond the instrument's 0.3° beam-limited footprint—23.9% of the total number of echoes across the study area—introducing an increased standard deviation in the difference to OIB of 17.8 m compared to 16.6 m when considering only the points within the 0.3° beam limited footprint. We also examine this elevation bias in terms of surface slope and roughness (see Figure S2). The differences between AltiKa and OIB exceeding 10 m are recorded in areas of slope higher than 0.4° and of surface roughness higher than 7 m. The presence of crevasses from which the returned echo is more complex could also potentially bias the elevation measurements recorded (Lacroix et al., 2007; Partington et al., 1987).

We also compared rates of surface elevation change computed from AltiKa data to those determined from the OIB measurements over 327 grid cells common to both data sets and falling within the CryoSat-2 SARIn mask (Figures 1e and 1f). Without a backscatter correction applied, the median difference between AltiKa and OIB rates of elevation change is −5.5 ± 2.5 cm/year with an associated standard deviation of 43.0 cm/year. Across this subset of grid cells, the backscatter correction applied to AltiKa elevation change is 4.8 cm/year on average with a standard deviation of 30.7 cm/year, and across the study area as a whole, the magnitude of this correction is 1.0 cm/year with a standard deviation of 16.5 cm/year. Applying this correction leads to a better agreement with the laser altimetry rates of elevation change with a median difference of −0.6 ± 2.4 cm/year and standard deviation of 42.7 cm/year. This analysis shows that there is far better agreement between the OIB and AltiKa measurements of elevation change in comparison to elevation.

3.2. Comparison Between Ka-Band and Ku-Band Satellite Altimetry

As a second test, we compared the AltiKa estimates of ice sheet surface elevation to independent estimates derived from CryoSat-2, to investigate potential differences in the degree of signal penetration recorded by
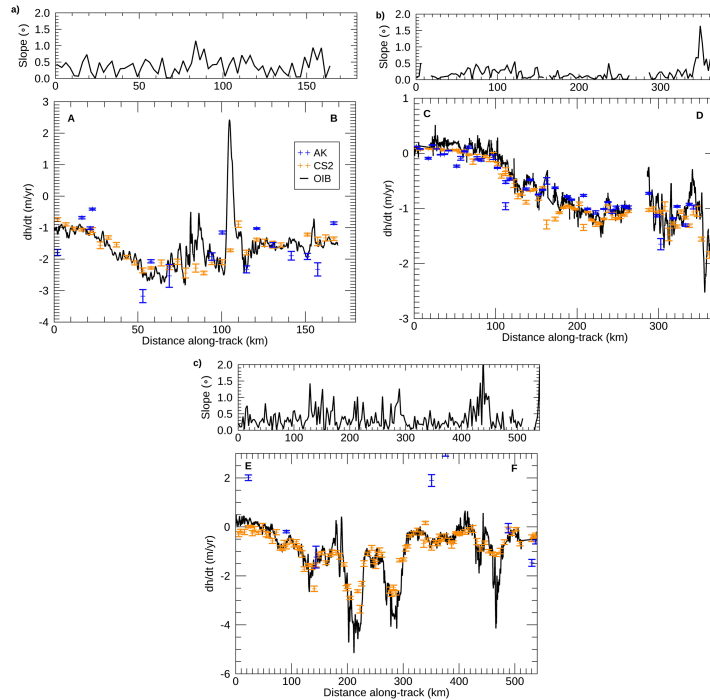
Figure 2. Rates of elevation change profiles from Operation IceBridge ATM, AltiKa, and CryoSat-2 and ATM surface slope profiles (a) along airborne sorties of Thwaites Glacier from A to B, (b) Pine Island Glacier from C to D, and (c) at the Getz Ice Shelf grounding line from E to F (locations shown on Figure 1e).

each sensor. At the 3,580 common grid cells that contained at least five airborne measurements, the median difference between CryoSat-2 and OIB measurements of elevation is -0.7 ± 0.2 m, consistent with previous studies (Slater et al., 2018). By comparison, the median difference between AltiKa and CryoSat-2 (computed as AltiKa-CryoSat-2) elevation data at 27,192 coincident grid cells is 2.5 ± 0.1 m, which confirms that AltiKa elevations are on average positively biased. Because the AltiKa bias is present in comparisons to both OIB and CryoSat-2, and because there is little evidence of bias between OIB and CryoSat-2, we do not believe that it is associated with differences in the degree of radar penetration. Rather, the largest differences are in areas of high slope and roughness, suggesting that this bias is related to the different instrument characteristics and in particular to the different footprint sizes and acquisition modes.

Next, we compared AltiKa and CryoSat-2 estimates of ice sheet surface elevation change to examine whether the positive bias in AltiKa elevation measurements is also present in the rates of elevation change recorded by AltiKa. This comparison also extends the area over which the AltiKa data can be evaluated with respect to independent observations, as the OIB data are limited to a small (<2%) portion of the mainly coastal Amundsen Sea Sector. Across the region as a whole, the rate of elevation change recorded by AltiKa and CryoSat-2 averages 5.3 ± 1.0 cm/year and 8.2 ± 1.2 cm/year lowering between 2013 and 2019, respectively. Within the coastal margins (the SARIn mask of CryoSat-2; see Figure 1d), the average rate of surface lowering recorded by AltiKa and CryoSat-2 is 14.4 ± 1.6 cm/year and 18.1 ± 2.0 cm/year, whereas in the interior (the LRM mask of CryoSat-2), the surface elevation increased at an average rate of 0.6 ± 0.6 cm/year and 1.3 ± 1.0 cm/year, respectively. At 27,192 common locations, the median difference between AltiKa and CryoSat-2 measurements of surface elevation change is -0.1 ± 0.1 cm/year with an associated standard deviation of 11.5 cm/year. This difference is small and comparable to or smaller than the differences
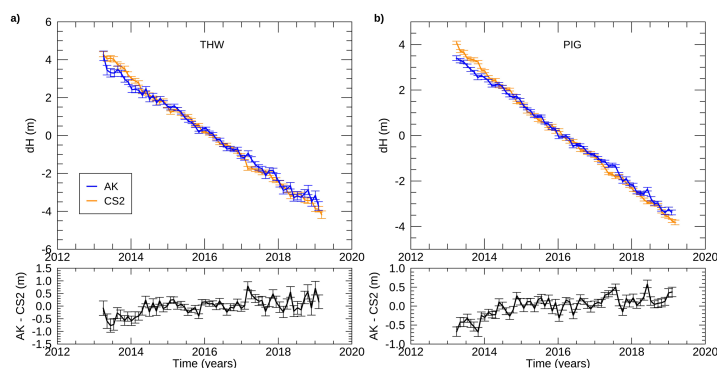
Figure 3. Time series of elevation change over (a) Thwaites Glacier and (b) Pine Island Glacier fast-flowing trunks (shown on Figure 1d) from AltiKa and CryoSat-2 and elevation change difference.

between each instrument and the OIB data themselves (-0.6 ± 2.4 cm/year between AltiKa and OIB and -8.1 ± 1.5 cm/year between Cryosat-2 and OIB, at 327 common grid cells). We also compute the robust dispersion estimate (RDE) of the difference between AltiKa and CryoSat-2 as defined by Smith et al. (2017). The RDE is 3.5 cm/year and shows that although local differences exceeding 20 cm/year do occur (e.g., Figure 3), the small regional differences suggest that there is no significant bias in either AltiKa and CryoSat-2 estimate of elevation change in this particular sector of Antarctica, where the changes are dominated by changes in ice dynamics. Other factors that may be responsible for local differences between AltiKa and CryoSat-2 include differences in the low-level satellite data processing chains and differences in the satellite radar acquisition modes, and without equal treatment of these factors, it is not possible to further isolate the potential effects of radar signal penetration.

We also compared AltiKa and Cryosat-2 rates of elevation change to OIB along continuous sorties flown by the aircraft, to examine changes over diverse terrain in more detail: one along Thwaites Glacier, one along the centerline of Pine Island Glacier, and another following approximately the ice sheet grounding line inland of the Getz Ice Shelf (see Figure 1e). Along the Thwaites sortie, AltiKa records fewer measurements than Cryosat-2 but both sensors have comparable performances with RMS differences of 0.58 and 0.54 m/year, respectively (Figure 2a). AltiKa and CryoSat-2 perform similarly well along the Pine Island Glacier sortie, yielding RMS differences of 0.22 and 0.21 m/year relative to OIB, respectively (Figure 2b). Along the Getz Ice Shelf sortie, however, AltiKa performs poorly due to the presence of steep and rough terrain and acquires 9 times fewer measurements (Figure 2c). Although there is rapid thinning at several outlet glaciers, AltiKa fails to detect this and records a RMS difference of 2.85 m/year relative to OIB. This highlights the limits of AltiKa, which struggles to track surfaces in areas of complex terrain with rapidly changing slopes because of its smaller beam footprint and tracking window size, which are not very suited for high slope areas such as the ice sheet margins. Thus, deriving total volume change from AltiKa might be challenging, as most of the ice losses are occurring in the areas least well sampled by AltiKa. By comparison, the SARIn mode of CryoSat-2 performs extremely well despite the challenging terrain, tracking local thinning at a series of outlet glaciers along the sortie, with an RMS difference of 0.43 m/year relative to OIB.

We also examined temporal variations in the surface elevation of the fast-flowing sections of Thwaites (Figure 3a) and Pine Island Glaciers (Figure 3b) recorded by AltiKa and CryoSat-2 to assess to which extent AltiKa can be used to examine elevation change trends at the scale of individual glaciers. Previous studies have identified rapid and increasing rates of surface lowering across the fast-flowing trunks of the Thwaites and Pine Island Glaciers (Shepherd et al., 2001; Wingham et al., 2009). This signal reflects glacier thinning associated with widespread ice dynamical imbalance (Konrad et al., 2017). Observations recorded by AltiKa show that the surface at Thwaites Glacier has lowered at a rate of 100 ± 20 cm/year between 2013 and 2019 and thinning exceeded 50 cm/year at distances up to 173 km from the grounding line. Over Pine Island Glacier, AltiKa recorded a rate of elevation change of 117 ± 9 cm/year over the same period with

thinning spreading inland up to 363 km from the glacier's terminus. Thinning rates recorded at these two glaciers peaked at 343 ± 33 cm/year and 216 ± 9 cm/year at Thwaites and Pine Island Glaciers, respectively. We compared these Ka-band observations with CryoSat-2 data. Over Thwaites Glacier, CryoSat-2 is recording a rate of elevation change of 136 ± 14 cm/year showing that AltiKa is slightly underestimating the elevation trend at this particular glacier, likely because AltiKa surveys only 45% of the glacier, compared to an almost complete coverage of Thwaites Glacier (97%) by Cryosat-2. On the other hand, the elevation change trend recorded by Cryosat-2 at Pine Island Glacier is in close agreement with AltiKa with a rate of 128 ± 9 cm/year.

4. Discussion and Conclusions

We provide observations of ice sheet surface elevation change from Ka-band satellite radar altimetry. Using SARAL/AltiKa measurements and a least squares model fit, we map ice thinning across the Amundsen Sea Sector of West Antarctica between March 2013 and March 2019, and we evaluate these estimates using two independent data sets—OIB airborne laser altimetry and CryoSat-2 satellite Ku-band radar altimetry. In general, the AltiKa, IceBridge, and CryoSat-2 data are in excellent agreement, with difference in elevation and elevation change in the range −59 to 68 m and −110 to 114 cm/year for 99.7% of the data, respectively. We surmise that the small positive bias in elevation between AltiKa and IceBridge is related to AltiKa's coarser ground footprint and the sloping terrain of the study region. The slope correction we applied to the AltiKa data set reduced this bias by 63%, but a small residual slope effect remains. Despite being less suited to survey the ice sheets surface than CryoSat-2 because of its orbit inclination and smaller beam width compared to the magnitude of the slope found in the margins of the ice sheet, AltiKa is still able to detect elevation change with good levels of agreement with both airborne laser altimetry and Cryosat-2. The very small difference in elevation trends between AltiKa and IceBridge, and CryoSat-2 and IceBridge, is an indicator that trends in radar altimeter penetration are negligible in this region. Although deriving total volume change from AltiKa might be challenging, as it does not sample parts of the ice sheet margins where the surface slope and roughness are high with a sufficient spatial coverage, it is still able to detect changes in the surface elevation of Thwaites and Pine Island Glaciers for instance. The new Ka-band altimetry record presented in this study reveals that the surface elevation at Thwaites and Pine Island Glaciers has reduced by 7.9 ± 1.1 m and 6.8 ± 0.5 m, respectively, between 2013 and 2019 with a change in elevation of 2.5 ± 0.8 m and 2.3 ± 0.3 m in the last 2 years (2017–2019) of our survey. These additional 2 years of data added by our study to the long altimetry record already available show that the surface elevation lowering on Pine Island and Thwaites Glacier has continued at a similar pace compared to the 2013–2017 period. However, compared to surface elevation change estimates recorded during the 2000's from a combination of ERS-2 and ENVISAT (Shepherd et al., 2019), the rate of elevation change over the fast-flowing section of Thwaites Glacier has increased by 43 % and decreased by 9 % over Pine Island Glacier compared to the AltiKa record from 2013 to 2019. Overall, our study highlights the capability of AltiKa, the first space-borne Ka-band altimeter, for measuring surface elevation change in West Antarctica.

References

Adodo, F. I., Remy, F., & Picard, G. (2018). Seasonal variations of the backscattering coefficient measured by radar altimeters over the Antarctic Ice Sheet. *The Cryosphere*, *12*(5), 17671778. https://doi.org/10.5194/tc-12-1767-2018

Bamber, J. L., Gomez-Dans, J. L., & Griggs, J. A. (2009). A new 1 km digital elevation model of the Antarctic derived from combined satellite radar and laser data—Part 1: Data and methods. *The Cryosphere*, *3*(1), 101–111.

Brenner, A. C., Bindschadler, R. A., Thomas, R. H., & Zwally, H. J. (1983). Slope-induced errors in radar altimetry over continental ice sheets. *Journal of Geophysical Research*, *88*(C3), 1617–1623.

Brown, G. (1977). The average impulse response of a rough surface and its applications. *IEEE Transactions on Antennas and Propagation*, *25*(1), 67–74.

Davis, C. H. (1997). A robust threshold retracking algorithm for measuring ice-sheet surface elevation change from satellite radar altimeters. *IEEE Transactions on Geoscience and Remote Sensing*, *35*(4), 974–979.

Davis, C. H., & Ferguson, A. C. (2004). Elevation change of the Antarctic ice sheet, 1995-2000, from ERS-2 satellite radar altimetry. *IEEE Transactions on Geoscience and Remote Sensing*, *42*(11), 2437–2445.

ESA (2012). CryoSat-2 Product Handbook, ESRIN-ESA and Mullard Space Science Laboratory, University College London. Retrieved from http://emits.sso.esa.int/emits-doc/ESRIN/7158/CryoSat-PHB-17apr2012.pdf

Flament, T., & Remy, F. (2012). Dynamic thinning of Antarctic glaciers from along-track repeat radar altimetry. *Journal of Glaciology*, *58*(211), 830–840.

Helm, V., Humbert, A., & Miller, H. (2014). Elevation and elevation change of Greenland and Antarctica derived from Cryosat-2. *The Cryosphere*, *8*(4), 1539–1559.

Joughin, I., Smith, B. E., & Medley, B. (2014). Marine ice sheet collapse potentially under way for the Thwaites Glacier Basin, West Antarctica. *Science*, *344*(6185), 735–738. https://doi.org/10.1126/science.1249055

Konrad, H., Gilbert, L., Cornford, S., Payne, A., Hogg, A., Muir, A., & Shepherd, A. (2017). Uneven onset and pace of ice-dynamical imbalance in the Amundsen Sea embayment, west Antarctica. *Geophysical Research Letters*, *44*, 910–918. https://doi.org/10.1002/2016GL07073

Lacroix, P., Legrésy, B., Coleman, R., Dechambre, M., & Rémy, F. (2007). Dual-frequency altimeter signal from Envisat on the Amery ice-shelf. *Remote Sensing of Environment*, *109*(3), 285–294.

Legresy, B., Papa, F., Remy, F., Vinay, G., Van den Bosch, M., & Zanife, O. Z. (2005). ENVISAT radar altimeter measurements over continental surfaces and ice caps using the ICE-2 retracking algorithm. *Remote Sensing of Environment*, *95*(2), 150–163.

Levinsen, J. F., Simonsen, S. B., Sorensen, L. S., & Forsberg, R. (2016). The impact of DEM resolution on relocating radar altimetry data over ice sheets. *IEEE Journal of Selected Topics in Applied Earth Observations and Remote Sensing*, *9*(7), 3158–3163.

Liu, H., Jezek, K. C., & Li, B. (1999). Development of an Antarctic digital elevation model by integrating cartographic and remotely sensed data: A geographic information system based approach. *Journal of Geophysical Research*, *104*(B10), 23,199–23,213.

McMillan, M., Leeson, A., Shepherd, A., Briggs, K., Armitage, T. W. K., Hogg, A., et al. (2016). A high-resolution record of Greenland mass balance: High-resolution Greenland mass balance. *Geophysical Research Letters*, *43*, 7002–7010. https://doi.org/10.1002/2016GL069666

McMillan, M., Shepherd, A., Muir, A., Gaudelli, J., Hogg, A., & Cullen, R. (2017). Assessment of Cryosat-2 interferometric and non-interferometric SAR altimetry over ice sheets. *Advances in Space Research*, *62*, 1281–1291.

McMillan, M., Shepherd, A., Sundal, A., Briggs, K., Muir, A., Ridout, A., et al. (2014). Increased ice losses from Antarctica detected by CryoSat. *Geophysical Research Letters*, *41*, 3899–3905. https://doi.org/10.1002/2014GL060111

Michel, A., Flament, T., & Remy, F. (2014). Study of the penetration bias of ENVISAT altimeter observations over Antarctica in comparison to ICESat observations. *Remote Sensing*, *6*(10), 9412–9434.

Mouginot, J., Rignot, E., & Scheuchl, B. (2014). Sustained increase in ice discharge from the Amundsen Sea Embayment, West Antarctica, from 1973 to 2013. *Geophysical Research Letters*, *41*, 1576–1584. https://doi.org/10.1002/2013GL059069

Nilsson, J., Gardner, A., Sorensen, L. S., & Forsberg, R. (2016). Improved retrieval of land ice topography from CryoSat-2 data and its impact for volume-change estimation of the Greenland Ice Sheet. *The Cryosphere*, *10*(6), 2953–2969.

Nilsson, J., Vallelonga, P., Simonsen, S. B., Sørensen, L. S., Forsberg, R., Dahl-Jensen, D., et al. (2015). Greenland 2012 melt event effects on CryoSat-2 radar altimetry: Effect of Greenland melt on Cryosat-2. *Geophysical Research Letters*, *42*, 3919–3926. https://doi.org/10.1002/2015GL063296

Partington, K., Cudlip, W., McIntyre, N., & King-Hele, S. (1987). Mapping of Amery Ice Shelf, Antarctica, surface features by satellite altimetry. *Annals of Glaciology*, *9*, 183–188. https://doi.org/10.3189/S0260305500000586

Pritchard, H. D., Arthern, R. J., Vaughan, D. G., & Edwards, L. A. (2009). Extensive dynamic thinning on the margins of the Greenland and Antarctic ice sheets. *Nature*, *461*(7266), 971–975. https://doi.org/10.1038/nature0847

Rémy, F., Flament, T., Michel, A., & Blumstein, D. (2015). Envisat and SARAL/AltiKa observations of the Antarctic ice sheet: A comparison between the Ku-band and Ka-band. *Marine Geodesy*, *38*(sup1), 510–521. https://doi.org/10.1080/01490419.2014.985347

Remy, F., Mazzega, P., Houry, S., Brossier, C., & Minster, J. (1989). Mapping of the topography of continental ice by inversion of satellite-altimeter data. *Journal of Glaciology*, *35*(119), 98–107.

Ridley, J. K., & Partington, K. C. (1988). A model of satellite radar altimeter return from ice sheets. *Remote Sensing*, *9*(4), 601–624. https://doi.org/10.1080/01431168808954881

Rignot, E. (2008). Changes in West Antarctic ice stream dynamics observed with Alos Palsar Data. *Geophysical Research Letters*, *35*, L12505. https://doi.org/10.1029/2008GL033365

Rignot, E., Mouginot, J., & Scheuchl, B. (2011). *MEaSUREs InSAR-Based Antarctica Ice Velocity Map*. Boulder, Colo: NASA DAAC at the Natl. Snow and Ice Data Cent. https://doi.org/10.5067/MEASURES/CRYOSPHERE/nsidc-0484.001

Rignot, E., Mouginot, J., Scheuchl, B., van den Broeke, M., van Wessem, M. J., & Morlighem, M. (2019). Four decades of Antarctic Ice Sheet mass balance from 1979–2017. *Proceedings of the National Academy of Sciences*, *116*(4), 10951103. https://doi.org/10.1073/pnas.1812883116

Roemer, S., Legrésy, B., Horwath, M., & Dietrich, R. (2007). Refined analysis of radar altimetry data applied to the region of the subglacial Lake Vostok/Antarctica. *Remote Sensing of Environment*, *106*(3), 269284. https://doi.org/10.1016/j.rse.2006.02.026

Sandberg Sørensen, L., Simonsen, S. B., Forsberg, R., Khvorostovsky, K., Meister, R., & Engdahl, M. (2018). 25 years of elevation changes of the Greenland ice sheet from ERS, Envisat, and Cryosat-2 radar altimetry. *Earth and Planetary Science Letters*, *495*, 234–241.

Schröder, L., Horwath, M., Dietrich, R., Helm, V., van den Broeke, M. R., & Ligtenberg, S. R. M. (2019). Four decades of Antarctic surface elevation changes from multi-mission satellite altimetry. *The Cryosphere*, *13*(2), 427–449.

Shepherd, A., Gilbert, L., Muir, A. S., Konrad, H., Mcmillan, M., Slater, T., et al. (2019). Trends in Antarctic ice sheet elevation and mass. *Geophysical Research Letters*, *46*, 8174–8183. https://doi.org/10.1029/2019GL082182

Shepherd, A., Wingham, D. J., Justin, A. D. M., & Hugh, F. J. C. (2001). Inland thinning of Pine Island Glacier, West Antarctica. *Science*, *291*(5505), 862–864.

Shepherd, A., Wingham, D. J., & Mansley, J. A. D. (2002). Inland thinning of the Amundsen Sea Sector, West Antarctica. *Geophysical Research Letters*, *29*(10), 1364. https://doi.org/10.1029/2001GL014183

Simonsen, S. B., & Sandberg Sørensen, L. (2017). Implications of changing scattering properties on Greenland ice sheet volume change from Cryosat-2 altimetry. *Remote Sensing of Environment*, *190*, 2017–2216. https://doi.org/10.1016/j.rse.2016.12.012

Slater, T., Shepherd, A., McMillan, M., Muir, A., Gilbert, L., Hogg, A. E., et al. (2018). A new digital elevation model of Antarctica derived from CryoSat-2 altimetry. *The Cryosphere*, *12*(4), 1551–1562. https://doi.org/10.5194/tc-12-1551-2018

Smith, B., Gourmelen, N., Huth, A., & Joughin, I. (2017). Connected subglacial lake drainage beneath Thwaites Glacier, West Antarctica. *The Cryosphere*, *11*(1), 451–467. https://doi.org/10.5194/tc-11-451-2017

Steunou, N., Desjonquères, J. D., Picot, N., Sengenes, P., Noubel, J., & Poisson, J. C. (2015). AltiKa Altimeter: Instrument Description and In Flight Performance. *Marine Geodesy*, *38*(sup1), 2242. https://doi.org/10.1080/01490419.2014.988835

Studinger, M. (2014a). updated 2018. IceBridge ATM L2 Icessn elevation, slope, and roughness, Version 2. [2013 to 2016] Boulder, Colorado USA. NASA National Snow and Ice Data Center Distributed Active Archive Center.: https://doi.org/10.5067/CPRXXK3F39RV.

Studinger, M. (2014b). updated 2018. IceBridge ATM L4 surface elevation rate of change, Version *1*. [2013 to 2016]. Boulder, Colorado USA. NASA National Snow and Ice Data Center Distributed Active Archive Center.: https://doi.org/10.5067/BCW6CI3TXOCY.

Suryawanshi, M. R., Chander, S., Oza, S. R., & Bahuguna, I. M. (2019). Variability in the ice sheet elevations over Antarctica derived from repetitive SARAL/AltiKa radar altimeter data (2013–2016). *Journal of Earth System Science*, *128*(3), 1–11. https://doi.org/10.1007/s12040-019-1093-x

Verron, J., Sengenes, P., Lambin, J., Noubel, J., Steunou, N., Guillot, A., et al. (2015). The SARAL/AltiKa altimetry satellite mission. *Marine Geodesy*, *38*(sup1), 2–21. https://doi.org/10.1080/01490419.2014.1000471

Verron, J., Bonnefond, P., Aouf, L., Birol, F., Bhowmick, S., Calmant, S., ... Vergara, O. (2018). The Benefits of the Ka-Band as Evidenced from the SARAL/AltiKa Altimetric Mission: Scientific Applications. *Remote Sensing*, *10*(2), 163. https://doi.org/10.3390/rs10020163

Wingham, D., Francis, C. R., Baker, S., Bouzinac, C., Cullen, R., de Chateau-Thierry, P., et al. (2006). CryoSat: A mission to determine the fluctuations in Earth's land and marine ice fields. *Advances in Space Research*, *37*, 841–871. https://doi.org/10.1016/j.asr.2005.07.027

Wingham, D. J., Rapley, C. G., & Griffiths, H. (1986). New techniques in satellite altimeter tracking systems. In T. D. Guyenne & J. J. Hunt (Eds.), *Proceedings of the IGARSS Symposium* (Vol. SP-254, pp. 1339–1344). Zurich: European Space Agency.

Wingham, D. J., Ridout, A. J., Scharroo, R., Arthern, R. J., & Shum, C. K. (1998). Antarctic elevation change from 1992 to 1996. *Science*, *282*(5388), 456–458. https://doi.org/10.1126/science.282.5388.45

Wingham, D. J., Wallis, D. W., & Shepherd, A. (2009). Spatial and temporal evolution of Pine Island Glacier thinning, 1995–2006. *Geophysical Research Letters*, *36*, L17501. https://doi.org/10.1029/2009GL039126

Yang, Q., Yang, Y., Wang, Z., Zhang, B., & Jiang, H. (2018). Elevation change derived from SARAL/ALtiKa Altimetric Mission: Quality assessment and performance of the Ka-band. *Remote Sensing*, *10*, 539.

APPENDIX D

Surface Melting Drives Fluctuations in Airborne

Radar Penetration in West Central Greenland

Surface Melting Drives Fluctuations in Airborne Radar Penetration in West Central Greenland

Inès N. Otosaka[1] [ID], Andrew Shepherd[1] [ID], Tânia G. D. Casal[2], Alex Coccia[3], Malcolm Davidson[2], Alessandro Di Bella[4] [ID], Xavier Fettweis[5] [ID], René Forsberg[4] [ID], Veit Helm[6] [ID], Anna E. Hogg[7] [ID], Sine M. Hvidegaard[4] [ID], Adriano Lemos[1,8] [ID], Karlus Macedo[3], Peter Kuipers Munneke[9] [ID], Tommaso Parrinello[10], Sebastian B. Simonsen[4] [ID], Henriette Skourup[4] [ID], and Louise Sandberg Sørensen[4] [ID]

[1]Centre for Polar Observation and Modelling, School of Earth and Environment, University of Leeds, Leeds, UK, [2]ESA-ESTEC, Noordwijk, The Netherlands, [3]Metasensing, Noordwijk, The Netherlands, [4]Technical University of Denmark, DTU Space, Lyngby, Denmark, [5]University of Liège, Liège, Belgium, [6]Alfred Wegener Institute, Helmholtz Centre for Polar and Marine Research, Bremerhaven, Germany, [7]School of Earth and Environment, University of Leeds, Leeds, UK, [8]Now at University of Gothenburg, Göteborg, Sweden, [9]Institute for Marine and Atmospheric Research Utrecht, Utrecht University, Utrecht, The Netherlands, [10]ESA-ESRIN, Frascati, Italy

Abstract Greenland Ice Sheet surface melting has increased since the 1990s, affecting the rheology and scattering properties of the near-surface firn. We combine firn cores and modeled firn densities with 7 years of CryoVEx airborne Ku-band (13.5 GHz) radar profiles to quantify the impact of melting on microwave radar penetration in West Central Greenland. Although annual layers are present in the Ku-band radar profiles to depths up to 15 m below the ice sheet surface, fluctuations in summer melting strongly affect the degree of radar penetration. The extreme melting in 2012, for example, caused an abrupt 6.2 ± 2.4 m decrease in Ku-band radar penetration. Nevertheless, retracking the radar echoes mitigates this effect, producing surface heights that agree to within 13.9 cm of coincident airborne laser measurements. We also examine 2 years of Ka-band (34.5 GHz) airborne radar data and show that the degree of penetration is half that of coincident Ku-band.

Plain Language Summary Radar waves emitted by satellites can be used to measure changes in surface elevation of the Greenland Ice Sheet. However, they do not reflect off the ice sheet surface itself but penetrate into the snow to a depth of about 15 m for radar wavelengths of 2.3 cm. When the snow melts, meltwater can percolate into the snow or refreeze at the surface. Layers of refrozen ice sharply reduce the degree of radar penetration and may be mistaken for an elevation increase in radar measurements. Here, we combine firn cores and modeled firn densities with 7 years of airborne radar data collected during field campaigns in West Central Greenland to quantify this effect. We identify internal layers corresponding to annual stratigraphy within the snowpack, and we show that more melt means less radar penetration into the firn. The unprecedented surface melting which occurred across Greenland in 2012 caused a sharp reduction in the degree of radar penetration, from 11.5 to 5.3 m. However, if the effects of penetration are corrected for, radar altimeters can accurately measure the surface elevation of the ice sheet.

1. Introduction

In recent decades, increased melting at the surface of the Greenland Ice Sheet (van den Broeke et al., 2016) has had a marked impact on rates of runoff (Enderlin et al., 2014; van Angelen et al., 2014) and glacier flow (van de Wal et al., 2008), and has also affected the structure of the near-surface firn owing to the redistribution and refreezing of surface meltwater (de la Peña et al., 2015; Machguth et al., 2016). These processes, and the associated changes in firn properties, present challenges for satellite radar altimetry surveys of the ice sheet mass balance when converting observations of volume change to mass change (McMillan et al., 2016). Surface melting has a large impact on the firn stratigraphy and density as meltwater can refreeze at the surface, or percolate into the snowpack and refreeze to form ice lenses (Benson, 1996), or refreeze in between already existing ice layers and form thicker ice slabs (MacFerrin et al., 2019). Ice cores provide records of density and stratigraphy at point locations (Mosley-Thompson et al., 2001) and firn densification models provide estimates of densities across the ice sheet (e.g., Kuipers Munneke et al., 2015). Radars have also

been widely used over glaciers and ice sheets to map their structure (MacGregor et al., 2015), calculate accumulation rates (Miège et al., 2017), and track changes in their elevation (Shepherd et al., 2019).

Radar systems transmit electromagnetic pulses and record the amplitude and time delay of the waves scattered back from discontinuities in the dielectric properties. Their echoes are sensitive to density variations in the firn column, and the firn structure can reveal continuous internal scattering horizons, corresponding to isochrones (Hawley et al., 2006). Both ground-based (Brown et al., 2012) and airborne radar, such as the snow radar flown during NASA Operation IceBridge (Koenig et al., 2016; Medley et al., 2013; Montgomery et al., 2020) or the European Space Agency's Airborne SAR/Interferometric Radar Altimeter System (ASIRAS) operating at Ku-band (de la Peña et al., 2010; Helm et al., 2007; Overly et al., 2016; Simonsen et al., 2013), have been used to track isochrones and derive accumulation rates. Unlike ground-based and airborne radar, satellite radar measurements lack the vertical resolution to resolve the internal structure of the firn column due to the smaller bandwidth and coarser spatial resolution of the radar footprint. Nonetheless, satellite radar altimeters are sensitive to variations in the firn properties as the radar signal penetrates into the snowpack. Additionally, the radar signal penetration is frequency dependent. At present, two frequencies are used by satellite radar altimeters: Ku-band (13.5 GHz) is used by CryoSat-2 and Sentinel 3A/B, and Ka-band (37 GHz) is used by AltiKa. Studies have shown that at Ku-band, the radar signals can penetrate up to ~15 m into firn, while the penetration depth of higher-frequency Ka-band radars is reduced to ~0.5 m (Rémy et al., 2015). The altimeter echo recorded is therefore a combination of surface and volume scattering (Ridley & Partington, 1988). The ratio between surface and volume scattering varies spatially and temporally according to changes in the surface and subsurface properties and may impact the height retrieval from radar altimeters (Simonsen & Sørensen, 2017).

In this study, we use airborne Ku-band radar data acquired using the ASIRAS instrument, Ka-band radar data acquired using the KAREN radar (the MetaSensing Ka-band altimeter), airborne laser data, shallow firn cores (< 6 m), and firn density models to characterize and assess the impact of spatial and temporal fluctuations in the properties of the near-surface firn in West Central Greenland. This study is performed along the glaciological transect established during the Expéditions Glaciologiques Internationales au Groenland (EGIG) in 1958 (Renaud et al., 1963). The EGIG line extends from the ablation zone at the Western margin of the ice sheet, across the percolation and dry snow zones to the Summit, and further toward the Eastern margin and is therefore a representative location of density variations across the Greenland Ice Sheet (Parry et al., 2007).

2. Data and Methods

The EGIG line (Figure 1a) has been surveyed for more than a decade as part of ESA's Cryosat Validation Experiment (CryoVEx). According to previous in situ investigations of snow density and stratigraphy, EGIG line sites T3 to T21 lie in the percolation zone with site T21 marking the start of the dry snow zone (Morris & Wingham, 2011; Scott et al., 2006). In this study, we use data collected between 2006 and 2017 over a ~675 km transect of the EGIG line, starting about 14 km from Ilullissat airport at an elevation of 157 m above sea level (m.a.s.l.), 115 km before site T1, and ending 149 km beyond site T41 at an altitude of 2,956 m.a.s.l.

Shallow firn cores were collected in October 2016 (T1, T4, and T5) and April 2017 (T5, T9, T12, T19, T30, and T41) (Table S1 in the supporting information). The stratigraphy was recorded by illuminating the cores to identify ice lenses. Firn density was measured by weighing the different stratigraphic layers (see Supporting Information S1). These in situ density measurements are used to evaluate two firn densification models: (1) the stand-alone Institute for Marine and Atmospheric Research Utrecht firn densification model (IMAU-FDM) (Ligtenberg et al., 2011, 2018), forced at the surface by RACMO (Noël et al., 2018). IMAU-FDM simulates the density and temperature in a vertical, one-dimensional firn column through time at a vertical resolution of 5 cm and (2) the CROCUS snow model (Brun et al., 1992) embedded in the Modèle Atmosphérique Régional (MAR) (version 3.10, Fettweis et al., 2017, 2020) to derive the MAR firn densification model (MAR-FDM). CROCUS simulates the transfer of mass and energy between a fixed number of layers of snow, firn, or ice with a vertical resolution varying from 5 to 500 cm.

Airborne radar data were collected in 2004, 2006, 2008, 2011, 2012, 2014, 2016, and 2017, along segments of the EGIG line of varying length. For all CryoVEx airborne surveys, the same aircraft and instrumental setup
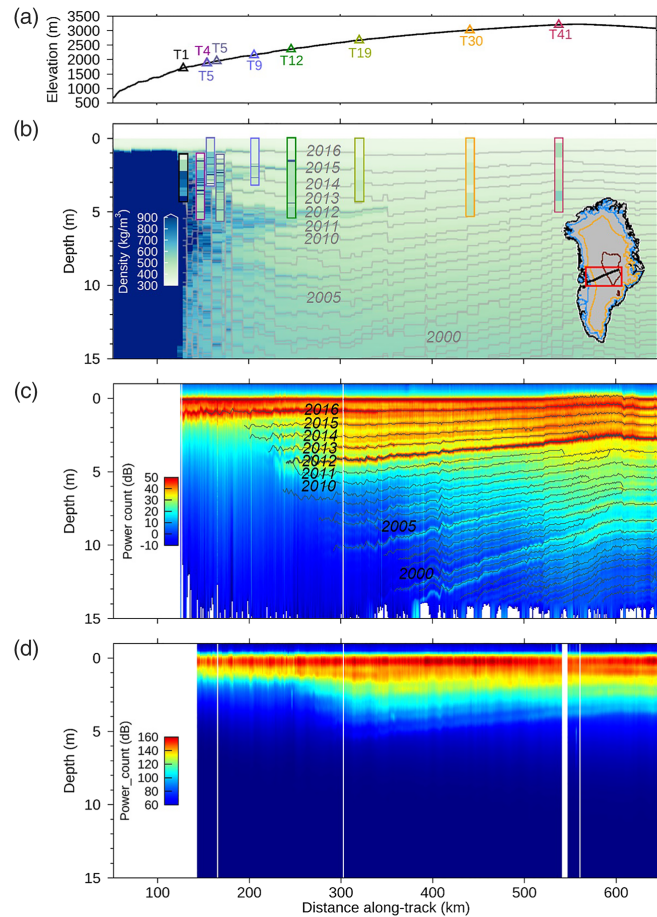
Figure 1. (a) Elevation profile along the EGIG line. (b) IMAU-FDM density profile (31/03/2017) and firn core densities. The isochrones traced from IMAU-FDM are indicated by gray lines. The firn cores from 2016 are offset by the net SMB relative to 2017. The inset shows the location of the study area. (c) ASIRAS Ku-band radar profile. The traced layers are indicated by black lines. (d) KAREN Ka-band radar profile. The two radar profiles were acquired on 31/03/2017 and 01/04/2017. Along-track distance is relative to Ilulissat airport.

were used, which includes an airborne laser scanner (ALS), the ASIRAS radar, and the KAREN radar in two surveys in 2016 and 2017. The ALS is a Riegl LMS-Q140-i60 laser scanner operating at 904 nm (red), which gives surface heights in 0.7 m intervals across a 300-m-wide swath with an accuracy of 0.1 m (Skourup et al., 2019). ASIRAS is a Ku-band radar designed as a prototype for the SIRAL altimeter on board CryoSat-2 operating at a central frequency of 13.5 GHz with a bandwidth of 1.0 GHz, range resolution of 0.109 m in air, and a nominal footprint size of 10 m across-track and 3 m along-track at a flight elevation of ~300 m a.g.l. (Cullen, 2010). KAREN is a Ka-band radar altimeter operating at a central frequency of 34.5 GHz—the same frequency used by AltiKa—with a bandwidth of ~0.5 GHz, range resolution of 0.165 m in air, and a footprint size of 10 m across-track and 5 m along-track (version "levc"). Data acquired when the aircraft roll angle exceeded $\pm 1.5°$ were discarded.

Figure 2. (a) Scatterplot of firn core densities versus model (IMAU- and MAR-FDM) densities. (b) Scatterplot of the IMAU-FDM isochrones depths versus ASIRAS internal layers depths.

We applied three different retracking algorithms to locate the ice sheet surface in the radar echoes as different processing strategies have been shown to affect the elevation measurements when the radar penetration depth varies (Slater et al., 2019). We used (1) an offset center of gravity (OCOG) retracker (Wingham et al., 1986), (2) a 30% threshold center of gravity (TCOG) retracker (Davis, 1997) similar to the retracker implemented in CryoSat-2 ground segment, and (3) a 50% threshold first maximum retracking algorithm (TFMRA, Helm et al., 2014). Each retracker's performance was evaluated by comparing their elevations to those recorded by the ALS, after calibrating ASIRAS and KAREN relative to the ALS along runway over-flights (Tables S2 and S3). We aligned each radar waveform to the ice sheet surface and took the mean radar waveforms in 1 km segments along-track to reduce noise. We converted the radar two-way travel time to depth using a depth-density profile from the MAR output. Finally, internal layers present within each ASIRAS profile were traced in an automated way with their chronology resolved relative to the surface (de la Peña et al., 2010; Hawley et al., 2006) (see Supporting Information S1).

3. Results

We evaluated the modeled firn densities by comparison to those measured in the shallow cores (Figure 1b). The IMAU- and MAR-FDM densities are highly correlated with the cores ($r = 0.93$ and 0.89, respectively) and show good overall agreement, with root-mean-square differences (RMSD) of 64 and 104 kg/m^3, respectively (Figure 2a). However, we note a spatial pattern in the difference between the in situ and modeled densities. At sites below 2,000 m (T1 to T5), IMAU-FDM overestimates firn density by 10% on average and underestimates firn density by 11% at higher elevation sites. MAR-FDM exhibits a similar bias, with an overestimation of 21% on average at sites below 2,000 m, and an 11% underestimation of firn density at higher elevation sites. The largest departure from the firn cores is recorded for both models at site T1, located at an elevation of 1,698 m in the low percolation zone. At this site, we measured a total of 40 cm of ice from the firn core while IMAU- and MAR-FDM simulated a total of 188 and 294 cm of ice in the corresponding firn column, indicating that the firn ice content is overestimated in the lower section of the EGIG line (Figure S1a).

The ASIRAS radar profiles across the EGIG line (Figure 1c) show a clear sequence of internal layers starting at an elevation of ~2,200 m, which we attribute to melt and refreezing in the percolation zone and to autumn hoar in the dry snow zone. We compare the distribution and sequence of internal layers present within the 2017 ASIRAS profile to isochrones derived from the 2017 IMAU-FDM firn density and chronology. We identify annual isochrones in the IMAU-FDM profile by locating the maximum firn density in data of the same age. The ASIRAS internal layers and IMAU-FDM chronology are highly correlated ($r = 0.99$, Figure 2b) with a robust dispersion estimate (RDE) of 71 cm. However, compared to the radar layers, IMAU-FDM annual isochrones are consistently found deeper in the firn column, with a systematic bias of 17.1%. The bias between the modeled isochrones and the observed layers accumulates with depth, shifting the distribution of annual layers compared to the radar observations. After adjusting the IMAU-FDM isochrones for this systematic bias, the radar layers and modeled isochrones are well-aligned with an overall RDE of 26 cm and
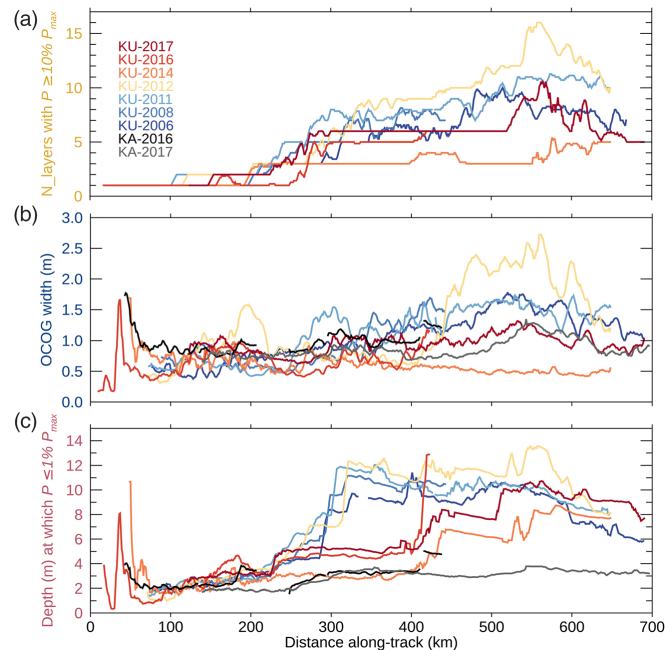
Figure 3. (a) Number of layers above 10% of the maximum surface return. (b) OCOG width. (c) Depth at which power falls below 1% of the maximum surface return.

RMSEs of 14 cm for the top 2016 isochrone and 21 cm for the 2012 isochrone (Figure S5). The close agreement between the sequence and depth of the ASIRAS internal layers with the IMAU-FDM chronology leads us to conclude they are recording the same physical features.

The layers recorded in the ASIRAS profiles show marked interannual variability, with a clear transition after 2012 (Figure S2). Until 2012, the top two isochrones are the strongest peaks in the radar return. Afterwards in 2014, however, the strongest peaks correspond to the surface layer and the 2012 isochrone. In 2016 and 2017, even though the 2012 isochrone is located deeper in the snowpack, the associated waveform peak remains relatively high—at 33% and 29% of the maximum peak respectively. The strong dielectric contrast of the 2012 melt layer—reducing the energy transmitted to the deeper firn column—is linked to the formation of an ice lens following the intense melt event of that year (Nghiem et al., 2012). This attenuation of the radar backscatter is seen in both the percolation and the dry snow zone. In the percolation zone, we recorded a 1-cm-thick ice lens at a depth of 4.4 m in the firn core collected at site T12 in 2017 (at an elevation of 2,352 m). This layer is aligned with the 2012 isochrone measured at a depth of 4.4 ± 0.2 m in ASIRAS data collected in the same year. At elevations above 2,500 m and prior to the melt event in 2012, the Ku-band radar records significant power (above 1% of the maximum surface return) to a depth of 11.5 ± 1.3 m below the ice sheet surface (Figure 4a). After the melt event, the attenuation in the firn column is mainly driven by the strong reflection at the 2012 melt layer, and as a result, the degree of radar penetration is reduced to 5.3 ± 2.0 m in 2014 and 7.5 ± 2.0 m in 2017. The strong reduction in radar penetration coincides with a peak in the density anomaly recorded by IMAU-FDM of 32.9 kg/m^3 and by MAR-FDM of 63.0 kg/m^3, which demonstrates that the near-surface firn densities and degree of the radar penetration are linked (Figure 4b).

We observe strong spatial variations in the degree of radar penetration into the near-surface firn along the EGIG line (Figure 3). In all years, few or no internal layers are present in the ASIRAS data in the ablation and percolation zones below ~2,200 m, after which their abundance begins to increase with surface elevation as the firn density falls. The number of layers with significant power (above 10% of the maximum surface
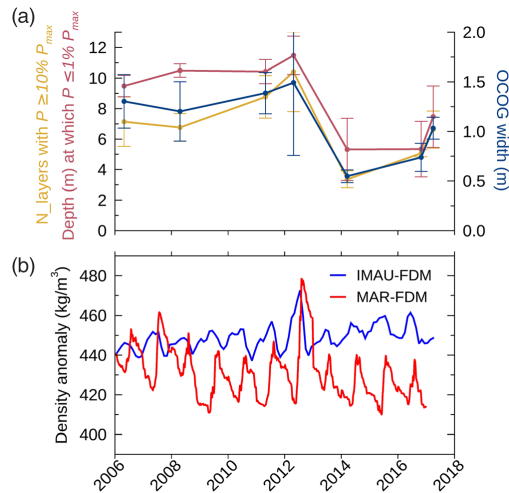
Figure 4. (a) Temporal variations of the mean of three proxies for penetration depth derived from ASIRAS radar profiles presented on Figure 3 over the section 300–600 km along-track. Error bars indicate the standard deviation. (b) Density anomaly from IMAU- and MAR-FDMs centered around the mean over the same section (see Supporting Information S1).

return) varies in a similar manner to the OCOG retracker width, indicating that strong near-surface scattering has masked scattering at depth. In the ablation and percolation zones, water percolates into the winter snow and new ice lenses or layers are formed each year, preventing the radar signal from penetrating deep into the firn. This process leads to a reduction of the OCOG width, because the main scattered energy is concentrated nearer the ice sheet surface. In all years, the OCOG retracker width and the number of layers show a tendency to increase with elevation and reach maxima at the highest elevation of the transect. However, the maximum number of layers visible and the maximum OCOG retracker width vary from year to year; in 2014, for example, the maxima of both parameters above 2,500 m are more than three times lower than in 2012. Furthermore, compared to 2012, the range of variations in OCOG width is reduced by 86% in 2014 over the same section, which shows that spatial variations in volume scattering are also less prominent after the 2012 melt event.

We evaluate the impact of volume scattering fluctuations on the performance of three alternative radar retrackers—OCOG, TCOG, and TFMRA. Both the TCOG and TFMRA retrackers track the very first peak recorded by the radar altimeter and identify the surface at similar locations with a mean difference of 7.1 cm and standard deviation of 1.9 cm. On the other hand, the OCOG retracker follows the center of gravity of the radar echoes. At elevations above 3,000 m, the scattering horizon is shifted toward the snow surface after the melt event in 2014 compared to 2012, resulting in a 73-cm increase in the altimetry range measurement using the OCOG retracker. We compare the heights from each of the retrackers to the ALS heights (Table S4). Over a total of 2,496 km of flights acquired on five different years, the mean difference between the ALS and OCOG heights was 107 cm, with a standard deviation of 55 cm. By comparison, the TCOG and TFMRA retracked heights are in far better agreement with the ALS data, with mean differences of 14 and 20 cm, and standard deviations of 20 and 21 cm, respectively. Despite the large fluctuations in volume scattering that have occurred along the EGIG line as a consequence of changes in the snowpack structure, the TCOG and TFMRA retracking of radar heights is stable, demonstrating that these algorithms are effective methods of mitigating the impact of radar penetration variations.

4. Discussion

The two firn densification models we have tested at the EGIG line are able to reproduce the mean density of the shallow firn column with typical differences of 10% (IMAU) and 15% (MAR-FDM) by comparison to in situ measurements. At site T1 in particular, the firn ice content is largely overestimated by the models with more than 59% and 92% of the total length of the firn core simulated as ice by IMAU- and MAR-FDM, respectively, compared to only 13% from the field observations. This indicates that surface melt and refreezing might not be quantified properly in the lower percolation zone of the EGIG line. However, using the density measured from the firn cores or the density outputs from either of these models to convert the radar travel time to depth leads to mean differences within 13 cm. Nevertheless, small biases in modeled firn density do accumulate with depth, offsetting the vertical distribution of annual ice layers (Figure 2b). We also investigate to which extent firn densification models are able to capture the distribution of annual melt layers within the firn column compared to radar-derived layers. This requires a firn model with a fine vertical resolution, such as the IMAU-FDM, to resolve the different layers, which are typically spaced between 30 and 100 cm apart. Although the chronology and spatial distribution of isochrones derived from the IMAU-FDM show good agreement with the internal layers detected by ASIRAS, there is a systematic bias of 17.1% between the two data sets, which we suspect is due to an underestimation of the firn densification rate. This shows that capturing the density variability in the firn column is more challenging than simulating the mean density of the column as suggested by firn model intercomparison studies (Vandecrux et al., 2018; Verjans et al., 2019).

We link the sharp reduction in the degree of radar penetration depth after 2012 to the 2012 melt event. Over elevations of 2,500 m, the 2012 isochrone is recorded in the Ku-band altimetry echoes at a depth of 1.5 ± 0.2 m with a significant power of 82% of the maximum surface return and in 2014 at a depth of 3.7 ± 0.2 m with a significant power of 60% (Figure 4a). Over the same part of the transect, the melt layer is also captured by the IMAU- and MAR-FDM with a high density peak after the 2012 summer, which is double the density of the previous summer's peak. In general, when surface melting occurs, the degree of radar penetration into the near-surface firn reduces sharply. The density fluctuations recorded above 2,500 m in 2012 are the largest since 2006 (Figure 4b) and coincide with the fluctuations in radar penetration recorded in the same year. This is shown by the 63% decrease in the OCOG width, the 68% reduction in the number of layers with a high power return, and the 6.2 ± 2.4 m decrease in the radar penetration depth. Such density fluctuations lead to instantaneous upwards (toward the surface) shifts in the distribution of power within the radar echo, followed by gradual downwards (away from the surface) returns to pre-melt conditions. These saw-tooth variations in radar penetration lead to aliased fluctuations in the elevation of the scattering surface, explaining effects that have been highlighted (and corrected for) in analyses of satellite radar altimetry (McMillan et al., 2016; Nilsson et al., 2015; Slater et al., 2019).

We explored two approaches to mitigate the impact of these density fluctuations on surface elevation derived from radar altimetry. First, we found that the application of threshold waveform echo retracking is able to provide estimates that agreed to within 20 cm of coincident laser altimetry. We also examined the sensitivity of higher-frequency Ka-band radar data to volume scattering, as an alternative means of mitigating firn density fluctuations. At higher frequencies, surface scattering is relatively stronger than volume scattering, and we find that the penetration depth is smaller at Ka-band than Ku-band. For example, in 2016 and 2017, although significant power was recorded in ASIRAS Ku-band radar at depths of up to 6.8 ± 0.3 m below the surface along the high altitude section of the EGIG line (300 to 600 km), the corresponding KAREN Ka-band radar penetration was 3.4 ± 0.3 m. We also compared Ka-band surface elevation estimates to those recorded by the ALS (Table S5). Over a total of 782 km of KAREN flight tracks, the mean difference between the KAREN and laser data, when using OCOG, TCOG, and TFMRA retracking algorithms, was 16.0, 12.5, and 15.6 cm, respectively, with standard deviations of 10.8, 10.9, and 11.3 cm. A more detailed assessment of the Ka-band penetration depth was not possible due to the reduced bandwidth of KAREN compared to ASIRAS, which prevents internal layering from being resolved (Figure 1d).

5. Conclusions

We present an extensive and coincident set of near-surface firn density and airborne radar and laser measurements acquired between 2006 and 2017 along the EGIG line in West Central Greenland. Using these data, we examine the impacts of firn density fluctuations on spatial and temporal variations in the scattering of airborne ASIRAS Ku-band radar waveforms. The largest fluctuations in radar penetration over this period are recorded after 2012 with an abrupt decrease of 6.2 ± 2.4 m in the Ku-band radar penetration. We link this decrease in radar penetration to the density fluctuations associated with the 2012 extreme melt event. As the frequency and extent of extreme melt events is likely to increase in the coming decades (Hall et al., 2013), the effects of fluctuations in radar penetration are an important consideration for satellite radar altimetry. We find that simple methods of threshold retracking are efficient at mitigating this effect on Ku-band airborne radar data and the impact of such events are likely to last for a shorter period of time on Ka-band data due to its reduced penetration depth.

Data Availability Statement

The ASIRAS, KAREN, and ALS raw data are freely available from the European Space Agency at https://earth.esa.int/web/guest/campaigns. Ice core data, IMAU-FDM, MAR-FDM, ASIRAS, and KAREN profiles are available on PANGAEA at https://doi.pangaea.de/10.1594/PANGAEA.921673.

References

van Angelen, J. H., van den Broeke, M. R., Wouters, B., & Lenaerts, J. T. M. (2014). Contemporary (1960–2012) evolution of the climate and surface mass balance of the Greenland ice sheet. *Surveys in Geophysics*, 35(5), 1155–1174. https://doi.org/10.1007/s10712-013-9261-z

Benson, C. S. (1996). *Stratigraphic studies in the snow and firn of the Greenland ice sheet (No. SIPRE-RR-70)*. Wilmette, IL: U.S. Army Snow, Ice and Permafrost Research Establishment.

Brown, J., Bradford, J., Harper, J., Pfeffer, W. T., Humphrey, N., & Mosley-Thompson, E. (2012). Georadar-derived estimates of firn density in the percolation zone, western Greenland ice sheet. *Journal of Geophysical Research*, *117*, F01011. https://doi.org/10.1029/2011JF002089

Brun, E., David, P., Sudul, M., & Brunot, G. (1992). A numerical model to simulate snow-cover stratigraphy for operational avalanche forecasting. *Journal of Glaciology*, *38*(128), 13–22. https://doi.org/10.1017/S0022143000009552

Cullen, R. (2010). *CryoVEx airborne data products description. Noordwijk*, The Netherlands: European Space Agency, ESTEC.

Davis, C. H. (1997). A robust threshold retracking algorithm for measuring ice-sheet surface elevation change from satellite radar altimeters. *IEEE Transactions on Geoscience and Remote Sensing*, *35*(4), 974–979. https://doi.org/10.1109/36.602540

de la Peña, S., Howat, I. M., Nienow, P. W., van den Broeke, M. R., Mosley-Thompson, E., Price, S. F., et al. (2015). Changes in the firn structure of the western Greenland Ice Sheet caused by recent warming. *The Cryosphere*, *9*(3), 1203–1211. https://doi.org/10.5194/tc-9-1203-2015

de la Peña, S., Nienow, P., Shepherd, A., Helm, V., Mair, D., Hanna, E., et al. (2010). Spatially extensive estimates of annual accumulation in the dry snow zone of the Greenland Ice Sheet determined from radar altimetry. *The Cryosphere*, *4*(4), 467–474. https://doi.org/10.5194/tc-4-467-2010

Enderlin, E. M., Howat, I. M., Jeong, S., Noh, M.-J., van Angelen, J. H., & van den Broeke, M. R. (2014). An improved mass budget for the Greenland ice sheet. *Geophysical Research Letters*, *41*(3), 866–872. https://doi.org/10.1002/2013gl059010

Fettweis, X., Box, J. E., Agosta, C., Amory, C., Kittel, C., Lang, C., et al. (2017). Reconstructions of the 1900–2015 Greenland Ice Sheet surface mass balance using the regional climate MAR model. *The Cryosphere*, *11*(2), 1015–1033. https://doi.org/10.5194/tc-11-1015-2017

Fettweis, X., Hofer, S., Krebs-Kanzow, U., Amory, C., Aoki, T., Berends, C. J., et al. (2020). GrSMBMIP: Intercomparison of the modelled 1980–2012 surface mass balance over the Greenland Ice Sheet. *The Cryosphere Discussions*. https://doi.org/10.5194/tc-2019-321, in review

Hall, D. K., Comiso, J. C., Digirolamo, N. E., Shuman, C. A., Box, J. E., & Koenig, L. S. (2013). Variability in the surface temperature and melt extent of the Greenland Ice Sheet from MODIS. *Geophysical Research Letters*, *40*, 2114–2120. https://doi.org/10.1002/grl.50240

Hawley, R. L., Morris, E. M., Cullen, R., Nixdorf, U., Shepherd, A. P., & Wingham, D. J. (2006). ASIRAS airborne radar resolves internal annual layers in the dry-snow zone of Greenland. *Geophysical Research Letters*, *33*, L04502. https://doi.org/10.1029/2005GL025147

Helm, V., Humbert, A., & Miller, H. (2014). Elevation and elevation change of Greenland and Antarctica derived from CryoSat-2. *The Cryosphere*, *8*(4), 1539–1559. https://doi.org/10.5194/tc-8-1539-2014

Helm, V., Rack, W., Cullen, R., Nienow, P., Mair, D., Parry, V., & Wingham, D. J. (2007). Winter accumulation in the percolation zone of Greenland measured by airborne radar altimeter. *Geophysical Research Letters*, *34*, L06501. https://doi.org/10.1029/2006GL029185

Koenig, L. S., Ivanoff, A., Alexander, P. M., MacGregor, J. A., Fettweis, X., Panzer, B., et al. (2016). Annual Greenland accumulation rates (2009–2012) from airborne snow radar. *The Cryosphere*, *10*(4), 1739–1752. https://doi.org/10.5194/tc-10-1739-2016

Kuipers Munneke, P., Ligtenberg, S. R. M., Noël, B. P. Y., Howat, I. M., Box, J. E., Mosley-Thompson, E., et al. (2015). Elevation change of the Greenland Ice Sheet due to surface mass balance and firn processes, 1960-2014. *The Cryosphere*, *9*(6), 2009–2025. https://doi.org/10.5194/tc-9-2009-2015

Ligtenberg, S., Helsen, M., & van den Broeke, M. (2011). An improved semi-empirical model for the densification of Antarctic firn. *The Cryosphere*, *5*(4), 809–819. https://doi.org/10.5194/tc-5-809-2011

Ligtenberg, S. R. M., Kuipers Munneke, P., Noël, B. P. Y., & van den Broeke, M. R. (2018). Brief communication: Improved simulation of the present-day Greenland firn layer (1960–2016). *The Cryosphere*, *12*(5), 1643–1649. https://doi.org/10.5194/tc-12-1643-2018

MacFerrin, M., Machguth, H., As, D. V., Charalampidis, C., Stevens, C. M., Heilig, A., et al. (2019). Rapid expansion of Greenland's low-permeability ice slabs. *Nature*, *573*(7774), 403–407. https://doi.org/10.1038/s41586-019-1550-3

MacGregor, J. A., Fahnestock, M. A., Catania, G. A., Paden, J. D., Prasad Gogineni, S., Young, S. K., et al. (2015). Radiostratigraphy and age structure of the Greenland Ice Sheet. *Journal of Geophysical Research: Earth Surface*, *120*, 212–241. https://doi.org/10.1002/2014JF003215

Machguth, H., MacFerrin, M., van As, D., Box, J. E., Charalampidis, C., Colgan, W., et al. (2016). Greenland meltwater storage in firn limited by near-surface ice formation. *Nature Climate Change*, *6*(4), 390–393. https://doi.org/10.1038/nclimate2899

McMillan, M., Leeson, A., Shepherd, A., Briggs, K., Armitage, T. W. K., Hogg, A., et al. (2016). A high-resolution record of Greenland mass balance: High-resolution Greenland mass balance. *Geophysical Research Letters*, *43*, 7002–7010. https://doi.org/10.1002/2016GL069666

Medley, B., Joughin, I., Das, S. B., Steig, E. J., Conway, H., Gogineni, S., et al. (2013). Airborne-radar and ice-core observations of annual snow accumulation over Thwaites Glacier, West Antarctica confirm the spatiotemporal variability of global and regional atmospheric models. *Geophysical Research Letters*, *40*, 3649–3654. https://doi.org/10.1002/grl.50706

Miège, C., Forster, R. R., Box, J. E., Burgess, E. W., Mcconnell, J. R., Pasteris, D. R., & Spikes, V. B. (2017). Southeast Greenland high accumulation rates derived from firn cores and ground-penetrating radar. *Annals of Glaciology*, *54*(63), 322–332.

Montgomery, L., Koenig, L., Lenaerts, J. T. M., & Kuipers Munneke, P. (2020). Accumulation rates (2009–2017) in Southeast Greenland derived from airborne snow radar and comparison with regional climate models. *Annals of Glaciology*, 1–9. https://doi.org/10.1017/aog.2020.8

Morris, E. M., & Wingham, D. J. (2011). The effect of fluctuations in surface density, accumulation and compaction on elevation change rates along the EGIG line, central Greenland. *Journal of Glaciology*, *57*(203), 416–430. https://doi.org/10.3189/002214311796905613

Mosley-Thompson, E., Mcconnell, J., Bales, R., Lin, P. N., Steffen, K., Thompson, L., et al. (2001). Local to regional-scale variability of annual net accumulation on the Greenland Ice Sheet from PARCA cores. *Journal of Geophysical Research*, *106*(D24), 33,839–33,851. https://doi.org/10.1029/2001JD900067

Nghiem, S. V., Hall, D. K., Mote, T. L., Tedesco, M., Albert, M. R., Keegan, K., et al. (2012). The extreme melt across the Greenland Ice Sheet in 2012. *Geophysical Research Letters*, *39*, L20502. https://doi.org/10.1029/2012GL053611

Nilsson, J., Vallelonga, P., Simonsen, S. B., Sørensen, L. S., Forsberg, R., Dahl-Jensen, D., et al. (2015). Greenland 2012 melt event effects on CryoSat-2 radar altimetry: Effect of Greenland melt on Cryosat-2. *Geophysical Research Letters*, *42*, 3919–3926. https://doi.org/10.1002/2015GL063296

Noël, B., van de Berg, W. J., van Wessem, J. M., van Meijgaard, E., van As, D., Lenaerts, J. T. M., et al. (2018). Modelling the climate and surface mass balance of polar ice sheets using RACMO2—Part 1: Greenland (1958–2016). *The Cryosphere*, *12*(3), 811–831. https://doi.org/10.5194/tc-12-811-2018

Overly, T. B., Hawley, R. L., Helm, V., Morris, E. M., & Chaudhary, R. N. (2016). Greenland annual accumulation along the EGIG line, 1959-2004, from ASIRAS airborne radar and neutron-probe density measurements. *The Cryosphere*, *10*(4), 1679–1694. https://doi.org/10.5194/tc-10-1679-2016

Parry, V., Nienow, P., Mair, D., Scott, J., Hubbard, B., Steffen, K., & Wingham, D. (2007). Investigations of meltwater refreezing and density variations in the snowpack and firn within the percolation zone of the Greenland Ice Sheet. *Annals of Glaciology*, *46*, 61–68. https://doi.org/10.3189/172756407782871332

Rémy, F., Flament, T., Michel, A., & Blumstein, D. (2015). Envisat and SARAL/AltiKa observations of the Antarctic ice sheet: A comparison between the Ku-band and Ka-band. *Marine Geodesy*, *38*(sup1), 510–521. https://doi.org/10.1080/01490419.2014.985347

Renaud, A., Schumacher, E., Hughes, B., Oeschgerand, H., & Mühlemann, C. (1963). Tritium variations in Greenland ice. *Journal of Geophysical Research*, *68*(13), 3783–3783. https://doi.org/10.1029/JZ068i013p03783

Ridley, J. K., & Partington, K. (1988). A model of satellite radar altimeter return from ice sheets. *Remote Sensing*, *9*(4), 601–624. https://doi.org/10.1080/01431168808954881

Scott, J. B. T., Nienow, P., Mair, D., Parry, V., Morris, E., & Wingham, D. J. (2006). Importance of seasonal and annual layers in controlling backscatter to radar altimeters across the percolation zone of an ice sheet. *Geophysical Research Letters*, *33*, L24502. https://doi.org/10.1029/2006GL027974

Shepherd, A., Gilbert, L., Muir, A. S., Konrad, H., Mcmillan, M., Slater, T., et al. (2019). Trends in Antarctic Ice Sheet elevation and mass. *Geophysical Research Letters*, *46*, 8174–8183. https://doi.org/10.1029/2019GL082182

Simonsen, S. B., & Sørensen, L. S. (2017). Implications of changing scattering properties on Greenland Ice Sheet volume change from Cryosat-2 altimetry. *Remote Sensing of Environment*, *190*, 207–216. https://doi.org/10.1016/j.rse.2016.12.012

Simonsen, S. B., Stenseng, L., Adalgeirsdóttir, G., Fausto, R. S., Hvidberg, C. S., & Lucas-Picher, P. (2013). Assessing a multilayered dynamic firn-compaction model for Greenland with ASIRAS radar measurements. *Journal of Glaciology*, *59*(215), 545–558. https://doi.org/10.3189/2013JoG12J158

Skourup, H., Olesen, A. V., Sandberg Sørensen, L., Simonsen, S., Hvidegaard, S. M., Hansen, N., et al. (2019). ESA CryoVEx/EU ICE-ARC 2017

Slater, T., Shepherd, A., Mcmillan, M., Armitage, T. W. K., Otosaka, I., & Arthern, R. J. (2019). Compensating changes in the penetration depth of pulse-limited radar altimetry over the Greenland Ice Sheet. *IEEE Transactions on Geoscience and Remote Sensing*, *57*(12), 9633–9642. https://doi.org/10.1109/TGRS.2019.2928232

van de Wal, R. S. W., Boot, W., van den Broeke, M. R., Smeets, C. J. P. P., Reijmer, C. H., Donker, J. J. A., & Oerlemans, J. (2008). Large and rapid melt-induced velocity changes in the ablation zone of the Greenland Ice Sheet. *Science*, *321*(5885), 111–113. https://doi.org/10.1126/science.1158540

van den Broeke, M. R., Enderlin, E. M., Howat, I. M., Kuipers Munneke, P., Noel, B. P. Y., van de Berg, W. J., et al. (2016). On the recent contribution of the Greenland Ice Sheet to sea level change. *The Cryosphere*, *10*(5), 1933–1946. https://doi.org/10.5194/tc-10-1933-2016

Vandecrux, B., Fausto, R. S., Langen, P. L., As, D., MacFerrin, M., Colgan, W. T., et al. (2018). Drivers of firn density on the Greenland ice sheet revealed by weather station observations and modeling. *Journal of Geophysical Research: Earth Surface*, *123*, 2563–2576. https://doi.org/10.1029/2017JF004597

Verjans, V., Leeson, A. A., Stevens, C. M., MacFerrin, M., Noël, B., & van den Broeke, M. R. (2019). Development of physically based liquid water schemes for Greenland firn-densification models. *The Cryosphere*, *13*(7), 1819–1842. https://doi.org/10.5194/tc-13-1819-2019

Wingham, D., Rapley, C., & Griffiths, H. (1986). New techniques in satellite altimeter tracking systems. *Proceedings of IEEE International Geoscience & Remote Sensing Symposium*, 1339–1344.

References

Abshire, J. B., Sun, X., Riris, H., Sirota, J. M., McGarry, J. F., Palm, S., Yi, D. and Liiva, P. (2005), 'Geoscience Laser Altimeter System (GLAS) on the ICESat Mission: On-orbit measurement performance', *Geophysical Research Letters* **32**(21).

Adodo, F. I., Rémy, F. and Picard, G. (2018), 'Seasonal variations of the backscattering coefficient measured by radar altimeters over the Antarctic Ice Sheet', *The Cryosphere* **12**(5), 1767–1778.

Adusumilli, S., Fricker, H. A., Medley, B., Padman, L. and Siegfried, M. R. (2020), 'Inter-annual variations in meltwater input to the Southern Ocean from Antarctic ice shelves', *Nature Geoscience* .

Adusumilli, S., Fricker, H. A., Siegfried, M. R., Padman, L., Paolo, F. S. and Ligtenberg, S. R. M. (2018), 'Variable Basal Melt Rates of Antarctic Peninsula Ice Shelves, 1994-2016', *Geophysical Research Letters* **45**(9), 4086–4095.

Amarouche, L., Thibaut, P., Zanife, O. Z., Dumont, J. P., Vincent, P. and Steunou, N. (2004), 'Improving the Jason-1 Ground Retracking to Better Account for Attitude Effects', *Marine Geodesy* **27**(1-2), 171–197.

Armitage, T. W. K. and Ridout, A. L. (2015), 'Arctic sea ice freeboard from AltiKa and comparison with CryoSat-2 and Operation IceBridge', *Geophysical Research Letters* **42**(16), 6724–6731.

REFERENCES

Armitage, T. W. K., Wingham, D. J. and Ridout, A. L. (2014), 'Meteorological Origin of the Static Crossover Pattern Present in Low-Resolution-Mode CryoSat-2 Data Over Central Antarctica', *IEEE Geoscience and Remote Sensing Letters* **11**(7), 1295–1299.

Arthern, R. J., Wingham, D. J. and Ridout, A. L. (2001), 'Controls on ERS altimeter measurements over ice sheets: Footprint-scale topography, backscatter fluctuations, and the dependence of microwave penetration depth on satellite orientation', *Journal of Geophysical Research: Atmospheres* **106**(D24), 33471–33484.

Aschwanden, A., Fahnestock, M. A., Truffer, M., Brinkerhoff, D. J., Hock, R., Khroulev, C., Mottram, R. and Khan, S. A. (2019), 'Contribution of the Greenland Ice Sheet to sea level over the next millennium', *Science advances* **5**(6), eaav9396–eaav9396.

Bamber, J. and Dawson, G. (2020), 'Complex evolving patterns of mass loss from Antarctica's largest glacier', *Nature Geoscience* **13**(2), 127–131.

Bamber, J. L. (1994), 'Ice sheet altimeter processing scheme', *International Journal of Remote Sensing* **15**(4), 925–938.

Bamber, J. L., Gomez-Dans, J. L. and Griggs, J. A. (2009), 'A new 1 km digital elevation model of the Antarctic derived from combined satellite radar and laser data - Part 1: Data and methods', *The Cryosphere* **3**(1), 101–111.

Bamber, J. L., Vaughan, D. G. and Joughin, I. (2000), 'Widespread Complex Flow in the Interior of the Antarctic Ice Sheet', *Science* **287**(5456), 1248–1250.

Banwell, A. F., MacAyeal, D. R. and Sergienko, O. V. (2013), 'Breakup of the Larsen B Ice Shelf triggered by chain reaction drainage of supraglacial lakes', *Geophysical Research Letters* **40**(22), 5872–5876.

Barletta, V. R., Bevis, M., Smith, B. E., Wilson, T., Brown, A., Bordoni, A., Willis, M., Khan, S. A., Rovira-Navarro, M., Dalziel, I., Smalley, R., Kendrick, E., Konfal, S., Caccamise, D. J., Aster, R. C., Nyblade, A. and Wiens, D. A. (2018), 'Observed

rapid bedrock uplift in Amundsen Sea Embayment promotes ice-sheet stability', *Science* **360**(6395), 1335–1339.

Benn, D. I., Cowton, T., Todd, J. and Luckman, A. (2017), 'Glacier Calving in Greenland', *Current Climate Change Reports* **3**(4), 282–290.

Benn, D. I., Warren, C. R. and Mottram, R. H. (2007), 'Calving processes and the dynamics of calving glaciers', *Earth-Science Reviews* **82**(3), 143–179.

Bennett, M. R. (2003), 'Ice streams as the arteries of an ice sheet: their mechanics, stability and significance', *Earth-Science Reviews* **61**(3), 309–339.

Benson, C. S. (1996), 'Stratigraphic Studies in the Snow and Firn of the Greenland Ice Sheet'.

Berthier, E., Scambos, T. A. and Shuman, C. A. (2012), 'Mass loss of Larsen B tributary glaciers (Antarctic Peninsula) unabated since 2002', *Geophysical Research Letters* **39**(13).

Bevis, M., Harig, C., Khan, S. A., Brown, A., Simons, F. J., Willis, M., Fettweis, X., van den Broeke, M. R., Madsen, F. B., Kendrick, E., Caccamise, D. J., van Dam, T., Knudsen, P. and Nylen, T. (2019), 'Accelerating changes in ice mass within Greenland, and the ice sheet's sensitivity to atmospheric forcing', *Proceedings of the National Academy of Sciences* **116**(6), 1934–1939.

Bevis, M., Wahr, J., Khan, S. A., Madsen, F. B., Brown, A., Willis, M., Kendrick, E., Knudsen, P., Box, J. E., van Dam, T., Caccamise, D. J., Johns, B., Nylen, T., Abbott, R., White, S., Miner, J., Forsberg, R., Zhou, H., Wang, J., Wilson, T., Bromwich, D. and Francis, O. (2012), 'Bedrock displacements in Greenland manifest ice mass variations, climate cycles and climate change', *Proceedings of the National Academy of Sciences* **109**(30), 11944.

Birol, F. and Niño, F. (2015), 'Ku- and Ka-band Altimeter Data in the Northwestern Medi-

terranean Sea: Impact on the Observation of the Coastal Ocean Variability', *Marine geodesy* **38**(sup1), 313–327.

Böning, C. W., Behrens, E., Biastoch, A., Getzlaff, K. and Bamber, J. L. (2016), 'Emerging impact of Greenland meltwater on deepwater formation in the North Atlantic Ocean', *Nature Geoscience* **9**(7), 523–527.

Bouzinac, C. (2012), CryoSat Product Handbook, Report.

Bowling, J. S., Livingstone, S. J., Sole, A. J. and Chu, W. (2019), 'Distribution and dynamics of Greenland subglacial lakes', *Nature Communications* **10**(1), 2810.

Brenner, A. C., Blndschadler, R. A., Thomas, R. H. and Zwally, H. J. (1983), 'Slope-induced errors in radar altimetry over continental ice sheets', *Journal of Geophysical Research: Oceans* **88**(C3), 1617–1623.

Brenner, A. C., DiMarzio, J. R. and Zwally, H. J. (2007), 'Precision and accuracy of satellite radar and laser altimeter data over the continental ice sheets', *IEEE Transactions on Geoscience and Remote Sensing* **45**(2), 321–331.

Broeke, M. R., Enderlin, E. M., Howat, I. M., Kuipers Munneke, P., Noël, B. P., Berg, W. J. v. d., Meijgaard, E. v. and Wouters, B. (2016), 'On the recent contribution of the Greenland ice sheet to sea level change', *The Cryosphere* **10**(5), 1933.

Bronner, E., Guillot, A. and Picot, N. (2016), SARAL/AltiKa Products Handbook, Report.

Brown, G. (1977), 'The average impulse response of a rough surface and its applications', *IEEE Transactions on Antennas and Propagation* **25**(1), 67–74.

Brown, J., Bradford, J., Harper, J., Pfeffer, W. T., Humphrey, N. and Mosley-Thompson, E. (2012), 'Georadar-derived estimates of firn density in the percolation zone, western Greenland ice sheet', *Journal of Geophysical Research: Earth Surface* **117**(F1), n/a–n/a.

Brun, E., David, P., Sudul, M. and Brunot, G. (1992), 'A numerical model to simulate snow-cover stratigraphy for operational avalanche forecasting', *Journal of Glaciology* **38**(128), 13–22.

Bunce, C., Carr, J. R., Nienow, P. W., Ross, N. and Killick, R. (2018), 'Ice front change of marine-terminating outlet glaciers in northwest and southeast Greenland during the 21st century', *Journal of Glaciology* **64**(246), 523–535.

Caesar, L., Rahmstorf, S., Robinson, A., Feulner, G. and Saba, V. (2018), 'Observed fingerprint of a weakening Atlantic Ocean overturning circulation', *Nature (London)* **556**(7700), 191–196.

Caron, L., Ivins, E. R., Larour, E., Adhikari, S., Nilsson, J. and Blewitt, G. (2018), 'GIA Model Statistics for GRACE Hydrology, Cryosphere, and Ocean Science', *Geophysical Research Letters* **45**(5), 2203–2212.

Carr, J. R., Vieli, A. and Stokes, C. (2013), 'Influence of sea ice decline, atmospheric warming, and glacier width on marine-terminating outlet glacier behavior in northwest Greenland at seasonal to interannual timescales', *Journal of Geophysical Research: Earth Surface* **118**(3), 1210–1226.

Christianson, K., Bushuk, M., Dutrieux, P., Parizek, B. R., Joughin, I. R., Alley, R. B., Shean, D. E., Abrahamsen, E. P., Anandakrishnan, S., Heywood, K. J., Kim, T.-W., Lee, S. H., Nicholls, K., Stanton, T., Truffer, M., Webber, B. G. M., Jenkins, A., Jacobs, S., Bindschadler, R. and Holland, D. M. (2016), 'Sensitivity of Pine Island Glacier to observed ocean forcing', *Geophysical Research Letters* **43**(20), 10,817–10,825.

Chu, V. W. (2014), 'Greenland ice sheet hydrology: A review', *Progress in physical geography* **38**(1), 19–54.

Church, J., Clark, P., Cazenave, A., Gregory, J., Jevrejeva, S., Levermann, A., Merrifield, M., Milne, G., Nerem, R., Nunn, P., Payne, A., Pfeffer, W., Stammer, D. and Unnikrishn, A. (2013), Sea Level Change Supplementary Material, Report.

REFERENCES

Colleoni, F., De Santis, L., Siddoway, C. S., Bergamasco, A., Golledge, N. R., Lohmann, G., Passchier, S. and Siegert, M. J. (2018), 'Spatio-temporal variability of processes across Antarctic ice-bed-ocean interfaces', *Nature Communications* **9**(1), 2289.

Cullen, R. (2010), CryoVEx Airborne Data Products Description, Report, European Space Agency.

Das, S. B., Joughin, I., Behn, M. D., Howat, I. M., King, M. A., Lizarralde, D. and Bhatia, M. P. (2008), 'Fracture Propagation to the Base of the Greenland Ice Sheet During Supraglacial Lake Drainage', *Science* **320**(5877), 778–781.

Davis, C. H. (1993), 'A surface and volume scattering retracking algorithm for ice sheet satellite altimetry', *IEEE Transactions on Geoscience and Remote Sensing* **31**(4), 811–818.

Davis, C. H. (1997), 'A robust threshold retracking algorithm for measuring ice-sheet surface elevation change from satellite radar altimeters', *IEEE Transactions on Geoscience and Remote Sensing* **35**(4), 974–979.

Davis, C. H. and Ferguson, A. C. (2004), 'Elevation change of the Antarctic ice sheet, 1995-2000, from ERS-2 satellite radar altimetry', *IEEE Transactions on Geoscience and Remote Sensing* **42**(11), 2437–2445.

Davis, C. H., Li, Y., McConnell, J. R., Frey, M. M. and Hanna, E. (2005), 'Snowfall-Driven Growth in East Antarctic Ice Sheet Mitigates Recent Sea-Level Rise', *Science* **308**(5730), 1898–1901.

Davis, C. H. and Segura, D. M. (2001), 'An algorithm for time series analysis of ice sheet surface elevations from satellite altimetry', *IEEE Transactions on Geoscience and Remote Sensing* **39**(1), 202–206.

Davis, P. E. D., Jenkins, A., Nicholls, K. W., Brennan, P. V., Abrahamsen, E. P., Heywood, K. J., Dutrieux, P., Cho, K. and Kim, T. (2018), 'Variability in Basal Melting

Beneath Pine Island Ice Shelf on Weekly to Monthly Timescales', *Journal of Geophysical Research: Oceans* **123**(11), 8655–8669.

de la Peña, S., Howat, I., Nienow, P., Van den Broeke, M., Mosley-Thompson, E., Price, S., Mair, D., Noël, B. and Sole, A. (2015), 'Changes in the firn structure of the western Greenland Ice Sheet caused by recent warming', *The Cryosphere* **9**(3), 1203–1211.

de la Peña, S., Nienow, P., Shepherd, A., Helm, V., Mair, D., Hanna, E., Huybrechts, P., Guo, Q., Cullen, R. and Wingham, D. (2010), 'Spatially extensive estimates of annual accumulation in the dry snow zone of the Greenland Ice Sheet determined from radar altimetry', *The Cryosphere* **4**(4), 467–474.

De Rydt, J., Reese, R., Paolo, F. S. and Gudmundsson, G. H. (2021), 'Drivers of Pine Island Glacier speed-up between 1996 and 2016', *The Cryosphere* **15**(1), 113–132.

DeConto, R. M. and Pollard, D. (2016), 'Contribution of Antarctica to past and future sea-level rise', *Nature* **531**(7596), 591–591.

Depoorter, M. A., Bamber, J. L., Griggs, J. A., Lenaerts, J. T. M., Ligtenberg, S. R. M., van den Broeke, M. R. and Moholdt, G. (2013), 'Calving fluxes and basal melt rates of Antarctic ice shelves', *Nature* **502**(7469), 89–92.

Dieng, H. B., Cazenave, A., Meyssignac, B. and Ablain, M. (2017), 'New estimate of the current rate of sea level rise from a sea level budget approach', *Geophysical Research Letters* **44**(8), 3744–3751.

Dupont, T. K. and Alley, R. B. (2005), 'Assessment of the importance of ice-shelf buttressing to ice-sheet flow', *Geophysical research letters* **32**(4), L04503–n/a.

Dutrieux, P., De Rydt, J., Jenkins, A., Holland, P. R., Ha, H. K., Lee, S. H., Steig, E. J., Ding, Q., Abrahamsen, E. P. and Schröder, M. (2014), 'Strong sensitivity of Pine Island ice-shelf melting to climatic variability', *Science* **343**(6167), 174–178.

REFERENCES

Edwards, T. L., Brandon, M. A., Durand, G., Edwards, N. R., Golledge, N. R., Holden, P. B., Nias, I. J., Payne, A. J., Ritz, C. and Wernecke, A. (2019), 'Revisiting Antarctic ice loss due to marine ice-cliff instability', *Nature* **566**(7742), 58–64.

Enderlin, E. M., Howat, I. M., Jeong, S., Noh, M., Angelen, J. H. and Broeke, M. R. (2014), 'An improved mass budget for the Greenland ice sheet', *Geophysical Research Letters* **41**(3), 866–872.

Escudier, P., Couhert, A., Mercier, F., Mallet, A., Thibaut, P., Tran, N., Amarouche, L., Picard, B., Carrere, L., Dibarboure, G., Ablain, M., Richard, J., Steunou, N., Dubois, P., Rio, M.-H. and Dorandeu, J. (2018), *Satellite Radar Altimetry: Principle, Accuracy, and Precision*, 1 edn, CRC Press, pp. 1–70.

Evans, D. L., Alpers, W., Cazenave, A., Elachi, C., Farr, T., Glackin, D., Holt, B., Jones, L., Liu, W. T., McCandless, W., Menard, Y., Moore, R. and Njoku, E. (2005), 'Seasat-A 25-year legacy of success', *Remote sensing of environment* **94**(3), 384–404.

Fahnestock, M., Adbalati, W., Luo, S. and Gogineni, S. (2001), 'Internal layer tracing and age-depth-accumulation relationships for the northern Greenland ice sheet', *Journal of Geophysical Research: Atmospheres* **106**(D24), 33789–33797.

Farinotti, D., Huss, M., Fürst, J. J., Landmann, J., Machguth, H., Maussion, F. and Pandit, A. (2019), 'A consensus estimate for the ice thickness distribution of all glaciers on Earth', *Nature Geoscience* **12**(3), 168–173.

Farrell, W. E. (1972), 'Deformation of the Earth by surface loads', *Reviews of Geophysics* **10**(3), 761–797.

Farrell, W. E. and Clark, J. A. (1976), 'On Postglacial Sea Level', *Geophysical Journal International* **46**(3), 647–667.

Fausto, R. S., Box, J. E., Vandecrux, B., Van As, D., Steffen, K., Macferrin, M. J., Machguth, H., Colgan, W., Koenig, L. S., McGrath, D., Charalampidis, C. and Braith-

waite, R. J. (2018), 'A snow density dataset for improving surface boundary conditions in Greenland ice sheet firn modeling', *Frontiers in Earth Science* .

Felikson, D., A. Catania, G., Bartholomaus, T. C., Morlighem, M. and Noël, B. P. Y. (2021), 'Steep Glacier Bed Knickpoints Mitigate Inland Thinning in Greenland', *Geophysical Research Letters* **48**(2), e2020GL090112.

Fettweis, X., Box, J. E., Agosta, C., Amory, C., Kittel, C., Lang, C., van As, D., Machguth, H. and Gallée, H. (2017), 'Reconstructions of the 1900-2015 Greenland ice sheet surface mass balance using the regional climate MAR model', *The Cryosphere* **11**(2), 1015–1033.

Fettweis, X., Hofer, S., Krebs-Kanzow, U., Amory, C., Aoki, T., Berends, C. J., Born, A., Box, J. E., Delhasse, A., Fujita, K., Gierz, P., Goelzer, H., Hanna, E., Hashimoto, A., Huybrechts, P., Kapsch, M. L., King, M. D., Kittel, C., Lang, C., Langen, P. L., Lenaerts, J. T. M., Liston, G. E., Lohmann, G., Mernild, S. H., Mikolajewicz, U., Modali, K., Mottram, R. H., Niwano, M., NoÃ≪l, B., Ryan, J. C., Smith, A., Streffing, J., Tedesco, M., van de Berg, W. J., van den Broeke, M., van de Wal, R. S. W., van Kampenhout, L., Wilton, D., Wouters, B., Ziemen, F. and Zolles, T. (2020), 'GrSMBMIP: intercomparison of the modelled 1980-2012 surface mass balance over the Greenland Ice Sheet', *The Cryosphere* **14**(11), 3935–3958.

Flament, T. and Remy, F. (2012), 'Dynamic thinning of Antarctic glaciers from along-track repeat radar altimetry', *Journal of Glaciology* **58**(211), 830–840.

Fretwell, P., Pritchard, H. D., Vaughan, D. G., Bamber, J. L., Barrand, N. E., Bell, R., Bianchi, C., Bingham, R. G., Blankenship, D. D., Casassa, G., Catania, G., Callens, D., Conway, H., Cook, A. J., Corr, H. F. J., Damaske, D., Damm, V., Ferraccioli, F., Forsberg, R., Fujita, S., Gim, Y., Gogineni, P., Griggs, J. A., Hindmarsh, R. C. A., Holmlund, P., Holt, J. W., Jacobel, R. W., Jenkins, A., Jokat, W., Jordan, T., King, E. C., Kohler, J., Krabill, W., Riger-Kusk, M., Langley, K. A., Leitchenkov, G., Leuschen, C., Luyendyk, B. P., Matsuoka, K., Mouginot, J., Nitsche, F. O., Nogi, Y., Nost, O. A., Popov, S. V., Rignot, E., Rippin, D. M., Rivera, A., Roberts, J.,

Ross, N., Siegert, M. J., Smith, A. M., Steinhage, D., Studinger, M., Sun, B., Tinto, B. K., Welch, B. C., Wilson, D., Young, D. A., Xiangbin, C. and Zirizzotti, A. (2013), 'Bedmap2: improved ice bed, surface and thickness datasets for Antarctica', *The Cryosphere* **7**(1), 375–393.

Fricker, H. A., Scambos, T., Bindschadler, R. and Padman, L. (2007), 'An Active Subglacial Water System in West Antarctica Mapped from Space', *Science* **315**(5818), 1544–1548.

Frieler, K., Clark, P. U., He, F., Buizert, C., Reese, R., Ligtenberg, S. R. M., van den Broeke, M. R., Winkelmann, R. and Levermann, A. (2015), 'Consistent evidence of increasing Antarctic accumulation with warming', *Nature Climate Change* **5**(4), 348–352.

Gardner, A. S., Moholdt, G., Scambos, T., Fahnstock, M., Ligtenberg, S., van den Broeke, M. and Nilsson, J. (2018), 'Increased West Antarctic and unchanged East Antarctic ice discharge over the last 7 years', *The Cryosphere* **12**(2), 521–547.

Gledhill, L. A. and Williamson, A. G. (2017), 'Inland advance of supraglacial lakes in north-west Greenland under recent climatic warming', *Annals of Glaciology* **59**(76pt1), 66–82.

Goelzer, H., Nowicki, S., Payne, A., Larour, E., Seroussi, H., Lipscomb, W. H., Gregory, J., Abe-Ouchi, A., Shepherd, A., Simon, E., Agosta, C., Alexander, P., Aschwanden, A., Barthel, A., Calov, R., Chambers, C., Choi, Y., Cuzzone, J., Dumas, C., Edwards, T., Felikson, D., Fettweis, X., Golledge, N. R., Greve, R., Humbert, A., Huybrechts, P., Le clec'h, S., Lee, V., Leguy, G., Little, C., Lowry, D. P., Morlighem, M., Nias, I., Quiquet, A., Rückamp, M., Schlegel, N.-J., Slater, D. A., Smith, R. S., Straneo, F., Tarasov, L., van de Wal, R. and van den Broeke, M. (2020), 'The future sea-level contribution of the Greenland ice sheet: a multi-model ensemble study of ISMIP6', *The Cryosphere* **14**(9), 3071–3096.

Goelzer, H., Robinson, A., Seroussi, H. and van de Wal, R. S. W. (2017), 'Recent Progress in Greenland Ice Sheet Modelling', *Current Climate Change Reports* **3**(4), 291–302.

Golledge, N. R., Keller, E. D., Gomez, N., Naughten, K. A., Bernales, J., Trusel, L. D. and Edwards, T. L. (2019), 'Global environmental consequences of twenty-first-century ice-sheet melt', *Nature* **566**(7742), 65–72.

Groh, A. and Horwath, M. (2016), 'The method of tailored sensitivity kernels for GRACE mass change estimates'.

Gudmundsson, G. H., Paolo, F. S., Adusumilli, S. and Fricker, H. A. (2019), 'Instantaneous Antarctic ice sheet mass loss driven by thinning ice shelves', *Geophysical Research Letters* **46**(23), 13903–13909.

Guerreiro, K., Fleury, S., Zakharova, E., Remy, F. and Kouraev, A. (2016), 'Potential for estimation of snow depth on Arctic sea ice from CryoSat-2 and SARAL/AltiKa missions', *Remote Sensing of Environment* **186**, 339–349.

Hall, D. K., Comiso, J. C., DiGirolamo, N. E., Shuman, C. A., Box, J. E. and Koenig, L. S. (2013), 'Variability in the surface temperature and melt extent of the Greenland ice sheet from MODIS', *Geophysical Research Letters* **40**(10), 2114–2120.

Hanna, E., Cappelen, J., Fettweis, X., Mernild, S. H., Mote, T. L., Mottram, R., Steffen, K., Ballinger, T. J. and Hall, R. J. (2021), 'Greenland surface air temperature changes from 1981 to 2019 and implications for ice-sheet melt and mass-balance change', *International Journal of Climatology* **41**(S1), E1336–E1352.

Hanna, E., Navarro, F. J., Pattyn, F., Domingues, C. M., Fettweis, X., Ivins, E. R., Nicholls, R. J., Ritz, C., Smith, B., Tulaczyk, S., Whitehouse, P. L. and Zwally, H. J. (2013), 'Ice-sheet mass balance and climate change', *Nature* **498**(7452), 51–59.

Hawley, R. L., Morris, E. M., Cullen, R., Nixdorf, U., Shepherd, A. P. and Wingham, D. J. (2006), 'ASIRAS airborne radar resolves internal annual layers in the dry-snow zone of Greenland', *Geophysical Research Letters* **33**(4), L04502.

REFERENCES

Helm, V., Humbert, A. and Miller, H. (2014), 'Elevation and elevation change of Greenland and Antarctica derived from CryoSat-2', *The Cryosphere* **8**(4), 1539–1559.

Helm, V., Rack, W., Cullen, R., Nienow, P., Mair, D., Parry, V. and Wingham, D. J. (2007), 'Winter accumulation in the percolation zone of Greenland measured by airborne radar altimeter', *Geophysical Research Letters* **34**(6), L06501.

Holland, D. M., Thomas, R. H., de Young, B., Ribergaard, M. H. and Lyberth, B. (2008), 'Acceleration of Jakobshavn Isbrae triggered by warm subsurface ocean waters', *Nature Geoscience* **1**(10), 659–664.

Howat, I. M. and Eddy, A. (2011), 'Multi-decadal retreat of Greenland's marine-terminating glaciers', *Journal of Glaciology* **57**(203), 389–396.

Howat, I., Negrete, A. and Smith, B. (2015), 'MEaSUREs Greenland Ice Mapping Project (GIMP) Digital Elevation Model, Version 1'.

Hurkmans, R., Bamber, J. L. and Griggs, J. A. (2012), 'Brief communication 'Importance of slope-induced error correction in volume change estimates from radar altimetry'', *The Cryosphere* **6**(2), 447–451.

Johannessen, O. M., Khvorostovsky, K., Miles, M. W. and Bobylev, L. P. (2005), 'Recent Ice-Sheet Growth in the Interior of Greenland', *Science* **310**(5750), 1013–1016.

Joughin, I., Alley, R. B. and Holland, D. M. (2012), 'Ice-Sheet Response to Oceanic Forcing', *Science* **338**(6111), 1172–1176.

Joughin, I., Howat, I. M., Fahnestock, M., Smith, B., Krabill, W., Alley, R. B., Stern, H. and Truffer, M. (2008), 'Continued evolution of Jakobshavn Isbrae following its rapid speedup', *Journal of Geophysical Research: Earth Surface* **113**(F4).

Joughin, I., Shean, D. E., Smith, B. E. and Dutrieux, P. (2016), 'Grounding line variability and subglacial lake drainage on Pine Island Glacier, Antarctica', *Geophysical Research Letters* **43**(17), 9093–9102.

Joughin, I., Smith, B. E. and Medley, B. (2014), 'Marine Ice Sheet Collapse Potentially Under Way for the Thwaites Glacier Basin, West Antarctica', *Science* **344**(6185), 735–738.

Joughin, I. and Tulaczyk, S. (2002), 'Positive Mass Balance of the Ross Ice Streams, West Antarctica', *Science* **295**(5554), 476–480.

Kern, M., Cullen, R., Berruti, B., Bouffard, J., Casal, T., Drinkwater, M. R., Gabriele, A., Lecuyot, A., Ludwig, M., Midthassel, R., Navas Traver, I., Parrinello, T., Ressler, G., Andersson, E., Martin-Puig, C., Andersen, O., Bartsch, A., Farrell, S., Fleury, S., Gascoin, S., Guillot, A., Humbert, A., Rinne, E., Shepherd, A., van den Broeke, M. R. and Yackel, J. (2020), 'The Copernicus Polar Ice and Snow Topography Altimeter (CRISTAL) high-priority candidate mission', *The Cryosphere* **14**(7), 2235–2251.

Khazendar, A., Fenty, I. G., Carroll, D., Gardner, A., Lee, C. M., Fukumori, I., Wang, O., Zhang, H., Seroussi, H., Moller, D., Noël, B. P. Y., van den Broeke, M. R., Dinardo, S. and Willis, J. (2019), 'Interruption of two decades of Jakobshavn Isbrae acceleration and thinning as regional ocean cools', *Nature Geoscience* **12**(4), 277–283.

Khazendar, A., Rignot, E., Schroeder, D. M., Seroussi, H., Schodlok, M. P., Scheuchl, B., Mouginot, J., Sutterley, T. C. and Velicogna, I. (2016), 'Rapid submarine ice melting in the grounding zones of ice shelves in West Antarctica', *Nature Communications* **7**(1), 13243.

Khvorostovsky, K. S. (2012), 'Merging and Analysis of Elevation Time Series Over Greenland Ice Sheet From Satellite Radar Altimetry', *IEEE Transactions on Geoscience and Remote Sensing* **50**(1), 23–36.

King, M. D., Howat, I. M., Candela, S. G., Noh, M. J., Jeong, S., Noël, B. P. Y., van den Broeke, M. R., Wouters, B. and Negrete, A. (2020), 'Dynamic ice loss from the greenland ice sheet driven by sustained glacier retreat', *Communications Earth & Environment* **1**(1), 1.

REFERENCES

Kjær, K. H., Khan, S. A., Korsgaard, N. J., Wahr, J., Bamber, J. L., Hurkmans, R., van den Broeke, M., Timm, L. H., Kjeldsen, K. K., Bjørk, A. A., Larsen, N. K., Jørgensen, L. T., Færch-Jensen, A. and Willerslev, E. (2012), 'Aerial Photographs Reveal Late-20th-Century Dynamic Ice Loss in Northwestern Greenland', *Science* **337**(6094), 569.

Koenig, L. S., Ivanoff, A., Alexander, P. M., MacGregor, J. A., Fettweis, X., Panzer, B., Paden, J. D., Forster, R. R., Das, I., McConnell, J. R., Tedesco, M. and Leuschen, C. (2016), 'Annual Greenland accumulation rates (2009-2012) from airborne snow radar'.

Konrad, H., Gilbert, L., Cornford, S. L., Payne, A., Hogg, A., Muir, A. and Shepherd, A. (2017), 'Uneven onset and pace of ice-dynamical imbalance in the Amundsen Sea Embayment, West Antarctica', *Geophysical Research Letters* **44**(2), 910–918.

Konrad, H., Shepherd, A., Gilbert, L., Hogg, A. E., McMillan, M., Muir, A. and Slater, T. (2018), 'Net retreat of Antarctic glacier grounding lines', *Nature Geoscience* **11**(4), 258–262.

Kuipers Munneke, P., Ligtenberg, S. R. M., Noël, B. P. Y., Howat, I. M., Box, J. E., Mosley-Thompson, E., McConnell, J. R., Steffen, K., Harper, J. T., Das, S. B. and Van Den Broeke, M. R. (2015), 'Elevation change of the Greenland Ice Sheet due to surface mass balance and firn processes, 1960-2014', *The Cryosphere* **9**(6), 2009–2025.

Kulp, S. A. and Strauss, B. H. (2019), 'New elevation data triple estimates of global vulnerability to sea-level rise and coastal flooding', *Nature Communications* **10**(1), 4844.

Lacroix, P., Dechambre, M., Legrésy, B., Blarel, F. and Rémy, F. (2008), 'On the use of the dual-frequency ENVISAT altimeter to determine snowpack properties of the Antarctic ice sheet', *Remote Sensing of Environment* **112**(4), 1712–1729.

Lacroix, P., Legrésy, B., Coleman, R., Dechambre, M. and Rémy, F. (2007), 'Dual-frequency altimeter signal from Envisat on the Amery ice-shelf', *Remote Sensing of Environment* **109**(3), 285–294.

Lawrence, I. R., Tsamados, M. C., Stroeve, J. C., Armitage, T. W. and Ridout, A. L. (2018), 'Estimating snow depth over Arctic sea ice from calibrated dual-frequency radar freeboards, journal = The Cryosphere', **12**(11), 3551–3564.

Laxon, S. (1994), 'Sea ice altimeter processing scheme at the EODC', *International Journal of Remote Sensing* **15**(4), 915–924.

Leeson, A. A., Shepherd, A., Briggs, K., Howat, I., Fettweis, X., Morlighem, M. and Rignot, E. (2015), 'Supraglacial lakes on the Greenland ice sheet advance inland under warming climate', *Nature Climate Change* **5**(1), 51–55.

Légrésy, B., Papa, F., Rémy, F., Vinay, G., van den Bosch, M. and Zanife, O.-Z. (2005), 'ENVISAT radar altimeter measurements over continental surfaces and ice caps using the ICE-2 retracking algorithm', *Remote Sensing of Environment* **95**(2), 150–163.

Lenaerts, J. T. M., Medley, B., Broeke, M. R. and Wouters, B. (2019), 'Observing and Modeling Ice Sheet Surface Mass Balance', *Reviews of Geophysics* **57**(2), 376–420.

Levinsen, J. F., Simonsen, S. B., Sorensen, L. S. and Forsberg, R. (2016), 'The Impact of DEM Resolution on Relocating Radar Altimetry Data Over Ice Sheets', *IEEE Journal of Selected Topics in Applied Earth Observations and Remote Sensing* **9**(7), 3158–3163.

Lhermitte, S., Sun, S., Shuman, C., Wouters, B., Pattyn, F., Wuite, J., Berthier, E. and Nagler, T. (2020), 'Damage accelerates ice shelf instability and mass loss in Amundsen Sea Embayment', *Proceedings of the National Academy of Sciences* **117**(40), 24735–24741.

Ligtenberg, S., Helsen, M. and Broeke, M. (2011), 'An improved semi-empirical model for the densification of Antarctic firn', *The Cryosphere* **5**(4), 809.

Ligtenberg, S. R. M., Horwath, M., Van Den Broeke, M. R. and Legresy, B. (2012), 'Quantifying the seasonal "breathing" of the Antarctic ice sheet', *Geophysical Research Letters* **39**, 6.

REFERENCES

Ligtenberg, S. R. M., Kuipers Munneke, P., Noël, B. P. Y. and van den Broeke, M. R. (2018), 'Brief communication: Improved simulation of the present-day Greenland firn layer (1960-2016)', *The Cryosphere* **12**(5), 1643–1649.

Ligtenberg, S. R. M., Kuipers Munneke, P. and van den Broeke, M. R. (2014), 'Present and future variations in Antarctic firn air content', *The Cryosphere* **8**(5), 1711–1723.

Liu, H., Jezek, K. C. and Li, B. (1999), 'Development of an Antarctic digital elevation model by integrating cartographic and remotely sensed data: A geographic information system based approach', *Journal of Geophysical Research: Solid Earth* **104**(B10), 23199–23213.

Liu, H., Jezek, K. C., Li, B. and Zhao, Z. (2015), 'Radarsat Antarctic Mapping Project Digital Elevation Model, Version 2'.

Looyenga, H. (1965), 'Dielectric constants of heterogeneous mixtures', *Physica* **31**(3), 401–406.

Macferrin, M., Machguth, H., As, D. v., Charalampidis, C., Stevens, C. M., Heilig, A., Vandecrux, B., Langen, P. L., Mottram, R., Fettweis, X., Broeke, M. R. v. D., Pfeffer, W. T., Moussavi, M. S. and Abdalati, W. (2019), 'Rapid expansion of Greenland's low-permeability ice slabs', *Nature* **573**(7774), 403–407.

Machguth, H., MacFerrin, M., van As, D., Box, J. E., Charalampidis, C., Colgan, W., Fausto, R. S., Meijer, H. A. J., Mosley-Thompson, E. and van de Wal, R. S. W. (2016), 'Greenland meltwater storage in firn limited by near-surface ice formation', *Nature Climate Change* **6**, 390.

Markus, T., Neumann, T., Martino, A., Abdalati, W., Brunt, K., Csatho, B., Farrell, S., Fricker, H., Gardner, A., Harding, D., Jasinski, M., Kwok, R., Magruder, L., Lubin, D., Luthcke, S., Morison, J., Nelson, R., Neuenschwander, A., Palm, S., Popescu, S., Shum, C., Schutz, B. E., Smith, B., Yang, Y. and Zwally, J. (2017), 'The Ice, Cloud, and land Elevation Satellite-2 (ICESat-2): Science requirements, concept, and implementation', *Remote Sensing of Environment* **190**, 260–273.

Martín-Español, A., Zammit-Mangion, A., Clarke, P. J., Flament, T., Helm, V., King, M. A., Luthcke, S. B., Petrie, E., Rémy, F., Schön, N., Wouters, B. and Bamber, J. L. (2016), 'Spatial and temporal Antarctic Ice Sheet mass trends, glacio-isostatic adjustment, and surface processes from a joint inversion of satellite altimeter, gravity, and GPS data', *Journal of Geophysical Research: Earth Surface* **121**(2), 182–200.

Masson-Delmotte, V., Zhai, P., Pörtner, H.-O., Roberts, D., Skea, J., Shukla, P., Pirani, A., Moufouma-Okia, W., Péan, C., Pidcock, R., Connors, S., Matthews, J., Chen, Y., Zhou, X., Gomis, M., Lonnoy, E., Maycock, T., Tignor, M. and Waterfield, T. (2018), 'Global Warming of 1.5°C. An IPCC Special Report on the impacts of global warming of 1.5°C above pre-industrial levels and related global greenhouse gas emission pathways, in the context of strengthening the global response to the threat of climate change, sustainable development, and efforts to eradicate poverty', *Intergovermental Panel on Climate Change* .

McMillan, M., Leeson, A., Shepherd, A., Briggs, K., Armitage, T. W. K., Hogg, A., Kuipers Munneke, P., van den Broeke, M., Noël, B., van de Berg, W. J., Ligtenberg, S., Horwath, M., Groh, A., Muir, A. and Gilbert, L. (2016), 'A high-resolution record of Greenland mass balance: High-Resolution Greenland Mass Balance', *Geophysical Research Letters* **43**(13), 7002–7010.

McMillan, M., Nienow, P., Shepherd, A., Benham, T. and Sole, A. (2007), 'Seasonal evolution of supra-glacial on the Greenland Ice Sheet', *Earth and Planetary Science Letters* **262**, 484–492.

McMillan, M., Shepherd, A., Muir, A., Gaudelli, J., Hogg, A. E. and Cullen, R. (2017), 'Assessment of CryoSat-2 interferometric and non-interferometric SAR altimetry over ice sheets', *Advances in Space Research* .

McMillan, M., Shepherd, A., Sundal, A., Briggs, K., Muir, A., Ridout, A., Hogg, A. and Wingham, D. (2014), 'Increased ice losses from Antarctica detected by CryoSat-2', *Geophysical Research Letters* **41**(11), 3899–3905.

Medley, B., Joughin, I., Das, S. B., Steig, E. J., Conway, H., Gogineni, S., Criscitiello, A. S., McConnell, J. R., Smith, B. E., van den Broeke, M. R., Lenaerts, J. T. M., Bromwich, D. H. and Nicolas, J. P. (2013), 'Airborne-radar and ice-core observations of annual snow accumulation over Thwaites Glacier, West Antarctica confirm the spatiotemporal variability of global and regional atmospheric models', *Geophysical Research Letters* **40**(14), 3649–3654.

Mercer, J. H. (1978), 'West Antarctic ice sheet and CO2 greenhouse effect: a threat of disaster', *Nature* **271**(5643), 321–325.

Meredith, M., Sommerkorn, M., Cassotta, S., Derksen, C., Ekaykin, A., Hollowed, A., Kofinas, G., Mackintosh, A., Melbourne-Thomas, J., Muelbert, M., Ottersen, G., Pritchard, H. and Schuur, E. (2019), 'Polar Regions', *Intergovernmental Panel on Climate Change* .

Michel, A., Flament, T. and Rémy, F. (2014), 'Study of the Penetration Bias of ENVISAT Altimeter Observations over Antarctica in Comparison to ICESat Observations', *Remote Sensing* **6**(10), 9412–9434.

Miège, C., Forster, R. R., Box, J. E., Burgess, E. W., McConnell, J. R., Pasteris, D. R. and Spikes, V. B. (2013), 'Southeast Greenland high accumulation rates derived from firn cores and ground-penetrating radar', *Annals of Glaciology* **54**(63), 322–332.

Mitrovica, J. X., Tamisiea, M. E., Davis, J. L. and Milne, G. A. (2001), 'Recent mass balance of polar ice sheets inferred from patterns of global sea-level change', *Nature* **409**(6823), 1026–1029.

Montgomery, L., Koenig, L., Lenaerts, J. T. M. and Kuipers Munneke, P. (2020), 'Accumulation rates (2009-2017) in Southeast Greenland derived from airborne snow radar and comparison with regional climate models', *Annals of Glaciology* pp. 1–9.

Moon, T., Joughin, I., Smith, B. and Howat, I. (2012), '21st-Century Evolution of Greenland Outlet Glacier Velocities', *Science* **336**(6081), 576–578.

Morlighem, M., Rignot, E., Binder, T., Blankenship, D., Drews, R., Eagles, G., Eisen, O., Ferraccioli, F., Forsberg, R., Fretwell, P., Goel, V., Greenbaum, J. S., Gudmundsson, H., Guo, J., Helm, V., Hofstede, C., Howat, I., Humbert, A., Jokat, W., Karlsson, N. B., Lee, W. S., Matsuoka, K., Millan, R., Mouginot, J., Paden, J., Pattyn, F., Roberts, J., Rosier, S., Ruppel, A., Seroussi, H., Smith, E. C., Steinhage, D., Sun, B., Broeke, M. R. v. d., Ommen, T. D. v., Wessem, M. v. and Young, D. A. (2020), 'Deep glacial troughs and stabilizing ridges unveiled beneath the margins of the Antarctic ice sheet', *Nature Geoscience* **13**(2), 132–137.

Morlighem, M., Williams, C. N., Rignot, E., An, L., Arndt, J. E., Bamber, J. L., Catania, G., Chauché, N., Dowdeswell, J. A., Dorschel, B., Fenty, I., Hogan, K., Howat, I., Hubbard, A., Jakobsson, M., Jordan, T. M., Kjeldsen, K. K., Millan, R., Mayer, L., Mouginot, J., Noël, B. P. Y., O'Cofaigh, C., Palmer, S., Rysgaard, S., Seroussi, H., Siegert, M. J., Slabon, P., Straneo, F., van den Broeke, M. R., Weinrebe, W., Wood, M. and Zinglersen, K. B. (2017), 'BedMachine v3: Complete Bed Topography and Ocean Bathymetry Mapping of Greenland From Multibeam Echo Sounding Combined With Mass Conservation', *Geophysical Research Letters* **44**(21), 11,051–11,061.

Morlighem, M., Wood, M., Seroussi, H., Choi, Y. and Rignot, E. (2019), 'Modeling the response of northwest Greenland to enhanced ocean thermal forcing and subglacial discharge', *The Cryosphere* **13**(2), 723–734.

Morris, E. M. and Wingham, D. J. (2011), 'The effect of fluctuations in surface density, accumulation and compaction on elevation change rates along the EGIG line, central Greenland', *Journal of Glaciology* **57**(203), 416–430.

Mosley-Thompson, E., McConnell, J., Bales, R., Lin, P. N., Steffen, K., Thompson, L., Edwards, R. and Bathke, D. (2001), 'Local to regional-scale variability of annual net accumulation on the Greenland ice sheet from PARCA cores', *Journal of Geophysical Research: Atmospheres* **106**(D24), 33839–33851.

Mouginot, J., Rignot, E., Bjørk, A. A., Van den Broeke, M., Millan, R., Morlighem, M.,

Noël, B., Scheuchl, B. and Wood, M. (2019), 'Forty-six years of Greenland Ice Sheet mass balance from 1972 to 2018', *Proceedings of the National Academy of Sciences* **116**(19), 9239–9244.

Mouginot, J., Rignot, E. and Scheuchl, B. (2014), 'Sustained increase in ice discharge from the Amundsen Sea Embayment, West Antarctica, from 1973 to 2013', *Geophysical Research Letters* **41**(5), 1576–1584.

Mouginot, J., Rignot, E., Scheuchl, B. and Millan, R. (2017), 'Comprehensive Annual Ice Sheet Velocity Mapping Using Landsat-8, Sentinel-1, and RADARSAT-2 Data', *Remote Sensing* **9**(4), 364.

Nerem, R. S., Beckley, B. D., Fasullo, J. T., Hamlington, B. D., Masters, D. and Mitchum, G. T. (2018), 'Climate-change-driven accelerated sea-level rise detected in the altimeter era', *Proceedings of the National Academy of Sciences* **115**(9), 2022–2025.

Nghiem, S. V., Hall, D. K., Mote, T. L., Tedesco, M., Albert, M. R., Keegan, K., Shuman, C. A., DiGirolamo, N. E. and Neumann, G. (2012), 'The extreme melt across the Greenland ice sheet in 2012', *Geophysical Research Letters* **39**(20).

Nias, I. J., Cornford, S. L., Edwards, T. L., Gourmelen, N. and Payne, A. J. (2019), 'Assessing Uncertainty in the Dynamical Ice Response to Ocean Warming in the Amundsen Sea Embayment, West Antarctica', *Geophysical Research Letters* **46**(20), 11253–11260.

Nilsson, J., Gardner, A., Sørensen, L. S. and Forsberg, R. (2016), 'Improved retrieval of land ice topography from CryoSat-2 data and its impact for volume-change estimation of the Greenland Ice Sheet', *The Cryosphere* **10**(6), 2953–2969.

Nilsson, J., Vallelonga, P., Simonsen, S. B., Sorensen, L. S., Forsberg, R., Dahl-Jensen, D., Hirabayashi, M., Goto-Azuma, K., Hvidberg, C. S., Kjaer, H. A. and Satow, K. (2015), 'Greenland 2012 melt event effects on CryoSat-2 radar altimetry', *Geophysical Research Letters* **42**(10), 3919–3926.

Noël, B., Berg, W. J. v. d., Wessem, J., Meijgaard, E. v., As, D. v., Lenaerts, J., Lhermitte, S., Kuipers Munneke, P., Smeets, C., Ulft, L. H. v. et al. (2018), 'Modelling the climate and surface mass balance of polar ice sheets using RACMO2–Part 1: Greenland (1958–2016)', *The Cryosphere* **12**(3), 811–831.

Noël, B., van de Berg, W. J., Lhermitte, S. and van den Broeke, M. R. (2019), 'Rapid ablation zone expansion amplifies north Greenland mass loss', *Science Advances* **5**(9), eaaw0123.

Otosaka, I. N., Shepherd, A., Casal, T. G. D., Coccia, A., Davidson, M., Di Bella, A., Fettweis, X., Forsberg, R., Helm, V., Hogg, A. E., Hvidegaard, S. M., Lemos, A., Macedo, K., Kuipers Munneke, P., Parrinello, T., Simonsen, S. B., Skourup, H. and Sørensen, L. S. (2020), 'Surface Melting Drives Fluctuations in Airborne Radar Penetration in West Central Greenland', *Geophysical Research Letters* **47**(17), e2020GL088293.

Otosaka, I., Shepherd, A. and Groh, A. (2021), 'Changes in the Elevation and Mass of the Northwest Greenland Ice Sheet', *in preparation* .

Otosaka, I., Shepherd, A. and McMillan, M. (2019), 'Ice Sheet Elevation Change in West Antarctica From Ka-Band Satellite Radar Altimetry', *Geophysical Research Letters* .

Overly, T. B., Hawley, R. L., Helm, V., Morris, E. M. and Chaudhary, R. N. (2016), 'Greenland annual accumulation along the EGIG line, 1959-2004, from ASIRAS airborne radar and neutron-probe density measurements', *The Cryosphere* **10**(4), 1679.

Palm, S. P., Yang, Y., Spinhirne, J. D. and Marshak, A. (2011), 'Satellite remote sensing of blowing snow properties over Antarctica', *Journal of Geophysical Research: Atmospheres* **116**(D16).

Palmer, S., McMillan, M. and Morlighem, M. (2015), 'Subglacial lake drainage detected beneath the Greenland ice sheet', *Nature Communications* **6**(1), 8408.

Palmer, S., Shepherd, A., Nienow, P. and Joughin, I. (2011), 'Seasonal speedup of the

Greenland Ice Sheet linked to routing of surface water', *Earth and Planetary Science Letters* **302**(3), 423–428.

Paolo, F. S., Fricker, H. A. and Padman, L. (2015), 'Volume loss from Antarctic ice shelves is accelerating', *Science* **348**(6232), 327–331.

Park, J. W., Gourmelen, N., Shepherd, A., Kim, S. W., Vaughan, D. G. and Wingham, D. J. (2013), 'Sustained retreat of the Pine Island Glacier', *Geophysical Research Letters* **40**(10), 2137–2142.

Parry, V., Nienow, P., Mair, D., Scott, J., Hubbard, B., Steffen, K. and Wingham, D. (2007), 'Investigations of meltwater refreezing and density variations in the snowpack and firn within the percolation zone of the Greenland ice sheet', *Annals of Glaciology* **46**, 61–68.

Partington, K. C., Cudlip, W., McIntyre, N. F. and King-Hele, S. (1987), 'Mapping of Amery Ice Shelf, Antarctica, Surface Features by Satellite Altimetry', *Annals of Glaciology* **9**, 183–188.

Pattyn, F. and Morlighem, M. (2020), 'The uncertain future of the Antarctic Ice Sheet', *Science* **367**(6484), 1331–1335.

Pattyn, F., Ritz, C., Hanna, E., Asay-Davis, X., DeConto, R., Durand, G., Favier, L., Fettweis, X., Goelzer, H., Golledge, N. R., Kuipers Munneke, P., Lenaerts, J. T. M., Nowicki, S., Payne, A. J., Robinson, A., Seroussi, H., Trusel, L. D. and van den Broeke, M. (2018), 'The Greenland and Antarctic ice sheets under 1.5°C global warming', *Nature Climate Change* **8**(12), 1053–1061.

Peltier, W. R. (2004), 'Global Glacial Isostasy and the Surface of the Ice-Age Earth: the ICE-5G (VM2) Model and GRACE', *Annual review of earth and planetary sciences* **32**(1), 111–149.

Prandi, P., Philipps, S., Pignot, V. and Picot, N. (2015), 'SARAL/AltiKa Global Statist-

ical Assessment and Cross-Calibration with Jason-2', *Marine Geodesy* **38**(sup1), 297–312.

Pritchard, H. D., Arthern, R. J., Vaughan, D. G. and Edwards, L. A. (2009), 'Extensive dynamic thinning on the margins of the Greenland and Antarctic ice sheets', *Nature* **461**(7266), 971–975.

Quenouille, M. H. (1956), 'Notes on bias in estimation', *Biometrika* **43**(3-4), 353–360.

Rémy, F., Flament, T., Michel, A. and Blumstein, D. (2015), 'Envisat and SARAL/AltiKa Observations of the Antarctic Ice Sheet: A Comparison Between the Ku-band and Ka-band', *Marine Geodesy* **38**(sup1), 510–521.

Rémy, F., Flament, T., Michel, A. and Verron, J. (2014), 'Ice sheet survey over Antarctica using satellite altimetry: ERS-2, Envisat, SARAL/AltiKa, the key importance of continuous observations along the same repeat orbit', *International Journal of Remote Sensing* **35**(14), 5497–5512.

Rémy, F. and Frezzotti, M. (2006), 'Antarctica ice sheet mass balance', *Comptes Rendus Geoscience* **338**(14), 1084–1097.

Rémy, F., Légrésy, B. and Benveniste, J. (2006), 'On the Azimuthally Anisotropy Effects of Polarization for Altimetric Measurements', *IEEE Transactions on Geoscience and Remote Sensing* **44**(11), 3289–3296.

Rémy, F., Mazzega, P., Houry, S., Brossier, C. and Minster, J. (1989), 'Mapping of the Topography of Continental Ice by Inversion of Satellite-altimeter Data', *Journal of Glaciology* **35**(119), 9.

Rémy, F., Memin, A. and Velicogna, I. (2017), *Applications of Satellite Altimetry to Study the Antarctic Ice Sheet*, CRC Press, pp. 505–522.

Renaud, A., Schumacher, E., Hughes, B., Oeschgerand, H. and Mühlemann, C. (1963), 'Tritium variations in Greenland Ice', *Journal of Geophysical Research* **68**(13), 3783–3783.

REFERENCES

Ridley, J. K. and Partington, K. (1988), 'A model of satellite radar altimeter return from ice sheets', *Remote Sensing* **9**(4), 601–624.

Rignot, E. (2008), 'Changes in West Antarctic ice stream dynamics observed with ALOS PALSAR data', *Geophysical Research Letters* **35**(12), L12505–n/a.

Rignot, E., Casassa, G., Gogineni, P., Krabill, W., Rivera, A. and Thomas, R. (2004), 'Accelerated ice discharge from the Antarctic Peninsula following the collapse of Larsen B ice shelf', *Geophysical research letters* **31**(18), L18401–n/a.

Rignot, E., Mouginot, J., Morlighem, M., Seroussi, H. and Scheuchl, B. (2014), 'Widespread, rapid grounding line retreat of Pine Island, Thwaites, Smith, and Kohler glaciers, West Antarctica, from 1992 to 2011', *Geophysical Research Letters* **41**(10), 3502–3509.

Rignot, E., Mouginot, J. and Scheuchl, B. (2011), 'MEaSUREs InSAR-Based Antarctica Ice Velocity Map'.

Rignot, E., Mouginot, J., Scheuchl, B., van den Broeke, M., van Wessem, M. J. and Morlighem, M. (2019), 'Four decades of Antarctic Ice Sheet mass balance from 1979-2017', *Proceedings of the National Academy of Sciences of the United States of America* **116**(4), 1095–1103.

Ritz, C., Edwards, T. L., Durand, G., Payne, A. J., Peyaud, V. and Hindmarsh, R. C. A. (2015), 'Potential sea-level rise from Antarctic ice-sheet instability constrained by observations', *Nature* **528**(7580), 115–118.

Riva, R. E. M., Bamber, J. L., Lavallée, D. A. and Wouters, B. (2010), 'Sea level fingerprint of continental water and ice mass change from GRACE', *Geophysical Research Letters, 37, 2010* **37**(19).

Riva, R. E. M., Gunter, B. C., Urban, T. J., Vermeersen, B. L. A., Lindenbergh, R. C., Helsen, M. M., Bamber, J. L., van de Wal, R. S. W., van den Broeke, M. R. and Schutz, B. E. (2009), 'Glacial Isostatic Adjustment over Antarctica from combined ICESat and GRACE satellite data', *Earth and Planetary Science Letters* **288**(3), 516–523.

Roemer, S., Legrésy, B., Horwath, M. and Dietrich, R. (2007), 'Refined analysis of radar altimetry data applied to the region of the subglacial Lake Vostok/Antarctica', *Remote Sensing of Environment* **106**(3), 269–284.

Scagliola, M. (2013), CryoSat footprints, Technical note.

Scambos, T. A., Bohlander, J. A., Shuman, C. A. and Skvarca, P. (2004), 'Glacier acceleration and thinning after ice shelf collapse in the Larsen B embayment, Antarctica', *Geophysical Research Letters* **31**(18).

Schmidtko, S., Heywood, K. J., Thompson, A. F. and Aoki, S. (2014), 'Multidecadal warming of Antarctic waters', *Science* **346**(6214), 1227–1231.

Schoof, C. (2007), 'Ice sheet grounding line dynamics: Steady states, stability, and hysteresis', *Journal of Geophysical Research: Earth Surface* **112**(F3).

Schröder, L., Horwath, M., Dietrich, R., Helm, V., Michiel, R. v. d. B. and Stefan, R. M. L. (2019), 'Four decades of Antarctic surface elevation changes from multi-mission satellite altimetry', *The Cryosphere* **13**(2), 427–449.

Schröder, L., Richter, A., Fedorov, D. V., Eberlein, L., Brovkov, E. V., Popov, S. V., Knöfel, C., Horwath, M., Dietrich, R., Matveev, A. Y., Scheinert, M. and Lukin, V. V. (2017), 'Validation of satellite altimetry by kinematic GNSS in central East Antarctica', *The Cryosphere* **11**(3), 1111–1130.

Schwatke, C., Dettmering, D., Börgens, E. and Bosch, W. (2015), 'Potential of SARAL/AltiKa for Inland Water Applications', *Marine geodesy* **38**(sup1), 626–643.

Scott, J. B. T., Mair, D., Nienow, P., Parry, V. and Morris, E. (2006), 'A ground-based radar backscatter investigation in the percolation zone of the Greenland ice sheet', *Remote Sensing of Environment* **104**(4), 361–373.

Seroussi, H., Nakayama, Y., Larour, E., Menemenlis, D., Morlighem, M., Rignot, E. and Khazendar, A. (2017), 'Continued retreat of Thwaites Glacier, West Antarctica,

controlled by bed topography and ocean circulation', *Geophysical Research Letters* **44**(12), 6191–6199.

Seroussi, H., Nowicki, S., Payne, A. J., Goelzer, H., Lipscomb, W. H., Abe-Ouchi, A., Agosta, C., Albrecht, T., Asay-Davis, X., Barthel, A., Calov, R., Cullather, R., Dumas, C., Galton-Fenzi, B. K., Gladstone, R., Golledge, N. R., Gregory, J. M., Greve, R., Hattermann, T., Hoffman, M. J., Humbert, A., Huybrechts, P., Jourdain, N. C., Kleiner, T., Larour, E., Leguy, G. R., Lowry, D. P., Little, C. M., Morlighem, M., Pattyn, F., Pelle, T., Price, S. F., Quiquet, A., Reese, R., Schlegel, N. J., Shepherd, A., Simon, E., Smith, R. S., Straneo, F., Sun, S., Trusel, L. D., Van Breedam, J., van de Wal, R. S. W., Winkelmann, R., Zhao, C., Zhang, T. and Zwinger, T. (2020), 'ISMIP6 Antarctica: a multi-model ensemble of the Antarctic ice sheet evolution over the 21st century', *The Cryosphere* **14**(9), 3033–3070.

Shepherd, A., Gilbert, L., Muir, A. S., Konrad, H., McMillan, M., Slater, T., Briggs, K. H., Sundal, A. V., Hogg, A. E. and Engdahl, M. (2019), 'Trends in Antarctic Ice Sheet Elevation and Mass', *Geophysical Research Letters* .

Shepherd, A., Hubbard, A., Nienow, P., King, M., McMillan, M. and Joughin, I. (2009), 'Greenland ice sheet motion coupled with daily melting in late summer', *Geophysical Research Letters* **36**(1), L01501.

Shepherd, A., Ivins, E., Rignot, E., Smith, B., van den Broeke, M., Velicogna, I., White-house, P., Briggs, K., Joughin, I., Krinner, G., Nowicki, S., Payne, T., Scambos, T., Schlegel, N., A, G., Agosta, C., Ahlstrøm, A., Babonis, G., Barletta, V. R., Bjørk, A. A., Blazquez, A., Bonin, J., Colgan, W., Csatho, B., Cullather, R., Engdahl, M. E., Felikson, D., Fettweis, X., Forsberg, R., Hogg, A. E., Gallee, H., Gardner, A., Gilbert, L., Gourmelen, N., Groh, A., Gunter, B., Hanna, E., Harig, C., Helm, V., Horvath, A., Horwath, M., Khan, S., Kjeldsen, K. K., Konrad, H., Langen, P. L., Lecavalier, B., Loomis, B., Luthcke, S., McMillan, M., Melini, D., Mernild, S., Mohajerani, Y., Moore, P., Mottram, R., Mouginot, J., Moyano, G., Muir, A., Nagler, T., Nield, G., Nilsson, J., Noël, B., Otosaka, I., Pattle, M. E., Peltier, W. R., Pie, N., Rietbroek, R., Rott, H.,

Sandberg Sørensen, L., Sasgen, I., Save, H., Scheuchl, B., Schrama, E., Schröder, L., Seo, K.-W., Simonsen, S. B., Slater, T., Spada, G., Sutterley, T., Talpe, M., Tarasov, L., van de Berg, W. J., van der Wal, W., van Wessem, M., Vishwakarma, B. D., Wiese, D., Wilton, D., Wagner, T., Wouters, B., Wuite, J. and The, I. T. (2020), 'Mass balance of the Greenland Ice Sheet from 1992 to 2018', *Nature* **579**(7798), 233–239.

Shepherd, A. and Nowicki, S. (2017), 'Improvements in ice-sheet sea-level projections', *Nature Climate Change* **7**(10), 672–674.

Shepherd, A., Wingham, D. J., Justin, A. D. M. and Hugh, F. J. C. (2001), 'Inland Thinning of Pine Island Glacier, West Antarctica', *Science* **291**(5505), 862–864.

Shepherd, A., Wingham, D. J. and Mansley, J. A. D. (2002), 'Inland thinning of the Amundsen Sea sector, West Antarctica', *Geophysical Research Letters* **29**(10), 1364–2–4.

Simonsen, S. B. and Sorensen, L. S. (2017), 'Implications of changing scattering properties on Greenland ice sheet volume change from Cryosat-2 altimetry', *Remote Sensing of Environment* **190**, 207–216.

Simonsen, S. B., Stenseng, L., Aðalgeirsdóttir, G., Fausto, R. S., Hvidberg, C. S. and Lucas-Picher, P. (2013), 'Assessing a multilayered dynamic firn-compaction model for Greenland with ASIRAS radar measurements', *Journal of Glaciology* **59**(215), 545–558.

Skourup, H., Olesen, A. V., Sandberg Sorensen, L., Simonsen, S., Hvidegaard, S. M., Hansen, N., Olsesen, A. F., Coccia, A., Helm, V., Ladkin, R. S., Forsberg, R., Hogg, A. E., Otosaka, I., Shepherd, A., C., H. and Wilkinson, J. (2019), ESA CryoVEx/EU ICE-ARC 2017, Report.

Slater, D. A., Nienow, P. W., Goldberg, D. N., Cowton, T. R. and Sole, A. J. (2017), 'A model for tidewater glacier undercutting by submarine melting', *Geophysical Research Letters* **44**(5), 2360–2368.

REFERENCES

Slater, T., Hogg, A. E. and Mottram, R. (2020), 'Ice-sheet losses track high-end sea-level rise projections', *Nature Climate Change* **10**(10), 879–881.

Slater, T., Shepherd, A., McMillan, M., Armitage, T. W. K., Otosaka, I. and Arthern, R. J. (2019), 'Compensating Changes in the Penetration Depth of Pulse-Limited Radar Altimetry Over the Greenland Ice Sheet', *IEEE Transactions on Geoscience and Remote Sensing* **PP**(99), 1–10.

Slater, T., Shepherd, A., McMillan, M., Muir, A., Gilbert, L., Hogg, A. E., Konrad, H. and Parrinello, T. (2018), 'A new digital elevation model of Antarctica derived from CryoSat-2 altimetry', *The Cryosphere* **12**(4), 1551–1562.

Smith, B. E., Fricker, H. A., Joughin, I. R. and Tulaczyk, S. (2017), 'An inventory of active subglacial lakes in Antarctica detected by ICESat (2003-2008)', *Journal of Glaciology* **55**(192), 573–595.

Smith, B. E., Gourmelen, N., Huth, A. and Joughin, I. (2017), 'Connected subglacial lake drainage beneath Thwaites Glacier, West Antarctica', *The Cryosphere* **11**(1), 451–467.

Smith, B., Fricker, H. A., Gardner, A. S., Medley, B., Nilsson, J., Paolo, F. S., Holschuh, N., Adusumilli, S., Brunt, K., Csatho, B., Harbeck, K., Markus, T., Neumann, T., Siegfried, M. R. and Zwally, H. J. (2020), 'Pervasive ice sheet mass loss reflects competing ocean and atmosphere processes', *Science* **368**(6496), 1239–1242.

Sørensen, L. S., Simonsen, S. B., Forsberg, R., Khvorostovsky, K., Meister, R. and Engdahl, M. E. (2018), '25 years of elevation changes of the Greenland Ice Sheet from ERS, Envisat, and CryoSat-2 radar altimetry', *Earth and Planetary Science Letters* **495**, 234–241.

Sørensen, L. S., Simonsen, S. B., Nielsen, K., Lucas-Picher, P., Spada, G., Adalgeirsdottir, G., Forsberg, R. and Hvidberg, C. S. (2011), 'Mass balance of the Greenland ice sheet (2003-2008) from ICESat data - the impact of interpolation, sampling and firn density', *The Cryosphere* **5**(1), 173–186.

Steunou, N., Picot, N., Sengenes, P., Noubel, J. and Frery, M. L. (2015), 'AltiKa Radiometer: Instrument Description and In-Flight Performance', *Marine Geodesy* **38**(sup1), 43–61.

Stevens, L. A., Behn, M. D., McGuire, J. J., Das, S. B., Joughin, I., Herring, T., Shean, D. E. and King, M. A. (2015), 'Greenland supraglacial lake drainages triggered by hydrologically induced basal slip', *Nature* **522**(7554), 73–76.

Stokes, C. R., Sanderson, J. E., Miles, B. W. J., Jamieson, S. S. R. and Leeson, A. A. (2019), 'Widespread distribution of supraglacial lakes around the margin of the East Antarctic Ice Sheet', *Scientific Reports* **9**(1), 13823.

Studinger, M. (2014, updated 2018*a*), 'IceBridge ATM L2 Icessn Elevation, Slope, and Roughness, Version 2'.

Studinger, M. (2014, updated 2018*b*), 'IceBridge ATM L4 Surface Elevation Rate of Change, Version 1'.

Sun, X., Abshire, J. B., Borsa, A. A., Fricker, H. A., Yi, D., DiMarzio, J. P., Paolo, F. S., Brunt, K. M., Harding, D. J. and Neumann, G. A. (2017), 'ICESAT/GLAS Altimetry Measurements: Received Signal Dynamic Range and Saturation Correction', *IEEE Transactions on Geoscience and Remote Sensing* **55**(10), 5440–5454.

Suryawanshi, M. R., Chander, S., Oza, S. R. and Bahuguna, I. M. (2019), 'Variability in the ice sheet elevations over Antarctica derived from repetitive SARAL/AltiKa radar altimeter data (2013-2016)', *Journal of Earth System Science* **128**(3), 64.

Sutterley, T. C., Velicogna, I., Rignot, E., Mouginot, J., Flament, T., Van Den Broeke, M. R., info:eu, r. d. n., Van Wessem, J. M. and Reijmer, C. H. (2014), 'Mass loss of the Amundsen Sea Embayment of West Antarctica from four independent techniques', *Geophysical Research Letters* **41**(23), 8421–8428.

Tedesco, M. and Fettweis, X. (2020), 'Unprecedented atmospheric conditions (1948-2019)

drive the 2019 exceptional melting season over the Greenland ice sheet', *The Cryosphere* **14**(4), 1209–1223.

The IMBIE Team (2018), 'Mass balance of the Antarctic Ice Sheet from 1992 to 2017', *Nature* **558**(7709), 219–222.

Thomas, R. H., Martin, T. V. and Zwally, H. J. (1983), 'Mapping Ice-Sheet Margins from Radar Altimetry Data', *Annals of Glaciology* **4**, 283–288.

Thomas, R., Rignot, E., Kanagaratnam, P., Krabill, W. and Casassa, G. (2004), 'Force-perturbation analysis of Pine Island Glacier, Antarctica, suggests cause for recent acceleration', *Annals of Glaciology* **39**, 133–138.

Tilling, R., Kurtz, N. T., Bagnardi, M., Petty, A. A. and Kwok, R. (2020), 'Detection of Melt Ponds on Arctic Summer Sea Ice From ICESat-2', *Geophysical Research Letters* **47**(23), e2020GL090644.

van Angelen, J., van den Broeke, M., Wouters, B. and Lenaerts, J. (2014), 'Contemporary (1960-2012) Evolution of the Climate and Surface Mass Balance of the Greenland Ice Sheet', *Surveys in Geophysics* **35**(5), 1155–1174.

van de Wal, R. S. W., Boot, W., van den Broeke, M. R., Smeets, C. J. P. P., Reijmer, C. H., Donker, J. J. A. and Oerlemans, J. (2008), 'Large and Rapid Melt-Induced Velocity Changes in the Ablation Zone of the Greenland Ice Sheet', *Science* **321**(5885), 111–113.

van den Broeke, M., Bamber, J., Ettema, J., Rignot, E., Schrama, E., van de Berg, W. J., van Meijgaard, E., Velicogna, I. and Wouters, B. (2009), 'Partitioning recent Greenland mass loss', *Science* **326**(5955), 984–986.

Vandecrux, B., Fausto, R. S., Langen, P. L., As, D., Macferrin, M., Colgan, W. T., Ingeman-Nielsen, T., Steffen, K., Jensen, N. S., Moller, M. T. and Box, J. E. (2018), 'Drivers of Firn Density on the Greenland Ice Sheet Revealed by Weather Station Observations and Modeling', *Journal of Geophysical Research: Earth Surface* **123**(10), 2563–2576.

Vaughan, D. G., Marshall, G. J., Connolley, W. M., Parkinson, C., Mulvaney, R., Hodgson, D. A., King, J. C., Pudsey, C. J. and Turner, J. (2003), 'Recent Rapid Regional Climate Warming on the Antarctic Peninsula', *Climatic Change* **60**(3), 243–274.

Velicogna, I., Mohajerani, Y., Geruo, A., Landerer, F., Mouginot, J., Noel, B., Rignot, E., Sutterley, T., van den Broeke, M., van Wessem, J. and Wiese, D. (2020), 'Continuity of ice sheet mass loss in Greenland and Antarctica from the GRACE and GRACE Follow-On missions', *Geophysical Research Letters* **47**(8), e2020GL087291.

Verjans, V., Leeson, A. A., Stevens, C. M., MacFerrin, M., Noël, B. and van den Broeke, M. R. (2019), 'Development of physically based liquid water schemes for Greenland firn-densification models', *The Cryosphere* **13**(7), 1819–1842.

Verron, J., Bonnefond, P., Aouf, L., Birol, F., Bhowmick, S. A., Calmant, S., Conchy, T., Crétaux, J.-F., Dibarboure, G., Dubey, A. K., Faugère, Y., Guerreiro, K., Gupta, P. K., Hamon, M., Jebri, F., Kumar, R., Morrow, R., Pascual, A., Pujol, M.-I., Rémy, E., Rémy, F., Smith, W. H. F., Tournadre, J. and Vergara, O. (2018), 'The Benefits of the Ka-Band as Evidenced from the SARAL/AltiKa Altimetric Mission: Scientific Applications', *Remote Sensing* **10**(2), 163.

Verron, J., Sengenes, P., Lambin, J., Noubel, J., Steunou, N., Guillot, A., Picot, N., Coutin-Faye, S., Sharma, R., Gairola, R. M., Murthy, D. V. A. R., Richman, J. G., Griffin, D., Pascual, A., Rémy, F. and Gupta, P. K. (2015), 'The SARAL/AltiKa Altimetry Satellite Mission', *Marine Geodesy* **38**(sup1), 2–21.

Wahr, J. M. (1985), 'Deformation induced by polar motion', *Journal of Geophysical Research: Solid Earth* **90**(B11), 9363–9368.

Wake, L. M., Lecavalier, B. S. and Bevis, M. (2016), 'Glacial Isostatic Adjustment (GIA) in Greenland: a Review', *Current Climate Change Reports* **2**(3), 101–111.

WCRP Global Sea Level Budget Group (2018), 'Global sea-level budget 1993-present', *Earth Syst. Sci. Data* **10**(3), 1551–1590.

REFERENCES

Wilson, N., Straneo, F. and Heimbach, P. (2017), 'Satellite-derived submarine melt rates and mass balance (2011-2015) for Greenland's largest remaining ice tongues', *The Cryosphere* **11**(6), 2773–2782.

Wingham, D., Francis, C., Baker, S., Bouzinac, C., Brockley, D., Cullen, R., de Chateau-Thierry, P., Laxon, S., Mallow, U. and Mavrocordatos, C. (2006), 'CryoSat: A mission to determine the fluctuations in Earth's land and marine ice fields', *Advances in Space Research* **37**(4), 841–871.

Wingham, D. J., Ridout, A. J., Scharroo, R., Arthern, R. and Shum, C. K. (1998), 'Antarctic Elevation Change from 1992 to 1996', *Science* **282**(5388), 456–458.

Wingham, D. J., Wallis, D. W. and Shepherd, A. (2009), 'Spatial and temporal evolution of Pine Island Glacier thinning, 1995-2006', *Geophysical Research Letters* **36**(17), L17501–np.

Wingham, D., Rapley, C. and Griffiths, H. (1986), New techniques in satellite altimeter tracking systems, *in* 'Proceedings of IGARSS', Vol. 86, pp. 1339–1344.

Winkelmann, R., Levermann, A., Ridgwell, A. and Caldeira, K. (2015), 'Combustion of available fossil fuel resources sufficient to eliminate the Antarctic Ice Sheet', *Science Advances* **1**(8), e1500589.

Wood, M., Rignot, E., Fenty, I., An, L., Bjørk, A., van den Broeke, M., Cai, C., Kane, E., Menemenlis, D., Millan, R., Morlighem, M., Mouginot, J., Noël, B., Scheuchl, B., Velicogna, I., Willis, J. K. and Zhang, H. (2021), 'Ocean forcing drives glacier retreat in Greenland', *Science Advances* **7**(1), eaba7282.

Wood, M., Rignot, E., Fenty, I., Menemenlis, D., Millan, R., Morlighem, M., Mouginot, J. and Seroussi, H. (2018), 'Ocean-Induced Melt Triggers Glacier Retreat in Northwest Greenland', *Geophysical Research Letters* **45**(16), 8334–8342.

Woodhouse, I. H. (2006), *Introduction to microwave remote sensing*, Taylor & Francis.

Wouters, B., Martin-Español, A., Helm, V., Flament, T., van Wessem, J. M., Ligtenberg, S. R., Van den Broeke, M. R. and Bamber, J. L. (2015), 'Dynamic thinning of glaciers on the Southern Antarctic Peninsula', *Science* **348**(6237), 899–903.

Wright, A. and Siegert, M. (2012), 'A fourth inventory of Antarctic subglacial lakes', *Antarctic science* **24**(6), 659–664.

Yang, Q., Yang, Y., Wang, Z., Zhang, B. and Jiang, H. (2018), 'Elevation Change Derived from SARAL/ALtiKa Altimetric Mission: Quality Assessment and Performance of the Ka-Band', *Remote Sensing* **10**(4), 539.

Zwally, H. J., Bindschadler, R. A., Brenner, A. C., Major, J. A. and Marsh, J. G. (1989), 'Growth of Greenland Ice Sheet: Measurement', *Science* **246**(4937), 1587–1589.

Zwally, H. J., Li, J., Brenner, A. C., Beckley, M., Cornejo, H. G., DiMarzio, J., Giovinetto, M. B., Neumann, T. A., Robbins, J., Saba, J. L., Yi, D. and Wang, W. (2011), 'Greenland ice sheet mass balance: distribution of increased mass loss with climate warming; 2003-07 versus 1992-2002', *Journal of Glaciology* **57**(201), 88–102.